All-Optical Interferometric Switches for Data Regeneration in Fiber Optic Networks

by

Shelby Jay Savage

Submitted to the Department of Electrical Engineering and Computer Science
in partial fulfillment of the requirements for the degree of

Doctor of Philosophy in Electrical Engineering

at the

MASSACHUSETTS INSTITUTE OF TECHNOLOGY

May 2007
[June 2007)

Author ....
Department of Electrical Engineering and Computer Science
May 22, 2007

Certified by ....
Erich P. Ippen
Elihu Thomson Professor of Electrical Engineering
Thesis Supervisor

Certified by ....
Scott A. Hamilton
MIT Lincoln Laboratory, Assistant Group Leader
Thesis Supervisor

Accepted by ....
Arthur C. Smith
Chairman, Department Committee on Graduate Students

All-Optical Interferometric Switches for Data Regeneration in Fiber Optic Networks

by

Shelby Jay Savage

Submitted to the Department of Electrical Engineering and Computer Science
on May 22, 2007, in partial fulfillment of the
requirements for the degree of
Doctor of Philosophy in Electrical Engineering

Abstract

In the thirty years since the installation of the first fiber optic data link, data rates in installed fiber links have risen from a few Mb/s to tens of Gb/s. In the laboratory, data rates in a single optical fiber have already reached tens of Tb/s. These data rates greatly exceed electronic processing rates, so researchers have turned to all-optical signal processing to achieve many basic network tasks, like wavelength conversion, packet switching, and data regeneration.

As data rates increase, the impairments caused by propagation through the glass of optical fiber become worse. Chromatic dispersion causes the temporal broadening of optical bits during propagation, leading to interference between neighboring bits. Nonlinear effects, like the nonlinear index of refraction and four-wave mixing, can cause interference between neighboring wavelength channels. The interaction of dispersion and nonlinearities can lead to variations in the timing of bits and the appearance of optical energy where there had been none.

All these effects make 1-bits and 0-bits difficult to distinguish. Today, these distortions are overcome by electronic regenerators. Optical data streams are converted to electrical signals, processed electronically, converted back to an optical signal, and returned to the optical network. In this way, regenerators prevent the accumulation of noise and prevent noise from contributing to the production of more noise. The electronic solution is costly because of the extra hardware required for optical to electrical to optical conversions and performs poorly because of the losses incurred by those conversions.

In this thesis, we investigate two regenerators that restore the data quality of ON/OFF keyed data without a conversion of the data to the electrical domain. Both regenerators are based on all-optical switches that take two inputs: the data pulses from the network, and a locally generated clock-pulse train. The all-optical switches then modulate the data pattern onto the clock-pulse train, which becomes the new data stream.

The first switch we consider, the WMFUNI, uses the nonlinear properties of fiber to produce the switching action. Using the WMFUNI regenerator, we demonstrate the propagation of 10 Gb/s data over 20,000 km of commercial optical fiber. We also demonstrate the WMFUNI's ability to operate on 40-Gb/s data. Unfortunately, fiber has only a weak nonlinearity, so the WMFUNI is large (~40 cm×40 cm).

The second switch uses the much stronger nonlinearity of a semiconductor optical amplifier (SOA). SOA-based switches can be integrated onto chip-scale optics. The switch we test, the SOA-MZI, fits on a ~0.5 cm×1 cm chip. Using the SOA-MZI regenerator, we demonstrate the propagation of 10 Gb/s data over 10,000 km of commercial optical fiber. We also show in simulation that the SOA-MZI's operation may be extended to 40 Gb/s.

Thesis Supervisor: Erich P. Ippen
Title: Elihu Thomson Professor of Electrical Engineering

Thesis Supervisor: Scott A. Hamilton
Title: MIT Lincoln Laboratory, Assistant Group Leader

Acknowledgments

This dissertation is the labor of many, including the engineers directly involved in my research and the friends and family who gave me encouragement and hope throughout my graduate studies. I know how much of my success I owe to others, and it is my pleasure to acknowledge them here.

It has been a great privilege to work with Professor Erich Ippen, whose patience and knowledge have been great sources of support for all seven years that he has been my advisor. His broad interests outside engineering have been a model for my own academic career. I also thank Professor Franz Kärtner for his service on my thesis committee and for the kindness I have known from him since my undergraduate days at MIT.

I was fortunate, when I needed it the most, to find an excellent supervisor at Lincoln Laboratory. Scott Hamilton has been my mentor and friend almost from the beginning of my graduate work. His boundless energy and sincere concern for my education were indispensable to the completion of my Doctorate. I was also fortunate to find fellow students to share my work in. Dr. Bryan Robinson has been a constant source of ideas and intuition. I have always enjoyed our mathematical, religious, and political discussions, which have enriched my life at MIT. Jade Wang has shared with me all the trials and uncertainties of graduate school, and without that shared experience and mutual concern I am sure I could not have finished this thesis. I learned much of what I have presented here from our daily struggles with the theory and equipment of our field.

Working at Lincoln Laboratory was the best academic choice I made at MIT. I thank Dr. Johnathan D. Moores for first introducing me to optical communications. His intelligence and kindness helped me decide to stay at MIT. I also thank Dr. Todd Ulmer for his friendship, advice, and musical talents. Many others at Lincoln Laboratory have contributed to this work, including Prof. Thomas Murphy, Dr. David Caplan, Dr. Steve Constantine, Chad Demers, Peg Danek, Claudia Fennelly, and Dr. Jeffrey Roth. I also thank my group leaders, Dr. William Keicher and Dr.

Donald Boroson, for supporting my work throughout my education.

A large share of credit for the completion of this thesis also belongs to those friends who reminded me unceasingly that life is more than engineering. I am thankful that Andy Copeland has been with me all the way through undergraduate and graduate education; there aren't many of us left from those first years at MIT. I thank John McKay for many wonderful conversations and long friendship. Jamie Byrum and Garrett Cradduck have always encouraged me by reminding me of the world that awaits me outside academics. I also thank Susanna Mierau, Lora Reineck, Andrew Shtulman, Christina Silcox, and Ryan Hall for their friendship through the years.

I owe an unpayable debt to my father, my mother, and my brother. My father is an engineer himself and first sparked my own interest in the world of machines. He has always been a great source of peace in my restless life. My mother is devoted to her sons. She pushed us to succeed and gave us everything we needed and more than we deserved. Her industry and keeness have always been a model for me. My brother, one year younger than I am, is my only lifelong friend and peer. I always wish him the best and am thankful for his unique place in my life.

To everyone I have mentioned and to those I have forgotten, I offer this thesis with the hope that it is worthy of our efforts. But still, vitae summa brevis, spem nos vetat incohare longam.

Contents

List of Figures

List of Tables

Chapter 1

Introduction

In 1977 GTE sent telephone voice data, coded as pulses of light, through kilometers of glass optical fiber at 6 Mb/s [1]. Now we measure the capacity of commercial optical fiber links in tens of Gb/s, and research groups have reported transmission of data at tens of Tb/s with spectral efficiencies above 3 b/s/Hz [2, 3, 4]. These data rates far exceed the processing speeds of electronic hardware. This problem is overcome by demultiplexing these high data rate channels down to many lower rate channels, which are then converted to electronic data channels. The channels are then processed electronically, converted back to optical signals, and finally multiplexed up to the optical data rate to propagate further in the network. For applications requiring complex logical operations, this solution remains the best one [5, 6].

For some applications, however, processing of the optical data signals in the optical domain (i.e., without an optical-electrical-optical conversion) offers several possible advantages, like higher speed and lower power consumption. For example, all-optical logic has been demonstrated at 100 Gb/s [7]. This speed advantage suggests that optical data can be processed at rates much faster than electronics and, therefore, without the need for demultiplexing and optical-to-electrical conversions. In fact, such logic has been experimentally tested in wavelength conversion [8, 9, 10], label swapping [11], packet synchronization [12], packet switching [13, 14], and data regeneration [15, 16, 17, 18].

This thesis considers the application of all-optical signal processing to data regeneration. Data in optical fiber networks are most often coded using ON/OFF keying (OOK), in which pulse envelopes are modulated onto a carrier wavelength of light. The presence of a pulse of light represents a 1-bit and the absence of a pulse represents a 0-bit. These pulses distort over long-distance propagation in fiber so that 0s and 1s become difficult to distinguish, as we will see in Section 1.1. To prevent runaway degradation of the data signal, we can place data regenerators periodically along the optical link to restore pulse quality so that errors do not accumulate. In this thesis I present two interferometric all-optical switches designed to regenerate OOK data and assess their performance in data regeneration.

1.1 Networks and Fiber Propagation

Data from electronic systems have to be multiplexed up to optical rates. There are several methods for doing so, two of which are shown in Figure 1-1. Commercial systems typically use wavelength-division multiplexing (WDM). In WDM systems, data in the optical link are divided among many channels, each with a different carrier wavelength. Figure 1-1 (a) shows part of a WDM system. The data are OOK in this case, although the data could instead be coded using phase-shift keying or one of many other modulation formats. Each channel is a train of data pulses modulated onto a distinct carrier wavelength, shown in the figure with different shades of grey. Transceivers (Tx/Rx) add and drop wavelength channels to and from the link. The technology for WDM systems is well-developed because of commercial and industrial investment, and very high data rates are possible. For example, Alcatel has demonstrated an experimental 2,100-km WDM optical link at 6.4 Tb/s [19]. Unfortunately, the time required to reconfigure transceivers to add and drop different wavelength channels is long compared to the length of a packet of data. Therefore, WDM networks are circuit-switched rather than packet-switched networks.

Slotted optical time-division multiplexed systems, on the other hand, provide the possibility of a packet-switched optical network [14]. Figure 1-1 (b) shows part of a slotted OTDM optical link. All the data are part of a single ultra-fast channel and are

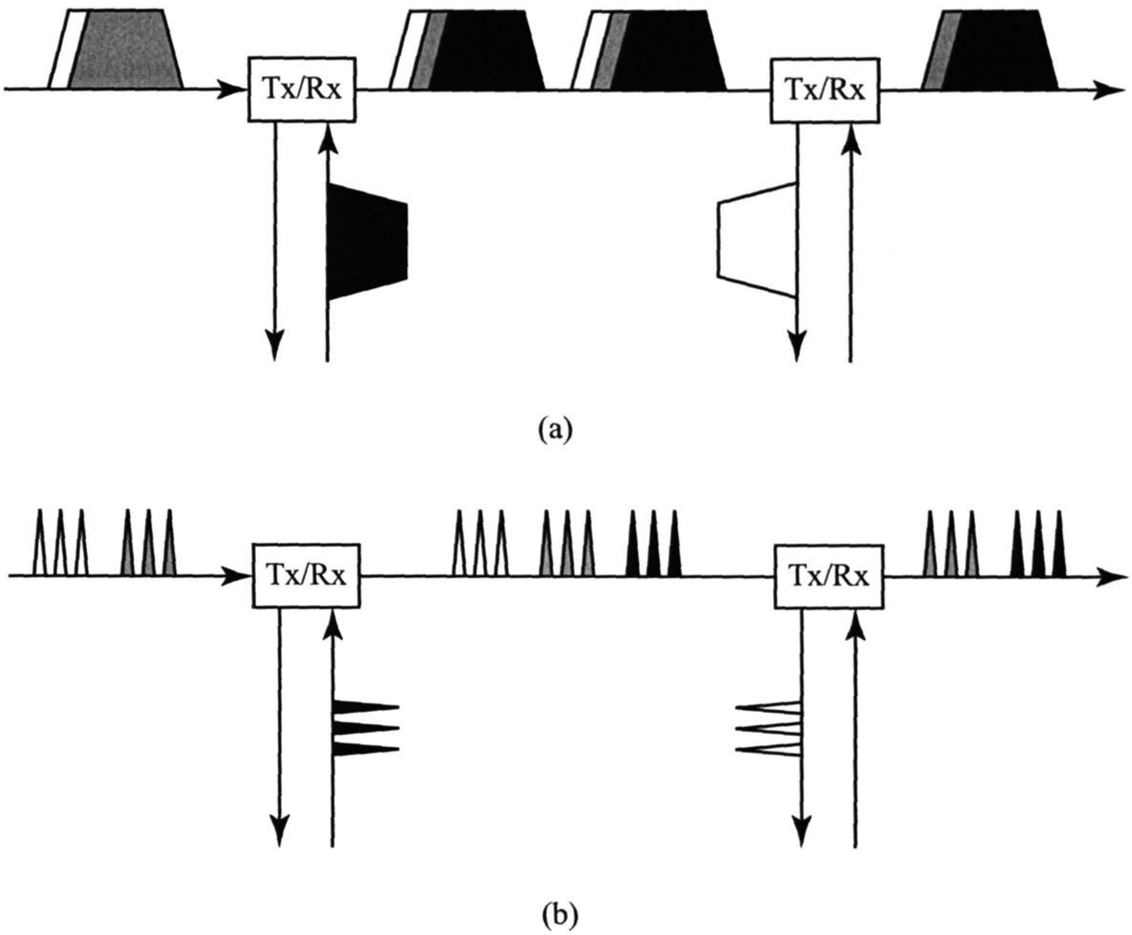

Figure 1-1: Two methods of multiplexing data: (a) wavelength-division multiplexing and (b) slotted optical time-division multiplexing.

composed, in this case, of OOK pulses modulated onto a single optical wavelength. This time, the different shades of grey denote different time slots in the data stream rather than different wavelengths. Transceivers burst data onto the optical channel in distinct time slots. This system allows on-demand resource allocation by a centralized processor and improves the efficiency of bandwidth allocation [20, 21]. Nonetheless, many of the basic tools required to make such a system work, like ultrafast data regeneration, still require development.

In fact, both of these multiplexing systems can, at high data rates and long propagation distances, require inline data regeneration because the optical fiber distorts data pulses during propagation. One effect is loss in the fiber, which decreases optical power by $\sim$0.25 dB/km. This loss can be compensated with Erbium-doped fiber amplifiers (EDFAs), which add noise to the optical signal. The other dominant distorting effects are chromatic dispersion, which causes different groups of wavelengths to have different group velocities, and the nonlinear index of refraction, which causes more intense light to experience a higher index of refraction. In higher rate systems the interactions that these distortions produce among pulses, both within and across wavelength channels, become more severe. This is especially true when higher rates are achieved with shorter optical pulses.

Figure 1-2 shows the results of a simulation of data pulse propagation in TrueWave fiber. The optical link, shown at the top of the figure, contains three 80-km spools of TrueWave fiber separated by EDFAs that restore the time-averaged power of the data signal. The EDFAs are assumed to be prefect so that they add no noise to the data signal. The only distorting effects included in the model are the chromatic dispersion (approximated out to third order) and the nonlinear index of refraction. The link also includes a dispersion compensation module, which perfectly compensates the chromatic dispersion in the 240 km of TrueWave. So, in the absence of a nonlinear index, the pulses will propagate undistorted through the link. The top plot in the figure shows the intensity envelope of the input data pulses. The optical pulses are modulated onto a 1550-nm carrier and have a width of 2.5 ps. The data rate is 100 Gb/s and the data pattern is a $2^5 - 1$ pseudorandom bit stream (PRBS). At the input to the link and after each EDFA, the data stream has a time-averaged optical power of 25 mW. The next two plots show the intensity envelope of the data pulses after one and two passes through the optical link. The 1s no longer have uniform intensity, and optical energy appears in the 0 spaces. We can see that some of the 0s and 1s have become indistinguishable, leading to errors at the data receiver.

1.2 Regeneration of Optical Data

A simple way to correct the data pulse distortions incurred during propagation through the TrueWave fiber above is intensity thresholding, shown in Figure 1-3.

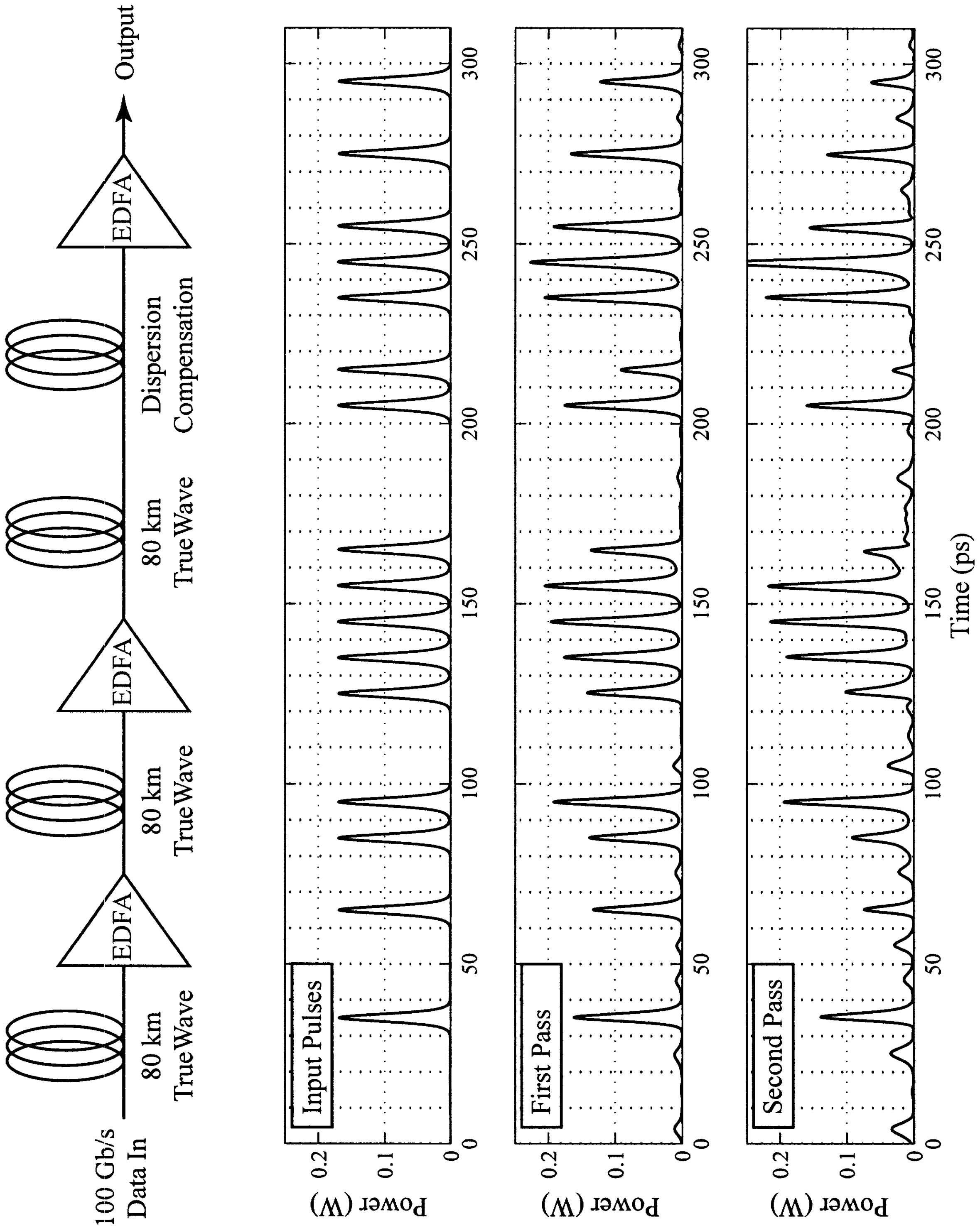

Figure 1-2: Simulation of the propagation of 2.5-ps wide pulses through 240 km of TrueWave optical fiber. The dispersion compensation module perfectly compensates any chromatic dispersion added by the TrueWave fiber, and the amplifiers are assumed to be noiseless.

The top diagram in the figure shows an ideal thresholder, which blocks optical pulses below a certain peak intensity threshold. Above that threshold it outputs a single intensity. Thus, the thresholder extinguishes optical power in the 0s and restores the 1s to a fixed peak intensity. Of course, no real thresholder works this way. A real thresholder may not have an instantaneous response time and will not have a perfect step-function nonlinearity. The bottom plot shows a more realistic thresholder with a raised sine-function nonlinearity. Its output reduces the optical power in the 0s and reduces variability in the intensity of the 1s, but not perfectly. The thresholder will occasionally flip a bit's value, for example, when a noise spike adds too much energy to a 0-bit. In most circumstances, however, the thresholder improves the signal-to-noise ratio so that noise will not accumulate and so that the noise will not contribute to interactions that produce even more noise.

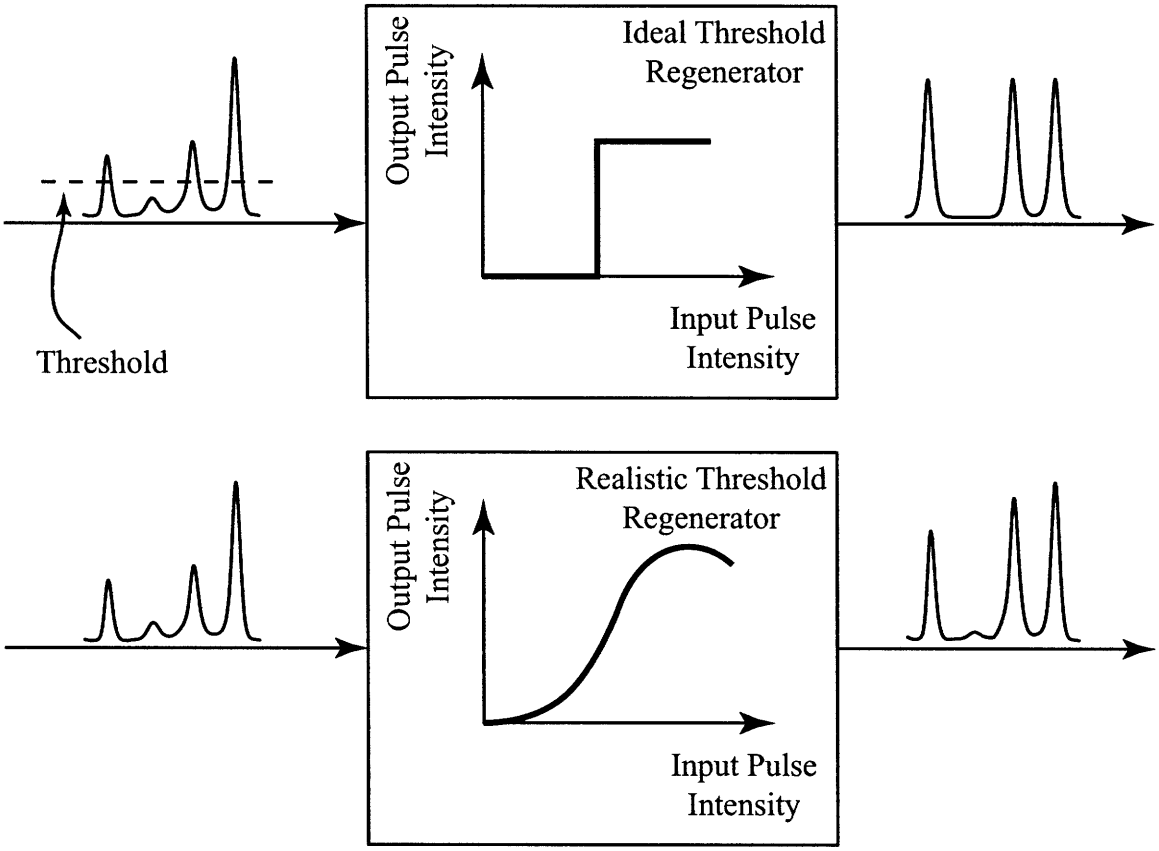

Figure 1-3: The thresholder is a simple regenerator that extinguishes noise in the 0s and restores 1s to their proper intensity. The top diagram shows an ideal thresholder acting on distorted data pulses. The bottom diagram shows a more realistic thresholder.

Thresholder regenerators are simple enough that all-optical designs exist and have been tested in transmission experiments. One common design is based on the nonlinear optical loop mirror (NOLM) [22], which has been demonstrated in regeneration experiments at 42.66 Gb/s over 10,000 km of transmission [23]. Nonetheless the thresholder does not accomplish everything an ideal regenerator should. For example, it does not necessarily correct phase distortions under the pulse's envelope. It also does not correct the random drifts of pulses from the center of their bit periods (timing jitter). Finally, it does not correct any polarization drifts that the data pulses have accumulated during propagation.

These problems can be solved with more complicated regenerators that correct timing jitter and restore pulse polarization by either modifying the data pulses directly or, more commonly, replacing them altogether. Ideally, such a regenerator accomplishes four things, the 4Rs of regeneration. First, it Re-amplifies the data to restore signal strength lost in propagation. Second, it Reshapes data pulses, restoring both the envelope shape and a flat phase under the envelope. Third, it Retimes the data pulses so that neighboring bits will not interfere with each other. Fourth, it Repolarizes the pulses so that variations in polarization at the regenerator's input do not affect the output polarization. The two regenerators presented in this thesis are all-optical 4R regenerators.

Today, however, such regenerators are electronic. Figure 1-4 one such regenerator. Optical data that have become distorted after long-distance propagation enter a demultiplexer, which divides the optical data among many electronic-rate data channels. Photodiodes then convert these channels to electrical signals, which are detected in electronic regenerators. These regenerators decide whether each bit is a 1 or 0 and then modulate the appropriate bit value onto the output of a laser transmitter.

The electronic solution requires extra hardware for demultiplexing the data and converting the data between the optical and electrical domains, and both these domain conversions add loss to the link. Instead, we can use the speed of all-optical switches to design a regenerator that operates at the line rate, eliminating the need for demultiplexing. Figure 1-5 shows a basic schematic for a broad class of all-optical

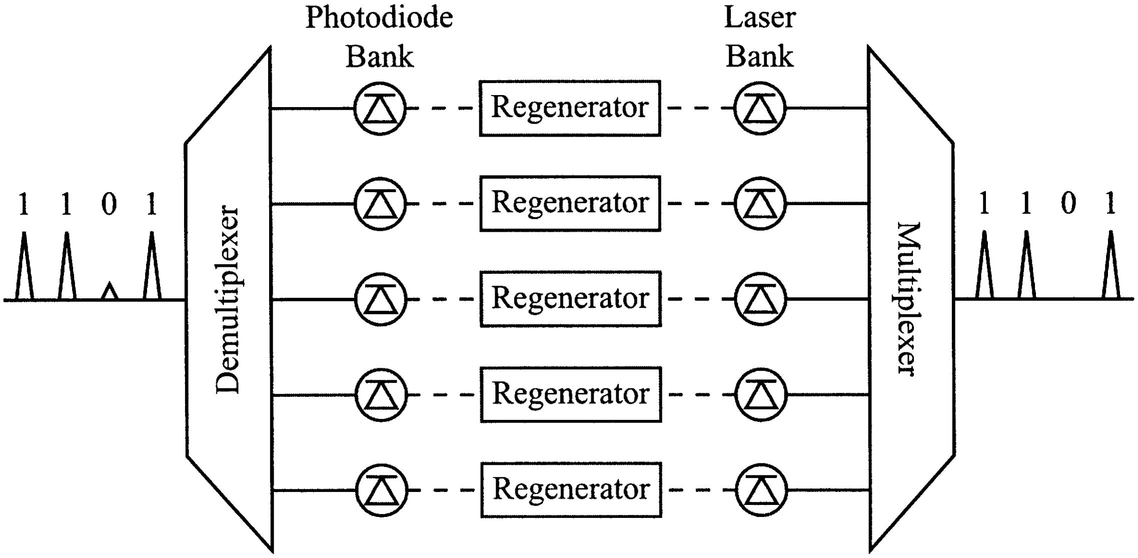

Figure 1-4: Schematic for an electronic regenerator. The regenerator boxes may also include network routing or other functionality.

regenerators. Incoming network data pulses (white) are distorted after propagation through optical fiber. The power of these pulses is split between a clock recovery circuit and an all-optical switch. The clock recovery circuit produces a clock signal (black), which may be optical or electrical, depending on the design. In the regenerators presented in this thesis, the clock is an optical pulse train, and the all-optical switch modulates the data pattern of the input data pulses (white) onto the clock pulses (black). In other designs, clock pulses enter the all-optical switch not to replace the data pulses, but to re-form them. One such regenerator uses synchronous

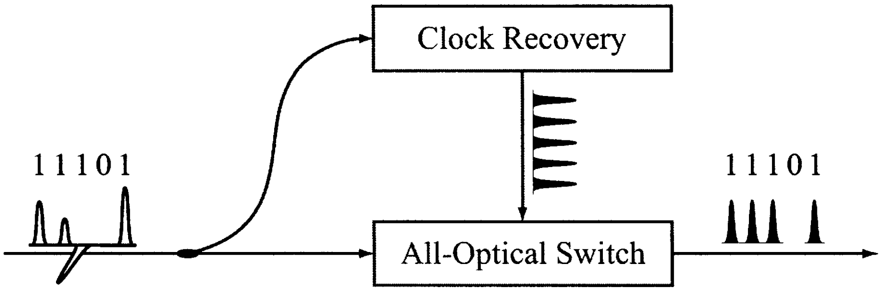

Figure 1-5: Schematic for a broad class of all-optical regenerators. In this case the clock pulses (black) are modulated with the original data pattern. In some regenerators, however, the clock pulses are used to improve the quality of the incoming data pulses, rather than replace them.

modulation, described in Chapter 2.

1.3 Organization of Work

This thesis presents an evaluation of two all-optical regenerators, both based on interferometric all-optical switches. Before presenting the results of this evaluation, Chapter 2 reviews four classes of regenerators with an emphasis on interferometer-based regenerators. Two of the classes are 2R regenerators that only re-amplify and reshape the pulses. One is a 3R regenerator that re-amplifies, reshapes, and retimes the pulses. The fourth class can be adapted to both 3R and 4R regeneration. Chapter 2 also discusses the importance of nonlinear materials for interferometric switches.

Chapter 3 discusses the two most common nonlinear media used in interferometer-based switches and regenerators. The first is optical fiber, which possesses a nearly instantaneous nonlinear index of refraction. The second is the semiconductor optical amplifier (SOA), which possesses a much stronger nonlinearity but also has a much longer response time. This chapter may be omitted on a first reading.

Chapter 4 discusses the experimental evaluation of a fiber-based all-optical regenerator: the wavelength-maintaining folded ultrafast nonlinear interferometer (WM-FUNI). Fiber-based regenerators have the advantage of being nearly instantaneous medium. SOAs, on the other hand, have long recovery times. So the effects on the SOA of a bit can linger through the next several bits, producing undesirable interference between neighboring bits. Fiber switches, however, can operate on bits without such interference. We have demonstrated operation of the WMFUNI in 10-Gb/s regeneration over 20,000-km of transmission. We have also shown that the WMFUNI operates at data rates up to 40 Gb/s.

Chapter 5 discusses the experimental evaluation of an SOA-based all-optical regenerator: the SOA Mach-Zehnder interferometer (SOA-MZI). The principle advantage of SOA-based regenerators and switches is their ability to be integrated onto semiconductor chips. We have demonstrated successful operation of an integrated SOA-MZI regenerator in a 10,000-km transmission experiment at 10 Gb/s. Simulations of the

SOA-MZI regenerator, presented in Section 5.2, show how the SOA-MZI's operation may be extended to 40 Gb/s.

This thesis evaluates the ability of all-optical regenerators to extend the propagation distances of high data-rate communications. All-optical solutions, however, are not the only possibilities. Chapter 6 will consider briefly how all-optical solutions may develop in the future, and how they may compare with other methods of high-rate communication, including opto-electronic regeneration and specially designed optical links that do not need regeneration.

Bibliography

[1] J. Hecht, *City of Light: The Story of Fiber Optics.* New York: Oxford University Press, 1999.

[2] A. Gnauck, G. Charlet, P. Tran, P. Winzer, C. Doerr, J. Centanni, E. Burrows, T. Kawanishi, T. Sakamoto, and K. Higuma, "25.6-Tb/s C+L-Band Transmission of Polarization-Multiplexed RZ-DQPSK Signals," *Optical Fiber Communication Conference, Postdeadline Session*, 2007.

[3] H. Masuda, A. Sano, T. Kobayashi, E. Yoshida, Y. Miyamoto, Y. Hibino, K. Hagimoto, T. Yamada, T. Furuta, and H. Fukuyama, "20.4-Tb/s (204 × 111 Gb/s) Transmission over 240 km Using Bandwidth-Maximized Hybrid Raman/EDFAs," *Optical Fiber Communication Conference, Postdeadline Session*, 2007.

[4] D. Foursa, A. Lucera, C. Davidson, J.-X. Cai, W. Anderson, Y. Cai, P. Corbett, W. Patterson, H. Li, M. Mazuczyk, M. Nissove, A. N. Pilipetskii, and N. Bergano, "2Tb/s (200×10Gb/s) Data Transmission over 7,300km Using 150km Spaced Repeaters Enabled by ROPA," *Optical Fiber Communication Conference, Postdeadline Session*, 2007.

[5] H. Caulfield, C. Vikram, and A. Zavalin, "Optical logic redux," *Optik*, vol. 117, no. 5, pp. 199–209, 2006.

[6] R. Keyes, "Optical Logic-in the Light of Computer Technology," *Journal of Modern Optics*, vol. 32, no. 5, pp. 525–535, 1985.

[7] K. L. Hall and K. A. Rauschenbach, "100-Gbit/s bitwise logic," *Optics Letters*, vol. 23, pp. 1271–1273, Aug. 1998.

[8] S. Nakamura, Y. Ueno, and K. Tajima, "168-Gb/s all-optical wavelength conversion with asymmetric-Mach-Zehnder-type switch," *IEEE Photonics Technology Letters*, vol. 13, no. 10, pp. 1091–1093, 2001.

[9] J. Leuthold, L. Möller, J. Jaques, S. Cabot, L. Zhang, P. Bernasconi, M. Cappuzzo, L. Gomez, E. Laskowski, E. Chen, *et al.*, "160 Gbit/s SOA all-optical wavelength converter and assessment of its regenerative properties," *Electronics Letters*, vol. 40, no. 9, pp. 554–555, 2004.

[10] C. Schubert, R. Ludwig, S. Watanabe, E. Futami, C. Schmidt, J. Berger, C. Boerner, S. Ferber, and H. Weber, "160 Gbit/s wavelength converter with 3R-regenerating capability," *Electronics Letters*, vol. 38, no. 16, pp. 903–904, 2002.

[11] D. Blumenthal, B. Olsson, G. Rossi, T. Dimmick, L. Rau, M. Masanovic, O. Lavrova, R. Doshi, O. Jerphagnon, J. Bowers, *et al.*, "All-optical label swapping networks and technologies," *Journal of Lightwave Technology*, vol. 18, no. 12, pp. 2058–2075, 2000.

[12] D. Apostolopoulos, O. Zouraraki, D. Petrantonakis, P. Bakopoulos, D. Tsiokos, E. Kehayas, and H. Avramopoulos, "Bit- and Packet-Level Self-Synchronization for All-Optical Label-Switched Network Nodes with Transparency to Network-Traffic," *Optical Fiber Communication Conference*, 2006.

[13] J. Wang, B. Robinson, S. Hamilton, and E. Ippen, "40-Gbit/s all-optical header processing for packet routing," *Optical Fiber Communication Conference, 2006*, p. 3, 2006.

[14] S. Hamilton, B. Robinson, T. Murphy, S. Savage, and E. Ippen, "100 Gb/s optical time-division multiplexed networks," *Journal of Lightwave Technology*, vol. 20, no. 12, pp. 2086–2100, 2002.

[15] B. Lavigne, E. Balmefrezol, P. Brindel, B. Dagens, R. Brenot, L. Pierre, J.-L. Moncelet, D. de la Grandiere, J.-C. Remy, J.-C. Bouley, B. Thedrez, and O. Leclerc, "Low input power all-optical 3R regenerator based on SOA devices for 42.66 Gbit/s ULH WDM RZ transmissions with 23 dB span loss and all-EDFA amplification," *Optical Fiber Communications Conference*, 2003.

[16] Z. Zhu, M. Funabashi, Z. Pan, L. Paraschis, and S. Yoo, "10 000-Hop Cascaded In-Line All-Optical 3R Regeneration to Achieve 1 250 000-km 10-Gb/s Transmission," *IEEE Photonics Technology Letters*, vol. 18, no. 5, pp. 718–720, 2006.

[17] S. J. Savage, B. S. Robinson, S. A. Hamilton, and E. P. Ippen, "200-pass picosecond-pulse transmission through a regenerative recirculating fiber loop," in *CLEO 2006 Technical Digest*, (Long Beach, CA), May 2006.

[18] J. P. Wang, S. J. Savage, B. S. Robinson, S. A. Hamilton, E. P. Ippen, R. Mu, H. Wang, L. Spiekman, and B. B. Stefanov, "Regeneration using an SOA-MZI in a 100-pass 10,000-km recirculating fiber loop," in *CLEO 2007 Technical Digest*, (Baltimore, MD), May 2007.

[19] G. Charlet, J. Antona, S. Lanne, P. Tran, W. Idler, M. Gorlier, S. Borne, A. Klekamp, C. Simonneau, L. Pierre, Y. Frignac, M. Molina, F. Beaumont, J.-P. Hamaide, and S. Bigo, "6.4 Tb/s (159× 42.7 Gb/s) Capacity Over 21× 100 km Using Bandwidth-Limited Phase-Shaped Binary Transmission," *28th European Conference on Optical Communication*, vol. 5, 2002.

[20] S. G. Finn, "HLAN-An Architecture for Optical Multi-Access Networks," *1995 Digest of the LEOS Summer Topical Meetings*, pp. 45–46, 1995.

[21] R. A. Barry, V. W. S. Chan, K. L. Hall, E. S. Kintzer, J. D. Moores, K. A. Rauschenbach, E. A. Swanson, L. E. Adams, C. R. Doerr, S. G. Finn, H. A. Haus, E. P. Ippen, W. S. Wong, and M. Haner, "All-Optical Network Consortium–ultrafast TDM networks," *JLT/JSAC Special Issue on Optical Networks*, vol. 14, p. 999, June 1996.

[22] M. Jinno and T. Matsumoto, "Nonlinear Sagnac interferometer switch and its applications," *IEEE Journal of Quantum Electronics*, vol. 28, no. 4, pp. 875–882, 1992.

[23] F. Seguineau, B. Lavigne, D. Rouvillain, P. Brindel, P. Pierre, L. Pierre, and O. Leclerc, "Experimental demonstration of simple NOLM-based 2R regenerator for 42.66 Gbit/s WDM long-haul transmissions," *Optical Fiber Communication Conference*, vol. 1, 2004.

Chapter 2

Overview of Regeneration

In order to extend data propagation distances and increase data rates, researchers and businesses have tested many different regenerators, including both electronic and all-optical solutions (see references [1, 2] for broad reviews of these areas). This thesis presents our work on two all-optical regenerators. Therefore, Section 2.1 reviews four broad classes of all-optical regenerators. The last class of regenerators described in Section 2.1 will be interferometer-based designs. Both of the regenerators we present in this thesis have interferometer-based designs, so we will review this class of regenerators in more detail in Section 2.2. As we saw in Figure 1-5, clock recovery is an important component in all-optical regenerators. Although this thesis focuses on the all-optical switch component of regenerators, an understanding of regeneration would be incomplete without a review of research in clock recovery. So, Section 2.2 will also describe some clock recovery solutions from the literature.

2.1 Classes of Regenerators

An ideal regenerator accomplishes four tasks, which are called the 4Rs. First, it Re-amplifies the optical data signal to compensate losses. Second, it Reshapes the data pulses, producing the proper envelope and phase. Third, it Retimes data pulses that have randomly drifted from the centers of their bit periods. Fourth, it Repolarizes data pulses to correct any drifts in polarization caused by fiber propagation. Repolar-

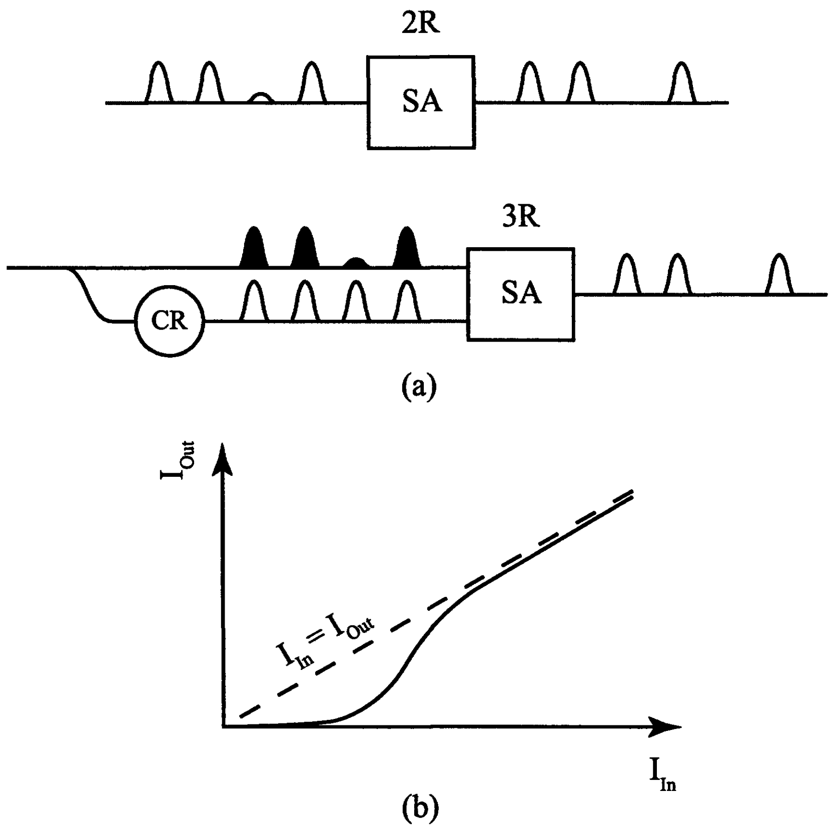

Figure 2-1: (a) Saturable absorbers can be used to produce all-optical switches. (b) The 2R self switch has an intensity-dependent transmittance, as shown in this plot of output pulse intensity versus input intensity.

ization ensures that all data packets leave the regenerator with the same polarization.

The four classes of all-optical regenerators described in this section cover most of the designs discussed in the literature. The first two are 2R regenerators, which re-amplify and reshape the data pulses. The third is a 3R regenerator, which re-amplifies, reshapes, and retimes the data. The fourth is a 4R regenerator and will be the subject of most of the rest of this thesis.

2.1.1 Intensity Self-Switches: Gain Modulation

Intensity self-switches use cross-gain modulation (XGM) to produce an intensity-dependent or pulse-energy-dependent gain or loss. These switches can be implemented in several ways, including with a semiconductor optical amplifier (SOA) or a saturable absorber (SA). Figure 2-1 (a) shows how an SA can be implemented as both a 2R and a 3R regenerator. The SA's transmittance depends on the input optical intensity, as shown in Figure 2-1 (b). At low intensities, the SA is opaque, but at high intensities it becomes transparent[1]. In the 2R case, this low-intensity opacity causes the SA regenerator to suppress small amounts of noise in the 0-bits. The 1s, as long as they have sufficient energy, pass through the SA unchanged.

In the 3R case, intense data pulses enter the SA along with weaker clock pulses, which are produced by a clock recovery unit (CR). The CR extracts the pulse rate from the network data pulses, producing a clock train with the same pulse rate and a different carrier wavelength. The presence of a data pulse switches the SA from opaque to transparent, which modulates the data pattern of the data pulses onto the clock pulses. SAs are rarely used this way as logical switches because the contrast between their opaque and transparent states are often only a few dB. For regeneration, however, such low contrast may be adequate.

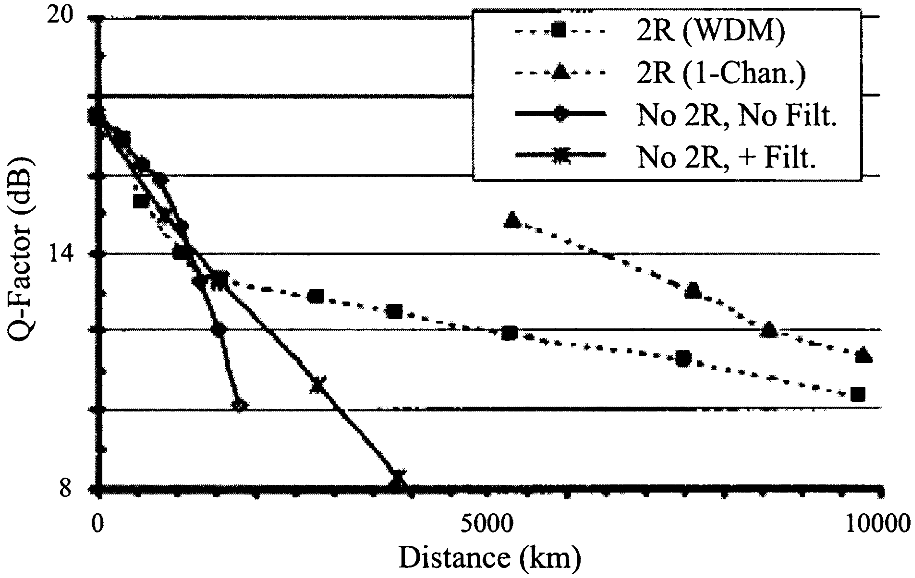

Figure 2-2: Experimental data showing the degradation of the Q-factor of a 40-Gb/s data stream versus propagation distance both with (solid) and without a cross-gain modulation regenerator (dashed). This plot comes from Figure 4 of Rouvillain, et al., OFC, 2002 [3].

---

[1] In fact, the SA's transmittance does not usually depend on instantaneous intensity. Rather, it often has a recovery time that causes its transmittance to depend on a weighted integral of the intensity over tens or even hundreds of picoseconds. In this simple description, we neglect this effect, although it has important consequences. For example, at high data rates, it causes the SA's behavior to depend on the value of previous bits, leading to undesirable pattern-dependent effects.

Figure 2-2 shows experimental data from [3] for a transmission experiment using an SA-based regenerator. The optical data were modulated onto a 40-Gb/s train of 8-ps pulses. The data pulses entered a loop containing 240 km of dispersion-compensated fiber and they propagated through the loop 41 times for a total propagation distance of ~10,000 km. The figure shows the Q-factor of the data train in the loop as a function of propagation distance. The Q-factor in ON/OFF keyed data is defined as

$$Q = \frac{|\mu_1 - \mu_0|}{\sigma_1 + \sigma_0},$$

where μ_1 and μ_0 are the means of the peak intensities of the 1s and 0s, and σ_1 and σ_0 are the standard deviations of the distribution of intensities of the 1s and 0s. The solid lines in the plot show the quick decline of the Q-factor when the loop contains no regenerator. When there is a data regenerator in the loop, the Q-factor drops much more slowly, as shown with the dashed lines in the plot.

2.1.2 Intensity Self-Switches: Self-Phase Modulation

In the previous section, we saw an intensity self-switch with an intensity-dependent transmissivity. This suppresses noise in the 0s, but does not suppress variations in the intensities of the 1s. A 2R regenerator could instead have an input-output response like that shown in Figure 2-3 (b). In this case, 1s entering the regenerator with a range of intensities all exit with the same intensity.

Figure 2-3 (a) shows a schematic of a 2R regenerator that produces the desired input-output response. A data pulse with carrier wavelength λ_0 enters an Erbium-doped fiber amplifier (EDFA), which increases the intensity of the pulse. The pulse then enters a section of nonlinear fiber, in which the index of refraction is higher for higher intensities. The pulse's intensity has an approximately Gaussian envelope so that the peak of the pulse moves more slowly than its tails, causing the leading tail to red shift and the lagging tail to blue shift. This effect is often referred to as self-phase modulation (SPM), and, for Gaussian pulses with the proper length of propagation, produces the middle spectrum plot shown in Figure 2-3 (a). The filter then passes

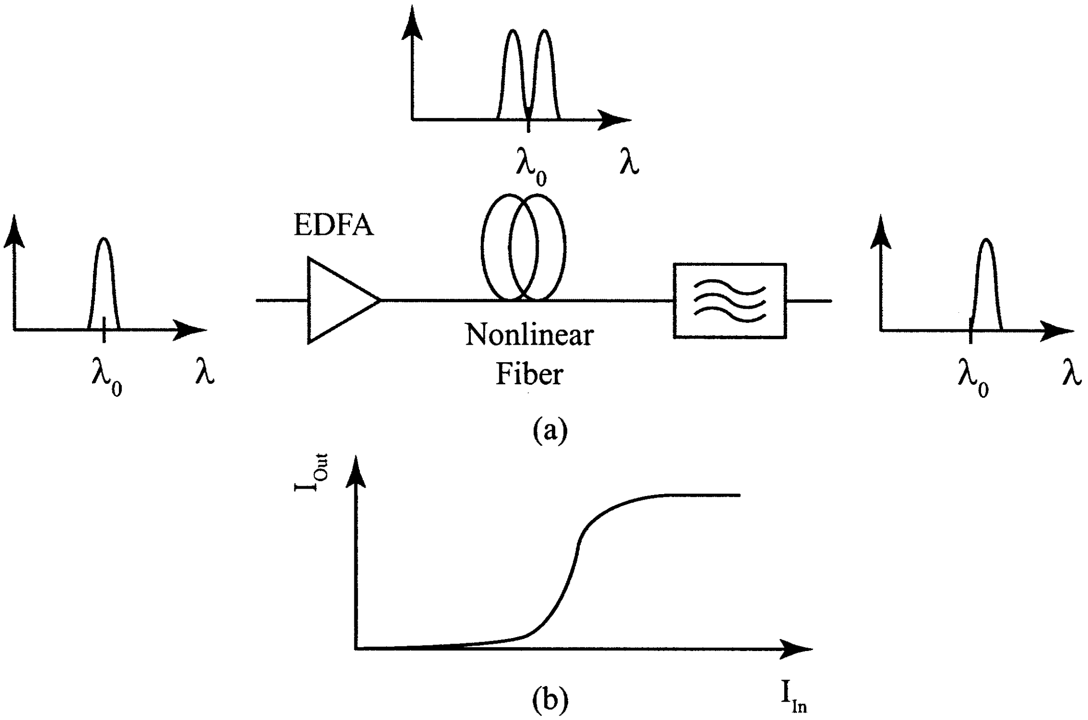

Figure 2-3: (a) Schematic of a 2R all-optical regenerator based on self-phase modulation. The plots show the pulse spectra at the input, at the end of the fiber, and after the band-pass filter. (b) Desired input-output response of this regenerator.

one of the two peaks in that spectrum.

Figure 2-4 shows experimental data from [4] for the SPM regenerator. The dotted line shows the output pulse intensity versus input pulse intensity. The solid line shows the same plot for a chain of two SPM regenerators, showing the desired step-function response.

The SPM regenerator has many useful properties. It gives 2R regeneration with a very simple design. Nonetheless, the regenerator does not retime or repolarize the data. Moreover, its operation depends on the pulse shape, as described above. So amplifier noise, which will not have the same time profile as the Gaussian pulse, may not be eliminated from the 1s. So, in the next two sections, we consider more complicated designs that overcome these problems.

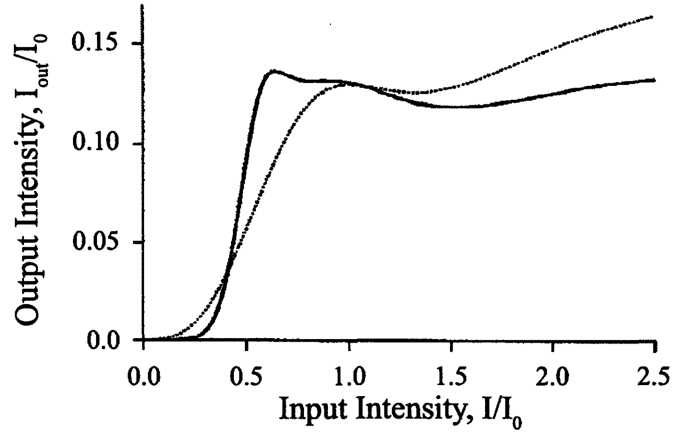

Figure 2-4: Output pulse intensity of the SPM regenerator versus input pulse intensity after one stage of the regenerator (dotted) and two stages (solid). The plots are experimental data from Figure 2 of Mamyshev, ECOC, 1998 [4].

2.1.3 Synchronous Modulation

Synchronous modulation has received a great deal of attention in the literature, especially from the private sector [5, 6, 7]. Figure 2-5 (a) shows the schematic of a synchronous-modulation regenerator. The energy of the data pulses is split in two. Part of the energy enters the clock recovery circuit (CR) that generates the clock pulse train, in this case an electronic pulse train, that drives an electro-optic modulator. The pulses then pass through a filter and a section of highly nonlinear fiber.

The electro-optic modulator (E/O modulator) retimes the data pulses. The clock pulses change the transmissivity of the E/O modulator, as shown in Figure 2-5 (b). The peak of the clock pulses correspond with the peak of the E/O modulator's transmissivity. In the figure, the data pulse leads the clock pulse, which causes its leading edge to be attenuated. This attenuation moves the center of mass of the pulse towards the center of the clock pulse. Many other devices have been used in place of the E/O modulator, including electro-absorption modulators, all-optical switches, and phase modulators. The filter serves a similar purpose in the frequency domain, dragging the data pulse's frequency center to the desired frequency.

The nonlinear fiber's purpose is subtler. When the pulse widths and intensities are at the right values, the fiber's second order chromatic dispersion, discussed in the next

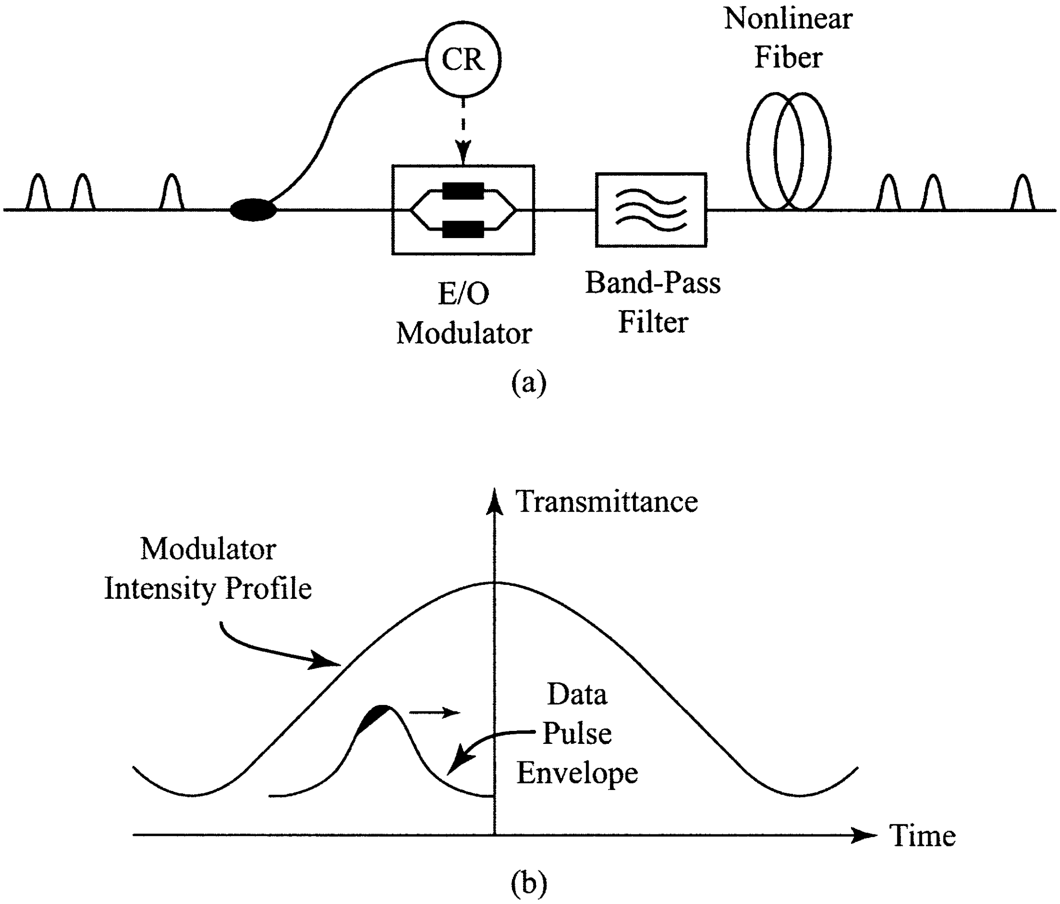

Figure 2-5: (a) Schematic of the synchronous modulator. (b) Effect of the E/O modulator on the pulse timing.

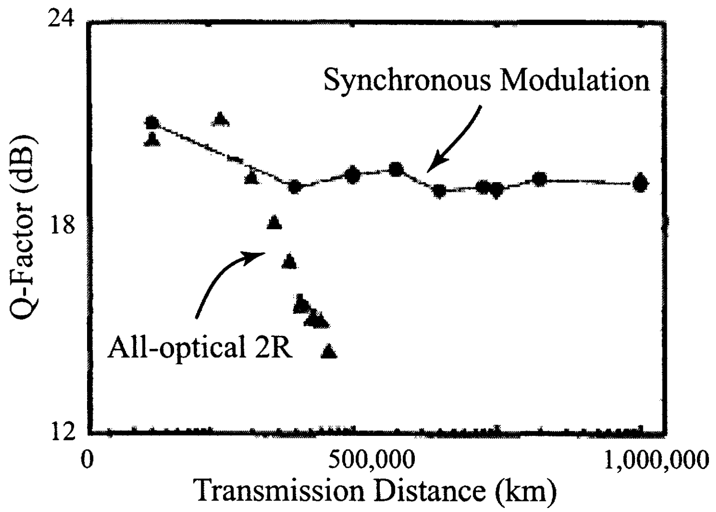

Figure 2-6: Plot of the Q-factor of data pulses as a function of propagation distance. One plot (triangles) shows the evolution of Q with a 2R regenerator, and the other (circles) shows the evolution of Q with 3R synchronous modulation. This plot comes from Figure 3 of Raybon, et al., OFC, 2002 [5].

chapter, and its self-phase modulation can cancel out, producing first order soliton pulses [8, 9]. First order soliton pulses propagate undistorted through lossless fiber. Moreover, they are stable to perturbations so that any pulse that deviates slightly from the ideal soliton shape will evolve during propagation into an ideal soliton. It is this property that allows the nonlinear fiber to reshape the pulses. The soliton effects also ensures that all the pulses possess the same peak intensity and that the energy in the 0s dissipates away during propagation.

Figure 2-6 shows the results of the transmission experiment given in [5]. The optical data were modulated onto a 40-Gb/s train of 8-ps pulses. The data pulses entered a loop containing 400 km of dispersion-compensated fiber and they propagated through the loop ~2500 times for a total propagation distance of ~1,000,000 km. The figure shows the Q-factor of the data train in the loop as a function of propagation distance. One plot (triangles) shows the evolution of Q when the loop contains a 2R regenerator. The accumulation of random timing jitter causes a steady degradation in the data quality. To correct the timing jitter, a 3R synchronous modulator was inserted into the loop, causing the value of Q to remain stable after 1,000,000 km of propagation.

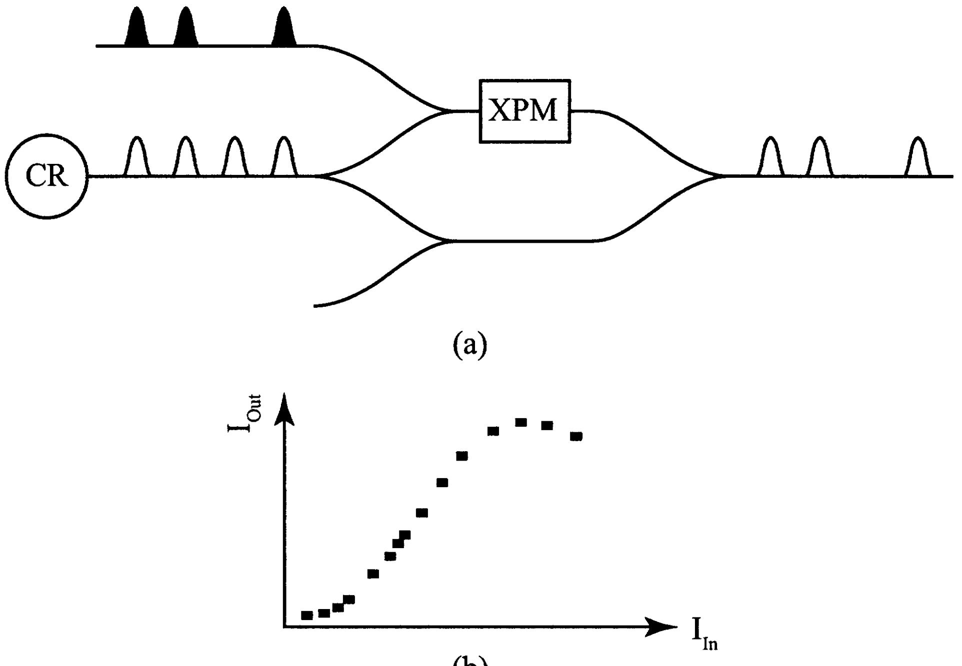

(a)

(b)

Figure 2-7: (a) Schematic of interferometer-based regenerator. Cross-phase modulation (XPM) is used to imbalance the interferometer. (b) Output pulse intensity versus input pulse intensity, showing the raised-sine response typical of interferometers.

2.1.4 Interferometric Switches

Synchronous-modulation regenerators do not repolarize the data pulses. In networks that have polarization-sensitive components, regenerators may need to convert the polarization of all input data pulses to a single constant output polarization. One solution is to use a regenerator that replaces the incoming network data pulses with a new set of data pulses modulated with the same data pattern.

One such regenerator is shown in Figure 2-7 (a). A clock recovery circuit (CR) produces a train of optical clock pulses. A 50/50 coupler splits the optical power into the two arms of the Mach-Zehnder interferometer (MZI). When the pulses from the two paths recombine at the MZI's output, they destructively interfere. A data pulse can be coupled into the interferometer's top arm. It then enters a medium with an intensity dependent index of refraction (XPM in the figure) where the pulse increases the optical path length of the top arm by a half wavelength. This process modulates the data pattern onto the clock pulses. Usually a filter at the output removes the

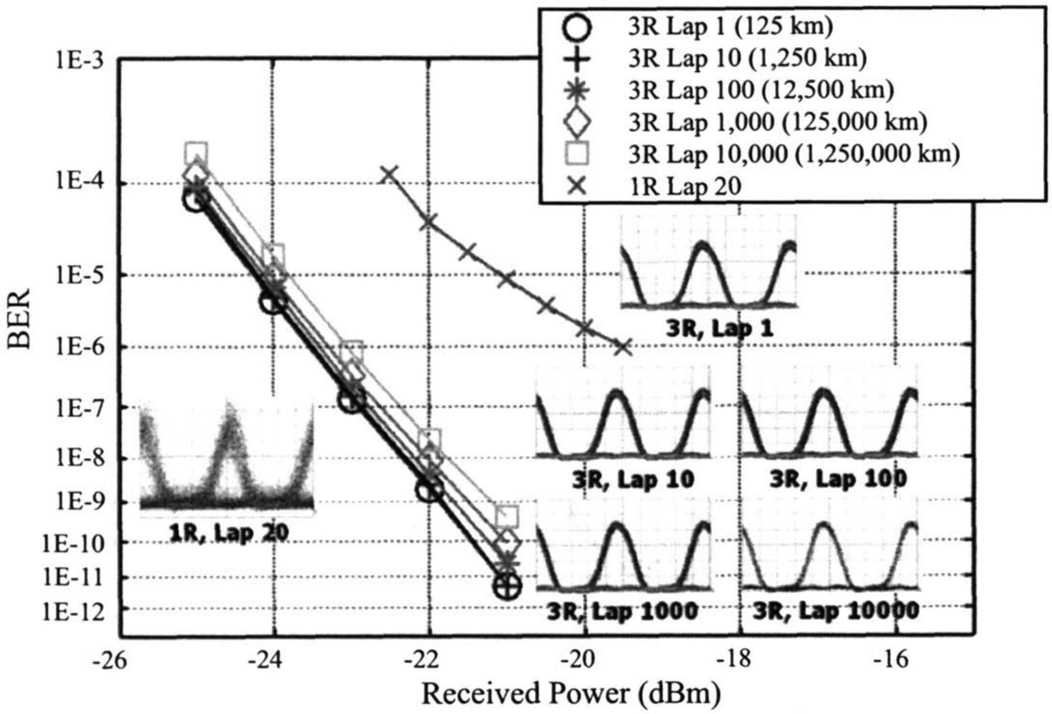

Figure 2-8: Bit-error rate data showing the performance of an MZI-based regenerator at 10 Gb/s over 1,250,000 km of propagation. The plots show the number of errors per bit as a function of the optical power input into an optical receiver. The optical data are regenerated after every 125 km of propagation. These data come from Figure 6 of Zhu, et al., Photonics Technology Letters, 2006 [10].

original data pulses and passes the clock pulses.

Figure 2-8 shows the results of the transmission experiment presented in [10]. The optical data were modulated onto a 10-Gb/s train of 40-ps pulses. The data pulses entered a loop containing 125 km of dispersion-compensated fiber and they propagated through the loop ~10,000 times for a total propagation distance of ~1,250,000 km. The figure shows the bit-error rate (BER) performance of the data pulse train after several different propagation distances. The vertical axis plots the number of errors per bit as detected by an optical receiver. The horizontal axis plots the optical power input into the receiver. The BER curves after 125 km, 1,250 km, 12,500 km, 125,000 km, and 1,250,000 km show nearly identical performance.

2.2 The Nonlinear Mach-Zehnder Regenerator

As discussed in Chapter 1, all-optical switches are often one of the basic components of all-optical regenerators. Many of the benefits as well as the deficiencies of all-optical regeneration are well-illustrated by one of the simplest all-optical switches. The nonlinear Mach-Zehnder interferometer (MZI), like many all-optical switches and regenerators, uses optical interference and ultrafast changes in the balancing of an interferometer to create optical switching. We will consider in Chapter 3 the materials and methods used to obtain these ultrafast changes in the interferometer balancing. In this section, it will be enough to look at MZI performance at a high level.

2.2.1 Mach-Zehnder All-Optical Switch

Figure 2-9 shows the basic schematic of a nonlinear MZI configured as an all-optical switch. In this case, the MZI is implemented using discrete free-space optics, although it can also be assembled from fiber optic components or integrated onto an optical chip. A 50/50 beam splitter divides the signal pulse's power into two arms. One arm is ideally linear and nondispersive. The second arm contains a medium whose optical path length is easily controlled. When the two path lengths are equal, the optical power in the two arms constructively interfere so that the signal pulse exits by Output Port A. When we change the optical path length in the second arm by 1/2 a wavelength, the signal pulse will instead exit from Output Port B.

When MZIs are used as electro-optic modulators, the second arm's path length depends on the value of a voltage placed across the material. Therefore, the speed of electro-optic modulators is limited by the speed of electronic drivers, as well as other related problems. Instead, as shown in the figure, we can place a nonlinear material in one arm of the interferometer whose optical path length can be changed by variations in the total optical power in the material. Thus an optical path length change can be induced by an ultrashort control pulse, as shown in Figure 2-9. Now the operating speed of the switch depends on the duration of the control pulse and

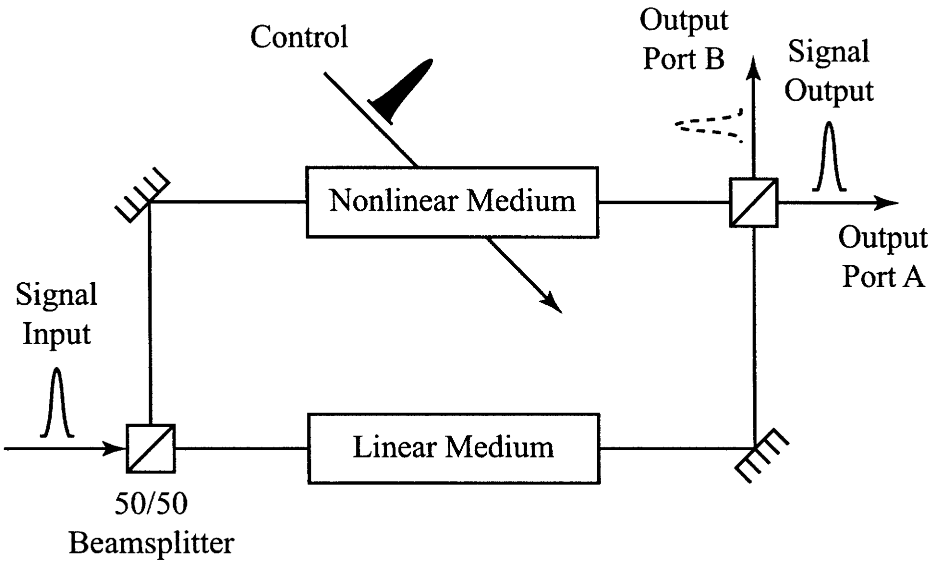

Figure 2-9: Nonlinear Mach-Zehnder interferometer.

the response time of the medium. In fiber that response time is $\sim 10^{-14}$ s.

We can calculate the optical power at Output Port A as a function of the control pulse power: simply split the optical power into the two paths, then account for the phase shift that each path adds to the optical signals propagating through them, and finally add the optical fields together at Output Port A. There are 5 sources of phase shift in the MZI: 1. propagation through free-space (because the observer at Output Port A observes a phase change if the free-space path length changes), 2. reflection off mirrors, 3. reflection off beamsplitters, 4. transmission through the beamsplitters, and, most important, 5. transmission through the linear and nonlinear media in Figure 2-9. Fortunately, as can be quickly seen in Figure 2-9, the first 4 sources of phase shift are the same for the upper and lower paths from Input to Output Port A. As we shall see, we are only interested in the relative phase between the two interferometer arms, so we only need to calculate the phase shifts caused by the linear and nonlinear media.

Calculating the phase shifts is simple. Suppose that the signal pulses have a free-space carrier wavelength of λ_0. Also, let L_l be the physical length of the linear medium and let L_{nl} be the physical length of the nonlinear medium. If the lower arm contains only linear material with an index of refraction equal to n_0^l, then the linear medium's optical path length is $n_0^l L_l$. Now, we assume that the upper arm contains a nonlinear medium with an instantaneous nonlinear index of refraction given by $n_0^{nl}+n_2 I_c$, where n_0^{nl} is the linear component of the index of refraction, n_2 is the nonlinear component of the index, and I_c is the intensity of the control pulse, which temporally overlaps the signal pulse (note that there is an implied assumption here that the signal pulse is too weak to affect the nonlinear index). The optical path length of the nonlinear medium is $(n_0^{nl} + n_2 I_c)L_{nl}$.

Now we can calculate the relative phase shift induced between the signal pulses in the two arms of the interferometer. Taking the difference of the two optical path lengths, we have

$$n_0^l L_l - (n_0^{nl} + n_2 I_c)L_{nl}. \tag{2.1}$$

Dividing by $\lambda_0/2\pi$ gives us the relative phase shift:

$$\Phi_{rel} = \frac{2\pi}{\lambda_0}[n_0^l L_l - (n_0^{nl} + n_2 I_c)L_{nl}]. \tag{2.2}$$

For simplicity let us assume that the MZI can be made so that $n_0^l L_l - n_0^{nl} L_{nl} = -\lambda_0$, from which we obtain

$$\Phi_{rel} = n_2 I_c L_{nl} - 2\pi. \tag{2.3}$$

Assume that at the input we have a signal with a field given by

$$\mathbf{E}_s = \hat{x} E_0 \cos(\omega_0 t + \psi), \tag{2.4}$$

where E_0 is a positive real number and ψ is an arbitrary phase. At the first beamsplitter, the intensity of $\mathbf{E}_s$ is split equally into the two arms. Intensity is proportional to the square of the field, so the field's magnitude in each arm is $1/\sqrt{2}$ times the intensity at the input. At Output Port A, the optical field in each arm goes through another beamsplitter, yielding another factor of $1/\sqrt{2}$. Thus at the output we have the field

$$\mathbf{E}_{out} = \frac{1}{2}\hat{x} E_0 \cos(\omega_0 t + \psi) + \frac{1}{2}\hat{x} E_0 \cos(\omega_0 t + \psi + \Phi_{rel}) \tag{2.5}$$

where each term in Equation 2.5 is the field from one of the two arms. Notice that Equation 2.5 justifies our use of relative rather than absolute phase, because adding some constant phase to both terms does not affect the calculation of the time-averaged output intensity:

$$
\begin{aligned}
I_{out} &= \frac{1}{\mu_0}\left\langle |\mathbf{E}_{out} \times \mathbf{B}_{out}| \right\rangle = \frac{1}{c\mu_0}\left\langle |\mathbf{E}_{out}|^2 \right\rangle \\
&= \frac{1}{c\mu_0}\left\langle \left| \frac{1}{2}E_0 \cos\left(\omega_0 t + \psi\right) + \frac{1}{2}E_0 \cos\left(\omega_0 t + \psi + \frac{\Phi_{rel}}{2}\right) \right|^2 \right\rangle \\
&= \frac{1}{c\mu_0}\left\langle \left| E_0 \cos\left(\omega_0 t + \psi\right) \cos\left(\frac{\Phi_{rel}}{2}\right) \right|^2 \right\rangle \qquad (2.6) \\
&= \frac{1}{2c\mu_0} E_0^2 \cos^2\left(\frac{\Phi_{rel}}{2}\right) \\
&= I_{in} \cos^2\left(\frac{n_2 I_c L_{nl}}{2} - \frac{\pi}{2}\right) = I_{in} \sin^2\left(\frac{n_2 I_c L_{nl}}{2}\right),
\end{aligned}
$$

where $\mathbf{B_{out}}$ is the magnetic field, c is the speed of light, and μ_0 is the permeability of free space. Φ_{rel} is linearly related to I_c, so we can control the phase shift between the pulses in the two arms to cause constructive or destructive interference at Output Port A. The output intensity, in normalized units, is plotted versus $n_2 I_c L_{nl}$. Φ_{rel} in Figure 2-10.

We can easily apply this interferometer to all-optical switching. As can be seen in Figure 2-10, by changing the control pulse intensity I_c, we can turn the output power I_{out} on and off. Also notice that if $I_c = 0$ or $I_c = \pi/(n_2 L_{nl})$, then the I_{out} curve is at a zero derivative point. This fact implies that variations in I_c at these two points leads to no variation in I_{out} to first order. This property is useful in data regeneration because, as we shall see, the control pulses will be replaced by data pulses from the network. These data pulses will have amplitude noise, so we will want our switch to be insensitive to small variations in the amplitude.

Although simple, the nonlinear Mach-Zehnder design in Figure 2-9 has several problems. First, there may be undesirable and uncontrollable asymmetries between the two arms. If the carrier wavelength is 1550 nm, then even small variations in temperature between the two arms could affect the difference in their optical path lengths

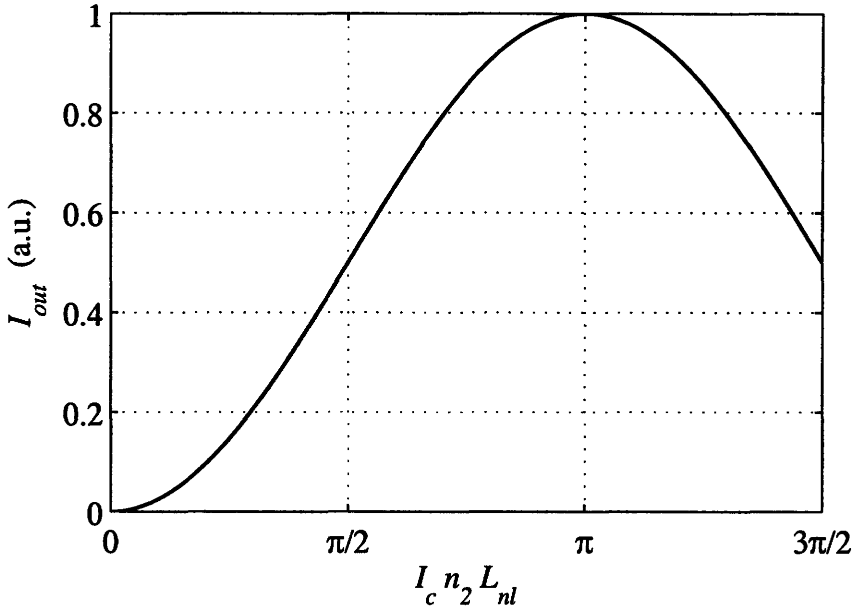

Figure 2-10: Normalized output intensity of the nonlinear Mach-Zehnder interferometer versus Φ_{rel}.

enough to move the bias point of the switch from I_{out} is ON to I_{out} is OFF. Even acoustic vibration from ambient sound could noticeably affect the switch's performance. Active electronic control of the path length could stabilize these asymmetric variations, but it adds hardware and complexity. One solution to this problem is the single-arm interferometer, like that presented in Chapter 4. This solution works well for interferometric switches with large dimensions. Another solution is to reduce the size of the interferometer so that environmental changes affect both arms equally. This type of solution is presented in Chapter 5.

Another problem with the nonlinear Mach-Zehnder interferometer arises when the medium used in the nonlinear arm does not have an instantaneous response. In Chapter 5 we will discuss an MZI that uses a semiconductor-based nonlinear medium that includes several recovery effects ranging in speed from several femtoseconds to several nanoseconds [11]. The long carrier-density recovery time will affect switching if the nonlinear response exceeds one bit length. A control pulse might then induce a phase shift both in the pulse it temporally overlaps and in a subsequent pulse. We will see how this problem can be overcome by using control pulses in both arms of the interferometer.

2.2.2 Clock Recovery

In Figure 1-5 we saw that all-optical 3R regenerators typically have two components: the all-optical switch and a clock recovery circuit. This thesis presents our work in the all-optical switch component, but an understanding of clock recovery is important in the evaluation of a regenerator's performance. Clock recovery has received a lot of attention in the literature. Electronic solutions often use a phase-locked loop to recover an electronic clock from an optical data pulse train [12]. A number of all-optical solutions have been proposed as well, including designs based on fiber ring lasers [13], semiconductor ring lasers [14], Fabry-Pérot filters [15, 16], and stimulated Brillouin scattering [17, 18].

There are several important criteria by which we judge clock recovery circuits. First, there is the precision of the recovered clock. Second, there is the speed of recovery. This second criterion is important because there are practical limits to the length of optical delays. So, when a data packet arrives, the network components cannot wait an arbitrary amount of time for a recovered clock. Moreover, data packets may arrive from different sources and so may not be synchronous. Thus, a new clock will have to be extracted for each arriving data packet, which requires fast "burst mode" clock recovery.

The two criteria above are incompatible because perfectly precise clock recovery requires infinite time so that the clock recovery circuit can, in effect, calculate the Fourier transform to find the center frequency of the data signal. The proper balance between the two criteria is an engineering decision that depends on network design. Shorter data packets, for example, will require less precise clock recovery.

We consider the performance for a couple of the all-optical solutions mentioned above. Figure 2-11 (a) shows a schematic of a ring laser. The amplifier (triangle) provides gain in the ring, and, as we will describe below, the modulator forces the laser to produce optical pulses. The only supported cavity modes are sinusoidal waves

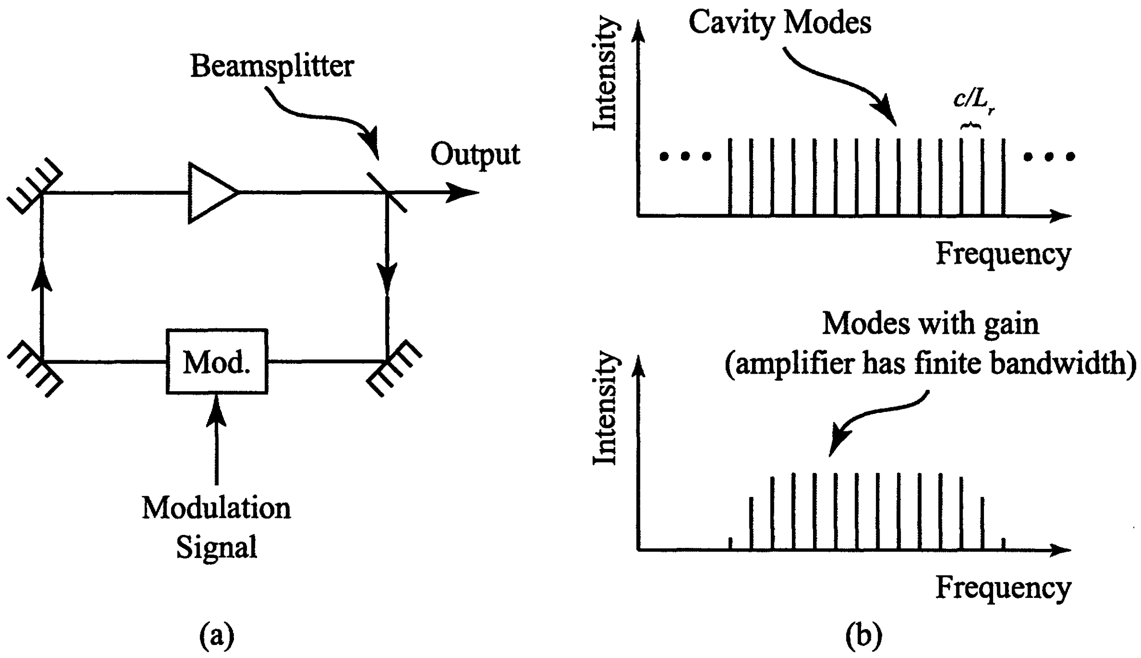

Figure 2-11: (a) Schematic of a ring laser. (b) The top plot shows the cavity frequency modes and the bottom plot shows the cavity modes with net gain.

with wavelengths that evenly divide the ring's length, L_r. So, the output electric field amplitude can be expressed as

$$E = \sum_k a_k \cos\left(2\pi f_k t + \phi_k\right),$$

where $f_k = kc/L_r$, a_k is the mode's amplitude, and ϕ_k is the phase of the mode. The cavity modes are shown in the top plot of Figure 2-11 (b). The amplifier in the cavity has a limited bandwidth, and cavity modes that fall outside its bandwidth experience net loss and, therefore, cannot be supported in the ring. The supported modes, then, are shown in the bottom plot of Figure 2-11 (b).

If the ϕ_k are randomly distributed, then the output electric field will appear random as well. On the other hand, if we mode-lock the laser so that the ϕ_k become equal to each other, then it will produce narrow pulses. We can force the laser to mode-lock by applying an amplitude modulation of the desired pulse frequency to the modulator in the ring. In an all-optical clock recovery system, the drive signal for the modulator is an optical data pulse stream, and the modulator itself is a nonlinear

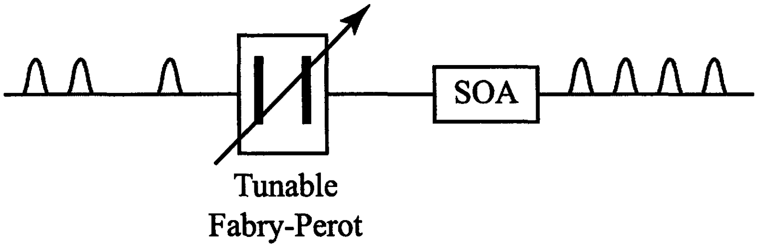

Figure 2-12: Clock recovery circuit based on the Fabry-Pérot filter. The filter fills in the 0s with pulses, and the semiconductor optical amplifier (SOA) equalizes the pulse intensities.

optical medium.

For fiber ring clock recovery circuits [13], the free space ring shown in Figure 2-11 (a) is replaced by a fiber ring. The fiber makes the ring long compared to the pulse period, so that clock recovery with mode-locked fiber lasers is a slow process. As mentioned above, packet-switched networks require very fast recovery after only a few of data pulses.

Other solutions do offer fast burst-mode clock recovery. One such simple solution is based on Fabry-Pérot filters [16], which has been shown to recover a clock within a few bits [19]. Figure 2-12 shows the basic schematic, which has only two components. One is the Fabry-Pérot filter with a free spectral range equal to the data pulse rate. Data pulses that enter the Fabry-Pérot filter will partially reflect in a cavity with a round trip time equal to the bit period. Therefore, pulses in the data pattern's 1-bits fill in the 0s, where there are no pulses. There is, however, variation in the peak intensities of these pulses, so an SOA equalizes the pulse intensities.

Figure 1-5 showed that OOK regenerators have two basic components: a switch to reform or replace the data pulses and a clock recovery circuit to retime them. Section 2.1 reviewed several implementations of the switch component, and this section has reviewed several implementations of clock recovery circuits. The Fabry-Pérot solution in particular has shown promise as a burst-mode circuit. This thesis, however, focuses on the switches. Before discussing the two switches we have evaluated, however, Chapter 2 will develop the theory of the nonlinear media that our all-optical switches use.

Bibliography

[1] O. Leclerc, B. Lavigne, E. Balmefrezol, P. Brindel, L. Pierre, D. Rouvillain, and F. Seguineau, "Optical regeneration at 40 Gb/s and beyond," *Journal of Lightwave Technology*, vol. 21, no. 11, pp. 2779–2790, 2003.

[2] A. Scavennec and O. Leclerc, "Toward high-speed 40-Gbit/s transponders," *Proceedings of the IEEE*, vol. 94, no. 5, pp. 986–996, 2006.

[3] D. Rouvillain, F. Seguineau, L. Pierre, P. Brindel, H. Choumane, G. Aubin, J. Oudar, and O. Leclerc, "40 Gbit/s optical 2R regenerator based on passive saturable absorber for WDM long-haul transmissions," *Optical Fiber Communication Conference*, 2002.

[4] P. Mamyshev, "All-optical data regeneration based on self-phase modulation effect," *European Conference on Optical Communication*, 1998.

[5] G. Raybon, Y. Su, J. Leuthold, R. Essiambre, T. Her, C. Joergensen, P. Steinvurzel, and K. Feder, "40 Gbit/s pseudo-linear transmission over one million kilometers," *Optical Fiber Communication Conference*, 2002.

[6] S. Bigo, O. Leclerc, and E. Desurvire, "All-optical fiber signal processing and regeneration for soliton communications," *IEEE Journal of Selected Topics in Quantum Electronics*, vol. 3, no. 5, pp. 1208–1223, 1997.

[7] K. Suzuki, H. Kubota, A. Sahara, and M. Nakazawa, "40 Gbit/s single channel optical soliton transmission over 70000 km using in-line synchronous modulation and optical filtering," *Electronics Letters*, vol. 34, no. 1, pp. 98–100, 1998.

[8] G. Agrawal, *Nonlinear Fiber Optics.* San Diego, California: Academic Press, third ed., 2001.

[9] K. Tai, A. Tomita, J. Jewell, and A. Hasegawa, "Generation of subpicosecond solitonlike optical pulses at 0.3 THz repetition rate by induced modulational instability," *Applied Physics Letters*, vol. 49, p. 236, 1986.

[10] Z. Zhu, M. Funabashi, Z. Pan, L. Paraschis, and S. Yoo, "10 000-Hop Cascaded In-Line All-Optical 3R Regeneration to Achieve 1 250 000-km 10-Gb/s Transmission," *IEEE Photonics Technology Letters*, vol. 18, no. 5, pp. 718–720, 2006.

[11] K. L. Hall, G. Lenz, A. M. Darwish, and E. P. Ippen, "Subpicosecond gain and index nonlinearities in InGaAsP diode lasers," *Optics Communications*, vol. 111, pp. 589–612, Oct. 1994.

[12] O. Kamatani and S. Kawanishi, "Ultrahigh-speed clock recovery with phase lock loop based on four-wave mixing in a traveling-wave laser diode amplifier," *Journal of Lightwave Technology*, vol. 14, no. 8, pp. 1757–1767, 1996.

[13] K. Smith and J. Lucek, "All-optical clock recovery using a mode-locked laser," *Electronics Letters*, vol. 28, no. 19, pp. 1814–1816, 1992.

[14] K. Vlachos, G. Theophilopoulos, A. Hatziefremidis, and H. Avramopoulos, "30 Gb/s all-optical clock recovery circuit," *IEEE Photonics Technology Letters*, vol. 12, no. 6, pp. 705–707, 2000.

[15] M. Jinno and T. Matsumoto, "Optical tank circuits used for all-optical timing recovery," *Quantum Electronics, IEEE Journal of*, vol. 28, no. 4, pp. 895–900, 1992.

[16] G. Contestabile, A. Presi, M. Ciaramella, E. Sant'Anna, and I. Pisa, "40-GHz all-optical clock extraction using a semiconductor-assisted fabry-Pérot filter," *IEEE Photonics Technology Letters*, vol. 16, no. 11, pp. 2523–2525, 2004.

[17] D. Butler, J. Wey, M. Chbat, G. Burdge, and J. Goldhar, "Optical clock recovery from a data stream of an arbitrary bit rate by use of stimulated Brillouin scattering," *Optics Letters*, vol. 20, no. 6, pp. 560–562, 1995.

[18] C. Johnson, K. Demarest, C. Allen, R. Hui, K. Peddanarappagari, and B. Zhu, "Multiwavelength all-optical clock recovery," *Photonics Technology Letters, IEEE*, vol. 11, no. 7, pp. 895–897, 1999.

[19] C. Bintjas, K. Yiannopoulos, N. Pleros, G. Theophilopoulos, M. Kalyvas, H. Avramopoulos, and G. Guekos, "Clock Recovery Circuit for Optical Packets," *IEEE Photonics Technology Letters*, vol. 14, no. 9, pp. 1363–1365, 2002.

Chapter 3

Nonlinear Media

Many implementations of all of the four regenerators described in Chapter 2 use some kind of nonlinear optical medium to produce the produce the switching. The most used nonlinear media are optical fiber and semiconductor optical amplifiers (SOAs), both of which we will discuss in this chapter. We will develop models for both, and simulations based on the models will appear in this chapter and Chapter 5.

The principle advantages of the SOA are its small size and strong nonlinearity, which allows small switching energies. Indeed, the small size of SOAs and the materials from which they are made allow them to be integrated onto optical chips. Such integrated designs have been tested in all-optical switches [1], regenerators [2, 3], data-packet switches [4], and many other applications. The optical response of SOAs, however, can long compared to bit periods (SOA recovery times are typically $\sim$ 100 ps; at 40 Gb/s, bit-periods are 25 ps). This long response time can cause effects in the switch to linger for several bits, which is undesirable if we require independent bit-by-bit switching.

Where such bit-by-bit operation is required, optical fiber can be used instead because of its nearly instantaneous response time. As we shall see, however, optical fiber has a weak nonlinearity so that long lengths of fiber are required to obtain enough of whatever nonlinear effect is required. Nonetheless, fiber has be tested in many applications including wavelength conversion [5], all-optical switching [6], and regeneration [7, 8].

3.1 A Brief Introduction to Nonlinear Optics

This thesis discusses two all-optical regenerators [3, 8]. The wavelength-maintaining folded ultrafast nonlinear interferometer, examined in Chapter 4, uses dispersion-shifted optical fiber as its nonlinear medium. The SOA Mach-Zehnder interferometer, examined in Chapter 5, uses SOAs as its nonlinear medium. We can study both of these media with the tools provided by nonlinear optics, which we briefly introduce here.

To describe the propagation of waves through nonlinear media, we need to derive a nonlinear wave equation. We start, as always, with Maxwell's equations in SI units:

$$\begin{aligned}
\nabla \times \mathbf{E}(\mathbf{r},t) &= -\frac{\partial \mathbf{B}(\mathbf{r},t)}{\partial t} \\
\nabla \times \mathbf{B}(\mathbf{r},t) &= \mu_0\epsilon_0\frac{\partial \mathbf{E}(\mathbf{r},t)}{\partial t} + \mu_0\mathbf{J}(\mathbf{r},t) \\
\nabla \cdot \mathbf{E}(\mathbf{r},t) &= \frac{1}{\epsilon_0}\rho(\mathbf{r},t) \\
\nabla \cdot \mathbf{B}(\mathbf{r},t) &= 0.
\end{aligned}$$

The charge density, $\rho(\mathbf{r},t) = \rho_f(\mathbf{r},t) + \rho_b(\mathbf{r},t)$, contains two components. The bound charges, ρ_b, describe the distribution of charges bound to the atoms in the medium of propagation. In the absence of fields, the atoms are on average charge neutral. When an **E**-field is present, electrons are pulled away from their nuclei, polarizing the medium and yielding a non-zero ρ_b. The bound charges can always be represented by $\rho_b = -\nabla \cdot \mathbf{P}$ [9], where **P** is the polarization vector. In a linear isotropic medium, $\mathbf{P} = \epsilon_0\chi_e\mathbf{E}$, where χ_e is called the electric susceptibility[1]. We will discuss the form **P** takes in nonlinear media later in this section. The free charge, ρ_f, such as charge that has been added to an otherwise neutral conductor, is typically zero in the dielectric waveguides we will be discussing.

Similarly, the current source, $\mathbf{J}(\mathbf{r},t) = \mathbf{J}_f(\mathbf{r},t) + \mathbf{J}_b(\mathbf{r},t) + \mathbf{J}_p(\mathbf{r},t)$, contains three components. $\mathbf{J}_f$ and $\mathbf{J}_b$ are the free and bound currents. Free currents are typically

---

[1] This form of **P** seems to imply a continuously divisible medium. In fact, this form is accurate for ordinary matter as well, as discussed in detail in Section 4.2.3 of [9].

defined as applied currents, as when an experimenter hooks up a battery and a wire. Bound currents, on the other hand, are those that are created by the effect of the magnetic field on the dipole moments of the matter with which it interacts. $\mathbf{J}_f$ will be zero in all the cases we will study. The bound current can always be represented as $\mathbf{J}_b = \nabla \times \mathbf{M}$, where $\mathbf{M}$ is the magnetization [9]. All the media we will consider in this thesis are linear, so that $M = \chi_m \mathbf{H}$ where $\mathbf{H} = \mathbf{B}/\mu_0 - \mathbf{M}$, and $\mathbf{H}$ is an auxiliary field that accounts for the interaction of the magnetic field and matter[2]. Finally, $\mathbf{J}_p$ is the current that exists when there is a time-varying polarization vector. That is, it is the current that is created by the motion of bound charges and is given by $\mathbf{J}_p = \partial \mathbf{P}/\partial t$.

We define two auxiliary fields, one of which we saw above:

$$\mathbf{D} = \epsilon_0 \mathbf{E} + \mathbf{P} \tag{3.1}$$

$$\mathbf{H} = \frac{1}{\mu_0}\mathbf{B} - \mathbf{M}, \tag{3.2}$$

where $\mu = \mu_0(1 + \chi_m)$ for linear magnetic media. In optics, most media are nonmagnetic, so we will assume that $\chi_m = 0$. Then we use the following expressions for the various charges and currents:

$$\mathbf{J}_f = 0, \quad \mathbf{J}_b = \nabla \times \mathbf{M}, \quad \mathbf{J}_p = \frac{\partial \mathbf{P}}{\partial t} \tag{3.3}$$

$$\rho_f = 0, \quad \rho_b = -\nabla \cdot \mathbf{P} \tag{3.4}$$

Using Equations 3.1 through 3.4, we obtain the standard form of the sourceless

---

[2] Many textbooks refer to **H** as the magnetic field; I prefer to call **B** the magnetic field because its divergence always vanishes, as it should for the magnetic field because of the nonexistence of the magnetic charge carrier. Doubters should consider A. Sommerfeld, who wrote "The unhappy term 'magnetic field' for **H** should be avoided as far as possible. It seems to us that this term has led into error none less than Maxwell himself..."

Maxwell's equations in matter:

$$\nabla \times \mathbf{E}(\mathbf{r},t) = -\frac{\partial \mathbf{B}(\mathbf{r},t)}{\partial t} \tag{3.5}$$

$$\nabla \times \mathbf{H}(\mathbf{r},t) = \frac{\partial \mathbf{D}(\mathbf{r},t)}{\partial t} \tag{3.6}$$

$$\nabla \cdot \mathbf{D}(\mathbf{r},t) = 0 \tag{3.7}$$

$$\nabla \cdot \mathbf{B}(\mathbf{r},t) = 0. \tag{3.8}$$

To derive the wave equation, we take the curl of Equation 3.5. Then we take the curl of Equation 3.6 and use it to eliminate **B** from Equation 3.5, obtaining

$$\nabla \times \nabla \times \mathbf{E} = -\mu_0\epsilon_0\frac{\partial^2 \mathbf{E}}{\partial t^2} - \mu_0\frac{\partial^2 \mathbf{P}}{\partial t^2}.$$

Now we can use the vector identity

$$\nabla \times \nabla \times \mathbf{E} = \nabla(\nabla \cdot \mathbf{E}) - \nabla^2\mathbf{E}.$$

In linear optics $\nabla \cdot \mathbf{D} = 0$ implies that $\nabla \cdot \mathbf{E} = 0$, but this is not necessarily true in nonlinear optics. Nonetheless, we can often use the approximation $\nabla \cdot \mathbf{E} = 0$, which we will do throughout this thesis. So, we obtain the desired nonlinear wave equation:

$$\nabla^2\mathbf{E} = \mu_0\epsilon_0\frac{\partial^2 \mathbf{E}}{\partial t^2} + \mu_0\frac{\partial^2 \mathbf{P}}{\partial t^2}. \tag{3.9}$$

We still have to discuss the representation of the polarization vector **P** in nonlinear media. To simplify the discussion, we will assume for now that the electric field and polarization vector are scalar functions, which we represent with E and P. If the medium is instantaneous, then we can represent the nonlinear polarization as a power series:

$$P(\mathbf{r},t) = A_0 + A_1E(\mathbf{r},t) + A_2E(\mathbf{r},t)^2 + \cdots . \tag{3.10}$$

The coefficients A_n fully characterize this nonlinear medium and they may depend on $\mathbf{r}$ or t if the medium is different from point to point or time to time.

Many nonlinear media, however, are not instantaneous. So, P is a function of E at several different times. As an example, let us suppose that $P(\mathbf{r},t)$ depends on $E(\mathbf{r},t)$ and $E(\mathbf{r},t-\Delta)$. Then we can expand P in a multivariable Taylor series [10]:

$$\begin{aligned} P(\mathbf{r},t) =&C_{1,0}E(\mathbf{r},t)+C_{1,1}E(\mathbf{r},t-\Delta) \\ &+C_{2,1}E(\mathbf{r},t)^2+2C_{2,2}E(\mathbf{r},t)E(\mathbf{r},t-\Delta)+C_{2,3}E(\mathbf{r},t-\Delta)^2+\cdots . \end{aligned} \tag{3.11}$$

We omit the constant term because the bound charge, $\rho_b = -\nabla\cdot\mathbf{P}$, is not changed by adding a constant to the polarization vector. In the $C_{n,j}$ coefficients, n refers to the order of the nonlinearity, and j simply indexes the various possible nth order terms. The 2 before the $C_{2,2}$ in Equation 3.11 refers to the fact that this term is, in fact, two terms: one for $E(\mathbf{r},t)E(\mathbf{r},t-\Delta)$ and the second for $E(\mathbf{r},t-\Delta)E(\mathbf{r},t)$. We can easily generalize. If $P(\mathbf{r},t)$ depends on $E(\mathbf{r},t-m\Delta)$, where m is an integer from 0 to M, then we get the multivariable Taylor series

$$\begin{aligned} P(\mathbf{r},t) =&\sum_j F_{1,j}E(\mathbf{r},t-j\Delta) \\ &+\sum_{j,k} F_{2,j,k}E(\mathbf{r},t-j\Delta)E(\mathbf{r},t-k\Delta) \\ &+\sum_{j,k,l} F_{3,j,k,l}E(\mathbf{r},t-j\Delta)E(\mathbf{r},t-k\Delta)E(\mathbf{r},t-l\Delta)+\cdots . \end{aligned} \tag{3.12}$$

The first index in the $F_{n,j,k,\cdots}$ coefficients refers to the order of the term and the remaining indices simply index the variables $E(\mathbf{r},t-m\Delta)$. The $F_{n,j,k,\cdots}$ may depend on $\mathbf{r}$ or t.

So, we have seen that an instantaneous medium's polarization can be fully characterized by a power series with coefficients A_k. If the medium's polarization depends on the electric field at several points in time, then the medium can be fully characterized by a multivariable power series with coefficients $C_{n,k}$. We take this process to its logical end and consider a medium that depends on the electric field at all times. So, now $P(\mathbf{r},t)$ is a "functional" of a continuum of variables $E(\star)$, where $\star$ can take any value, whereas before $\star$ only took the values $t-m\Delta$ for $m=0$ to M.

In standard notation, before we had $P(\mathbf{r},t) = P(E(\mathbf{r},t),\cdots,E(\mathbf{r},t-m\Delta))$ and now we have $P(\mathbf{r},t) = P[E(\mathbf{r},\star)]$ where the square braces mean that P is a functional of $E(\mathbf{r},\star)$. More often this is written as $P(\mathbf{r},t) = P[E(\mathbf{r},t)]$.

Now, we want to have something like a power series for functionals, and we can obtain such a series by taking the limit as Δ goes to 0 and M goes to infinity in Equation 3.12. When we do so, the sums in the equation become integrals:

$$\begin{aligned}
P(\mathbf{r},t) &= \epsilon_0 \int_{-\infty}^{\infty} R^{(1)}(\mathbf{r},\tau_1)E(\mathbf{r},t-\tau_1)\,d\tau_1 \\
&+\epsilon_0 \int\int_{-\infty}^{\infty} R^{(2)}(\mathbf{r},\tau_1,\tau_2)E(\mathbf{r},t-\tau_1)E(\mathbf{r},t-\tau_2)\,d\tau_1 d\tau_2 \\
&+\epsilon_0 \int\int\int_{-\infty}^{\infty} R^{(3)}(\mathbf{r},\tau_1,\tau_2,\tau_3)E(\mathbf{r},t-\tau_1)E(\mathbf{r},t-\tau_2)E(\mathbf{r},t-\tau_3)\,d\tau_1 d\tau_2 d\tau_3 + \cdots,
\end{aligned} \tag{3.13}$$

where $R^{(n)}$ are the response functions and they correspond with the coefficients $F_{n,j,\cdots}$ above.

So far, we have neglected the vector nature of $\mathbf{E}$ and $\mathbf{P}$. We can add them to Equation 3.11 easily. Instead of using the factors $E(\mathbf{r},t-m\Delta)$ to form the terms of Equation 3.12, we can use the factors $E_j(\mathbf{r},t-m\Delta)$, where j is an index that refers to the three polarization directions. When we take this into the limit, as in the derivation of Equation 3.13, we obtain

$$\begin{aligned}
P_j(\mathbf{r},t) =& P_j^{(1)}(\mathbf{r},t) + P_j^{(2)}(\mathbf{r},t) + \cdots \\
&= + \epsilon_0 \int_{-\infty}^{\infty} R_{jk}^{(1)}(\mathbf{r},\tau_1)E_k(\mathbf{r},t-\tau_1)\,d\tau_1 \\
&\quad + \epsilon_0 \int\int_{-\infty}^{\infty} R_{jkl}^{(2)}(\mathbf{r},\tau_1,\tau_2)E_k(\mathbf{r},t-\tau_1)E_l(\mathbf{r},t-\tau_2)\,d\tau_1 d\tau_2 + \cdots,
\end{aligned} \tag{3.14}$$

where the indexes refer to the three polarization directions and take the values x, y, or z. We have used the Einstein notation in which there is an implied sum over repeated indexes. For example, $R_{jkl}^{(2)}E_kE_l$ is the same as $\sum_{kl} R_{jkl}^{(2)}E_kE_l$. It is also common to represent this using bold fonts so that $\mathbf{R}^{(2)}\vdots\mathbf{EE} = \sum_{kl} R_{jkl}^{(2)}E_kE_l$. We will most often use the index notation for vectors and matrices in this thesis, except where it is convenient to use bold fonts.

We often use **E**-fields that are the sum of several frequencies, so it is also convenient to represent Equation 3.14 in the frequency domain. For simplicity we consider only the second-order term (i.e., the term with $R^{(2)}_{jkl}$ above), although all the results generalize easily to the other orders. We represent the **E**-field as a sum of frequency components:

$$E_j(\mathbf{r},t) = \int_{-\infty}^{\infty} \tilde{E}_j(\mathbf{r},\omega)e^{-i\omega t}\,d\omega, \tag{3.15}$$

where

$$\tilde{E}_j(\mathbf{r},\omega) = \frac{1}{2\pi}\int_{-\infty}^{\infty} E_j(\mathbf{r},t)e^{i\omega t}\,dt \tag{3.16}$$

with analogous relationships between $P_j(\mathbf{r},t)$ and $\tilde{P}_j(\mathbf{r},\omega)$. When we substitute Equation 3.15 into the second-order term of Equation 3.14, we obtain

$$P^{(2)}_j(\mathbf{r},t) = \int\int_{-\infty}^{\infty} \chi^{(2)}_{jkl}(\mathbf{r},\omega_1,\omega_2)\tilde{E}_k(\mathbf{r},\omega_1)\tilde{E}_l(\mathbf{r},\omega_2)e^{-i\omega_\sigma t}\,d\omega_1 d\omega_2, \tag{3.17}$$

where $P^{(2)}_j$ is the second-order polarization in the jth direction, $\omega_\sigma = \omega_1 + \omega_2$, and.

$$\chi^{(2)}_{jkl} = \int\int_{-\infty}^{\infty} R^{(2)}_{jkl}(\mathbf{r},t_1,t_2)e^{i(\omega_1 t_1+\omega_2 t_2)}\,dt_1 dt_2 \tag{3.18}$$

Finally, we can calculate the Fourier transform of the polarization vector to obtain $\tilde{P}^{(2)}_j(\mathbf{r},\omega)$. Using Equation 3.17 and the well-known formula for the delta function, $\delta(t)$,

$$\frac{1}{2\pi}\int_{-\infty}^{\infty} e^{ist}\,ds = \delta(t),$$

we obtain

$$\tilde{P}^{(2)}_j(\mathbf{r},\omega) = \int\int_{-\infty}^{\infty} \chi^{(2)}_{jkl}(\mathbf{r},\omega_1,\omega_2)E_k(\omega_1)E_l(\omega_2)\delta(\omega-\omega_\sigma)\,d\omega_1 d\omega_2, \tag{3.19}$$

where again $\omega_\sigma = \omega_1 + \omega_2$. This is an important result and shows that $\tilde{P}^{(2)}_j(\mathbf{r},\omega)$ is created by two monochromatic waves whose frequencies add to ω.

The mathematical development of functional power series above allows us to characterize many nonlinear dielectric media with the response tensors, $R^{(n)}_{jk\cdots}$, in the time domain or the susceptibility tensor, $\chi^{(n)}_{jk\cdots}$, in the frequency domain. With this basic notation, we return to the nonlinear wave equation, which we repeat here:

$$\nabla^2 \mathbf{E} = \mu_0 \epsilon_0 \frac{\partial^2 \mathbf{E}}{\partial t^2} + \mu_0 \frac{\partial^2}{\partial t^2} \left[\mathbf{P}^{(1)} + \mathbf{P}^{(2)} + \cdots \right]. \tag{3.20}$$

where $\mathbf{P} = \mathbf{P}^{(1)} + \mathbf{P}^{(2)} + \cdots$. It is convenient to separate the linear and nonlinear components of the polarization vector so that $\mathbf{P} = \mathbf{P}^{(1)} + \mathbf{P}^{\mathrm{NL}}$.

We would like to transform Equation 3.20 into the frequency domain. So, we substitute in the following Fourier integrals into Equation 3.20:

$$E_j(\mathbf{r}, t) = \int_{-\infty}^{\infty} \tilde{E}_j(\mathbf{r}, \omega) e^{-i\omega t} \, d\omega \tag{3.21}$$

$$P^{(1)}_j(\mathbf{r}, t) = \int_{-\infty}^{\infty} \tilde{P}^{(1)}_j(\mathbf{r}, \omega) e^{-i\omega t} \, d\omega \tag{3.22}$$

$$P^{\mathrm{NL}}_j(\mathbf{r}, t) = \int_{-\infty}^{\infty} \tilde{P}^{\mathrm{NL}}_j(\mathbf{r}, \omega) e^{-i\omega t} \, d\omega. \tag{3.23}$$

Integral 3.22 can be further evaluated by substituting Equation 3.21 into the identity

$$P^{(1)}_j(\mathbf{r}, t) = \int_{-\infty}^{\infty} R^{(1)}_{jk}(\mathbf{r}, t - \tau_1) E_k(\mathbf{r}, \tau_1) \, d\tau_1$$

which comes from Equation 3.14. We obtain

$$P^{(1)}_j(\mathbf{r}, t) = \int_{-\infty}^{\infty} \chi^{(1)}_{jk}(\mathbf{r}, \omega) \tilde{E}_j(\mathbf{r}, \omega) e^{-i\omega t} \, d\omega. \tag{3.24}$$

If we substitute Equations 3.21, 3.23, and 3.24 into Equation 3.20, we obtain the nonlinear wave equation in the frequency domain:

$$\nabla^2 \tilde{\mathbf{E}} = -\mu_0 \epsilon_0 \omega^2 \tilde{\mathbf{E}} - \mu_0 \epsilon_0 \omega^2 \chi^{(1)} \cdot \tilde{\mathbf{E}} - \mu_0 \omega^2 \tilde{\mathbf{P}}^{\mathrm{NL}}$$

where $\chi^{(1)} \cdot \tilde{\mathbf{E}}$ is the matrix form of $\chi^{(1)}_{jk} \tilde{E}_k$. We re-arrange the terms to get

$$\nabla^2 \tilde{\mathbf{E}} + \frac{\omega^2}{c^2} \epsilon(\omega) \cdot \tilde{\mathbf{E}} = -\omega^2 \mu_0 \tilde{\mathbf{P}}^{\mathrm{NL}} \tag{3.25}$$

where $\epsilon(\omega) = 1 + \chi^{(1)}$ and $c = 1/\sqrt{\epsilon_0 \mu_0}$.

3.2 Optical Fiber

Optical fibers are cylindrical waveguides, usually composed of two concentric media as shown in Figure 3-1. Long-distance communications fiber is drawn from fused-silica glass. The two layers are doped with different materials to change the index of refraction so that the core has a higher index that the cladding, allowing light to be guided by total internal reflection. As we know from basic waveguide theory, each frequency of light that can propagate in the waveguide can often do so in several different discrete modes, each with its own propagation speed through the fiber (you may think of this as resulting from different angles of reflection, although this is not entirely accurate). In standard mode fiber (SMF), however, the waveguide is designed to guide only a single mode of light, preventing dispersion due to the different speeds of different modes.

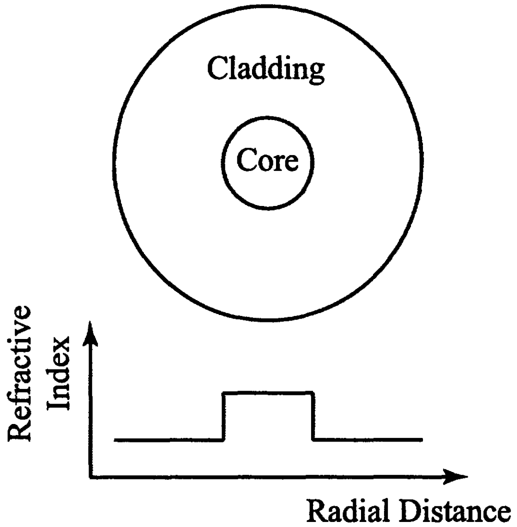

Figure 3-1: Figure of the cross-section of an optical fiber. The core's higher index of refraction allows total internal reflection.

Nonetheless, SMF still has a number of impairments. One of these impairments is chromatic dispersion in which the group velocity varies with frequency. Another is the nonlinear index of refraction, in which the index of refraction increases with

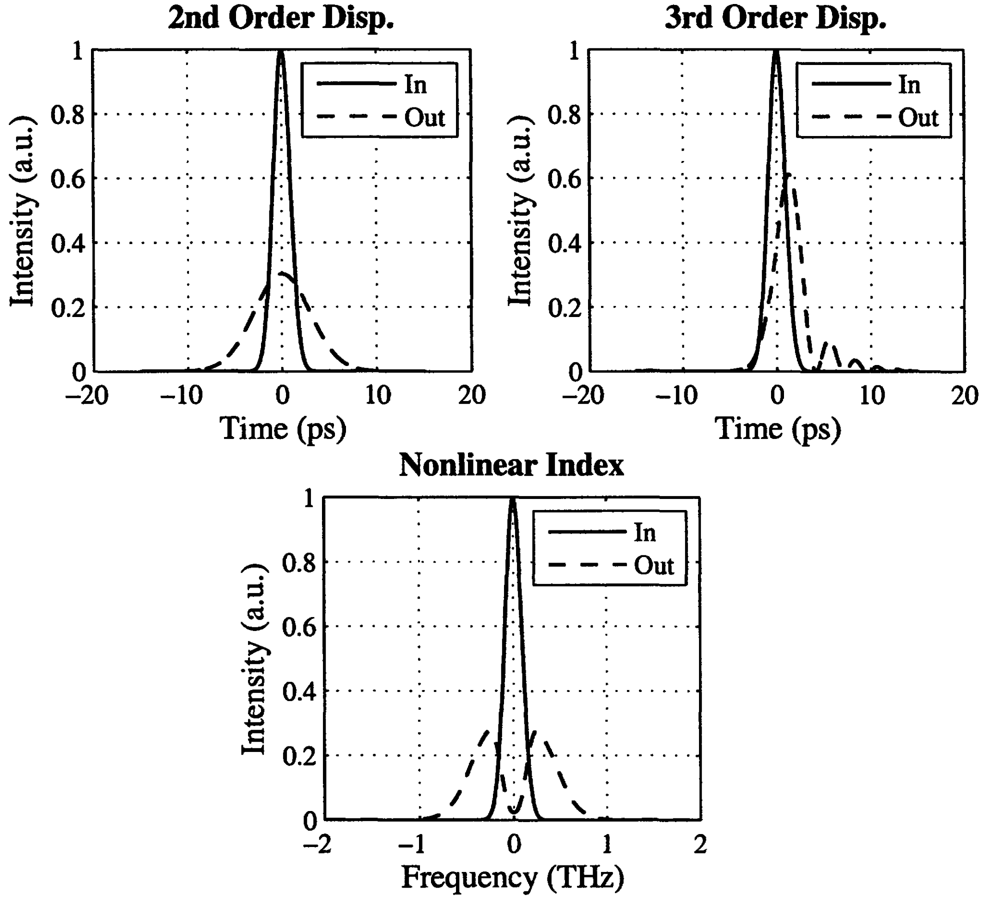

Figure 3-2: The top plots show the effects of second- and third-order dispersion on the intensity envelope. Second-order dispersion broadens the pulse width, and third-order dispersion causes ringing in one of the tails. The bottom plot shows the effects of the nonlinear index of refraction on a pulse's spectrum. The spectrum continues to broaden with more propagation.

higher optical intensities. Figure 3-2 shows the effects of these impairments on the intensity envelope of an optical pulse. The first plot shows second-order dispersion, which causes a linear change in group velocity with respect to optical frequency. As the figure shows, it leads to pulse broadening, which can cause the pulse's energy to enter the neighboring bit (intersymbol interference). Second-order dispersion also causes a blue-shifting of one tail of the pulse and a red-shifting of the other. The second is third order dispersion, which causes a quadratic change in group velocity with respect to optical frequency. It leads to a characteristic ringing in one tail of the pulse, also leading to intersymbol interference. The third is the nonlinear index of refraction, which leads to self-phase modulation. It causes a broadening of the pulse's optical spectrum. When there are several wavelength channels present, this spectral broadening can cause inter-channel interference. The interaction of these three effects is quite complicated, and modeling them is the subject of the rest of this section.

3.2.1 The Intensity-Dependent Index of Refraction

The intensity-dependent index of refraction is given by

$$n = n_0 + n_2 I \tag{3.26}$$

where n_0 is the linear index, n_2 is the nonlinear index, and I is the intensity of the electric field envelope. This intensity-dependent index is a consequence of the nonlinear interaction of the optical field with the medium of propagation. More specifically, in SI units, we have

$$\mathbf{D}(\mathbf{r}, t) = \epsilon_0 \mathbf{E}(\mathbf{r}, t) + \mathbf{P}(\mathbf{r}, t) \tag{3.27}$$

where $\mathbf{D}$ is the electric displacement, $\mathbf{E}$ is the electric field, and ϵ_0 is the permittivity of free space. The nonlinear effects are included in $\mathbf{P}$:

$$\mathbf{P}(\mathbf{r}, t) = \epsilon_0 \chi^{(1)} \cdot \mathbf{E}(\mathbf{r}, \mathbf{t}) + \mathbf{P_{NL}}(\mathbf{r}, \mathbf{t}). \tag{3.28}$$

$\chi^{(1)}$, the linear susceptibility, is a matrix that describes propagation for low optical intensities. $\mathbf{P_{NL}}$ is the nonlinear polarization

$$\mathbf{P_{NL}}(\mathbf{r},t) = \mathbf{P}^{(2)}(\mathbf{r},t) + \mathbf{P}^{(3)}(\mathbf{r},t) + \cdots \tag{3.29}$$

where, from Equation 3.14 in Section 3.1 we have

$$\begin{aligned}
\mathbf{P}^{(2)} &= \epsilon_0 \int\int_{-\infty}^{\infty} \mathbf{R}^{(2)}(\mathbf{r},\tau_1,\tau_2)\vdots\mathbf{E}(\mathbf{r},t-\tau_1)\mathbf{E}(\mathbf{r},t-\tau_2)\, d\tau_1 d\tau_2 \\
\mathbf{P}^{(3)} &= \epsilon_0 \int\int\int_{-\infty}^{\infty} \mathbf{R}^{(3)}(\mathbf{r},\tau_1,\tau_2,\tau_3)\vdots\mathbf{E}(\mathbf{r},t-\tau_1)\mathbf{E}(\mathbf{r},t-\tau_2)\mathbf{E}(\mathbf{r},t-\tau_3)\, d\tau_1 d\tau_2 d\tau_3
\end{aligned}$$

where the " $\vdots$ " notation is explained after Equation 3.14. Assuming the pulses are propagating down a one-dimensional waveguide in the z-direction, we can replace the $\mathbf{r}$ variable with the z variable[3]. We now assume that we can expand $\mathbf{E}(z,t)$ in a Fourier series as

$$\mathbf{E}(z,t) = \sum_n \tilde{\mathbf{E}}(z,\omega_n) e^{i(\beta_n z - \omega_n t)} \tag{3.30}$$

In Equation 3.30, we have assumed that the waves are propagating in the z-direction down a waveguide with a propagation constant of β_n. We also expand the polarization in a Fourier series to get

$$\mathbf{P}^{(b)}(\mathbf{r},t) = \sum_n \tilde{\mathbf{P}}^{(b)}(\mathbf{r},\omega_n) e^{-i\omega_n t}.$$

$\mathbf{E}$ and $\mathbf{P}$ are real, so $\tilde{\mathbf{E}}(\mathbf{r},\omega_n) = \tilde{\mathbf{E}}^*(\mathbf{r},-\omega_n)$ and $\tilde{\mathbf{P}}^{(b)}(\mathbf{r},\omega_n) = \tilde{\mathbf{P}}^{(b)*}(\mathbf{r},-\omega_n)$. The jth component of $\tilde{\mathbf{P}}^{(2)}$ is given by Equation 3.19

$$\tilde{P}_j^{(2)}(\mathbf{r},\omega) = \sum_{kl} \sum_{(nm)} \chi_{jkl}^{(2)}(\mathbf{r},\omega_n,\omega_m) \tilde{E}_k(\mathbf{r},\omega_n) \tilde{E}_l(\mathbf{r},\omega_m) e^{i(\beta_n+\beta_m)z} \tag{3.31}$$

where j, k, and l can be any of the Cartesian components of the field, x, y, and z. The integrals in Equation 3.19 become sums over n and m because there are only

---

[3] This assumes that we can average appropriately over the transverse x and y dimensions. We will consider this issue more carefully in Section 3.2.3.

a discrete number of frequencies. $\tilde{E}_j(\mathbf{r},\omega_n)$ is the jth vector component of $\tilde{\mathbf{E}}(\mathbf{r},\omega_n)$ of Equation 3.30. The notation (nm) requires that the sum be performed over ω_n and ω_m such that $\omega_m + \omega_n = \omega$. This fact is a consequence of the δ-function in Equation 3.19. More generally, the expression for $\tilde{\mathbf{P}}_j^{(b)}$ is given by

$$\begin{aligned}\tilde{P}_j^{(b)}(\mathbf{r},\omega) = \sum_{kl\cdots}\sum_{(nm\cdots)} \chi^{(b)}_{jkl\cdots}(\mathbf{r},\omega_n,\omega_m,\cdots)\cdot \\ \left[\tilde{E}_k(\mathbf{r},\omega_n)\tilde{E}_l(\mathbf{r},\omega_m)\cdots\right]\cdot e^{i(\beta_n+\beta_m+\cdots)z}.\end{aligned} \tag{3.32}$$

For a more thorough and similar description of the nonlinear polarization, see [11].

Now we show how the nonlinear polarization yields the intensity dependent index of refraction. We assume a medium where the only significant susceptibilities are $\chi^{(1)}$ and $\chi^{(3)}$. This assumption is reasonable in the silica glass of optical fibers, where $\chi^{(2)}$ is zero because of the amorphous nature of SiO_2. To begin, we consider the problem of two interacting plane waves at different optical frequencies. We simplify the problem by first assuming that the fields are copolarized along the x-axis:

$$\mathbf{E}_1(z,t) = \tilde{\mathbf{E}}(z,\omega_1)e^{-i\omega_1 t} + c.c. \text{ with } \tilde{\mathbf{E}}(z,\omega_1) = \hat{x}\tilde{E}_x(z,\omega_1)e^{i\beta_1 z} \tag{3.33}$$

$$\mathbf{E}_2(z,t) = \tilde{\mathbf{E}}(z,\omega_2)e^{-i\omega_2 t} + c.c. \text{ with } \tilde{\mathbf{E}}(z,\omega_2) = \hat{x}\tilde{E}_x(z,\omega_2)e^{i\beta_2 z} \tag{3.34}$$

where *c.c.* denotes the complex conjugate, and ω_1 and ω_2 are parameters for $\tilde{\mathbf{E}}$ rather than variables on which $\tilde{\mathbf{E}}$ is functionally dependent. We assume that $\mathbf{E}_1$ is much more intense than $\mathbf{E}_2$. Let us call $\mathbf{E}_1$ the pump and $\mathbf{E}_2$ the probe.

Equation 3.27 becomes, in the Fourier domain,

$$\tilde{\mathbf{D}}(z,\omega) = \epsilon_0\tilde{\mathbf{E}}(z,\omega) + \tilde{\mathbf{P}}(z,\omega) \tag{3.35}$$

We would like to calculate the effect of the pump on the probe. Thus, we are interested in calculating $\tilde{\mathbf{P}}^{(3)}(z,\omega_2)$, which is the nonlinear polarization of the component of $\tilde{\mathbf{D}}$

at frequency ω_2. The jth component of $\tilde{\mathbf{P}}^{(3)}(z,\omega)$ is given by

$$\begin{aligned}\tilde{P}_j^{(3)}(z,\omega=\omega_n+\omega_m+\omega_r) = \sum_{klp}\sum_{(nmr)} &\chi_{jklp}^{(3)}(z,\omega_n,\omega_m,\omega_r) \\ &\tilde{E}_j(z,\omega_n)\tilde{E}_k(z,\omega_m)\tilde{E}_l(z,\omega_r)e^{i(\beta_n+\beta_m+\beta_r)z}.\end{aligned} \tag{3.36}$$

If we substitute in ω_2 for $\omega_n+\omega_m+\omega_r$ we can calculate $\tilde{\mathbf{P}}^{(3)}(z,\omega_2)$:

$$\begin{aligned}\tilde{P}_j^{(3)}(z,\omega_2) = \sum_{klp}\sum_{(nmr)} &\chi_{jklp}^{(3)}(z,\omega_n,\omega_m,\omega_r) \\ &\tilde{E}_k(z,\omega_n)\tilde{E}_l(z,\omega_m)\tilde{E}_p(z,\omega_r)e^{i(\beta_n+\beta_m+\beta_r)z}.\end{aligned} \tag{3.37}$$

Four facts help us evaluate Equation 3.37.

1. The sum over (nmr) is covered in only six cases, assuming that $\omega_1 \neq \omega_2$. For example, $\omega_n = \omega_2$, $\omega_m = \omega_1$, and $\omega_r = -\omega_2$. The other 5 cases are just the other possible distinct assignments of $\pm\omega_{1,2}$ to $\omega_{n,m,r}$ that still yield $\omega_n+\omega_m+\omega_r = \omega_2$.

2. The $\mathbf{E}$ of Equation 3.30 is real, so $\tilde{\mathbf{E}}(z,-\omega_1)$ must equal $\tilde{\mathbf{E}}^*(z,\omega_1)$. Thus, $\tilde{\mathbf{E}}(z,\omega_1)\tilde{\mathbf{E}}(z,-\omega_1)$ equals $|\tilde{\mathbf{E}}(z,\omega_1)|^2$.

3. Silica is an isotropic medium, so $\chi_{jklp}^{(3)}$ must be zero if the indices, $jklp$, take on values that repeat an odd number of times. For example, $\chi_{xyyy}^{(3)} = \chi_{xyyz}^{(3)} = 0$ because in the first case x and y are repeated an odd number of times, and in the second x and z are repeated an odd number of times. If, for example, $\chi_{xyyy}^{(3)} \neq 0$, then a field in the $+y$-direction would create a response in the $+x$-direction. But the symmetry of an isotropic medium implies that there is no reason there should be a response in the $+x$-direction rather than the $-x$-direction. Moreover, because both $\mathbf{E}_1$ and $\mathbf{E}_2$ are polarized on the x-axis, the sum over klp in Equation 3.37 is nonzero only when klp are all x. Therefore, we are concerned only with $\chi_{jxxx}^{(3)}$, which is nonzero only when $j = x$. So, the only relevant nonzero $\chi_{jklp}^{(3)}$ is $\chi_{xxxx}^{(3)}$, and, for simplicity, we drop the subscripts.

4. The intrinsic permutation property states that $\chi^{(3)}_{jklp}(z, \omega_n, \omega_m, \omega_r) = \chi^{(3)}_{jkpl}(z, \omega_n, \omega_r, \omega_m)$. This equation is true because the names of the subscripts themselves are arbitrary and, therefore, interchangeable, although Equation 3.37 implies that a change in the order of ω's requires a corresponding change in the order of the subscripts of $\chi^{(3)}$.

These four points imply that all $\chi^{(3)}$ tensor values relevant to this problem have the subscripts $xxxx$ and have some ordering of ω_1, $-\omega_1$, and ω_2, and thus are all equal. Therefore, we drop all subscripts and arguments of $\chi^{(3)}$ to obtain

$$\tilde{\mathbf{P}}_{NL}(z, \omega_2) = \hat{x}\tilde{P}^{(3)}_x(z, \omega_2) = \hat{x}6\epsilon_0\chi^{(3)} \left|\tilde{E}_x(z, \omega_1)\right|^2 \tilde{E}_x(z, \omega_2)e^{i\beta_2 z} \tag{3.38}$$

where $\tilde{E}_x$ is defined in Equations 3.33 and 3.34. Substituting Equation 3.28 into Equation 3.27 and taking it into the Fourier domain, we have

$$\tilde{\mathbf{D}}(\mathbf{r}, \omega) = \epsilon_0\tilde{\mathbf{E}}(\mathbf{r}, \omega) + \epsilon_0\chi^{(1)} \cdot \tilde{\mathbf{E}}(\mathbf{r}, \omega) + \tilde{\mathbf{P}}_{\mathbf{NL}}(\mathbf{r}, \omega). \tag{3.39}$$

We are interested in the component of the field at the probe frequency ω_2 so we consider Equation 3.39 only at ω_2:

$$\tilde{\mathbf{D}}(\mathbf{r}, \omega_2) = \epsilon_0\tilde{\mathbf{E}}(\mathbf{r}, \omega_2) + \epsilon_0\chi^{(1)} \cdot \tilde{\mathbf{E}}(\mathbf{r}, \omega_2) + \tilde{\mathbf{P}}_{\mathbf{NL}}(\mathbf{r}, \omega_2). \tag{3.40}$$

We substitute Equation 3.38 and the positive frequency component of Equation 3.34 into equation 3.40. All of the vectors are nonzero only for their x components, so we drop the vector notation

$$\tilde{D}(z, \omega_2) = \left[\epsilon_0\tilde{E}_x(z, \omega_2) + \epsilon_0\chi^{(1)}\tilde{E}_x(z, \omega_2) + 6\epsilon_0\chi^{(3)} \left|\tilde{E}_x(z, \omega_1)\right|^2 \tilde{E}_x(z, \omega_2)\right] e^{i\beta_2 z}. \tag{3.41}$$

In Equation 3.41, $\tilde{D}(\omega_2)$ depends on both the pump field at carrier frequency ω_1 and the probe field at carrier frequency ω_2. We can rewrite Equation 3.41 as

$$\tilde{D}(z,\omega_2) = \epsilon_0 \left(1 + \chi^{(1)} + 6\chi^{(3)} \left|\tilde{E}_x(z,\omega_1)\right|^2\right) \tilde{E}_x(z,\omega_2)e^{i\beta_2 z} = \epsilon_{eff}\tilde{E}_x(z,\omega_2)e^{i\beta_2 z} \tag{3.42}$$

where

$$\epsilon_{eff} \equiv \epsilon_0 \left(1 + \chi^{(1)} + 6\chi^{(3)} \left|\tilde{E}_x(z,\omega_1)\right|^2\right). \tag{3.43}$$

By the definition of the index of refraction, we have $n^2 = c^2\mu\epsilon_{eff}$. In a nonmagnetic medium, this equation reduces to

$$n^2 = \frac{\epsilon_{eff}}{\epsilon_0}. \tag{3.44}$$

In Equation 3.42, we see that the proportionality of ϵ_{eff} to $|\tilde{E}_x(z,\omega_1)|^2$ implies an intensity-dependent refractive index. By Equation 3.33, the pump wave is given by $\mathbf{E}_1(z,t) = \hat{x}[\tilde{E}_x(z,\omega_1)e^{i(\beta_1 z - \omega_1 t)} + c.c.]$ so that the time averaged electric field intensity is given by

$$\langle|\mathbf{E}_1(z,t)|^2\rangle = 2\tilde{E}_x(z,\omega_1)\tilde{E}_x^*(z,\omega_1) = 2\left|\tilde{E}_x(z,\omega_1)\right|^2. \tag{3.45}$$

Thus, assuming a linear relationship between the index of refraction and the electric field intensity, we have

$$n = n_0 + 2n_2\left|\tilde{E}_x(z,\omega_1)\right|^2. \tag{3.46}$$

We substitute Equations 3.46 and 3.43 into Equation 3.44 to get

$$\left[n_0 + 2n_2\left|\tilde{E}_x(z,\omega_1)\right|^2\right]^2 = 1 + \chi^{(1)} + 6\chi^{(3)}\left|\tilde{E}_x(z,\omega_1)\right|^2. \tag{3.47}$$

The left side of Equation 3.47 equals

$$n_0^2 + 4n_0n_2\left|\tilde{E}_x(z,\omega_1)\right|^2 + 4n_2^2\left|\tilde{E}_x(z,\omega_1)\right|^4 \approx n_0^2 + 4n_0n_2\left|\tilde{E}_x(z,\omega_1)\right|^2 \tag{3.48}$$

where we assume that $n_2 \ll n_0$. If we substitute the approximation of Equation 3.48

into Equation 3.47, then we have

$$n_0^2 + 4n_0n_2\left|\tilde{E}_x(z,\omega_1)\right|^2 = 1 + \chi^{(1)} + 6\chi^{(3)}\left|\tilde{E}_x(z,\omega_1)\right|^2. \tag{3.49}$$

From Equation 3.49, we find that

$$n_0 = \sqrt{1 + \chi^{(1)}(\omega_2)} \tag{3.50}$$

and that

$$n_2 = \frac{3\chi^{(3)}(\omega_1)}{2n_0}. \tag{3.51}$$

Remember, that in this derivation it was assumed that the pump was much more intense than the probe. Therefore, the effect of the pump on the index of refraction seen by the probe was much more significant than the effect of the probe on the same index of refraction. This change in index of refraction changed the optical path length for the probe, in effect adding a phase shift to the probe. The case we studied in this section demonstrated the phase shift induced on a probe by a very intense pump. This effect, where a signal of one carrier frequency induces a phase shift in a signal of a different carrier frequency is called cross-phase modulation (XPM) [12]. Nonetheless, a probe signal, even in the absence of a pump signal, can induce a phase shift in itself. This effect is called self-phase modulation (SPM). In this thesis, we will limit our discussion to the case of an intense pump with a probe too weak to induce a noticeable phase shift in itself.

3.2.2 Dispersion

A short optical pulse contains many frequencies. In fact, the shorter the pulse is in time, the wider its frequency spectrum. In a dispersive medium, each frequency component propagates down the fiber at a different speed, leading to pulse distortion. These dispersive effects are very important in determining which nonlinear medium one should select for an all-optical switch or regenerator. We can express these dispersive effects mathematically by defining a frequency dependent propagation constant,

$\beta(\omega)$. After propagating a distance z, the component of the field at ω, $\tilde{E}(\omega)$, receives a phase shift of $\beta(\omega)z$ to become $\tilde{E}(\omega)e^{i\beta(\omega)z}$.

We consider first the case of the dispersion of a Gaussian pulse, because this problem can be solved analytically. We expand $\beta(\omega)$ in a Taylor series around the carrier frequency ω_0:

$$\beta(\omega) = \beta_0 + \beta_1(\omega - \omega_0) + \frac{1}{2}\beta_2(\omega - \omega_0)^2 + \cdots . \tag{3.52}$$

The constants β_n in 3.52 are equal to $\frac{\partial^n \beta}{\partial \omega^n}|_{\omega=\omega_0}$. β_0 is an initial and constant phase shift on the pulse. β_1 is the group delay and determines the velocity of the center of the Gaussian pulse envelope. β_2 is called the group velocity dispersion (GVD) and, as we will see later, causes the pulse width to increase. We write the electric field for the pulse at $z = 0$ as

$$E(z=0,t) = E_0 \exp\left[\frac{-2t^2 \ln 2}{T_0^2}\right] e^{-i\omega_0 t} \tag{3.53}$$

where we have dropped the *c.c.* because dispersion is a linear effect, making the *c.c.* term is unnecessary. This optical pulse's full width at half its maximum intensity (FWHM) is

$$T_{FWHM} = T_0. \tag{3.54}$$

The propagation of the Gaussian pulse in a dispersive medium is easily solved in the frequency domain, so we calculate the Fourier transform of this field:

$$\begin{aligned} \tilde{E}(z=0,\omega) &= \frac{1}{2\pi}\int_{-\infty}^{\infty} E(z=0,t)e^{-i\omega t}\,dt \\ &= \frac{1}{2\pi}\int_{-\infty}^{\infty} E_0 \exp\left[\frac{-2t^2 \ln 2}{T_0^2}\right] e^{-i(\omega-\omega_0)t}\,dt. \end{aligned} \tag{3.55}$$

We can easily solve this equation by completing the square in the exponent and consulting standard integral tables [13]:

$$\tilde{E}(z=0,\omega) = \frac{T_0}{2\sqrt{2\pi\ln 2}} \exp\left[\frac{-(\omega-\omega_0)^2 T_0^2}{8\ln 2}\right]. \tag{3.56}$$

Thus, the spectrum of the Gaussian pulse is another Gaussian pulse in ω with a spectral intensity FWHM of

$$\Delta\omega_{FWHM} = \frac{4\ln 2}{T_0} \tag{3.57}$$

In a purely dispersive medium, in which nonlinear effects are negligible, the field, after propagating a distance L, is given by

$$\begin{aligned}\tilde{E}(z=L,\omega) &= \tilde{E}(z=0,\omega)e^{i\beta(\omega)L} \\ &= \tilde{E}(z=0,\omega)e^{i[\beta_0+\beta_1(\omega-\omega_0)+\frac{1}{2}\beta_2(\omega-\omega_0)^2+\cdots]L}\end{aligned} \tag{3.58}$$

where we have substituted Equation 3.52 into $\beta(\omega)$. We neglect terms higher than β_2 because in fiber β_3 only becomes significant for very short pulses. Then we have from Equation 3.58

$$\begin{aligned}\tilde{E}(z=L,\omega) &= \tilde{E}(z=0,\omega)e^{i[\beta_0+\beta_1(\omega-\omega_0)+\frac{1}{2}\beta_2(\omega-\omega_0)^2]L} \\ &= \frac{T_0}{2\sqrt{2\pi\ln 2}} \exp\left[-\left(\frac{T_0^2}{8\ln 2} - \frac{i\beta_2 L}{2}\right)(\omega-\omega_0)^2 \right. \\ &\quad \left. + i\beta_1 L(\omega-\omega_0) + i\beta_0 L\right].\end{aligned} \tag{3.59}$$

Equation 3.59 is still a Gaussian pulse with the same spectral intensity FWHM given in Equation 3.57. So the spectrum of the pulse has the same envelope, but now has a phase shift equal to $\beta(\omega)L$. We take the inverse Fourier transform of Equation 3.59 to see how the pulse evolves in time at $z = L$:

$$\begin{aligned}E(z=L,t) &= \int_{-\infty}^{\infty} E(z=L,\omega)e^{i\omega t}\,d\omega \\ &= \frac{T_0}{2\sqrt{2\pi\ln 2}} e^{i(\beta_0 L-\omega_0 t)} e^{\phi} \exp\left[\frac{-(t-\beta_1 L)^2 T_0^2}{2\ln 2\left(\frac{T_0^4}{4(\ln 2)^2} + 4\beta_2^2 L^2\right)}\right]\end{aligned} \tag{3.60}$$

where ϕ is a phase factor given by

$$\phi(t, z = L) = \frac{-(\beta_1^2 L - t)^2}{4\left[\frac{T_0^2}{8\ln 2} - i\frac{\beta_2}{2}\right]}. \tag{3.61}$$

As can be seen in Equation 3.60, the pulse is still a Gaussian, although a new phase factor is present, and the pulse's width has changed. We now make several important definitions related to the coefficients, β_n, in the propagation constant that will help us to understand the physical significance of each coefficient. First, the phase velocity of the pulse, $v_\phi = \omega_0/\beta_0$, is the speed at which the carrier frequency propagates through the medium. Second, the group velocity, $v_g = 1/\beta_1$ is the speed at which the pulse envelope propagates through the medium. Last, we call β_2 the group velocity dispersion, which is related to the rate at which the pulse broadens in a second-order dispersive medium.

We can justify the definition for the phase velocity, v_ϕ, by looking at the factor $e^{i(\beta_0 z - \omega_0 t)}$ of Equation 3.60 and noticing that a point of constant phase exists at $\beta_0 z - \omega_0 t = 0$, so $v_\phi = dz/dt = \omega_0/\beta_0$. This exponential factor is the underlying carrier frequency. We can justify the other definitions by looking at the argument of the exponential in Equation 3.60:

$$\frac{-(t - \beta_1 z)^2 T_0^2}{2\ln 2\left(\frac{T_0^4}{4(\ln 2)^2} + 4\beta_2^2 z^2\right)}. \tag{3.62}$$

To justify the definition of the group velocity, we note that the center of the pulse exists where $t - \beta_1 z = 0$ and so, $v_g = dz/dt = 1/\beta_1$. To justify the group velocity dispersion, we note that β_2 influences the pulse width. A larger β_2 implies a larger denominator in Equation 3.62 and, therefore, a wider Gaussian in Equation 3.60. It is also useful to calculate the intensity FWHM, as we did in Equation 3.54:

$$T_{FWHM} = \frac{2\ln 2}{T_0}\sqrt{\frac{T_0^4}{4(\ln 2)^2} + 4\beta_2^2 z^2} \tag{3.63}$$

In Figure 3-2 we saw a Gaussian pulse propagating in a second order dispersive medium. As can be seen in the plot and in Equation 3.60, the pulse broadens and its peak intensity drops as the pulse propagates farther in fiber. This distortion, caused by the second-order dispersion, has a significant effect on the choice of nonlinear medium for an all-optical switch or regenerator. For example, the decreased peak intensity of the pulse reduces the effect of the nonlinear index of refraction, which is the key effect in fiber-based switches. The lower intensity causes a smaller phase shift, forcing the use of a longer nonlinear medium.

Dispersion causes other problems as well. In the regenerator described in Chapter 4, the signal pulses are separated temporally into two orthogonal polarizations. Ideally, the separation is larger than the pulse width. If it is not, as may happen because of dispersive broadening, the two orthogonally polarized pulses may induce unwanted phase shifts in each other. In some regenerators, this problem is solved by using a semiconductor optical amplifier with high nonlinearity and a short interaction length in order to decrease the dispersive effects. But if we consider using optical fiber as the nonlinear medium, as we will later in this thesis, we must use longer interaction lengths. The design of any fiber based all-optical switch must account for the long interaction lengths and dispersive effects of the fiber.

3.2.3 The Nonlinear Schrödinger Equation

In many cases in fiber optics, the dominant physical effects are second-order dispersion and the nonlinear index of refraction. Both of these effects are described by the nonlinear Schrödinger equation (NLS), a wave equation often used in modelling pulse propagation through an optical fiber. Here we provide an outline of the derivation of the NLS drawn largely from [12].

We derived the nonlinear wave equation in Section 3.1 in both the time domain (Equation 3.9) and the frequency domain (Equation 3.25). We now apply these results to opitcal pulse propagation through optical fiber, where the pulse is modulated on an optical carrier with frequency ω_0. To make the problem tractable, we must make some simple assumptions. First, we assume that the pulse's spectral width, $\delta\omega$, is small compared to ω_0. Second, we assume that the pulse is linearly polarized and maintains its polarization in the fiber. This assumption is not quite true, but it produces an accurate result nonetheless. The pulse takes the form

$$\mathbf{E}(\mathbf{r},t) = \hat{x}E_x(\mathbf{r},t) = \frac{1}{2}\hat{x}\left[E_s(\mathbf{r},t)e^{-i\omega_0 t} + c.c.\right] \tag{3.64}$$

where $E_s(\mathbf{r},t)$ is a slowly-varying envelope on the carrier and *c.c.* is the complex conjugate of the preceding term. Here, slow means that the pulse envelope is longer than ~0.1 ps for a carrier wavelength is 1550 nm ($\omega_0 \approx$ 1,215 TRad/s). This is necessary for $\Delta\omega \ll \omega_0$. We write the polarization vectors in the same form:

$$\mathbf{P}^{\mathrm{L}}(\mathbf{r},t) = \hat{x}P_x^{\mathrm{L}} = \frac{1}{2}\hat{x}\left[P^{\mathrm{L}}(\mathbf{r},t)e^{-i\omega_0 t} + c.c.\right] \tag{3.65}$$

$$\mathbf{P}^{\mathrm{NL}}(\mathbf{r},t) = \hat{x}P_x^{\mathrm{NL}} = \frac{1}{2}\hat{x}\left[P^{\mathrm{NL}}(\mathbf{r},t)e^{-i\omega_0 t} + c.c.\right] \tag{3.66}$$

These equations imply that the $\hat{x}$-polarized electric field induces only $\hat{x}$-directed polarization, which is true in the fused-silica glass used to make optical fiber. $\mathbf{P}^{\mathrm{NL}}$ includes the second- and higher-order terms of Equation 3.14. The glass in optical fiber is amorphous, so $R^{(2)}_{jkl} = 0$ [14]. Moreover, $R^{(n)}_{jkl}$ is small for $n > 3$, so we only need to include the effects of $R^{(1)}_{jk}$ and $R^{(3)}_{jklm}$.

We will also need the Fourier expansions of these quantities, so, for example

$$E_s(\mathbf{r},t) = \int_{-\infty}^{\infty} \tilde{E}_s(\mathbf{r},\omega)e^{-i\omega t}\,d\omega. \tag{3.67}$$

We will be consistent so that the Fourier transform of any variable in time is written as the same variable with a tilde over it.

The polarization vector, $\mathbf{P} = \mathbf{P}^{\mathrm{L}} + \mathbf{P}^{\mathrm{NL}}$, is given by the 1st and 3rd order terms from Equation 3.14:

$$P_j^{\mathrm{L}}(\mathbf{r},t) = \epsilon_0 \int_{-\infty}^{\infty} R^{(1)}_{jk}(\mathbf{r},\tau_1)E_k(\mathbf{r},t-\tau_1)\,d\tau_1 \tag{3.68}$$

$$P_j^{\mathrm{NL}}(\mathbf{r},t) = \epsilon_0 \int_{-\infty}^{\infty}\int_{-\infty}^{\infty}\int_{-\infty}^{\infty} R_{jklm}^{(3)}(\mathbf{r},\tau_1,\tau_2,\tau_3) \\ E_k(\mathbf{r},t-\tau_1)E_l(\mathbf{r},t-\tau_2)E_m(\mathbf{r},t-\tau_3)\,d\tau_1 d\tau_2 d\tau_3. \tag{3.69}$$

If we substitute Equations 3.64 and 3.65 into Equation 3.68, we easily obtain

$$\begin{aligned} P^{\mathrm{L}}(\mathbf{r},t) &= \epsilon_0 \int_{-\infty}^{\infty} R_{xx}^{(1)}(\mathbf{r},\tau_1)E_s(\mathbf{r},t-\tau_1)e^{-i\omega_0\tau_1}\,d\tau_1 \\ &= \epsilon_0 \int_{-\infty}^{\infty} \chi_{xx}^{(1)}(\mathbf{r},\omega+\omega_0)\tilde{E}_s(\mathbf{r},\omega)e^{-i\omega t}\,d\omega \end{aligned} \tag{3.70}$$

where

$$\chi_{jk}^{(1)}(\mathbf{r},\omega) = \int_{-\infty}^{\infty} R_{jk}^{(1)}(\mathbf{r},t)e^{i\omega\tau_1}\,d\tau_1.$$

In Equation 3.70, the **E**-fields are all x-polarized, so the only relevant $R_{jk}^{(1)}$ are $R_{jx}^{(1)}$. We assumed above that only the x-component of the polarization vector is excited, so the only nonzero component of $R_{jx}^{(1)}$ is $R_{xx}^{(1)}$.

Now we evaluate the nonlinear component of the polarization given in Equation 3.69. The third order response, $R_{jklm}^{(3)}$, has $4^3 = 256$ components. The **E**-field is x-polarized, so the only relevant components are $R_{jxxx}^{(3)}$. Again, we assume that only the x-directed polarization is excited, leaving only $R_{xxxx}^{(3)}$. If the medium responds instantaneously to the field, then $R_{xxxx}^{(3)}(\mathbf{r},\tau_1,\tau_2,\tau_3)$ is proportional to $\delta(\tau_1)\delta(\tau_2)\delta(\tau_3)$, which ensures that the polarization vector at time $t = t_0$, $\mathbf{P}(\mathbf{r},t_0)$, depends only on $\mathbf{E}(\mathbf{r},t)$ at time $t = t_0$. By assuming that the medium is instantaneous, we are neglecting the Raman effect, which has a response time of ~60-70 fs [12]. Our model, then, is accurate for pulses longer than ~1 ps. So, we let $R_{xxxx}^{(3)} = R^{(3)}\delta(\tau_1)\delta(\tau_2)\delta(\tau_3)$, which, combined with Equation 3.69, gives us the nonlinear polarization

$$\mathbf{P}^{\mathrm{NL}}(\mathbf{r},t) = \hat{x}\epsilon_0 R^{(3)}(\mathbf{r},t)E_x^3(\mathbf{r},t). \tag{3.71}$$

When we substitute Equation 3.64 into Equation 3.71, we get terms at frequencies of $3\omega_0$, ω_0, $-\omega_0$, and $-3\omega_0$. The terms at $\pm 3\omega_0$ require phase matching[4] to significantly affect the **E**-field. Phase matching is difficult to achieve unless chromatic dispersion

---

[4] For a quick discussion of phase matching, see Section 2.2 of Boyd [14].

is very low, so we neglect those terms to obtain

$$\mathbf{P}^{\mathrm{NL}}(\mathbf{r},t) = \hat{x}\frac{3}{8}\epsilon_0 R^{(3)}\left[\left|E_s^3(\mathbf{r},t)\right|^2 E_s e^{-i\omega_0 t} + c.c.\right].$$

Using Equation 3.66 to get

$$P^{\mathrm{NL}}(\mathbf{r},t) = \epsilon_0\epsilon_{\mathrm{NL}} E_s(\mathbf{r},t) \tag{3.72}$$

where

$$\epsilon_{\mathrm{NL}} = \frac{3}{4}R^{(3)}|E_s(\mathbf{r},t)|^2.$$

Now that we have expressions for $\mathbf{P}^L$ and $\mathbf{P}^{NL}$, we can start deriving the nonlinear Schrödinger equation. We derived the nonlinear wave equation in Section 3.1:

$$\nabla^2\mathbf{E} = \mu_0\epsilon_0\frac{\partial^2\mathbf{E}}{\partial t^2} + \mu_0\frac{\partial^2}{\partial t^2}\left[\mathbf{P}^{\mathrm{L}} + \mathbf{P}^{\mathrm{NL}}\right]. \tag{3.73}$$

It will be easier to work in the frequency domain, so we substitute in the Fourier expansions of $\mathbf{E}$, $\mathbf{P}^{\mathrm{L}}$, and $\mathbf{P}^{\mathrm{NL}}$. This is easy for all the quantities except $\mathbf{P}^{\mathrm{NL}}$, which has no simple Fourier expansion. The $\mathbf{E}$-field is slowly varying, so we can simplify the problem significantly by treating ϵ_{NL} as a constant [15]. Then the Fourier transform of P^{NL} is $\tilde{P}^{\mathrm{NL}} = \epsilon_0\epsilon_{\mathrm{NL}}\tilde{E}_s(\mathbf{r},\omega)$. So, we substitute Equations 3.64, 3.67, 3.65, 3.66, the bottom equality of 3.70, and $\tilde{P}^{\mathrm{NL}}$ into Equation 3.73 to obtain

$$\nabla^2\tilde{E}_s(\mathbf{r},\omega-\omega_0) + \epsilon(\omega)\frac{\omega^2}{c^2}\tilde{E}_s(\mathbf{r},\omega-\omega_0) = 0 \tag{3.74}$$

where $c = 1/\sqrt{\epsilon_0\mu_0}$ and

$$\epsilon(\omega) = 1 + \chi_{xx}^{(1)}(\omega) + \epsilon_{\mathrm{NL}}. \tag{3.75}$$

Many derivations now introduce the new variables $\bar{n}$, $\bar{\alpha}$, which we interpret as a refractive index and an absorption coefficient. These quantities are defined by

$$\epsilon = \left(\bar{n} + i\frac{c\bar{\alpha}}{2\omega}\right)^2, \quad \bar{n} = n + n_2|E_s|^2, \quad \bar{\alpha} = \alpha + \alpha_2|E_s|^2.$$

From these equations and Equation 3.75, we obtain

$$n = 1 + \frac{1}{2}\mathrm{Re}\left(\chi_{xx}^{(1)}\right), \quad \alpha = \frac{\omega}{nc}\mathrm{Im}\left(\chi_{xx}^{(1)}\right),$$
$$n_2 = \frac{3}{8n}\mathrm{Re}\left(R^{(3)}\right), \quad \alpha_2 = \frac{3\omega_0}{4nc}\mathrm{Im}\left(R^{(3)}\right).$$

α_2 is small for silica fibers, so we will ignore its effects.

We can solve Equation 3.74 with a separation of variables solution of the form

$$\tilde{E}_s(\mathbf{r}, t) = F(x,y)\tilde{A}(z, \omega - \omega_0)e^{i\beta_0 z}$$

where $\tilde{A}$ is a slowly varying envelope, and β_0 is the wave-number constant that we will set later. Substituting this solution into Equation 3.74, we obtain the equations

$$\frac{\partial^2 F}{\partial x^2} + \frac{\partial^2 F}{\partial y^2} + \left[\epsilon(\omega)\frac{\omega^2}{c^2} - \tilde{\beta}^2\right] F = 0 \tag{3.76}$$

$$2i\beta_0 \frac{\partial \tilde{A}}{\partial z} + \left(\tilde{\beta}^2 - \beta_0^2\right)\tilde{A} = 0 \tag{3.77}$$

where $\tilde{\beta}^2$ is the separation coefficient, and we used the slowly varying approximation to neglect the second derivative $\partial^2 \tilde{A}/\partial z^2$. We can also simplify the equations with an approximation of $\epsilon(\omega)$:

$$\epsilon = (n + \Delta n)^2 \approx n^2 + 2n\Delta n, \text{ where}$$
$$\Delta n = n_2 |E_s|$$

We will not go into detail, but Equation 3.76 can be solved approximately with perturbation methods [16, 17]. For the single-mode fibers used in long-distance communication, when $\epsilon = n^2$, then F is approximately a two-dimensional Gaussian whose peak coincides with the fiber axis. Then we perturb ϵ to include Δn to obtain a first-order perturbation solution. F is unchanged, but $\tilde{\beta}$ does change

$$\tilde{\beta}(\omega) = \beta(\omega) + \Delta\beta(\omega) \text{ where}$$
$$\Delta\beta(\omega) = \frac{\omega^2 n(\omega)}{c^2\beta(\omega)} \frac{\int_{-\infty}^{\infty}\int_{-\infty}^{\infty} \Delta n(\omega)|F(x,y)|^2\,dxdy}{\int_{-\infty}^{\infty}\int_{-\infty}^{\infty} |F(x,y)|^2\,dxdy}$$

Equation 3.77 determines the propagation of the pulse down the fiber. We can simplify it by noticing that $\tilde{\beta}^2 - \beta_0^2 = (\tilde{\beta} + \beta_0)(\tilde{\beta} - \beta_0) \approx 2\beta_0(\tilde{\beta} - \beta_0)$ to get

$$\frac{\partial\tilde{A}(z,\omega-\omega_0)}{\partial z}) = i\left[\beta(\omega) + \Delta\beta(\omega) - \beta_0\right]\tilde{A}(z,\omega-\omega_0). \tag{3.78}$$

This equation is in the frequency domain, and we would now like to return to the time domain. We first expand $\beta(\omega)$ and $\Delta\beta(\omega)$ in Taylor series around the carrier frequency ω_0 to obtain

$$\beta(\omega) = \beta_0 + (\omega-\omega_0)\beta_1 + \frac{1}{2}(\omega-\omega_0)^2\beta_2 + \cdots$$
$$\Delta\beta(\omega) = \Delta\beta_0 + (\omega-\omega_0)\Delta\beta_1 + \frac{1}{2}(\omega-\omega_0)^2\Delta\beta_2 + \cdots.$$

We can usually ignore β_n for $n > 3$ because $\Delta\omega \ll \omega_0$. We can also ignore $\Delta\beta_n$ for $n > 0$ because $\Delta\beta_0$ contains the effects we are interested in: the nonlinear index of refraction and the fiber loss.

We substitute these Taylor series into Equation 3.78. As we know from basic Fourier transform properties, multiplication by $\omega - \omega_0$ in the frequency domain is the same as $i\frac{\partial}{\partial t}$ in the time domain. We can see this easily in the formula

$$A(z,t) = \int_{-\infty}^{\infty} \tilde{A}(z,\omega-\omega_0)e^{-i(\omega-\omega_0)t}\,d\omega$$

So, Equation 3.78 becomes

$$\frac{\partial A}{\partial z} + \beta_1\frac{\partial A}{\partial t} + \frac{i}{2}\beta_2\frac{\partial^2 A}{\partial t^2} = i\Delta\beta_0 A.$$

Now, we use $\beta\omega \approx n(\omega)\omega/c$. We also assume that the transverse-mode profile, $F(x,y)$, does not change much with with small changes in frequency so that all frequencies contained in the pulse will have nearly the same $F(x, y)$. We then get

$$\frac{\partial A}{\partial z} + \beta_1 \frac{\partial A}{\partial t} + \frac{i}{2}\beta_2 \frac{\partial^2 A}{\partial t^2} + \frac{\alpha}{2} A = i\gamma(\omega_0)|A|^2 A \tag{3.79}$$

where

$$\gamma(\omega_0) = \frac{n_2(\omega_0)\omega_0}{cA_{eff}}$$

and

$$A_{eff} = \frac{\left(\int_{-\infty}^{\infty}\int_{-\infty}^{\infty} |F(x, y)|^2 \, dxdy\right)^2}{\int_{-\infty}^{\infty}\int_{-\infty}^{\infty} |F(x, y)|^4 \, dxdy}.$$

A_{eff} is the effective area and is a rough measure of the area of the transverse mode $F(x, y)$.

We can make one more simplification by transforming to a moving reference frame,

$$\tau = t - \beta_1 z \text{ and } U(z, \tau) = A(z, t)$$

to get

$$\frac{\partial U}{\partial z} = -\frac{1}{2} i\beta_2 \frac{\partial^2 U}{\partial \tau^2} + i\gamma|U|^2 U, \tag{3.80}$$

which is the desired nonlinear Schrödinger equation.

In Equation 3.80 the dispersion is expressed in the first term on the right side of the equation and the nonlinear phase modulation in the second term. The group delay, β_1, has fallen out of Equation 3.80 because the moving reference frame, given by $\tau = t - \beta_1 z$, moves with the group velocity of the pulse envelope. In this way, a pulse at carrier frequency ω_0 remains centered at $\tau = 0$. Zakharov and Shabat, in a monumental paper, discovered exact solutions to the NLS [18]. Nonetheless, adding other terms to this equation to account for effects other than dispersion and the nonlinear index of refraction, render the equation unsolvable. Methods exist that solve these equations numerically, and one such method, the split-step Fourier method [12], generated the plots in Figure 3-2.

We can understand Equation 3.80 better by considering two cases: one in which

γ is negligible and the other in which β_2 is negligible. If γ is negligible, we consider pulse propagation in the presence of dispersion alone:

$$\frac{\partial U}{\partial z} = -\frac{1}{2} i\beta_2 \frac{\partial^2 U}{\partial \tau^2}. \tag{3.81}$$

Equation 3.81 is solvable by taking its Fourier transform with respect to τ:

$$\frac{\partial \tilde{U}(z,\omega')}{\partial z} = \frac{1}{2} i\beta_2 \omega'^2 \tilde{U}(z,\omega') \tag{3.82}$$

which has the simple solution

$$\tilde{U}(z,\omega') = \tilde{U}(z=0,\omega') e^{\frac{i}{2}\beta_2 \omega'^2 z}. \tag{3.83}$$

Equation 3.83 describes the effects of second order dispersion, as we discussed in Section 3.2.2. Notice that the magnitude of $\tilde{U}(z,\omega')$ does not change. Nonetheless, the magnitude of the same function in the time domain, $U(z,\tau)$, broadens as the pulse propagates. Now, if β_2 is negligible, we consider pulse propagation in the presence of the nonlinearity alone.

$$\frac{\partial U}{\partial z} = i\gamma |U|^2 U. \tag{3.84}$$

Equation 3.84 is solved by considering U in polar form. We can easily verify the solution

$$U(z,\tau) = U(z=0,\tau) e^{i\gamma |U(z=0,\tau)|^2 z}. \tag{3.85}$$

From Equation 3.85, we see that a phase shift is added to the pulse that is proportional to γ and to the intensity of the pulse. This phase modulation is exactly what we expect from Section 3.2.1, where we discussed the nonlinear index of refraction. Also notice that, unlike the case above with just the dispersion term, the magnitude of the time domain pulse, $|U(z,\tau)|$, does not change. But, the magnitude of the same pulse in the frequency domain does change.

In single-mode fiber (SMF), only the HE_{11} mode is excited. Nonetheless, if z is the direction of propagation, then the electric field can be considered polarized in either the x or y direction to good approximation. Thus, even single-mode fiber supports two different modes of polarization [12]. Equation 3.80 does not account for two possible polarizations or loss in the fiber. To include these effects, we must use a coupled set of two partial differential equations:

$$\frac{\partial A_x}{\partial z} + \frac{i}{2}\beta_2\frac{\partial^2 A_x}{\partial \tau^2} + \frac{\alpha}{2}A_x = i\gamma\big(|A_x|^2 + \frac{2}{3}|A_y|^2\big)A_x + \frac{i\gamma}{3}A_x^* A_y^2 e^{-2i\Delta\beta z} \tag{3.86}$$

$$\frac{\partial A_y}{\partial z} + \frac{i}{2}\beta_2\frac{\partial^2 A_y}{\partial \tau^2} + \frac{\alpha}{2}A_y = i\gamma\big(|A_y|^2 + \frac{2}{3}|A_x|^2\big)A_y + \frac{i\gamma}{3}A_y^* A_x^2 e^{-2i\Delta\beta z}. \tag{3.87}$$

In these equations, α is the loss in the fiber, A_x and A_y are the electric field envelopes of the two polarizations, and $\Delta\beta = \beta_{1x} - \beta_{1y}$. So, these equations still account for dispersion and the nonlinear index of refraction, but also account for the fiber loss with α and linear birefringence with $\Delta\beta$. The linear birefringence causes each of the polarization components to propagate at different rates. In fact, microbending in the fiber causes the value of the birefringence to change randomly down the length of the fiber, causing the polarization to change quickly and unpredictably. This effect will be important in the design of all-optical regenerators. One last interesting point in these equations is the nonlinear terms: $i\gamma\big(|A_x|^2+\frac{2}{3}|A_y|^2\big)A_x$ and $i\gamma\big(|A_y|^2+\frac{2}{3}|A_x|^2\big)A_y$. Notice that the intensity of A_y affects the index of refraction seen by A_x only two-thirds as strongly as the intensity of A_x itself. This weakening of the nonlinear index of refraction between orthogonally polarized fields will also affect the design of fiber-based regenerators.

3.2.4 Effects of Loss on Phase Shift

For this thesis, we have tested all-optical regenerators that use silica optical fibers to provide the nonlinear medium. Optical fibers have inherently low loss. The single-mode fiber common in communications has a loss of about 0.25 dB/km at a wavelength of 1550 nm. As pulses propagate in fiber, their peak intensity falls and, therefore, the intensity-dependent index of refraction decreases. The all-optical switches we presented above all operate by inducing a π phase shift in one pulse with respect to another. These two pulses are then interfered at the output. Therefore, loss increases the length of fiber or the magnitude of optical power needed to induce that phase shift. Because longer fibers can entail more noise and distortion from effects like Rayleigh scattering and dispersion, we must consider carefully how substantial the loss is. We must also remember that each pulse has a nonuniform intensity, so low intensity wings on the pulse receive a smaller nonlinear phase shift than the high intensity peak.

Let $U(z,\tau)$ be the pulse envelope on a carrier of frequency ω_0. As we did for dispersion in section 3.2.2, we expand the change in $|U(z,\tau)|^2$ as a Taylor series:

$$\frac{\partial}{\partial z}|U(z,\tau)|^2 = -\alpha|U(z,\tau)|^2 - \alpha_{NL}|U(z,\tau)|^2 + \cdots \tag{3.88}$$

The first term on the right accounts for linear gain or loss (α is positive for loss and negative for gain). In this thesis, we will neglect higher order nonlinear loss terms. α_{NL}, for example, accounts for nonlinear losses such as two-photon absorption, which can become significant with high optical powers [19].

If we neglect higher order losses, then we have

$$|U(z,\tau)|^2 = |U(z=0,\tau)|^2 e^{-\alpha z}. \tag{3.89}$$

First, let us consider how much longer a fiber with loss must be to induce the same self-phase modulation that would be induced in a lossless fiber. To simplify the problem, we assume that the pulse has uniform intensity. In a lossless fiber of length L_0, the self-phase modulation induced from Equation 3.85 is

$$\begin{aligned}\Phi(\tau) &= \int_0^L \gamma|U(z=0,\tau)|^2\,dz \\ &= \gamma|U(z=0,\tau)|^2 L_0.\end{aligned} \tag{3.90}$$

In a lossy fiber of length L, the self-phase modulation induced is

$$\begin{aligned}\Phi(\tau) &= \int_0^L \gamma |U(z,\tau)|^2 \, dz \\ &= \gamma |U(z=0,\tau)|^2 \left(\frac{1-e^{-\alpha L}}{\alpha} \right).\end{aligned} \tag{3.91}$$

Equations 3.90 and 3.91 imply that if the phase shift induced in a lossless fiber of length L_0 is to be the same as that induced in a lossy fiber of length L, then we must have $L_0 = [1 - \exp(-\alpha L)]/\alpha$. The larger α is, the longer the lossy fiber must be.

3.2.5 Numerical Solution to the NLS

The most popular numerical method for solving the nonlinear Schrödinger equation is the split-step Fourier method [12]. The nonlinear Schrödinger equation with the loss term is:

$$\frac{\partial U(z,\tau)}{\partial z} = -\frac{1}{2} i\beta_2 \frac{\partial^2 U(z,\tau)}{\partial \tau^2} - \frac{\alpha}{2} U(z,\tau) + i\gamma |U(z,\tau)|^2 U(z,\tau). \tag{3.92}$$

The standard numerical method used to solve this equation is the split step Fourier method. In this method, Equation 3.92 can be rewritten in operator notation as

$$\frac{\partial U(z,\tau)}{\partial z} = (\hat{L} + \hat{N}) U(z,\tau) \tag{3.93}$$

where the operators are given by

$$\hat{L} f = -\frac{\alpha}{2} f - \frac{1}{2} i\beta_2 \frac{\partial^2 f}{\partial \tau^2}, \tag{3.94}$$

$$\hat{N} f = i\gamma |f|^2 f. \tag{3.95}$$

The formal solution to Equation 3.93 is

$$U(z=z_2,\tau) = e^{\Psi+\Omega} U(z=z_1,\tau) \tag{3.96}$$

where

$$\Psi = (z_2 - z_1)\hat{L} \text{ and } \Omega = \int_{z_1}^{z_2} \hat{N}(z,\tau)\,dz. \tag{3.97}$$

In general these two operators cannot be dealt with separately because $\exp(\Psi+\Omega) \neq \exp(\Psi)\exp(\Omega)$. But, if $z_2 - z_1$ is very small, then the approximation

$$\exp(\Psi+\Omega) \approx \exp(\Psi)\exp(\Omega) \tag{3.98}$$

can be used.

In the slit-step Fourier method, we consider the nonlinear and linear operators separately. First, we assume periodic boundary conditions with period T. The solution to the nonlinear part, as shown in Section 3.2.3, is simply

$$U(z,\tau) = U(z=0,\tau)e^{i\gamma|U(z=0,\tau)|^2 z}. \tag{3.99}$$

The solution to the linear part can be found by assuming $U(z,\tau)$ has a Fourier series solution:

$$U(z,\tau) = \sum_{n=-\infty}^{\infty} \tilde{U}_n(z)e^{i\omega_n\tau} \tag{3.100}$$

where $\omega_n = 2\pi n/T$. The linear part of Equation 3.93 is

$$\frac{\partial U(z,\tau)}{\partial z} = -\frac{1}{2}i\beta_2\frac{\partial^2 U(z,\tau)}{\partial\tau^2} - \frac{\alpha}{2}U(z,\tau). \tag{3.101}$$

If we substitute in Equation 3.100, we obtain

$$\sum_{n=-\infty}^{\infty} \frac{\partial\tilde{U}_n(z)}{\partial z}e^{i\omega_n\tau} = \sum_{n=-\infty}^{\infty} \Big(\frac{1}{2}i\beta_2\omega_n^2 - \frac{\alpha}{2}\Big)\tilde{U}_n(z)e^{i\omega_n z}, \tag{3.102}$$

yielding the system of equations

$$\frac{\partial\tilde{U}_n(z)}{\partial z} = \Big(\frac{1}{2}i\beta_2\omega_n^2 - \frac{\alpha}{2}\Big)\tilde{U}_n(z). \tag{3.103}$$

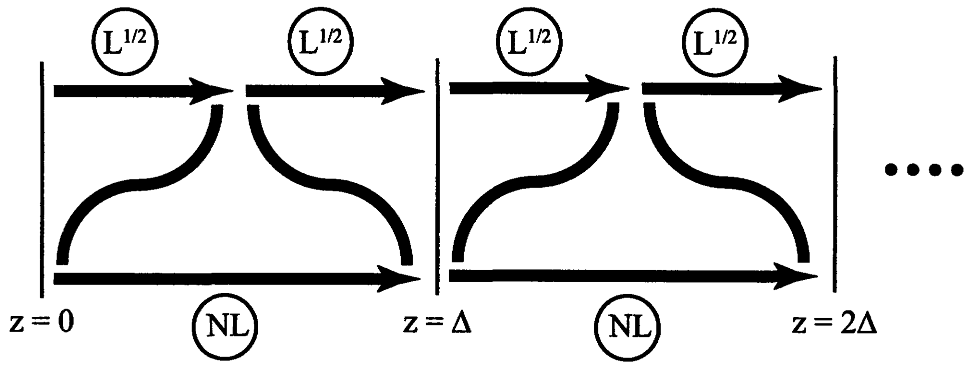

Figure 3-3: The split-step Fourier method of solutions involves alternate applications of the linear and nonlinear operators. Linear steps are labeled with an "L" and nonlinear steps are labeled with "NL." The axis shown is the discretized spatial axis.

The solutions to Equations 3.103 are

$$\tilde{U}_n(z) = \tilde{U}_n(z = 0)e^{(\frac{1}{2}i\beta_2\omega_n^2 - \frac{\alpha}{2})z}. \tag{3.104}$$

Thus, we have solved the linear part of the NLS in the frequency domain and the nonlinear part of the NLS in the time domain.

Now we consider putting these two solutions together. The spatial coordinate z is discretized into steps of length Δz. We begin with initial conditions of $U(z = 0, \tau)$, where U has period T along the temporal axis τ. To demonstrate the split step method, let us consider a slightly simpler version of it. First, we neglect dispersion and use Equation 3.99 to solve for U at $z = \Delta z$. Let us call the results of that calculation $U^{\mathbf{NL}}(z = \Delta z, \tau)$. Now we have to calculate the effects of dispersion by taking $U^{\mathbf{NL}}(z = \Delta z, \tau)$ into the frequency domain to get $\tilde{U}_n^{\mathbf{NL}}(z = \Delta z, \omega_n)$. We use $\tilde{U}_n^{\mathbf{NL}}(z = \Delta z, \omega_n)$ as the initial conditions for one spatial step of dispersion, from $z = 0$ to $z = \Delta z$. Then we return to the time domain to obtain $U(z = \Delta z, \tau)$. We repeat this procedure for all subsequent spatial steps. The solution will converge more quickly to the correct solution if we interleave the steps, as shown in Figure 3-3. Instead of solving an entire spatial step of dispersion and then using those initial conditions to solve another full spatial step of nonlinearity, we begin with a half step of dispersion, then a full step of nonlinearity, and finally a half step of dispersion. We then repeat for subsequent spatial steps.

To run this simulation on a computer, we cannot let the n of Equation 3.100 vary from $-\infty$ to ∞. Instead we truncate the series to vary from $-N$ to N, where we choose N based on the accuracy of simulation desired. Once we choose this truncation constant, we can use the fast Fourier transform and inverse fast Fourier transform to move between the frequency and time domains. The fast Fourier transform grows in computational difficulty by the order of $N \log N$, which is why this method is often preferred to much slower algorithms based on the finite difference method. Nonetheless, we must keep in mind that the approximations we have made can lead to error: space is discretized into small intervals so that we can make the assumption of Equation 3.98; the initial conditions, and, therefore, the solution is assumed to be periodic; in the frequency domain, higher frequencies are truncated from the Fourier series expansion of U; the FFT actually calculates the discrete time Fourier series rather than the desired continuous time Fourier series. We must also keep in mind that at the periodic boundaries, if the function is not continuous and does not have a continuous derivative, then the numerical solution may behave undesirably. After all, most physical pulse trains are continuous at bit-period boundaries and have continuous derivatives.

3.3 Semiconductor Optical Amplifiers

SOAs are pn-junctions designed to amplify light. Figure 3-4 (a) shows a schematic of the SOA. The depletion layer that forms around the pn-junction serves as the active region in which optical signals are amplified. An optical signal enters the active region (into the page) and is amplified when energy is transfered from the carriers to the optical field.

It is minority carriers that provide the gain. Consider, for example, the p-doped region of the SOA where the minority carriers are electrons. The semiconductor's periodic structure causes the available energy states of the electrons to be banded. Within these bands, there are so many available states that we can think of a band as a continuum of energy states. Between the bands is a gap containing energies that

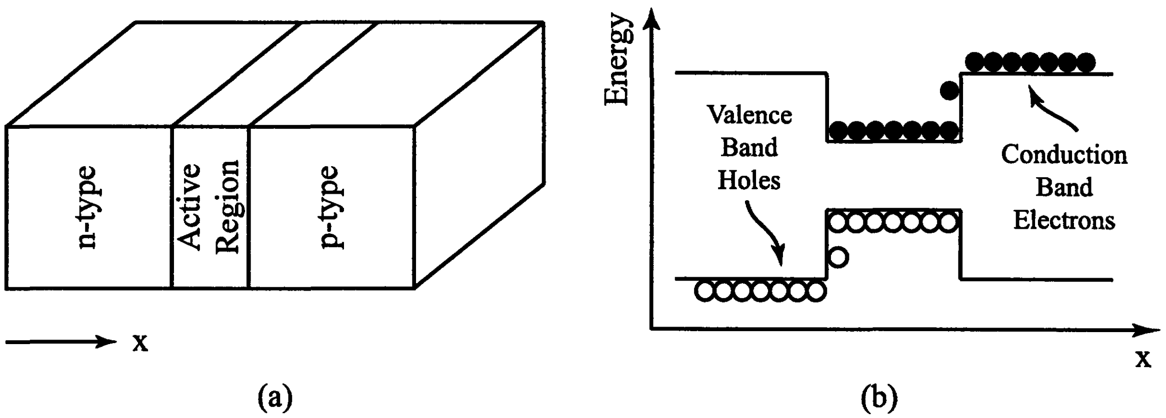

Figure 3-4: (a) The SOA is a *pn*-junction designed to produce gain. (b) Heterostructure designs trap carriers in a potential well in the active region.

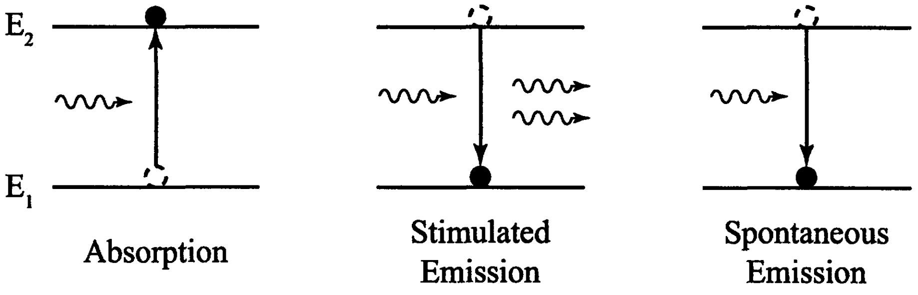

Figure 3-5: The three basic SOA processes are (a) absorption of light, (b) stimulated emission of light, and (c) spontaneous emission of light.

no electron can take. The size of this gap is the bandgap and it is the minimum photon energy that can be amplified. In the second generation of SOAs, a thin layer of a different semiconductor was placed between the *p*- and *n*-type regions, forming a heterostructure device in which the active region's bandgap is narrower. As shown in Figure 3-4, this narrower bandgap produces a potential well that traps carriers in the active region.

Ordinarily, there are very few minority-electrons in the *p*-region of the SOA, but when we forward bias the *pn*-junction minority carriers are injected into both regions. Electrons can occupy either the lower-energy valence band or the higher-energy conduction band. As we can see in Figure 3-5, which shows a simplified two-energy-level system, there are three basic processes. In (a), an electron in the lower energy state (E_1) absorbs a photon with energy $E_2 - E_1$ causing *stimulated absorption*. In (b), an electron in the higher energy state (E_2) is stimulated by the arrival of a photon to drop to the lower energy state, releasing another photon of the same energy and causing *stimulated emission.* This process is the source of gain in an SOA. Finally, in (c) an electron can drop spontaneously, releasing a photon of energy $E_2 - E_1$ in a process called *spontaneous emission*, which is a source of noise in SOAs. By injecting current through the diode, we increase the number of high-energy electrons so that stimulated emission exceeds absorption. There are, of course, analogous processes involving minority holes in the n-type region.

3.3.1 Basic Model

The model used for the SOA simulations presented in Chapter 5 is drawn from [20], and this section reproduces the derivation from that paper. As discussed in Section 3.3, it is the change in energy states of carriers that produces gain in SOAs. So, we start with an equation that describes time-evolution of the carrier density, $N(\mathbf{r}, t)$, in the SOA's active region:

$$\frac{\partial N}{\partial t} = D\nabla^2 N + kI - \frac{N}{\tau_c} - \frac{a\,(N - N_0)}{\hbar\omega_0}\,|\mathbf{E}|^2 . \tag{3.105}$$

D is the diffusion coefficient, I is the injection current (usually on the order of hundreds of mA), τ_c is the spontaneous carrier lifetime, $\hbar\omega_0$ is the photon energy, a is the gain coefficient, N_0 is the carrier density where gain and absorption cancel each other (the transparency point), and $\mathbf{E}$. Equation 3.105 and the assumptions used to derive it are discussed in [21], but it will be enough for us to consider it phenomenologically. Each of the terms in the Equation 3.105 corresponds with one of the processes described in Section 3.3. The first term on the right-hand side accounts for diffusion of the carriers in the SOA. The second term describes the repopulation of carriers by current injection into the SOA. The third term describes the depletion of carriers through spontaneous emission. Finally, the fourth term describes the depletion of carriers due to stimulated emission of photons.

Of course, we wish to obtain an equation that describes the effect the SOA has on an electromagnetic wave propagating through it. Wave propagation through the

SOA is described by

$$\nabla^2 \mathbf{E} - \frac{\epsilon}{c^2}\frac{\partial^2 \mathbf{E}}{\partial t^2} = 0, \tag{3.106}$$

where c is the speed of light. The dielectric parameter, ϵ, describes the optical properties of the SOA, including gain and index changes. It is clear that the gain is affected by changes in the carrier density, N, because carrier depletion produces the gain. Moreover, we know that the index of refraction is connected to the gain through the Kramers-Kronig relations. So ϵ is functionally dependent on N. We express ϵ as

$$\epsilon = n_b^2 + \chi, \tag{3.107}$$

where n_b is the background index of refraction. n_b a function of the transverse coordinates, x and y, because the SOA has a cylindrical waveguide structure that guides waves in the z direction. χ accounts for the effects of the charge carriers and is the portion of ϵ that contains the dependence on N.

χ's exact dependence on N is complicated, and consideration of it is beyond the scope of this thesis. For a more thorough discussion of this matter and others, see Chapter 2 of [22]. We will use a simple model for χ given by

$$\chi(N) = -\frac{\bar{n}c}{\omega_0}(\alpha + i)a(N - N_0). \tag{3.108}$$

In this equation, a is a constant which is related to the gain, $\bar{n}$ is the effective mode index, and α is a constant that accounts for carrier-dependent index changes, often referred to as the linewidth enhancement factor.

Equations 3.105, 3.106, 3.107, and 3.108 are the fundamental equations of the model, but they do not directly and easily provide us with the relationship between the input optical signal and the output optical signal. To simplify these equations, we assume that the SOA is an ideal traveling-wave amplifier and we assume that its active region is a rectangular waveguide that supports a single mode. If the input wave is linearly polarized and remains so, then we can use a separation of variables solution given by

$$\mathbf{E}(\mathbf{r},t) = \hat{x}\frac{1}{2}\left\{F(x,y)A(z,t)e^{i(k_0 z - \omega_0 t)} + \text{c.c.}\right\}. \tag{3.109}$$

$F(x,y)$ is the waveguide-mode distribution, $k_0 = \bar{n}\omega_0/c$, and $A(z,t)$ is the envelope of the optical pulse. When we substitute Equation 3.109 into Equation 3.106, we obtain the separation of variables solution given by

$$\frac{\partial^2 F}{\partial x^2} + \frac{\partial^2 F}{\partial y^2} + \left(n_b^2 - \bar{n}^2\right)\frac{\omega_0^2}{c^2}F = 0 \tag{3.110}$$

$$\frac{\partial A}{\partial z} + \frac{1}{v_g}\frac{\partial A}{\partial t} = \frac{i\omega_0 \Gamma}{2\bar{n}c}\chi A. \tag{3.111}$$

The group velocity is given by $v_g = c/n_g$, the group index is given by $n_g = \bar{n} + \omega_0(\partial\bar{n}/\partial\omega)$, and the mode confinement factor is given by

$$\Gamma = \frac{\int_0^w \int_0^d |F(x,y)|^2 \, dx\, dy}{\int_{-\infty}^{\infty} \int_{-\infty}^{\infty} |F(x,y)|^2 \, dx\, dy}$$

where w and d are the dimensions of the waveguide. Equation 3.111 neglects second derivatives of $A(z,t)$, which is called the slowly-varying envelope approximation. This approximation is allowed because the pulse's envelope is short compared to the wavelength of the carrier.

There are two unknowns in Equation 3.110: the transverse mode profile, $F(x,y)$, and the effective mode index, $\bar{n}$, which is related to the propagation constant, k_0. We can solve Equation 3.110 for $F(x.y)$ and $\bar{n}$ by applying the waveguide boundary conditions and using first-order perturbation theory, similar to the problem described in Section 3.2.3.

We can also simplify Equation 3.105. The waveguide dimensions, w and d, are small enough that the carrier density, N, is nearly uniform across the transverse dimensions. So, we can ignore the diffusion term $D\nabla^2 N$ because N is constant with respect to x and y. Thus, in Equation 3.105, the only quantity that varies over x and y is $\mathbf{E}$. So, we can easily average over the transverse dimensions by integrating over

x and y to obtain

$$\frac{\partial N}{\partial t} = \frac{I}{qV} - \frac{N}{\tau_c} - \frac{g(N)}{\hbar\omega_0}|A|^2 \tag{3.112}$$

where $g(N)$ is defined by

$$g(N) = \Gamma a(N - N_0). \tag{3.113}$$

We combine Equations 3.112 and 3.113 to get

$$\frac{\partial g}{\partial t} = \frac{g_0 - g}{\tau_c} - \frac{g}{E_{sat}}|A|^2 \tag{3.114}$$

with $E_{sat} = \hbar\omega_0 wd/(\Gamma a)$ and $g_0 = \Gamma a N_0(\tau_c kI/I_0 - 1)$. In Equationeqn:g1, $|A(z,t)|^2$ is normalized so that it equals the total optical power in the SOA.

Now only two equations, 3.111 and 3.114, give us the needed relationship between input optical signal and output optical signal, but they can be simplified further. First, by making the time transformation $\tau = t - z/v_g$ we can eliminate the term with v_g in Equation 3.111. Next, we can write the field amplitude as $A = \sqrt{P}\exp(i\phi)$. Then, by combining Equations 3.111, 3.114, 3.108, and 3.113 we obtain

$$\frac{\partial P}{\partial z} = gP \tag{3.115}$$

$$\frac{\partial \phi}{\partial z} = -\frac{1}{2}\alpha g \tag{3.116}$$

$$\frac{\partial g}{\partial \tau} = \frac{g_0 - g}{\tau_c} - \frac{gP}{E_{sat}}. \tag{3.117}$$

Equation 3.28 justifies our use of the letter g in Equation 3.113, because g is clearly the gain per unit length in the SOA. With one more simplification, we can eliminate z from the equations above. Equations 3.115 and 3.116 are easily solved by integration, which allows us to write all three equations above as

$$\begin{aligned} P_{out}(\tau) &= P_{in}e^{h\tau} \\ \phi_{out}(\tau) &= \phi_{in} - \frac{1}{2}\alpha h(\tau) \\ \frac{\partial h}{\partial \tau} &= \frac{g_0 L - h}{\tau_c} - \frac{P_{in}(\tau)}{E_{sat}}\left[e^h - 1\right]. \end{aligned} \tag{3.118}$$

$h(\tau)$ is the integrated gain given by

$$h(\tau) = \int_0^L g(z,\tau)\,dz,$$

where L is the length of the SOA in the z-direction. Equations 3.118 complete the SOA model that we will use in Chapter 5 to simulate SOA-MZI performance.

Bibliography

[1] H. Chen, G. Zhu, Q. Wang, J. Jaques, J. Leuthold, A. Piccirilli, and N. Dutta, "All-optical logic XOR using differential scheme and Mach-Zehnder interferometer," *Electronics Letters*, vol. 38, no. 21, pp. 1271–1273, 2002.

[2] Z. Zhu, M. Funabashi, Z. Pan, L. Paraschis, and S. Yoo, "10 000-Hop Cascaded In-Line All-Optical 3R Regeneration to Achieve 1 250 000-km 10-Gb/s Transmission," *IEEE Photonics Technology Letters*, vol. 18, no. 5, pp. 718–720, 2006.

[3] J. P. Wang, S. J. Savage, B. S. Robinson, S. A. Hamilton, E. P. Ippen, R. Mu, H. Wang, L. Spiekman, and B. B. Stefanov, "Regeneration using an SOA-MZI in a 100-pass 10,000-km recirculating fiber loop," in *CLEO 2007 Technical Digest*, (Baltimore, MD), May 2007.

[4] J. Wang, B. Robinson, S. Hamilton, and E. Ippen, "40-Gbit/s all-optical header processing for packet routing," *Optical Fiber Communication Conference, 2006*, p. 3, 2006.

[5] K. Inoue and H. Toba, "Wavelength conversion experiment using fiber four-wave mixing," *IEEE Photonics Technology Letter*, vol. 4, no. 1, pp. 69–72, 1992.

[6] B. Olsson and P. Andrekson, "Polarization independent Kerr-switch using a polarization diversity loop," *24th European Conference on Optical Communication*, vol. 1, 1998.

[7] S. Watanabe, F. Futami, R. Okabe, Y. Takita, S. Ferber, R. Ludwig, C. Schubert, C. Schmidt, and H. Weber, "160 Gbit/s optical 3R-regenerator in a fiber transmission experiment," *Optical Fiber Communications Conference*, 2003.

[8] S. J. Savage, B. S. Robinson, S. A. Hamilton, and E. P. Ippen, "200-pass picosecond-pulse transmission through a regenerative recirculating fiber loop," in *CLEO 2006 Technical Digest*, (Long Beach, CA), May 2006.

[9] D. J. Griffiths, *Introduction to Electrodynamics.* Upper Saddle River, New Jersey: Prentice Hall, third ed., 1999.

[10] F. B. Hildebrand, *Advanced Calculus for Applications.* Englewood Cliffs, New Jersey: Prentice-Hall, Inc., second ed., 1976.

[11] P. Butcher and D. Cotter, *The Elements of Nonlinear Optics.* Cambridge, United Kingdom: Cambridge University Press, 1990.

[12] G. P. Agrawal, *Nonlinear Fiber Optics.* Optics and Photonics, San Diego, California: Academic Press, fourth ed., 2007.

[13] I. S. Gradshteyn and I. M. Ryzhik, *Table of Integrals, Series, and Products.* San Diego, California: Academic Press, Inc., fourth ed., 1980.

[14] R. W. Boyd, *Nonlinear Optics.* San Diego, California: Academic Press, Inc., second ed., 2003.

[15] H. Haus, "Waves and Fields in Optoelectronics," *Prentice-Hall*, 1984.

[16] E. Hinch, *Perturbation Methods.* Cambridge University Press, 1991.

[17] C. Bender and S. Orszag, *Advanced Mathematical Methods for Scientists and Engineers. 1, Asymptotic Methods and Perturbation Theory.* Springer, 1999.

[18] V. E. Zakharov and A. B. Shabat, "Exact theory of two-dimensional self-focusing and one-dimensional self-modulation of waves in nonlinear media," *Soviet Physics JETP*, vol. 34, pp. 62–69, Jan. 1972.

[19] K. W. DeLong and G. I. Stegeman, "Two-photon absorption as a limitation to all-optical waveguide switching in semiconductors," *Applied Physics Letters*, vol. 57, p. 2063, Nov. 1990.

[20] G. Agrawal and N. Olsson, "Self-phase modulation and spectral broadening of optical pulses in semiconductor laser amplifiers," *IEEE Journal of Quantum Electronics*, vol. 25, no. 11, pp. 2297–2306, 1989.

[21] G. Agrawal and N. Dutta, *Long-Wavelength Semiconductor Lasers.* New York: Van Nostrand Reinhold, 1986.

[22] B. Robinson, *Semiconductor-Based All-Optical Switching for Optical Time-Division Multiplexed Networks.* PhD thesis.

Chapter 4

Wavelength-Maintaining Folded Ultrafast Nonlinear Interferometer

In Section 2.2.1 we saw that a Mach-Zehnder interferometer can be used as an all-optical switch. In this section we consider another interferometric switch, the wavelength-maintaining folded ultrafast nonlinear interferometer (WMFUNI), and its application to data regeneration. Figure 4-1 is a schematic of a simple regenerated optical fiber link. Clock pulses from a clock recovery circuit enter the signal input of the switch. Degraded data pulses from the network enter the control input, and the presence of a data pulse (i.e., a 1-bit) sets the switch to transmit the clock pulse, replacing the data pulses with undistorted clock pulses. The new data pulses then propagate in fiber until they arrive at the next regenerator.

An ideal regenerator should accomplish four things (the 4Rs). 1) It must re-amplify the signal. That is, it must restore all data pulses, representing 1-bits, to the

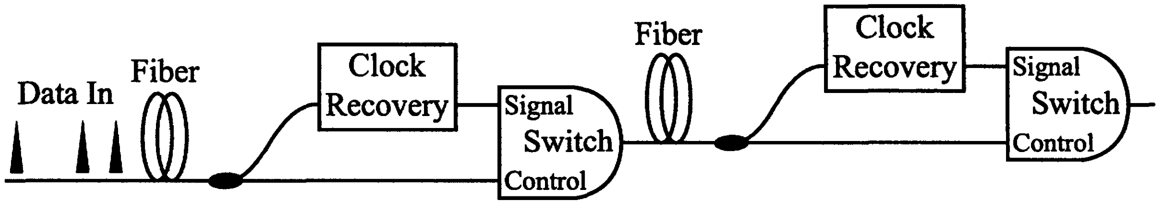

Figure 4-1: Schematic of a fiber link with data regeneration.

proper pulse energy. 2) It must reshape the pulses, which includes the underlying phase. 3) It must retime pulses that have acquired variations in timing. 4) It must repolarize the data. By this, we mean that the switch should output a constant output polarization, and the switch's behavior should be independent of the input control-pulse polarization. We will examine the WMFUNI's performance in all four of these criteria.

The best test of performance would be exactly that depicted in Figure 4-1. Testing a full link, with many regenerators, is impractical of course. Instead, we can test a single regenerator inserted in a loop of optical fiber. The data pulses then recirculate many times through the loop and regenerator. Section 4.4 presents loop regeneration experiments of the WMFUNI.

4.1 The Folded Ultrafast Nonlinear Interferometer

The ultrafast nonlinear interferometer (UNI) has been demonstrated to switch at 100 Gb/s [1] and has been considered for all-optical 3R regeneration [2]. The UNI does, however, suffer from slow polarization drifts, and its three polarization controllers must be actively monitored. Stabilization of the polarization drifts in the UNI would make practical operation more likely. In the folded UNI, a Faraday mirror added to one end of the optical path creates inherent polarization stabilization within the switch.

Like the UNI the folded ultrafast nonlinear interferometer (FUNI) [3, 4] is a single-arm interferometer. There are, however, several important differences between the two switches. The nonlinear medium of the FUNI is a length of optical fiber rather than a semiconductor optical amplifier (SOA). In SOA-based switches, data patterning on the input pulses causes amplitude patterning on the output pulses because of the long recovery times in SOAs [5]. Fiber, however, has a nearly instantaneous nonlinearity, which eliminates the amplitude variations on the output [6]. Also, as we will see, the FUNI uses a Faraday mirror to stabilize polarization within the switch.

4.1.1 FUNI description

The FUNI is assembled from commercially available discrete components. The circulator, shown with a curved arrow in Figure 4-2, passes optical power into port 1 out port 2 and power into port 2 out port 3. PC1 and PC2 are manual polarization controllers. The ~6-m length of birefringent fiber (BRF) has two different group velocities on its two polarization axes and is cross-spliced at 45° to the polarizer, allowing it to split each clock pulse into two orthogonally polarized components separated temporally by 10 ps. The nonlinear medium is dispersion shifted fiber (DSF), which has a smaller core than standard single-mode fiber (SMF). This smaller core is designed to reduce the amount of chromatic dispersion on pulses with wavelengths near 1550 nm [7]. The smaller core also increases the intensity of the light, creating a larger nonlinear effect. Finally, there is a Faraday mirror at the bottom of the diagram. The Faraday mirror reflects all the pulses and rotates their polarizations by 90°.

To explain switching in the FUNI, we consider two cases: for each clock pulse, a data pulse is either present or absent. First, consider the FUNI's operation in the absence of data pulses. The clock pulses enter at the signal port where PC1 aligns them to the polarizer. We align the birefringent fiber (BRF) at 45° to the polarizer, thus splitting the clock pulse into two temporally-separated orthogonal polarizations. The separation time between the polarizations is 10 ps. Both components propagate through 1 km of DSF, with a dispersion zero at 1551.4 nm. Then a Faraday mirror reflects the pulses and rotates them by 90°. Optical fiber can be thought of as a long series of stacked waveplates whose fast and slow axes are randomly oriented to each other, so the polarization of the pulses becomes distorted in the DSF. This 90° rotation causes polarization components originally aligned to the slow axes of these hypothetical waveplates to be aligned to the fast axes, and vice versa. So, during the return pass through the DSF and BRF, all of the relative delays and phase shifts accumulated in the forward pass are compensated, restoring the polarizations of the

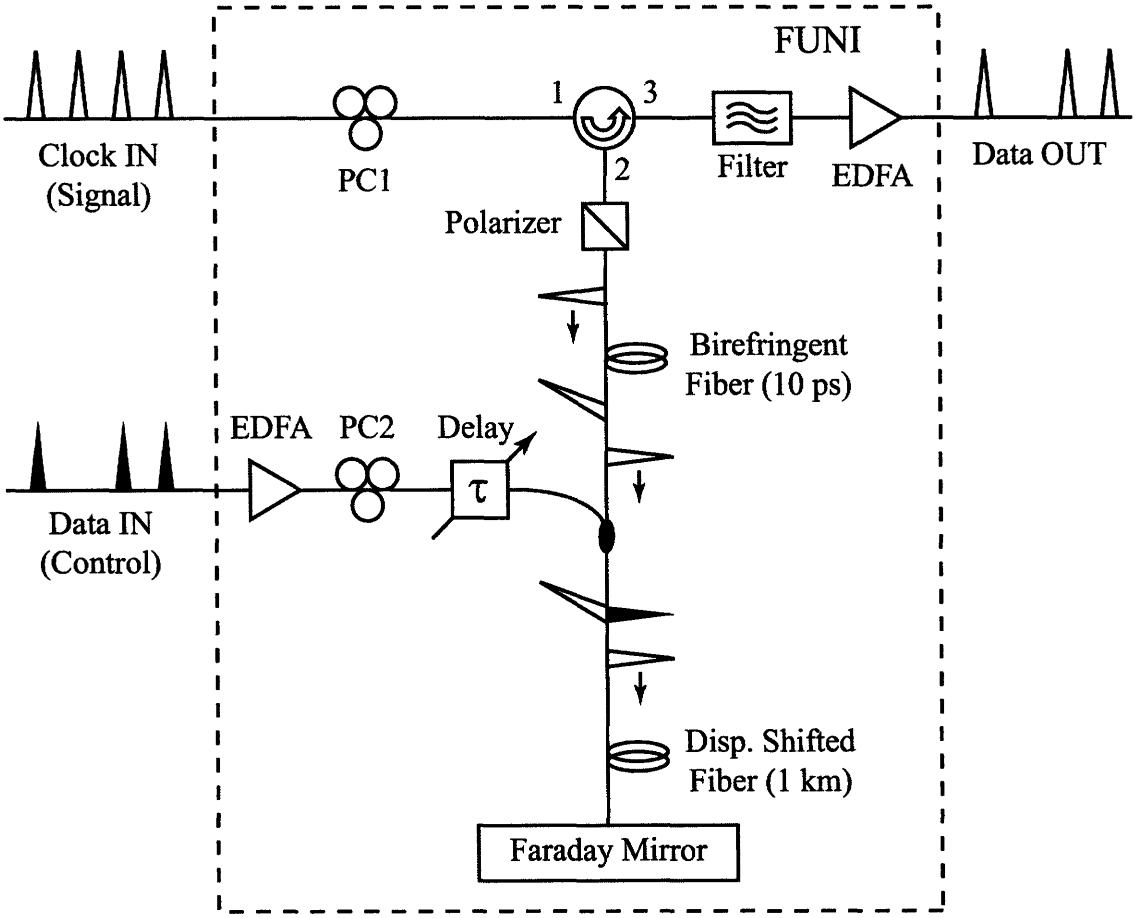

Figure 4-2: In the folded UNI, a Faraday mirror provides polarization stabilization. PC1 and PC2 are polarization controllers. The nonlinear medium is ~ 1 km of dispersion shifted fiber.

pulses (aside from a 90° rotation) and recombining the separated clock pulses. The polarizer then blocks the temporally-recombined clock pulses because they are now rotated by 90° from their original polarization.

The FUNI turns on when a data pulse enters the FUNI at the control port. These pulses are amplified in an erbium-doped fiber amplifier (EDFA) to produce sufficient intensity. Each data pulse co-propagates with one of the two temporally-separated orthogonal clock pulse polarizations. During propagation through the DSF, the nonlinear interaction between data and clock pulses induces a 180° relative phase shift between the orthogonal clock components. This phase shift rotates the clock pulse polarization by 90° so that, upon arrival at the polarizer, the clock pulse is aligned to the polarizer transmission axis and exits out port 3 of the circulator. A bandpass filter (BPF) passes the clock pulse and blocks the data pulse. Thus, the on-off keyed data pattern is modulated onto the clock pulse wavelength. Data pulses that are moving in the opposite direction of the clock pulses (e.g., after reflection) interact with both orthogonal clock polarizations, adding approximately the same total phase shift to each clock pulse polarization. Therefore, the contrast problem with the nonlinear optical loop mirror (NOLM) regenerator [8] at higher data rates does not appear in the FUNI. There may, however, be unwanted nonlinear polarization rotation effects at higher data rates.

Faraday rotation and similar phenomena have been investigated before as a means of polarization stabilization in switches similar to the FUNI. In one FUNI-like optical switch, polarization-maintaining fiber served as a nonlinear medium [9]. This technique has a possible disadvantage: the high birefringence of the polarization maintaining fiber results in the two orthogonal clock pulse components temporally overlapping or "walking-through" multiple control pulses during transmission through the device. Thus, the output contrast may be significantly degraded. Also, a data pattern on the control pulses can cause an unpredictable phase-shift in these clock pulses components. In another optical switch, dispersion-shifted fiber was tested as a nonlinear medium [10]. This switch, unlike the FUNI, does not split the signal pulses into two temporally-separated polarizations. Instead it relies on the fact that the control pulse, when temporally overlapping the signal pulse in a nonlinear medium, induces more phase shift in the co-polarized component of the signal pulse than in the cross-polarized component of the signal pulse.

4.1.2 Choice of Nonlinear Medium in the FUNI

As we reviewed in Section 3.2, optical fiber has both linear and nonlinear properties that we must consider when choosing the proper nonlinear medium for the FUNI. The linear effects play an important role in the tolerance of the switch to random variations in the timing between signal and control pulses (*timing jitter*). The nonlinear effects, which provide the switching operation, can create a phase shift that is not uniform across the signal pulse, leading to output pulses with larger spectra than desired. Moreover, the interaction of linear and nonlinear effects can cause splitting of the optical pulses.

So, full characterization of the various nonlinear media the FUNI can use is important in the design of the FUNI switch. We can easily measure the γ coefficient of Equation 3.80 [11], which characterizes the nonlinear index of refraction. The typical value in DSF is $\gamma = 2\ \mathrm{m}^{-1}\ \mathrm{W}^{-1}$, which is the value for the spools of fiber used in this work. With Equation 3.85 we can easily estimate what control pulse energy would be required to induce a π-phase shift in an ideal fiber with no loss and no dispersion. Assume that the control pulses are Gaussian with an intensity width of $\sim$ 3-ps when measured at the point of half-maximum intensity. Also remember that the optical pulses pass twice through the nonlinear fiber. We then find that a 500-m spool will require a pulse energy of $\sim$ 5 pJ/pulse and a 1000-m spool will require a pulse energy of $\sim$ 2.5 pJ/pulse. These values are close to the experimentally measured ones.

Linear dispersive effects can broaden pulses in time, but they can also increase the FUNI's tolerance to timing jitter. In the FUNI the control and signal pulses are at different wavelengths, allowing it to remove the control pulses once the switching operation is complete. Group-velocity dispersion implies that pulses with different carrier wavelengths propagate at different speeds through fiber, as discussed in Section 3.2.2. The nonlinear phase shift in the signal pulses only accumulate when the

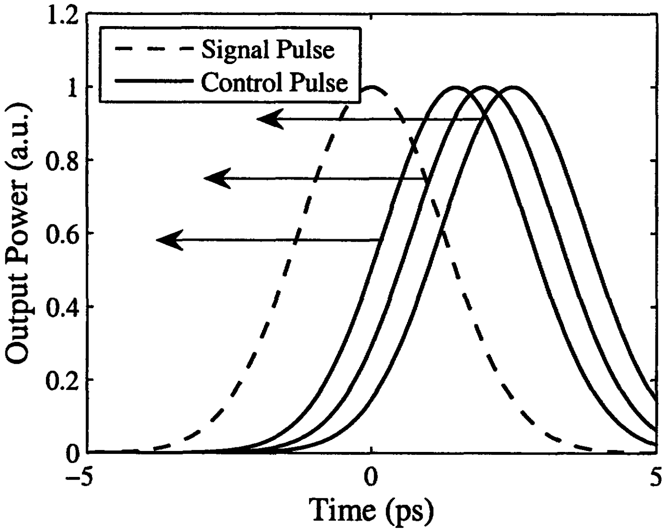

Figure 4-3: This plot shows the relative positions in time of a signal pulse and three possible control pulses with jitter, all at the beginning of the DSF. Each control pulse moves 4 ps with respect to the signal pulse, guaranteeing signal-control overlap during propagation through the DSF.

control pulse overlaps it, so the group velocities of the control and signal pulses should be nearly the same in order to create the π-phase shift with as little control-pulse energy as possible. In the regeneration application, there is, however, a good reason to increase the difference in the control and signal speeds. In regeneration, network data pulses are used as control pulses, and these data pulses may have timing jitter, in which case the positions of the optical data pulses will be randomly distributed around the center of the bit period. Sometimes, therefore, the control and signal pulses may only slightly overlap. If they have different speeds, then we can increase the chances that the pulses will overlap at least some of the time, as shown in Figure 4-3. A large walk-off between the signal and control pulses will also sharply reduce the interaction time, which increases the control-pulse energy needed to produce the π phase shift. Thus, a trade-off exists between low control-pulse energy and tolerance to timing jitter.

So, measurement of the dispersion of the nonlinear medium is important in the design of any fiber switch or regenerator. Figure 4-4 shows the setup used to measure dispersion in fiber. In this experiment, we directly measure the propagation time

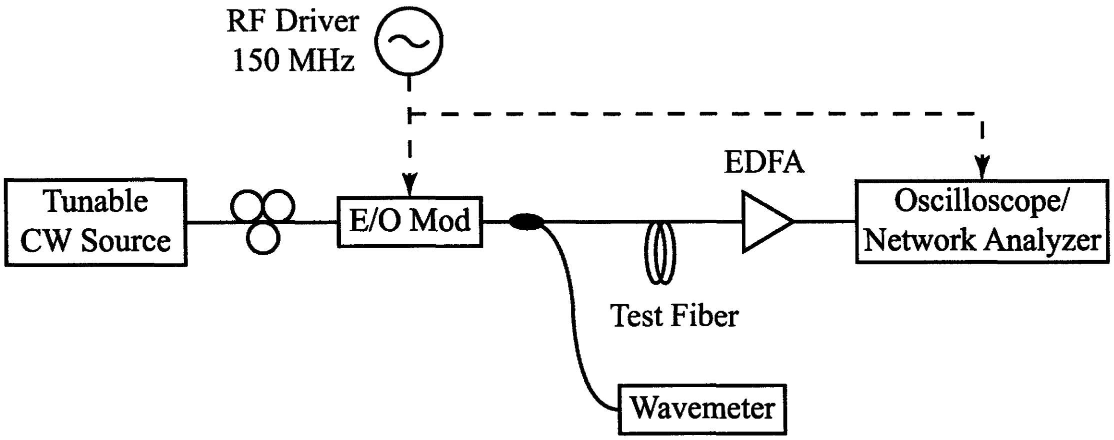

Figure 4-4: Experimental setup for dispersion measurement. The polarization controller adjusts the polarization of light from the continuous wave source to the polarization axis of the electro-optic modulator. An RF driver modulates a sine wave onto the CW light, which then passes through the test fiber. An oscilloscope or network analyzer then measures the relative propagation delay through the fiber as a function of wavelength.

of pulses traveling through the fiber as a function of carrier wavelength. A tunable source produces light of the desired wavelength, onto which a 150-MHz sine wave is modulated. A wavemeter is used to measure the carrier wavelength of the resulting pulses. These pulses then propagate through the test fiber to an oscilloscope or network analyzer, where the phase of a reference signal from the RF driver can be compared with the phase of the envelope of the optical pulses. From this comparison we can determine the propagation time to within an integer multiple of the pulse period. This means that we can only really measure relative propagation delays, which is all that is needed to determine the β_2 and β_3 components of the dispersion.

As we saw in Section 3.2.2, after an electric field propagates a distance z, the component of the field at ω, $\tilde{E}(\omega)$, receives a phase shift of $\beta(\omega)z$ to become $\tilde{E}(\omega)e^{i\beta(\omega)z}$. We expanded $\beta(\omega)$ in a Taylor series:

$$\beta(\omega) = \beta_0 + \beta_1(\omega - \omega_0) + \frac{1}{2!}\beta_2(\omega - \omega_0)^2 + \frac{1}{3!}\beta_3(\omega - \omega_0)^3 \cdots . \tag{4.1}$$

Each of the coefficients is a function of the center frequency, ω_0, around which we expand the series. In Section 3.2.2, we saw that $\beta_1(\omega_0)$ equals the propagation delay per meter of fiber of a pulse with carrier frequency ω_0. The setup of Figure 4-4 directly measures $\beta_1(\omega_0)$. We want, however, the values of β_2 and β_3. We know that

$$\beta_n(\omega_0) = \left.\frac{\partial^n \beta}{\partial \omega^n}\right|_{\omega=\omega_0} \tag{4.2}$$

So, we can calculate

$$\begin{aligned} \beta_2(\omega_0) &= \frac{\partial \beta_1(\omega_0)}{\partial \omega_0} \\ \beta_3(\omega_0) &= \frac{\partial^2 \beta_1(\omega_0)}{\partial {\omega_0}^2}. \end{aligned} \tag{4.3}$$

Figure 4-5 contains data for two different spools of fiber tested as nonlinear media in the FUNI. The first column contains the data for the 530-m spool used in this section, and the second column contains the data for the 1100-m spool used in Section 4.3. The top row contains the measured relative group delays of the 150-MHz pulses as a function of carrier wavelength. I have fit second-order polynomials to the data using a minimum mean-squared error criterion. From that polynomial fit, we can easily calculate the values of $\beta_2(\omega_0)$, shown in the second row, and $\beta_3(\omega_0)$, shown in the third row using Equations 4.3. Of course, the data are measured as a function of λ so we have to use the formula $\nu = \mathrm{c}/\lambda$. β_2 and β_3 give additional useful information about the behavior of the fiber. β_2 is important in determining how much the pulses broaden as they propagate through the fiber. When β_2 is small, the value of β_3 becomes significant. As we shall see, this can cause the splitting of pulses.

First, though, we consider how to measure directly the tolerance of an all-optical switch to timing jitter. In one simple method, the switch operates as it ordinarily does, with two input pulse trains. Then one measures the average output power of the switch as a function of the relative time delay between the control and signal pulses. The plot of output power versus relative delay is the switching window of the switch, and the wider this window is, the greater the tolerance to timing jitter. Unfortunately, manual adjustment of such a delay might be too slow for accurate

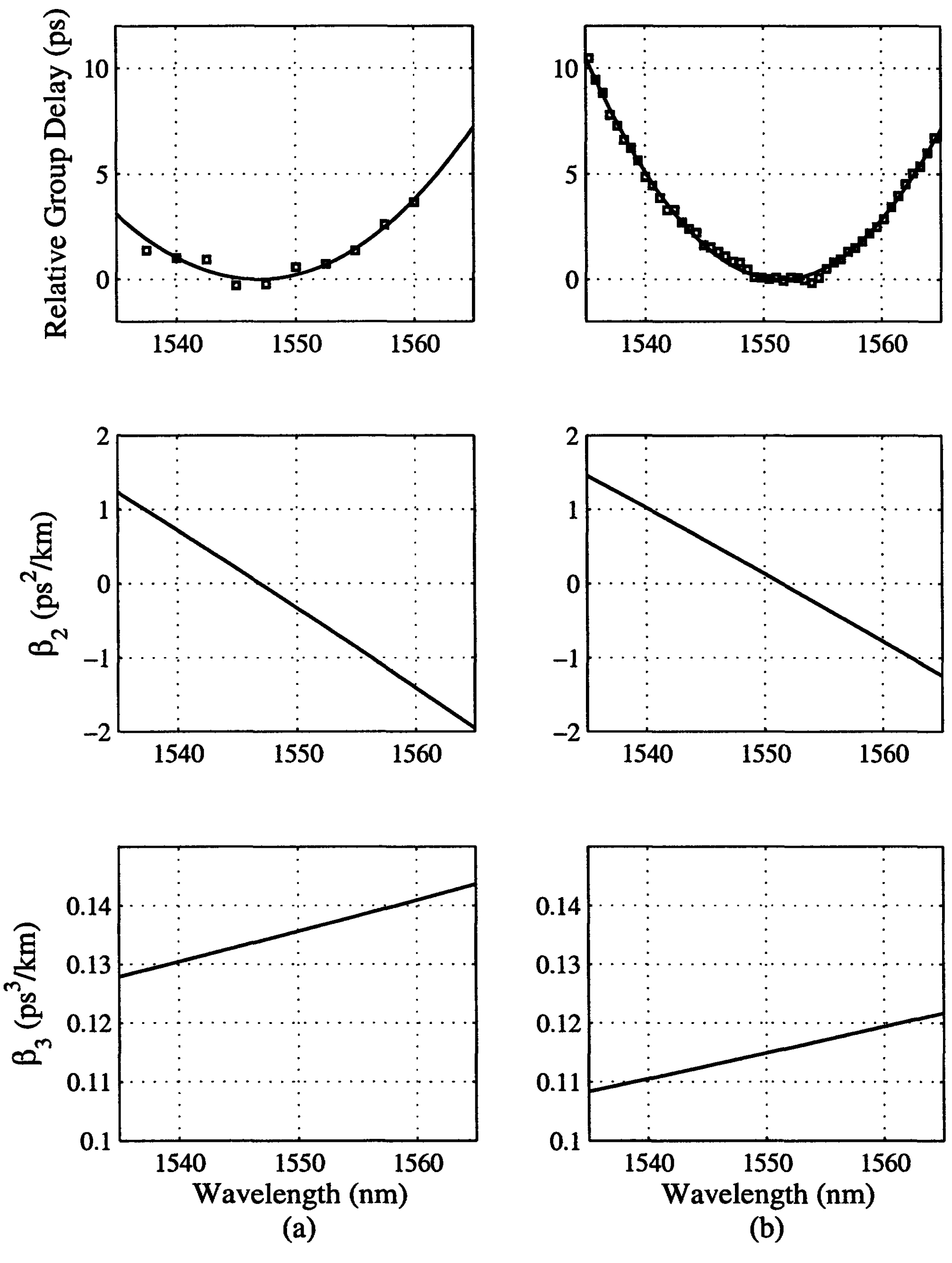

Figure 4-5: Dispersion data for (a) the 530-m spool used in this section and (b) the 1100-m spool used in Section 4.3.

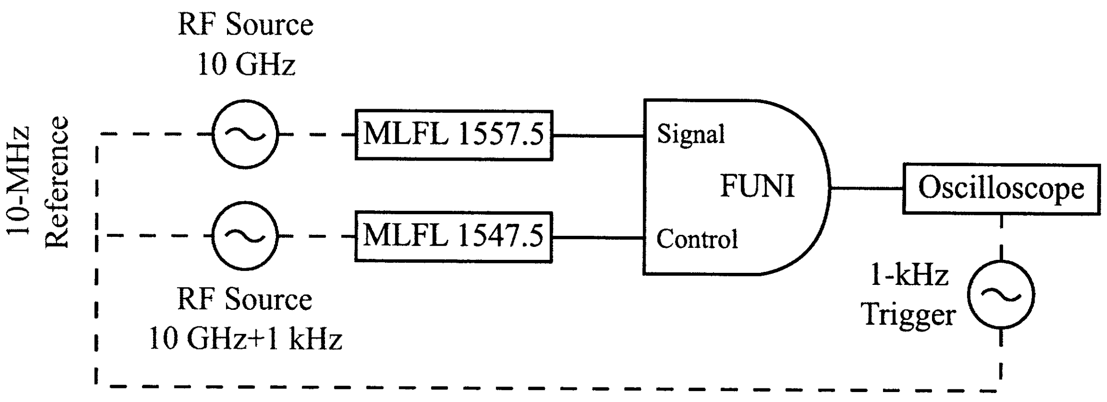

Figure 4-6: Experimental setup for switching window measurement. Two mode-locked fiber lasers provide the input pulse trains at slightly offset pulse frequencies. The oscilloscope, triggered at the offset frequency, displays the switching window.

measurement because of drifts in polarizations and fiber lengths. Instead, we can obtain a quickly varying delay between the two pulse trains by offsetting their pulse frequencies by ~ 1 kHz. Figure 4-6 shows the experimental setup for such a switching-window measurement. Two mode-locked fiber lasers generate the two input pulse trains at pulse frequencies offset by 1-kHz. The two RF sources are tied together with a 10-MHz reference clock. The average output power of the FUNI is measured at an oscilloscope triggered at the offset frequency, which is also synchronized with a 10-MHz reference clock.

Figure 4-7 shows switching windows for the FUNI using two different fiber spools as a nonlinear medium. Figure 4-7 (a) shows the switching window for the 530-m spool of dispersion-shifted fiber with the dispersion profile shown in Figure 4-5 (a). The control pulses had a carrier wavelength of 1549.8 nm and a pulse energy of 6 pJ. The signal pulses had a carrier wavelength of 1545.5 nm and a pulse energy of 0.15 pJ. The control pulse train had a pulse rate of 10 GHz and the signal pulse train had a pulse rate of 10 GHz+100 kHz. Neither pulse train had a data pattern for this switching window measurement. We determined all pulse widths by measuring the full widths of their intensity profiles at the point of half-maximum magnitude, referred to from here as the intensity full-width at half maximum or IFWHM. Both the signal pulses and the control pulses were 3 ps wide in the DSF. In the switching window

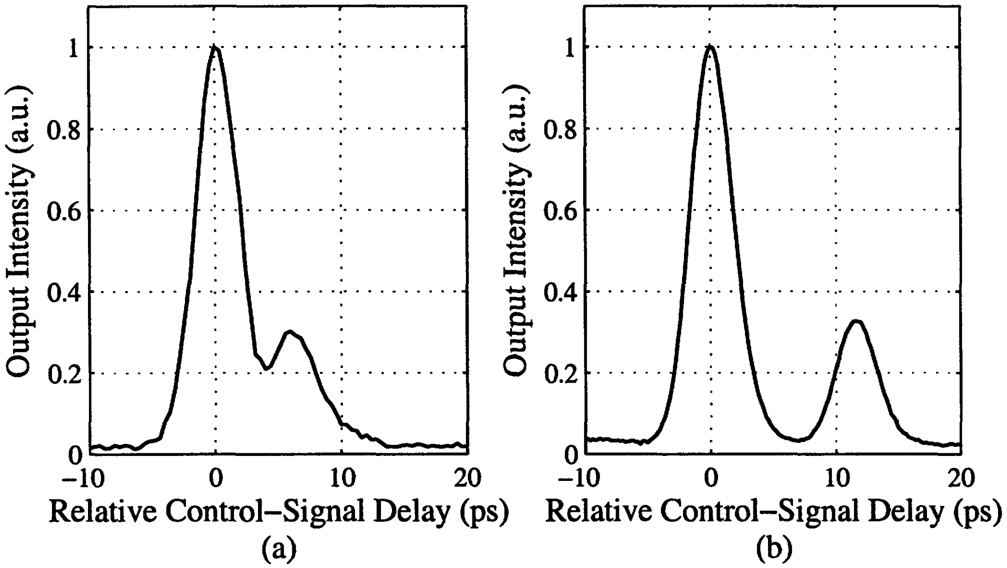

Figure 4-7: Switching windows for the FUNI (a) with 530 m of DSF as its nonlinear medium, and (b) with 1100 m of DSF as the nonlinear medium. In both cases the principle peak is 4.1 ps wide at its half-maximum point.

of Figure 4-7 (a), the width of the larger peak at its half-maximum point is 4.1 ps, implying a tolerance to timing jitter of approximately the same value.

Notice that there are two peaks in the switching window rather than just one. Recall from Figure 4-2 that the FUNI separates in time the two orthogonal polarizations of each signal pulse. The control pulse can overlap either of these two separated polarizations. The larger peak occurs when the control pulse overlaps the signal pulse component that has the same polarization. The smaller peak occurs when the control pulse overlaps the signal pulse component with the orthogonal polarization. As discussed in Section 3.2, the nonlinear effects are weaker on the orthogonal polarization, producing a smaller phase shift and less switching. We can easily adjust the control pulse polarization so that both peaks in the switching window have equal magnitudes. In this case, the control pulses must induce equal nonlinear phase shifts on both signal pulse polarizations (e.g., when the control pulse has a circular polarization). In some circumstances, this arrangement is preferred, as in the FUNI-based all-optical XOR switch [12]. Also notice that the peaks are 6.0 ps apart in this case, implying that the birefringent fiber in the switch creates 6.0 ps of delay between the two orthogonal polarization components of the signal pulses.

Figure 4-7 (b) shows the FUNI switching window when the nonlinear medium is 1100 m of dispersion-shifted fiber with the dispersion profile shown in Figure 4-5 (b). This time the control pulses had a carrier wavelength of 1557.5 nm and a pulse energy of 2.6 pJ in the DSF. The signal pulses had a carrier wavelength of 1547.5 nm and a pulse energy of 0.18 pJ. The signal pulse train had a pulse rate of 10 GHz+1 kHz and the control pulse train had a pulse rate of 10 Ghz. The control and signal pulses had pulse widths of 3 ps IFWHM. Once again, the larger peak of the switching window has a width of 4.1 ps at its half-maximum point. Note that the separation between the two peaks, however, is now 11.5 ps. For this experiment the birefringent fiber created 11.5 ps of delay between the orthogonal signal pulse components.

In the previous switching windows, we do not see any obvious evidence of β_3's effect on the pulses. Nonetheless, in dispersion-shifted fiber a nonzero β_3 can have a crippling effect on switching performance, and it must be accounted for in the design of the FUNI. It turns out that a nonlinear index of refraction, a slightly negative β_2, and a relatively large β_3 can interact, causing the splitting of an optical pulse into several smaller pulses. We can observe this effect in a switching window experiment. The fiber used as a nonlinear medium in this experiment has the dispersion profile shown in Figure 4-8.

Figure 4-9 shows two switching windows in a FUNI that uses this 2 km length of DSF as its nonlinear medium. In both experiments, the signal pulses had a carrier wavelength of 1547.9 nm, a pulse frequency of 10 GHz+1 kHz, a pulse energy of 0.28 pJ, and a pulse width of 3 ps. Also, the control pulses had a pulse frequency of 10 GHz, a pulse energy of 1 pJ, and a pulse width of 3 ps. The experiment was run at two different control-pulse carrier wavelengths. Figure 4-9 (a) shows the switching window when the control pulses have a carrier wavelength of 1552.1 nm. Figure 4-9 (b) shows the switching window when the control pulses have a carrier wavelength of 1556.3 nm. The change in carrier wavelength has changed the strength of the dispersion, resulting in the splitting of the pulse into several smaller pulses. The two peaks have become four because several control pulses per bit period now exist. Each

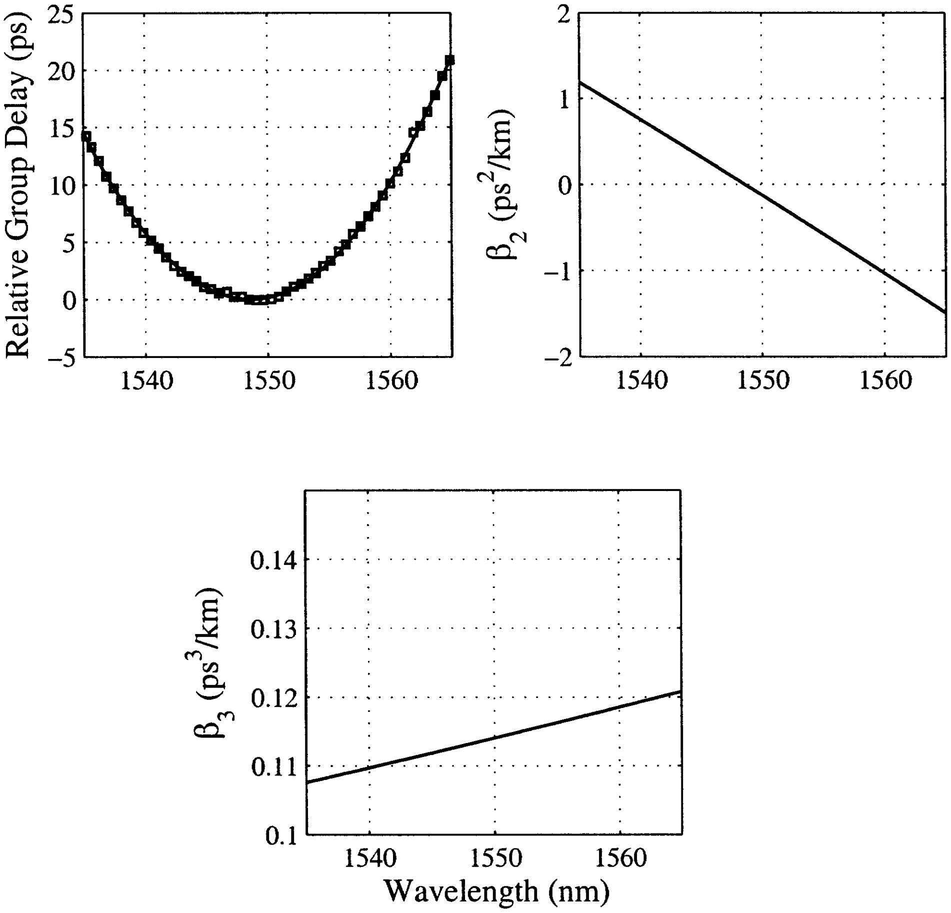

(a)

Figure 4-8: Dispersion data for the fiber used in the experiments shown in Figure 4-9.

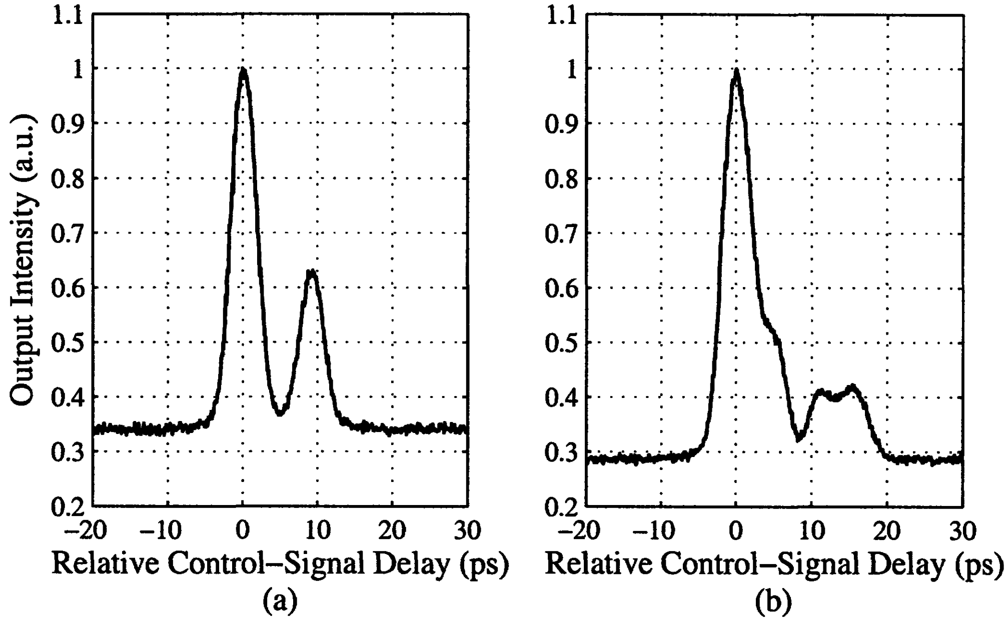

Figure 4-9: Switching windows of the 2 km fiber at a control-pulse carrier wavelength of (a) 1552.1 nm and (b) 1556.3 nm.

produces some phase shift: less than what is necessary for full switching, but enough to produce undesirable results.

4.1.3 The FUNI as an All-Optical Switch

In Sections 4.2 and 4.4 we will examine the FUNI's performance in all-optical regeneration. The FUNI is the all-optical switch component of the regenerator, so it is important to measure its performance in all-optical logic. Figure 4-10 shows the experimental setup for bit-error rate (BER) experiments. Two mode-locked fiber lasers, both driven by the same 10-GHz RF source, provide 10-GHz pulse streams of 3-ps pulses. A 10-Gb/s pulse pattern generator drives an electro-optic modulator. This modulator passes pulses corresponding to logical 1s and block pulses corresponding to logical 0s, thus modulating a $2^{31}-1$-length pseudorandom bit sequence (PRBS) onto the control pulse train. The output of the FUNI then enters a pre-amplified optical receiver. In this receiver, we can manually vary an optical attenuator to measure performance as a function of received optical power. Once attenuated, the optical signal

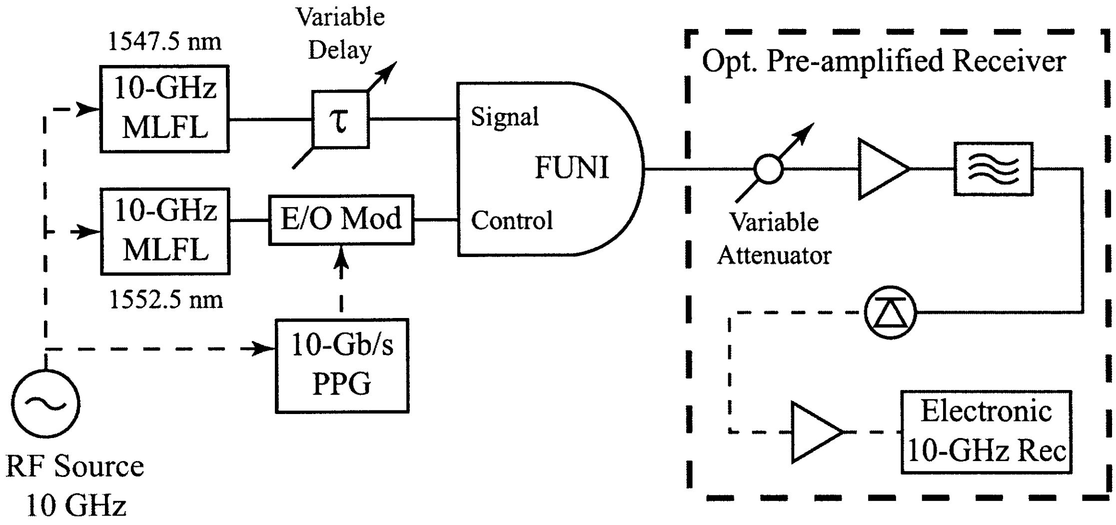

Figure 4-10: Experimental setup for bit-error rate measurements of the FUNI and other all-optical switches.

enters an Erbium-doped fiber pre-amplifier. A photodiode then converts the optical signal into an RF signal, which is amplified and low-pass filtered by an RF amplifier. The resulting RF signal is detected by a 10-GHz receiver, where we optimize the BER by adjusting timing and amplitude thresholds.

Figure 4-11 shows a plot of the bit-error rate as a function of the optical power that arrives at the receiver. In this case, the FUNI used the 500-m spool with the dispersion profile shown in Figure 4-5 (a). The signal pulses had a pulse frequency of 10-GHz, and carrier wavelength of 1550 nm, and pulse widths of 3 ps. The control pulses were modulated with a $2^{31} - 1$ PRBS, had a pulse frequency of 10-GHz, a carrier wavelength of 1545 nm, and pulse widths of 3 ps. In Figure 4-11 there are plots of the FUNI's bit-error rate performance and of the transmitter back-to-back, in which the output of the electro-optic modulator is input directly into the optically pre-amplified receiver. The FUNI's performance shows only a 0.35-dB power penalty when compared to the transmitter back-to-back at an error rate of 10^{-9}.

The receiver is adjusted to optimize the performance of the back-to-back BER, so obviously the FUNI cannot perform better than the back-to-back. Still it seems strange that a switch to be used in data regeneration actually makes the receiver performance worse. This test, however, is not a regeneration test. Instead, this test

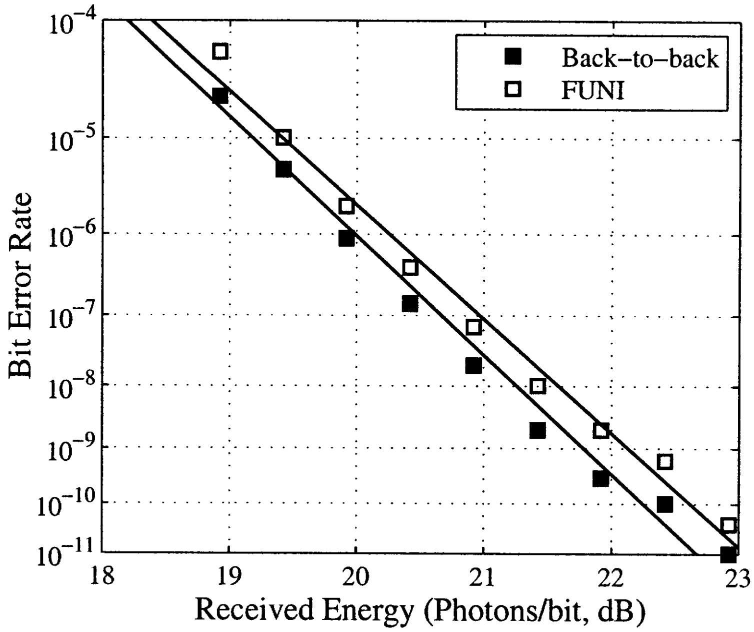

Figure 4-11: Bit-error rates of both the FUNI output and the transmitter back-to-back plotted as a function of the optical power at the receiver input. Also shown are linear fits minimizing the mean squared error.

just demonstrates that the optical receiver can be improved by adding some optical processing at its input. In a realistic regeneration test, the control input to the regenerator would be a degraded data stream with timing jitter and pulse distortions. A regenerator would then produce an improved data stream at its output. In the next section, I will present some methods of characterizing the regenerative performance of the FUNI. In Section 4.4 we will consider a more thorough test using 100-km of fiber to produce the pulse distortions. We will also see that multiple FUNI's can be cascaded without extra power penalty.

4.2 FUNI Regenerator Performance

As we discussed at the beginning of this chapter, the ideal 4R regenerator has important required properties. It must re-amplify the optical power of the data, reshape the data pulses, and retime data pulses that have acquired timing jitter. It must also repolarize the data, which requires two properties: the output of the regenerator must

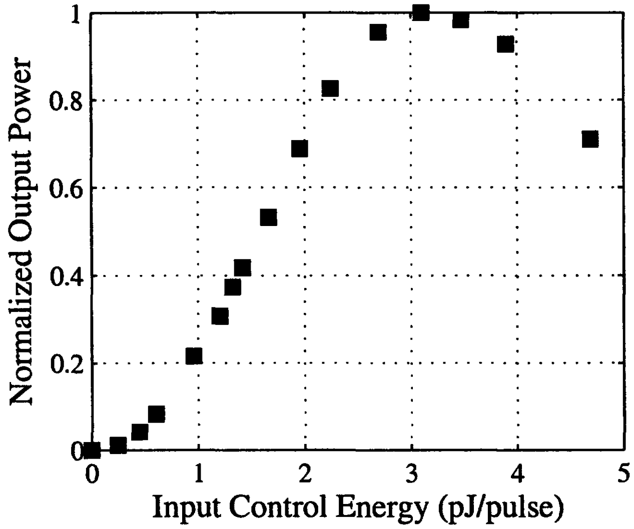

Figure 4-12: Normalized output pulse energy of FUNI with respect to input pulse energy.

have a constant polarization, and the regenerator's performance must be insensitive to the input polarization. Moreover, it should have very stable operation and, in most cases, it should be wavelength maintaining so that its input and output wavelengths are the same.

4.2.1 Re-amplification

Re-amplification does not refer just to a restoration of the optical energy averaged over many pulses, but rather to the restoration of each pulse to the same energy. Thus, the output pulse energy of the regenerator must be nonlinearly related to the input data pulse energy. Ideally, the regenerator would be a perfect thresholder, giving only two output pulse energies: zero energy if the input power is below some threshold, and some constant energy if the input power is above some threshold. Figure 4-12 shows the experimentally measured energy of the output pulse as a function of the energy of the input pulse for the FUNI. The zero derivative points, where the input power equals 0 and 1, dampen amplitude patterning in the FUNI output caused by amplitude variations in the data-pulse input amplitude. In this experiment, the data pulses had a carrier wavelength of 1557.5 nm and were modulated by a pseudorandom bit stream at 10 Gb/s. Each data pulse was 5 ps wide IFWHM in the DSF. The clock pulses had a carrier wavelength of 1547.5 nm, a pulse energy of 0.18 pJ, and widths of 3 ps IFWHM. The nonlinear medium used was 1100 km of DSF with the dispersion profile given in Figure 4-5. The birefringent fiber introduced an 11-ps optical delay in the signal pulse polarization components.

By interpolating a cosine curve to the data in Figure 4-12, we estimate that a 0.5-dB variation in the output power at the curve's peak leads to only a 0.06-dB variation in the output power. Note the similarity between the nonlinear response curve in Figure 4-12 and that of the MZI, calculated for Figure 2-10. Both curves are the raised cosine characteristic of interferometers. This nonlinearity is much weaker than that which an ideal thresholder would produce. A chain of several interferometric switches together has a response curve closer to the ideal thresholder, but we shall see in Section 4.4 that the raised-cosine nonlinearity is sufficient for regeneration.

4.2.2 Reshaping

The reshaping property is less obvious because it involves more than just reshaping the intensity envelope of the data pulses. It also requires the regenerator to maintain a nearly constant phase across the pulse so that we have approximately transform-limited pulses. In a pulse with a Gaussian envelope, we can test if it is transform-limited by measuring its time-bandwidth product, $\Delta t \Delta \nu$, where Δt is the square root of the second central-moment of the pulse's intensity envelope in the time domain and $\Delta \nu$ is the same measurement in the frequency domain. There are difficulties in making this measurement. First, it is often easier from experimental data to calculate Δt_{FWHM} and $\Delta \nu_{FWHM}$. Δt_{FWHM} is the intensity-envelope's full-width where the intensity is at half its maximum value, and $\Delta \nu_{FWHM}$ is the same measurement in the frequency domain. Second, the optical pulses we are studying are too short to measure directly with a photodiode. Instead, we use an intensity autocorrelation measurement in which the pulse being measured is used to sample itself. Our autocorrelator is a

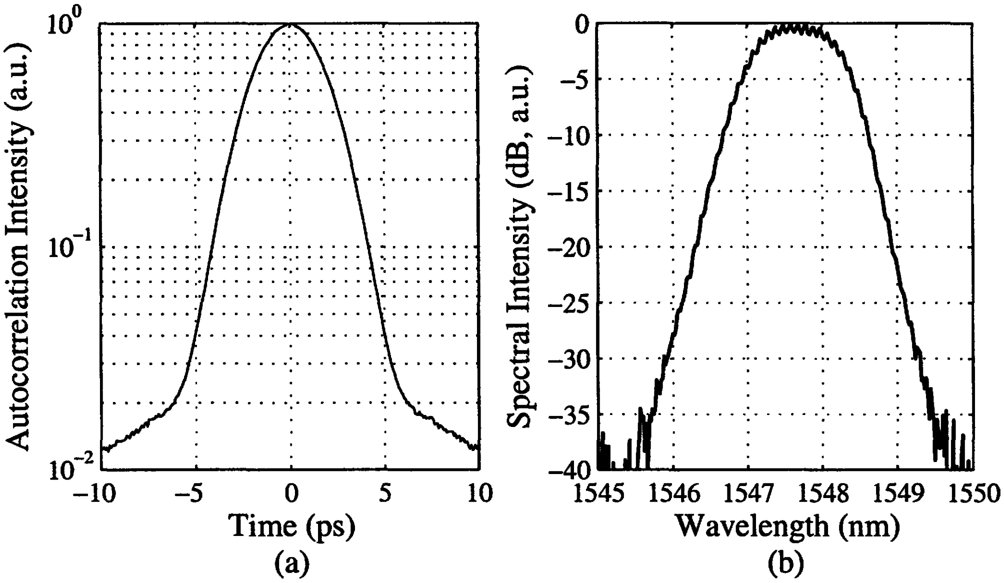

Figure 4-13: (a) Intensity autocorrelation, $A(\tau)$, of the FUNI's output pulse. This autocorrelation's full-width at half maximum is 4.53 ps. If we assume a Gaussian shape to the pulse, the intensity full-width at half maximum of the pulse itself is 3.20 ps. (b) Intensity of the output pulse's spectrum plotted versus wavelength ($\nu = c/\lambda$). The intensity full-width at half maximum is 1.22 nm or 155.4 GHz.

free-space optical device that, in effect, calculates

$$A(\tau) = \int_{-\infty}^{+\infty} I(t)I(t-\tau)\,dt, \tag{4.4}$$

where $I(t)$ is the intensity of the optical pulse.

Figure 4-13 (a) shows the intensity autocorrelation of the FUNI's output pulse and Figure 4-13 (b) shows the spectral intensity of the output pulse. As described in the figure, we can now make the estimates $\Delta t_{FWHM} = 3.20$ ps and $\Delta\nu_{FWHM} =$ 155.4 GHz. A transform-limited Gaussian pulse would have $\Delta t\Delta\nu = 1/2$ or, in terms of FWHM measurements, $\Delta t_{FWHM}\Delta\nu_{FWHM} = 0.441$. For the FUNI's output pulses, we have $\Delta t_{IFWHM}\Delta\nu_{FWHM} = 0.50$, which implies that we have a spectrum that is $\sim$ 13% larger than necessary for a pulse of this width.

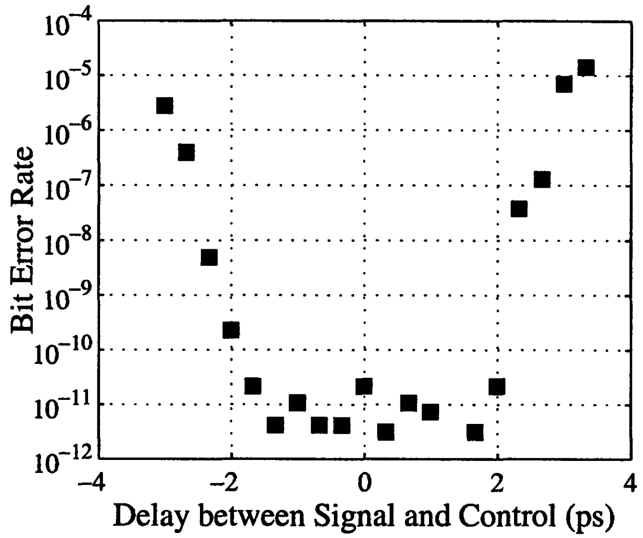

Figure 4-14: Plot of bit-error rate of the FUNI output versus the delay between the data pulses and the clock pulses. The optical energy per bit at the receiver was 6.3 aJ/bit or 26.9 dBphotons/bit.

4.2.3 Retiming

A regenerator must also retime pulses, correcting for changes in the relative spacing of the pulses that can be caused by effects like Gordon-Haus timing jitter [13]. The FUNI replaces incoming data pulses from the network with locally generated pulses, so the output jitter is only as bad as the local pulse source. Jitter in the incoming data pulses, however, can still degrade the FUNI's performance. If an incoming data pulse is far off center, then the data and clock pulses in the FUNI may not completely overlap. This partial overlap will decrease the nonlinear phase shift, thus causing a decrease in the output power. The FUNI's nonlinear response (see Figure 4-12) dampens the effects of timing jitter. We can better characterize the FUNI's insensitivity to timing jitter by manually adjusting the time delay in Figure 4-2 to change the relative delay between the data pulse and the clock pulse.

Figure 4-14 shows the effect that changing the relative delay has on the bit-error rate performance of the FUNI. The figure shows that delays up to 4 ps still yield BERs better than 10^{-9}. In this test, the control pulses had an energy of 3.2 pJ and a carrier wavelength of 1545 nm. The signal pulses had an energy of 0.1 pJ and a carrier wavelength of 1555 nm. Both pulse trains had a pulse rate of 10 GHz, and the control pulse train had a $2^{31} - 1$ PRBS modulated on it.

4.2.4 Repolarization

As discussed in Section 3.2, single-mode fiber supports two polarization modes, which we can approximately think of as horizontal and vertical polarization states. Some network components are sensitive to polarization, and other network components, like fiber, can create time-dependent polarization changes. So, we must consider the effects of polarization at the input and output of the FUNI. First, a regenerator should be insensitive to the state of the input polarization so that it will be unaffected by polarization changes in the network data pulses, like those caused by temperature changes in the fiber. Second, a regenerator should produce a constant polarization at its output, independent of any changes in the input, because network components farther along may be sensitive to sudden polarization changes.

The FUNI obviously produces a constant output polarization because the signal pulses that become the output have a constant polarization and because the FUNI has a polarizer near its output. Still, the FUNI is sensitive to changes in the input polarization. As mentioned in Section 3.2.1, the nonlinear phase shift induced by the control pulse on the orthogonal polarization is 2/3 that of the phase shift induced on the parallel polarization. A 2/3 decrease in phase shift in an ideal interferometer switch will cause a 1.25-dB drop in optical power in a logical 1-bit. In Figure 4-15, the polarization controller (PC) can shift the polarization of the control pulses to be orthogonal, instead of parallel, to the overlapped signal pulse. Doing so causes an even larger than expected 2.1 dB drop in optical power at the output. Moreover, even if we increase the optical power at the receiver by 2.1 dB to compensate for the drop in received optical power, the bit-error rate performance still degrades. In fact, with the control pulses at an orthogonal polarization to the overlapped signal pulse, there is a 0.6-dB power penalty at a BER of 10^{-9} when compared to the FUNI with the correct polarization. Remember from Figure 4-12 that a lower phase shift means the 1s are no longer generated at the top of the response curve. Therefore variations

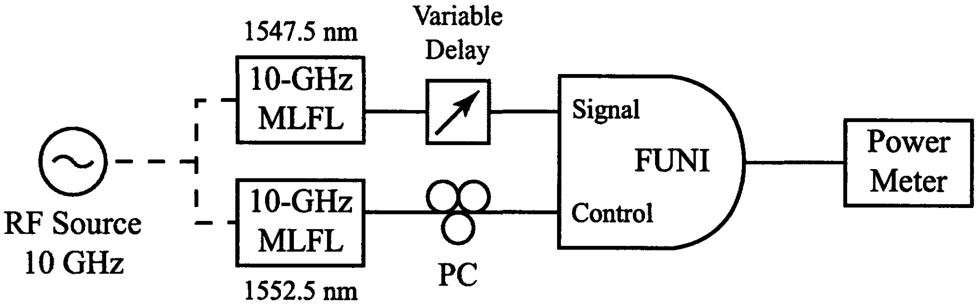

Figure 4-15: By changing the control polarization with the polarization controller (PC), we can measure the FUNI's sensitivity to input polarization.

in the input power will now cause larger variations in the output power. Section 4.3 will present a solution to this problem.

4.3 Wavelength Maintaining FUNI

At the beginning of Section 4.2, I mentioned the importance of wavelength-maintaining operation and of the need for stable operation in a regenerator. The FUNI does provide stability, within the optical switch, to vibrations, temperature changes, and other environmental effects. It is, however, affected by changes in input polarization. The FUNI is also wavelength converting, which can be useful in routing operations like label swapping [14]. Regenerators, however, usually make no such logical decisions and so they have no criterion by which to justify a change in wavelengths.

The FUNI can, however, be made both wavelength maintaining and insensitive to input polarizations. We can make these two changes at once by adding a simple SOA-based optical wavelength converter [15, 16]. Figure 4-16 shows the basic schematic for the wavelength-maintaining FUNI (WMFUNI). Both the signal and control pulse trains have a carrier wavelength of 1547.5 nm, a pulse rate of 10 GHz, and an IFWHM of 3 ps. The wavelength converter changes the carrier wavelength of the control pulses to the auxiliary wavelength of 1557.5 nm and increases their pulse widths to 5 ps. This wider pulse width increases the switching window of the FUNI so that we will not require the walk-off discussed in Section 4.1.2. The signal and control pulses then enter the FUNI, which produces a 1547.5 nm output, the same wavelength as the

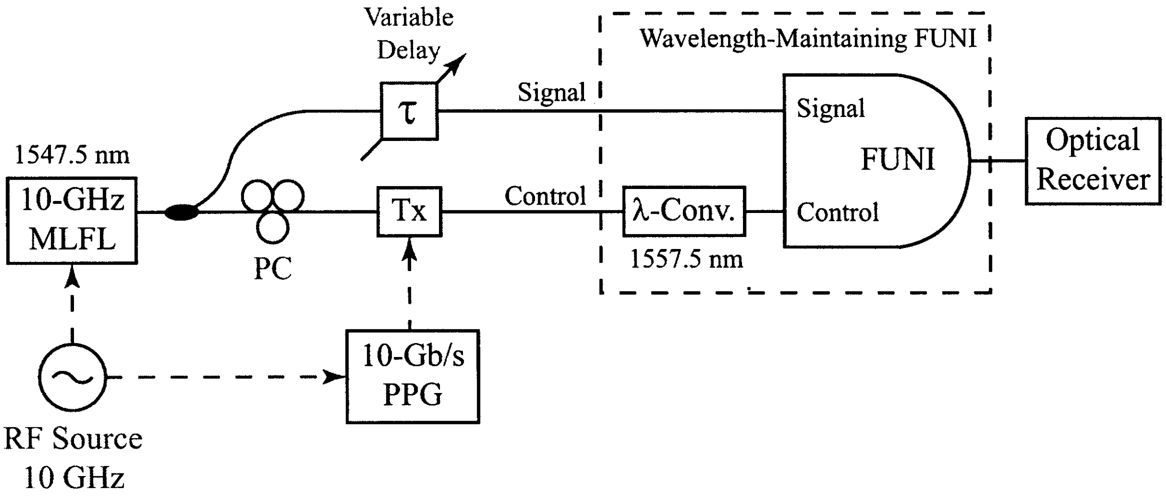

Figure 4-16: A wavelength converter (λ-conv.) changes the control pulse wavelength from 1547.5 nm to the auxiliary wavelength of 1557.5 nm.

original data input into the wavelength converter.

The FUNI is sensitive to changes in the control input polarization (see Section 4.2.4). As we shall see, the SOA wavelength converter has a constant output polarization, independent of the input polarization. Moreover, the bit-error rate performance of the wavelength converter is nearly independent of the input polarization. Therefore, the control input to the FUNI component of the WMFUNI is independent of the input polarization of the wavelength converter, making the WMFUNI's output independent of input polarization.

4.3.1 SOA Wavelength Converter

Figure 4-17 shows the SOA wavelength converter used in the WMFUNI. Leuthold et al. first proposed a similar idea in [17] and tested it at 40 Gb/s. Nielsen et al. tested the same setup shown in Figure 4-17 in [18] and found the BER performance to have a ~ 2.3-dB power penalty when compared to a transmitter back-to-back. Liu et al tested yet another similar wavelength converter at 160 Gb/s with a 2.5-dB penalty compared to back-to-back [19] and at 320 Gb/s with a 10-dB penalty compared to back-to-back [20].

In Figure 4-17, we see that a 1547.5-nm input is coupled together with a 1557.1-

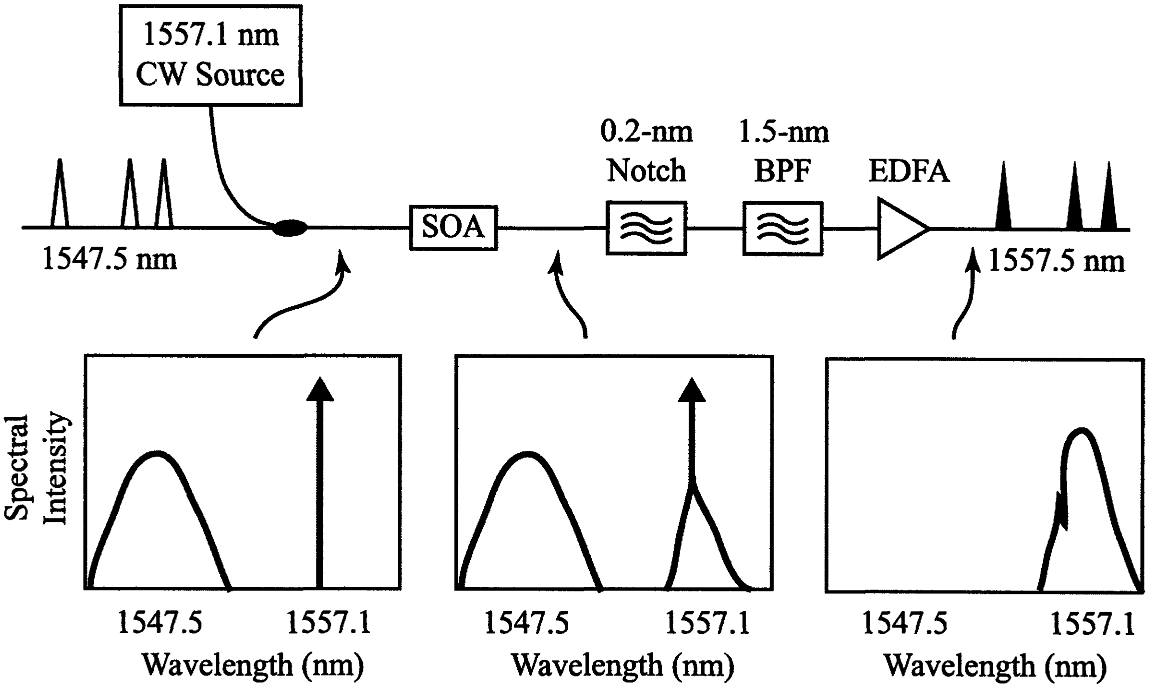

Figure 4-17: Schematic of the SOA wavelength converter. Two optical signals couple together into an SOA, the output of which passes through a notch filter, a band-pass filter, and an optical amplifier.

nm CW signal. Their spectra are shown in the first plot below the schematic. In Section 3.3, we saw that pulses in an SOA cause changes in the SOA gain, which lead to a time-dependent phase shift on any optical signal in the SOA. In the absence of an input pulse, there is no phase shift induced onto the CW in Figure 4-17. Thus, the 0.2-nm notch filter blocks the CW and the 1.5-nm BPF blocks the 1547.5-nm pulses, so that there is no optical power at the output. When an input pulse is present, the leading edge of the pulse causes a sudden drop in gain and a corresponding red-shifted chirping in the portion of the CW signal that coincides with the pulse's leading edge. There is a slower gain recovery in the pulse's trailing edge, where the CW will acquire a blue-shifted chirp. The second plot below the schematic in Figure 4-17 shows that this chirping has broadened the spectrum of the original 1557.1-nm CW line. After the SOA, the notch filter removes the CW line, and a 1.5-nm BPF removes the 1547.5-nm pulses as well as the blue-shifted side of the broadened CW spectrum, leaving only the red-shifted side. This produces a 1557.5-nm output pulse with the spectrum shown in the final plot of Figure 4-17.

The SOA wavelength converter cannot serve as a 4R regenerator. The signal power is not pulsed, so it does not correct any timing jitter in the input data pulses. Moreover, the $\sim$ 100-ps gain recovery time of the SOA causes amplitude patterning in the data output for data rates higher than $\sim$ 10 Gb/s. It does, however, have important advantages. The SOA wavelength converter is simple to turn on and operate and, once optimized, requires almost no attention from the user. It is also insensitive to changes in the polarization of the input data pulses. Varying the polarization of those pulses causes at most a 0.2-dB variation in the output power and a 0.2-dB power penalty when compared to its performance at the optimum polarization at a BER of 10^{-9}. Finally, it produces a nearly constant polarization output because the polarization of the CW beam is not significantly affected by the state of the input data pulses.

These polarization properties are very important in the design of the WMFUNI. As shown in Figure 4-16, the SOA wavelength converter changes the carrier wavelength of the incoming data pulses, which are then used as control pulses in the FUNI. In Section 4.2.4, we saw that the FUNI is sensitive to the polarization of the control pulses. The SOA wavelength converter produces a nearly constant output polarization, so that changes in the polarization of the network data pulses at the WMFUNI input do not affect the polarization of the control pulses in the FUNI. The SOA wavelength converter, however, does produce a small 0.2-dB amplitude ripple in the output power if there are large variations in the input data polarization. The FUNI, however, can suppress this ripple if it is operating around the zero derivative points in Figure 4-12.

Figure 4-18 shows the autocorrelation and spectrum of the output pulses of the SOA wavelength converter. The input data pulses had a carrier wavelength of 1547.5 nm, a pulse width of 3 ps, a data rate of 10 Gb/s, and were modulated with a $2^{31} - 1$ PRBS. These pulses were coupled into an SOA with a 1557.1-nm CW signal. The figure shows that the output pulses had an IFWHM of 4.7 ps and a spectral width of 119 GHz, which corresponds to a time-bandwidth product of $\Delta t_{FWHM} \Delta \nu_{FWHM} = 0.56$. This implies that the spectrum is about $\sim$ 27% greater

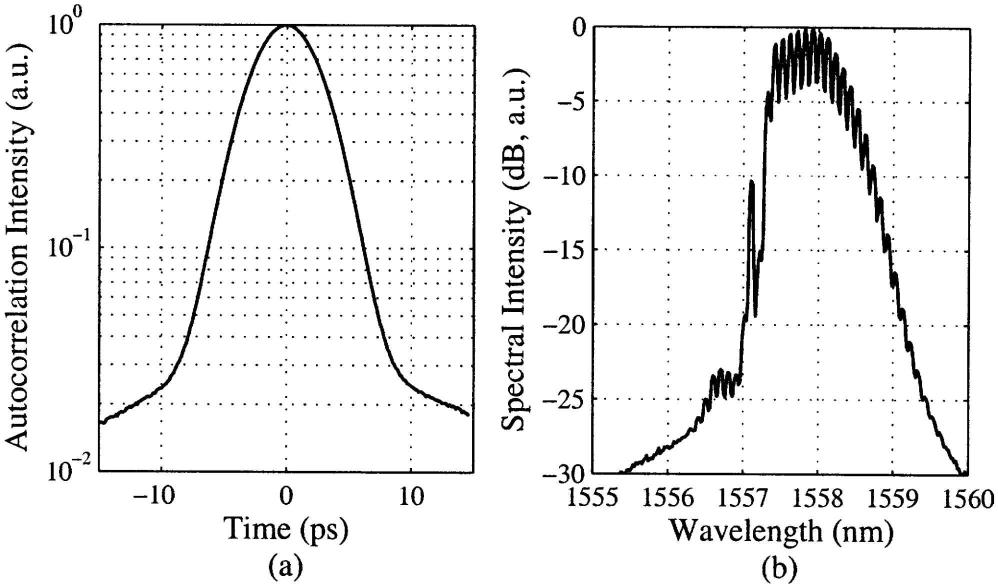

Figure 4-18: (a) Intensity autocorrelation, $A(\tau)$, of the SOA wavelength converter's output pulse. The autocorrelation full-width at half maximum is 6.63 ps. Assuming a Gaussian pulse, the pulse's IFWHM is 4.69 ps. (b) Intensity of the output pulse's spectrum plotted versus wavelength. The IFWHM is 0.95 nm or 119 GHz.

than necessary for 4.7-ps pulses, most likely because of the chirping induced in the SOA. The pulse widths leaving the wavelength converter and entering the control port of the FUNI are, therefore, wider than those of the experiments in Section 4.1. These wider pulses broaden the switching window of the WMFUNI so that we no longer require the signal-control walk-off described in Section 4.1.2.

Figure 4-19 shows the BER performance of the wavelength converter compared to a transmitter back-to-back. The figure shows a power penalty of 0.7 dB when compared to the back-to-back BER at an error rate of 10^{-9}. We shall see in the next section that this power penalty is reduced in the WMFUNI.

4.3.2 Wavelength-Maintaining FUNI Switching Performance

Section 4.2 presented an evaluation of the regeneration performance of the FUNI, especially its performance in re-amplification, reshaping, retiming, and repolarization. In the first three of those categories, the FUNI performed well, but its output amplitude and BER performance were affected by the input control pulse polarization.

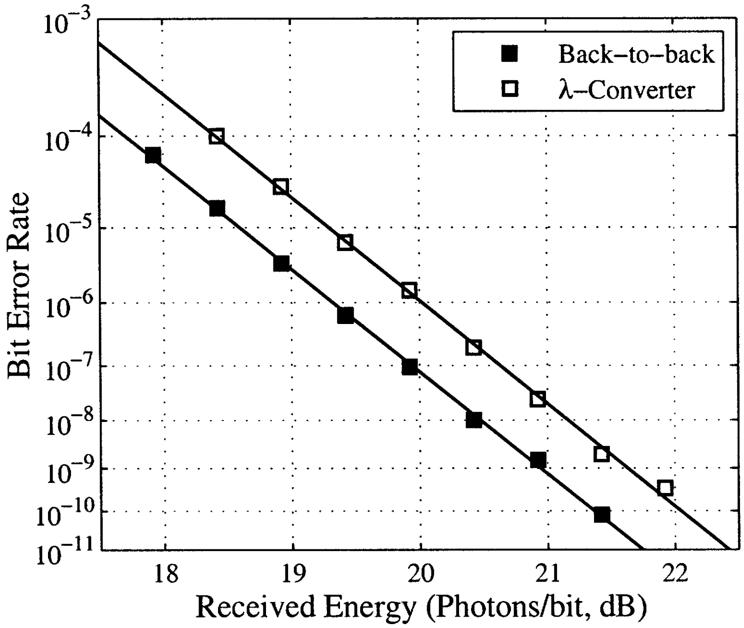

Figure 4-19: Bit-error rate performance of the wavelength converter compared to a transmitter back-to-back BER.

The FUNI does produce a constant output polarization, but with its sensitivity to input polarization, it cannot be called a repolarizing regenerator. In this section, we verify that the WMFUNI performs as well as the FUNI in optical switching, while also eliminating the FUNI's dependence on the polarization of the incoming network data pulses.

In WMFUNI experiments we use a single mode-locked fiber laser to produce optical pulse trains for both the network data pulses and the clock pulses, which is possible because both input pulse trains can have the same carrier wavelength. Figure 4-20 shows the autocorrelation and spectrum for the pulses used for both control and signal. The pulse rate was 10 GHz and the carrier wavelength was 1547.5 nm. The autocorrelation implies a time width of 3.5 ps and the spectrum shows a spectral bandwidth of 1.0 nm. These measurements produce a time-bandwidth product of $\Delta t_{FWHM}\Delta\nu_{FWHM} = 0.44$, which implies transform-limited pulses.

Figure 4-21 shows the autocorrelation and spectrum of the WMFUNI's output. In this experiment, both the signal and control inputs had a pulse rate of 10 GHz and a carrier wavelength of 1547.5 nm. The autocorrelation implies an output IFWHM

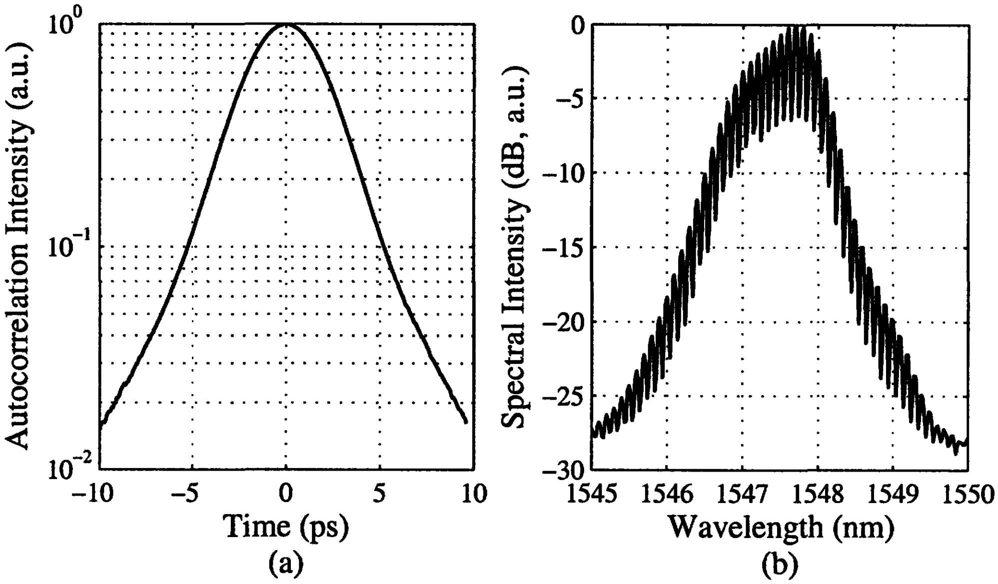

Figure 4-20: (a) Intensity autocorrelation, $A(\tau)$, of the WMFUNI's input pulses. The autocorrelation full-width at half maximum is 4.97 ps. Assuming a Gaussian pulse, the pulse's IFWHM is 3.51 ps. (b) Intensity of the input pulse's spectrum plotted versus wavelength. The IFWHM is 1.01 nm or 126 GHz.

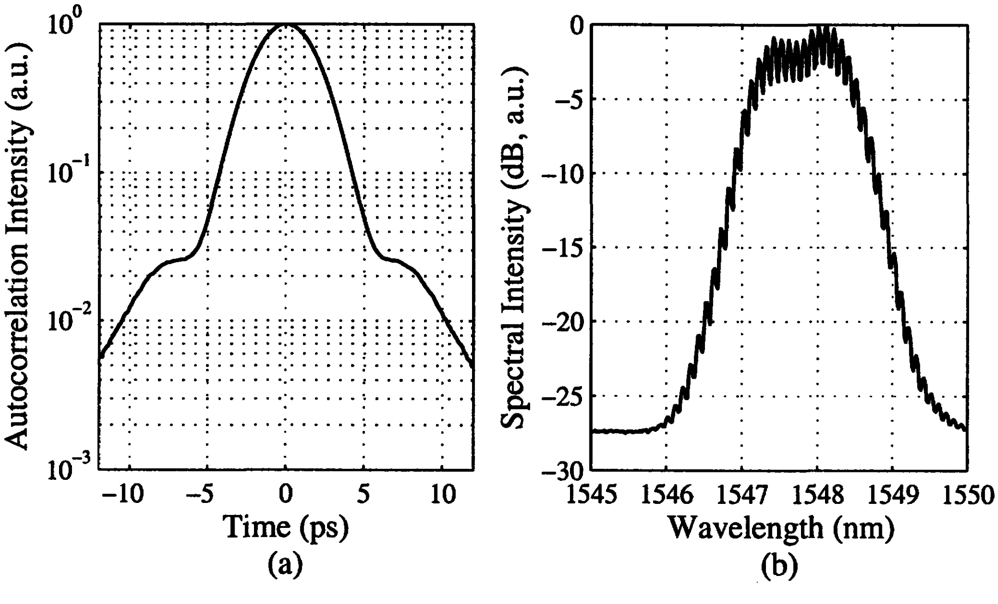

Figure 4-21: (a) Intensity autocorrelation, $A(\tau)$, of the wavelength-maintaining FUNI's output pulse. The autocorrelation full-width at half maximum is 4.57 ps. Assuming a Gaussian pulse, the pulse's IFWHM is 3.23 ps. (b) Intensity of the output pulse's spectrum plotted versus wavelength. The IFWHM is 1.3 nm or 162 GHz.

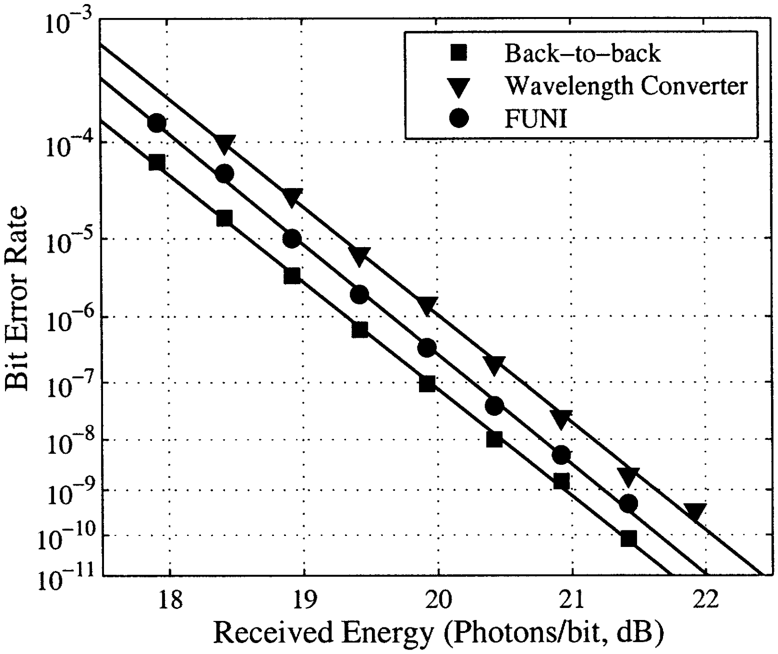

Figure 4-22: Bit-error rates curves for the SOA wavelength converter and for the WMFUNI, both compared to the transmitter back-to-back BER curve.

of 3.2 ps and a spectral bandwidth of 1.3 nm. These measurements produce a time-bandwidth product of $\Delta t_{FWHM}\Delta\nu_{FWHM} = 0.52$, a slight improvement over the wavelength converter's output time-bandwidth product of 0.56. The FUNI's output is not transform limited because of chirping of the signal pulses' phase. The control pulse has a Gaussian-like shape, and the phase shift is proportional to instantaneous intensity, so the signal pulse that it overlaps will receive a nonuniform phase shift.

Figure 4-22 shows the BER curves for the transmitter back-to-back, the SOA wavelength converter, and the WMFUNI. In these tests, the data-pulse trains were modulated with a $2^{31}-1$ PRBS. The SOA wavelength converter has a 0.7-dB penalty compared to the back-to-back at an error rate of 10^{-9}. The WMFUNI improves the BER performance to a smaller 0.3-dB penalty. Much of the difference in penalty is likely due to differences in the output-pulse spectra of the two devices. The WMFUNI's output pulses have spectral and temporal widths that are much closer to the transmitter back-to-back pulses, and so the receiver is likely more closely matched to the WMFUNI than to the SOA wavelength converter. It is also possible that the

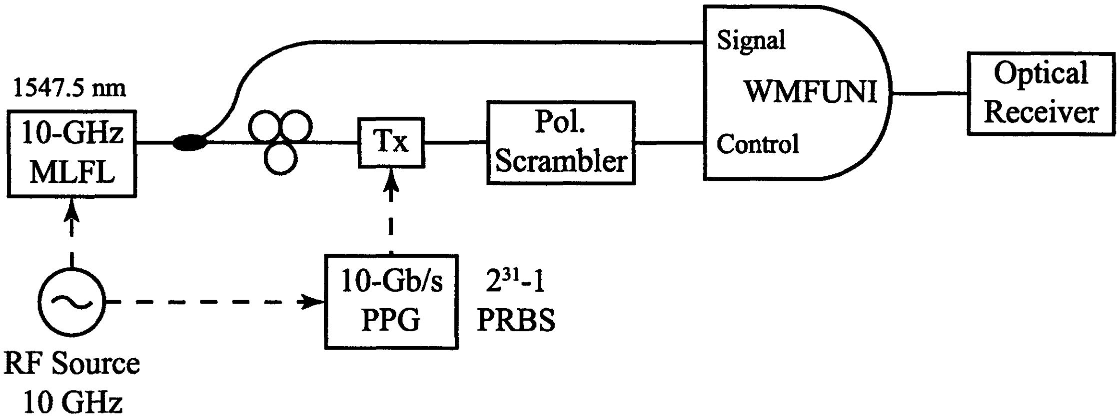

Figure 4-23: Setup used to test sensitivity of WMFUNI to polarization at the control input.

wavelength differences of the two outputs along with a wavelength dependent gain in the EDFA pre-amplifier contributes to the difference. Finally, a small amount of gain patterning due to carrier recovery in the SOA may introduce some amplitude patterning on the wavelength converter's output, which is then removed by the FUNI.

Thus, the WMFUNI functions well as an optical switch and 3R regenerator, but we must ensure that, unlike the FUNI, its output is independent of input control-pulse polarization. Figure 4-23 shows the experimental setup used to test the WMFUNI's sensitivity to input control-pulse polarization [16]. In regeneration the control pulses are the incoming data pulses, which may have a time varying polarization due to environmental changes on the transmission path or due to the different points of origin for arriving data packets. To simulate these effects, we inserted a polarization scrambler between the data transmitter and the WMFUNI's control input. The scrambler varies the polarization across all possible polarization states at several frequencies, going up to 700 kHz. In regeneration, the signal pulses are a locally generated clock source, so we can safely assume that there will be no polarization changes at the signal input. Figure 4-24 (a) shows two BER curves. One curve is the SOA wavelength converter's BER performance without a polarization scrambler and operating at its optimum input polarization. The other curve includes the effects of placing the polarization scrambler between the transmitter and the control input. The curves show that the polarization scrambler adds a 0.3-dB power penalty at an error rate of 10^{-9}. The bulk material SOA we use here is only slightly polarization sensitive, so this result is what we expect. Figure 4-24 (b) repeats the same experiment with the WMFUNI. Now the power penalty added by the polarization scrambler is only 0.08 dB, most likely due to the nonlinear response of the FUNI as shown in Figure 4-12, which suppresses any amplitude patterning added by the SOA wavelength converter.

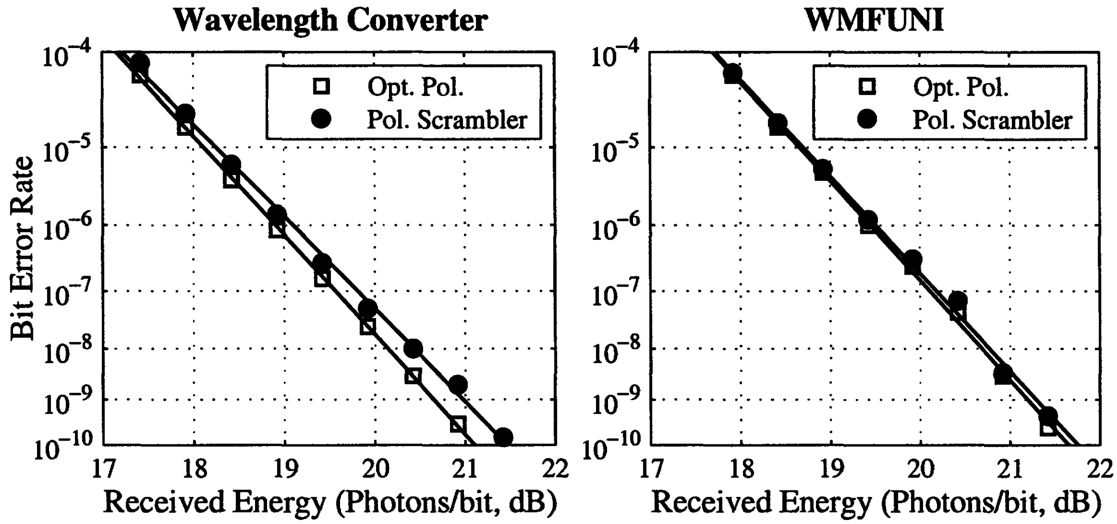

(a) (b)

Figure 4-24: Comparison of bit-error rate performances at a fixed optimum polarization with a scrambled input polarization in (a) the SOA wavelength converter and (b) the WMFUNI.

4.3.3 WMFUNI Regenerative Buffer

One application of regenerators is in optical data buffers. In a packet-switched network, it is important to be able to store data while users wait for the network to become available. The simplest such buffer is a loop of fiber with an electro-optic switch that can load data onto and remove data from the loop. An EDFA may be added to the loop to compensate loss [21], but the storage time is still limited by loss because the round-trip gain must remain low to prevent the loop from lasing. An alternative is to place a regenerator in the loop to restore data quality on each pass [22].

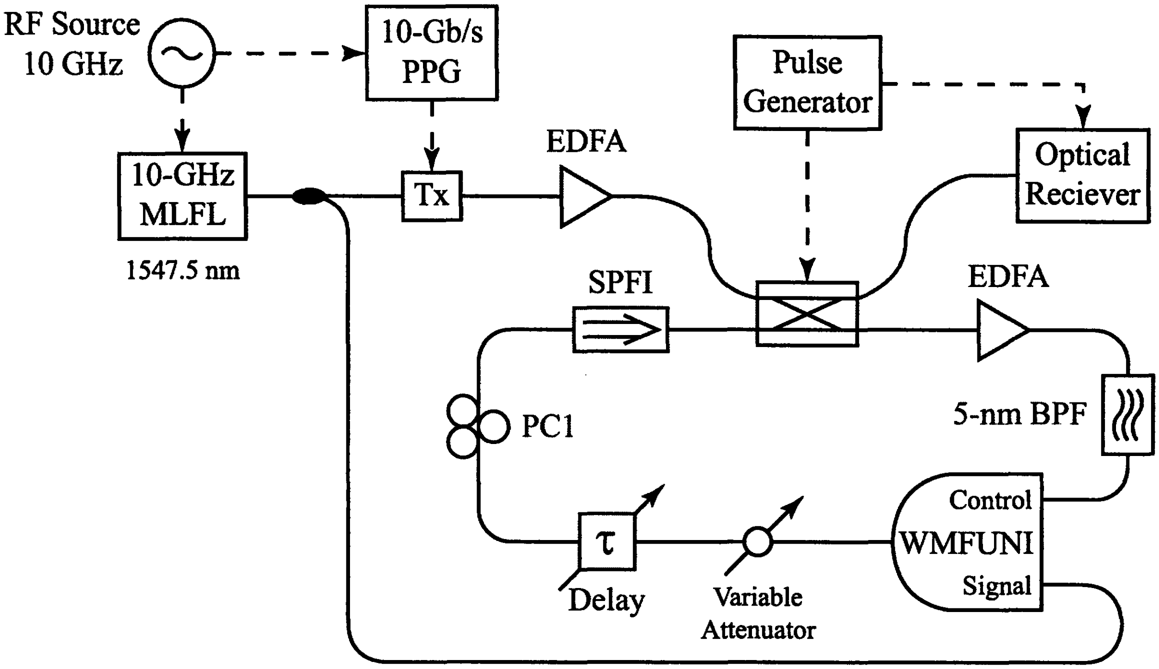

Figure 4-25: Schematic of a regenerative buffer using the wavelength-maintaining FUNI.

When that regenerator is an all-optical switch, like the WMFUNI, then the switch must be able to operate in a chain of switches. A single WMFUNI adds a 0.3-dB power penalty compared to the transmitter back-to-back. In a chain of WMFUNIs, we need later switches to add no power penalty. Figure 4-25 shows the WMFUNI regenerative buffer in which data pulses pass many times through a single WMFUNI, simulating a chain of switches. A 10-GHz RF source drives a mode-locked fiber laser, which produces a 10-GHz pulse train. A pattern generator drives a transmitter (Tx) that modulates a $2^{31} - 1$ PRBS onto the pulse train. The loop itself contains an EDFA to compensate losses in the loop, a 5-nm band-pass filter to eliminate out-of-band noise, a variable attenuator to control power in the loop, a single-polarization fiber isolator to maintain a constant polarization, and the WMFUNI to regenerate the data in the loop. There is also a variable delay so that the loop length can be set to an integer number of bit periods. This ensures that the signal pulses and control pulses temporally overlap in the WMFUNI during every pass the data take through the loop.

At the beginning of the experiment, a pulse generator sets the 2x2 in the loop to the cross state, loading data pulses into the loop. These data pulses enter the control input of the WMFUNI while synchronized clock pulses from the same MLFL enter the signal input. The WMFUNI outputs the clock pulses, now modulated with the bit pattern from the data pulses. After the loop is loaded with data, the pulse generator sets the 2x2 to the bar state so that the data remain in the loop for 20 passes. After 20 passes through the loop, the 2x2 returns to the cross state, sending the loop's data into the optical receiver and reloading the loop with another set of data. The pulse generator also sends a gate signal to the optical receiver that activates the receiver only during the unloading of the loop data into the receiver. Figure 4-26 shows BER curves for the WMFUNI and for the loop data after 5, 15, and 20 passes. All curves are compared to a transmitter back-to-back. The penalty remains low for all passes, demonstrating the cascadability of the WMFUNI.

4.4 Transmission Experiments in a Recirculating Loop

Section 4.2 presented tests demonstrating the FUNI's ability to re-amplify, reshape, and retime optical data. Section 4.3.2 showed that the addition of an SOA wavelength converter made the FUNI repolarizing as well. Finally, the previous section showed that the WMFUNI could be used in a cascade of switches without creating any error floor or runaway power penalty. In this section, we present a test of the regenerative abilities of the WMFUNI by inserting it into a 100-km recirculating loop in order to characterize its performance as a 4R regenerator in a long-haul fiber network.

Figure 4-27 shows the 100-km recirculating loop used to test the WMFUNI's regenerative performance [23]. As in the regenerative buffer of Section 4.3.3, the optical pulse train is generated by a 10-GHz mode-locked fiber laser that is then modulated in the transmitter (Tx) with a $2^{31} - 1$ PRBS. The loop itself contains two 50-km sections of large effective-area fiber (LEAF) along with 3.2 km of dispersion-compensation fiber (DCF). The DCF has a highly positive second-order dispersion to

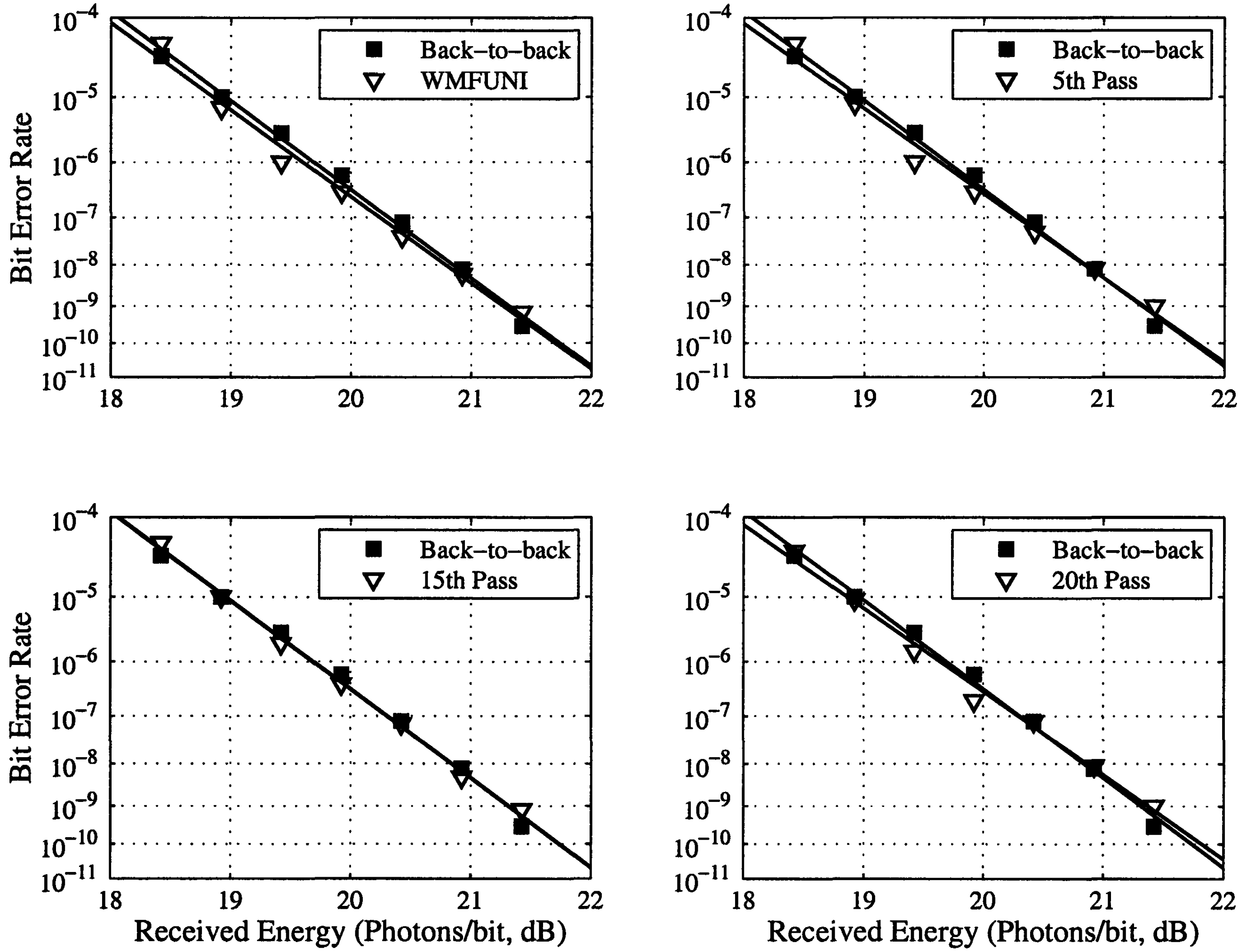

Figure 4-26: Bit-error rates of several loop passes through the WMFUNI regenerative buffer.

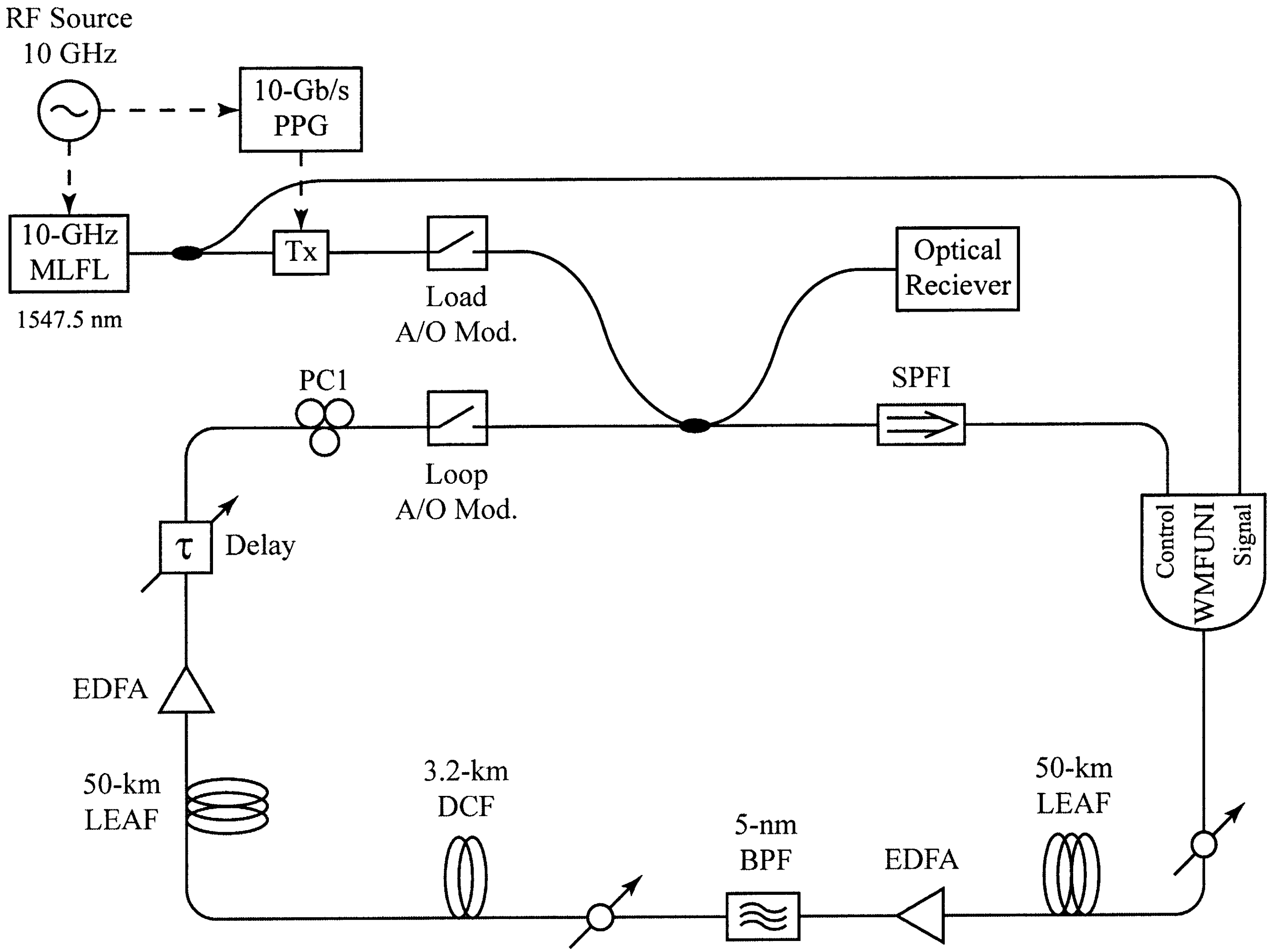

Figure 4-27: Schematic of the 100-km recirculating loop using the wavelength-maintaining FUNI.

compensate the negative second order dispersion that exists in the LEAF. Two EDFAs compensate loss in the loop. A single-polarization fiber isolator (SPFI) maintains a constant polarization. Two variable attenuators control power in the loop. A loop acousto-optic (A/O) modulator blocks pulses in the loop when necessary. There is also a variable delay to keep the loop length an integer number of bit periods long so that the control and signal pulses temporally overlap in the WMFUNI for all loop passes.

At the beginning of the loop experiment the load A/O modulator is closed, allowing data pulses to enter the loop. At the same time, the loop A/O modulator is open, discarding any pulses that are already in the loop. Once the loop is loaded with data, the loop A/O modulator closes, and the load A/O modulator opens. The data then recirculate through the loop 200 times, or ~21,000 km. Figure 4-28 shows the cross-correlation of the pulses in the loop when there is no regenerator. These data are taken by tapping off the loop data pulses right after the SPFI (tap not shown in figure). Similar to the autocorrelation, the cross-correlation calculates the function

$$C(\tau) = \int_{-\infty}^{+\infty} I(t) I_s(t - \tau)\, dt, \tag{4.5}$$

where $I(t)$ is the intensity envelope of the pulse in the loop, and $I_s(t)$ is the intensity envelope of the pulse used to used to sample the loop pulse. In this case, $I_s(t)$ is a 200-fs pulse generated in an adiabatic pulse compressor [24]. The top plot of Figure 4-28 shows pulses from passes 0 through 63 of the loop. The figure shows that after more and more passes through the loop, the pulses become wider, acquire a ringing tail, and quickly fall below the noise floor. The three smaller plots below show the 0th, 10th, and 20th passes through the loop. The cross-correlation of the 0-pass pulses have an IFWHM of 4.4 ps. After 10 passes, the cross-correlation of the data pulses have an IFWHM of 8.7 ps, and the pulses have acquired the tail that often appears when β_3 is significant. After 20 passes, the pulse cross-correlation's IFWHM has grown to 16 ps.

Figure 4-29 shows the same cross-correlation experiment, except with the WM-

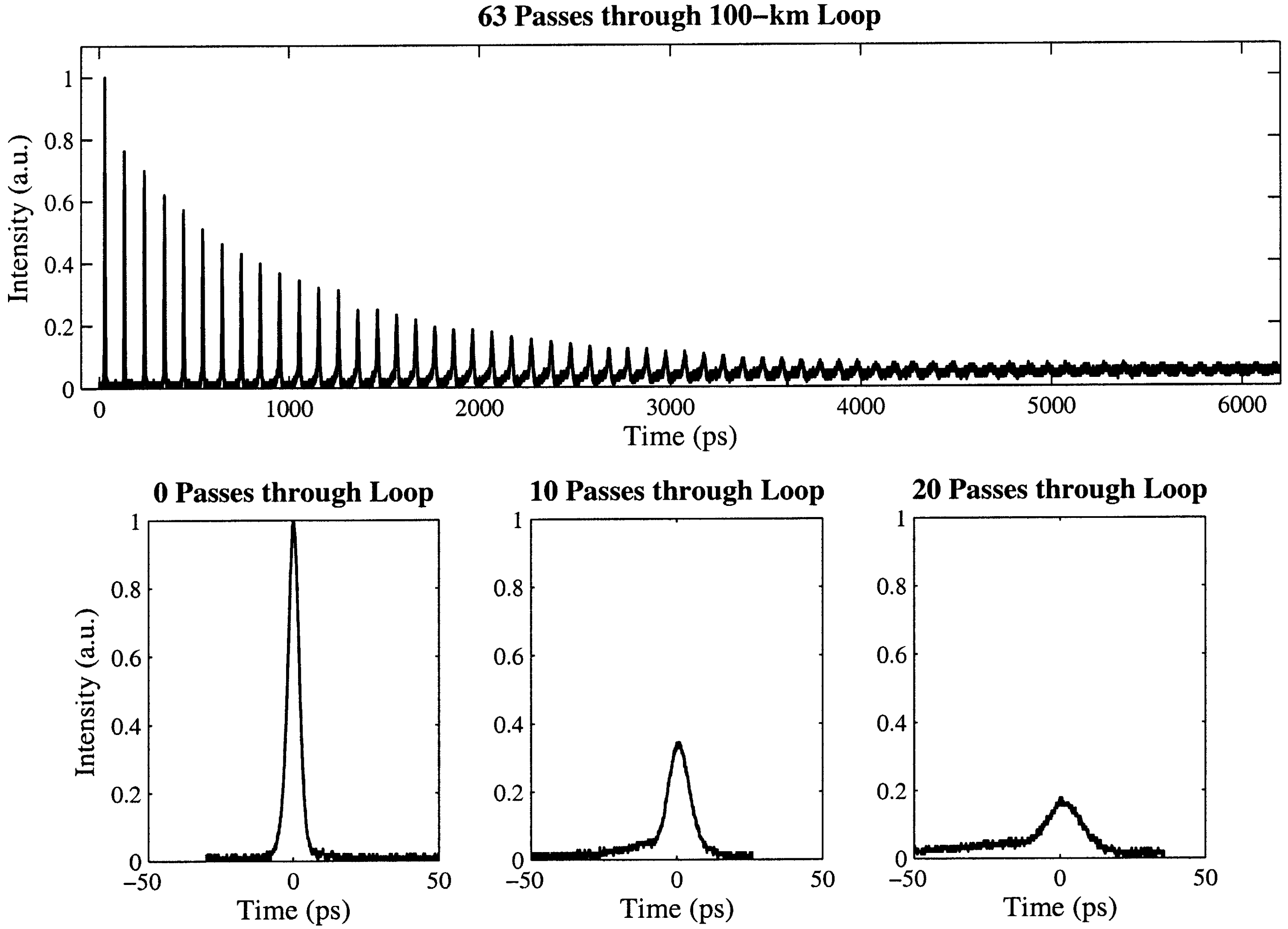

Figure 4-28: Cross-correlations of pulses through 100-km recirculating loop after 0 through 63 successive passes. The three smaller plots zoom in on pulses after passes 0, 10, and 20 passes.

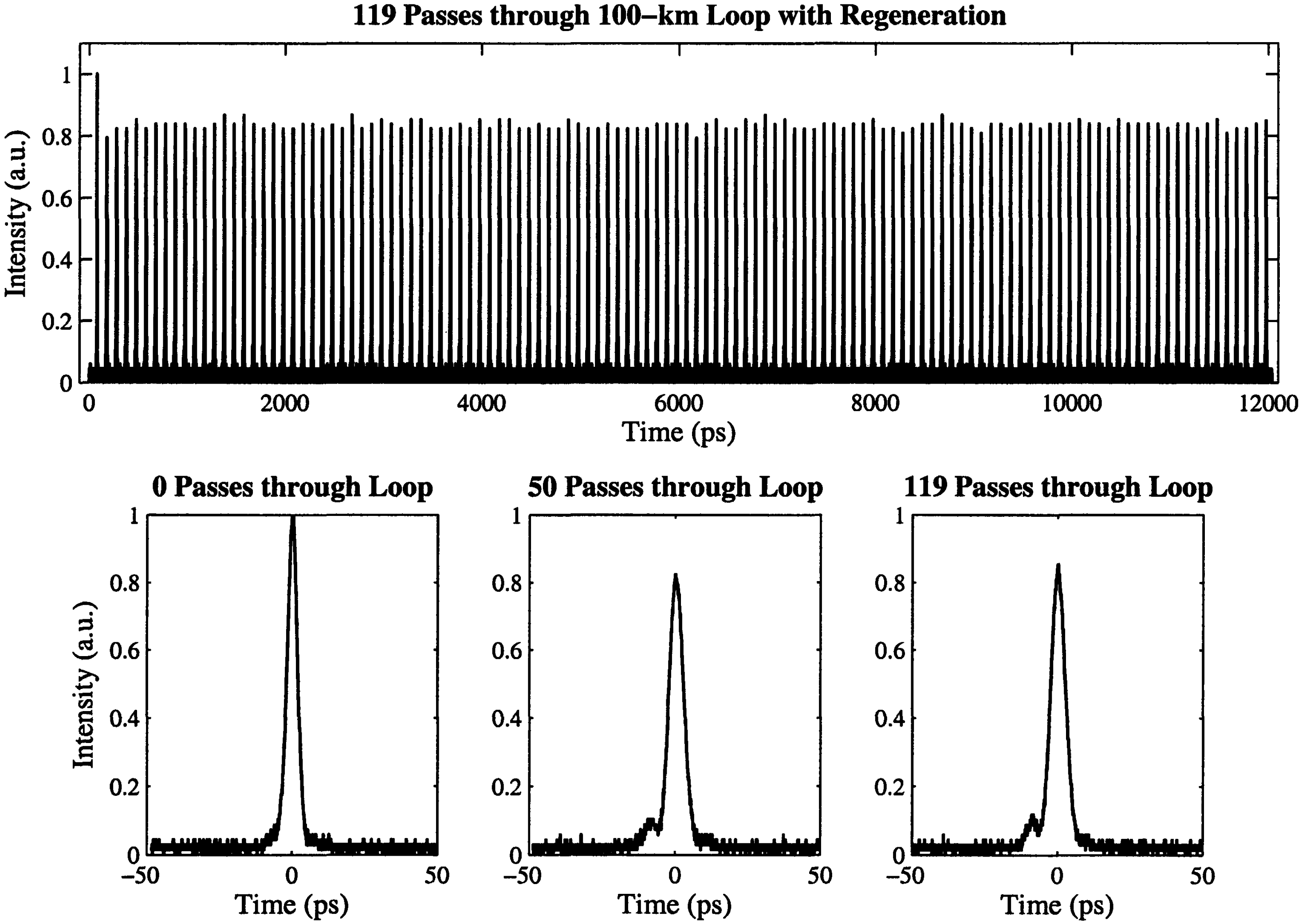

Figure 4-29: Cross-correlations of pulses through 100-km regenerative recirculating loop after 0 through 119 successive passes. The three smaller plots zoom in on passes 0, 50, and 119.

FUNI regenerator placed in the recirculating loop. This time, the cross-correlation data are taken by tapping off the loop data pulses right after the WMFUNI. The cross-correlation of the 0-pass pulses have an IFWHM of 4.0 ps. After 50 passes, the cross-correlation of the data pulses have an IFWHM of 5.8 ps. After 119 passes, the pulse cross-correlation's IFWHM is again 5.8 ps. The small side pulse on the cross-correlations of the 50th and 119th passes are about 10 ps from the main peak and so are probably due to a slight polarization misalignment caused by a nonlinear polarization rotation of the signal pulses in the FUNI. These side pulses can be suppressed by proper adjustment of the polarization of the output of the SOA wavelength converter.

Cross-correlations of the data pulses in the loop provide information about pulse shape, but without BER tests it is difficult to judge the regenerator's performance. There may, for example, be some undesirable feedback process in the regenerative loop that has changed all bits to be 1s. Figure 4-30 shows BER plots of the data pulses in the loop after 100 and 200 passes. The data are taken by tapping off the data pulses in the loop right after the WMFUNI. These data then enter a pre-amplified optical receiver, which is controlled by a gate signal from the same pulse generator that drives the two acousto-optic modulators. This gate signal ensures that the optical receiver only measures the bit-error rate during the 100th pass (as in the top plot of Figure 4-30) or the 200th pass (as in the bottom plot of Figure 4-30). In these data, the WMFUNI has a 0.06-dB power penalty penalty compared to the transmitter back-to-back at an error rate of 10^{-9}. After 100 passes through the loop, the loop data have a power penalty of 0.5 dB. After 200 passes, the loop data have a power penalty of only 0.6 dB compared to the back-to-back with no visible error floor.

The good performance of the WMFUNI regenerator in the 100-km loop suggests that it may be possible to extend the transmission distance between regenerators. Figure 4-32 shows a modified recirculating loop that has two separate paths within the loop. After the SPFI, the data pulses are split by a coupler into two paths. In one path the data pulses pass through the WMFUNI regenerator, and in the

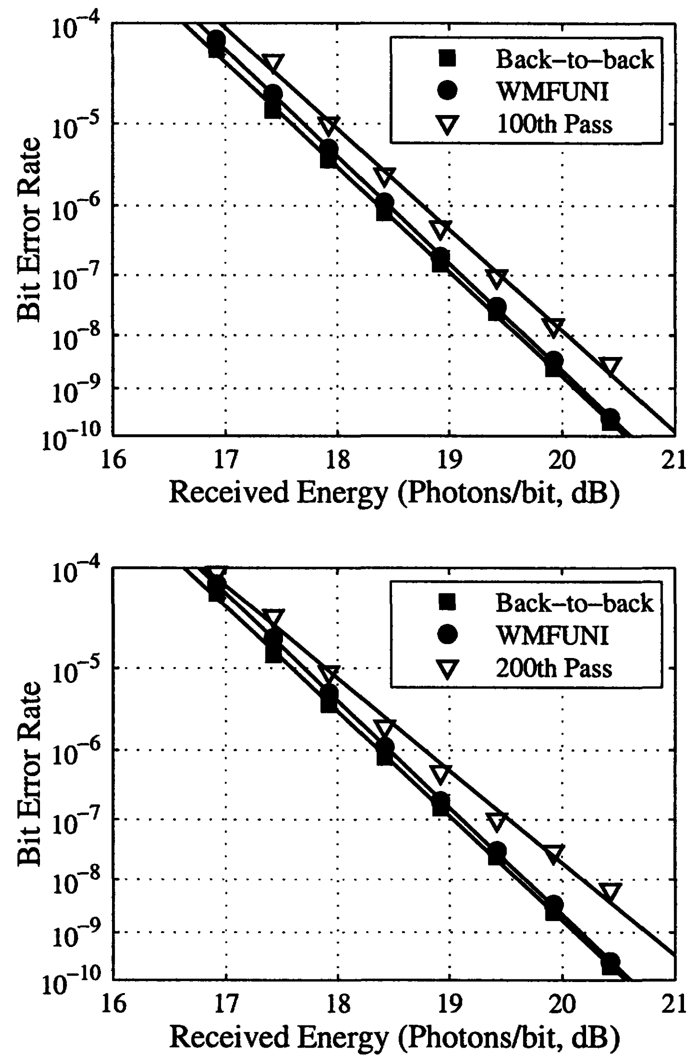

Figure 4-30: Bit-error rates after 100- and 200-loop passes through the WMFUNI recirculating loops, corresponding to 10,000 and 21,000 km of data propagation.

other path the pulses pass through 2.2 km of DSF. This 2.2 km section of DSF is placed in the loop to make equal the lengths of the two alternative paths in the loop. The two paths join together again in a 2x1 A/O modulator, which blocks one path and passes the other. A pulse generator drives all three A/O modulators. In Figure 4-32 we show cross-correlations of the loop data pulses taken right after the WMFUNI. In this experiment, the pulse generator switches the 2x1 so that the data pulses pass twice through the loop before being regenerated. Figure 4-32 shows cross-correlations of the data pulses after 0 to 100 passes through the loop. The four smaller plots show cross-correlations after 1, 2, 99, and 100 loop passes. The IFWHM

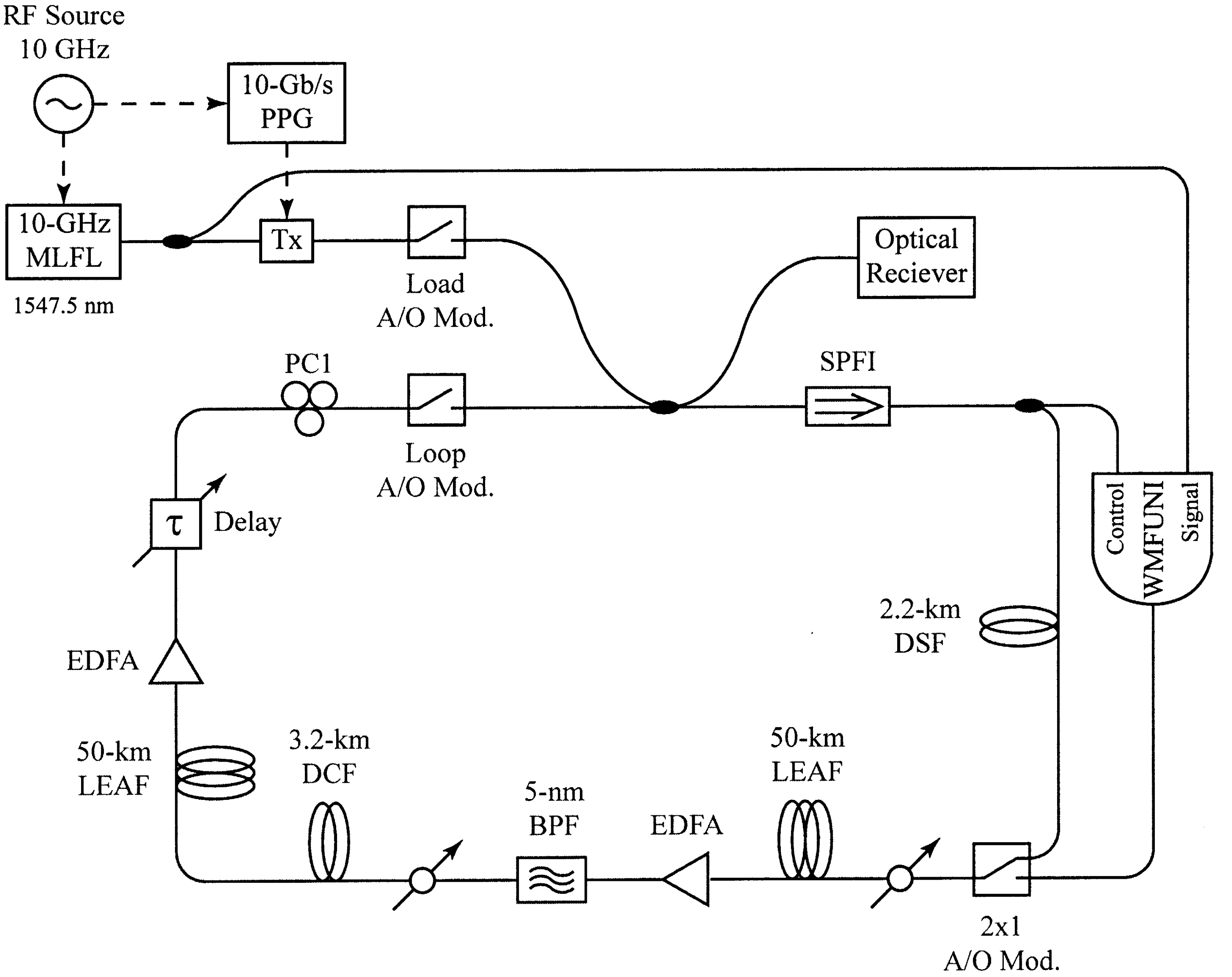

Figure 4-31: Schematic of the 100-km reconfigurable recirculating loop using the wavelength-maintaining FUNI. Two alternative paths through the loop allow use to adjust the distance between regeneration.

of these cross-correlations are 4.4 ps, 5.4 ps, 4.2 ps, and 6.2 ps. The regenerated pulses (odd numbered passes) show a stable pulse width. The unregenerated pulses (even numbered passes) seem to be loosing signal strength. Without bit-error rates, however, it is difficult to make a good judgment about regenerator performance.

4.5 40-Gb/s Operation of WMFUNI

In on/off keyed systems, the short $\sim$ 3-ps pulses used in the experiments above could be used at channel data rates up to $\sim$ 150 Gb/s. So far, I have only presented data at 10 Gb/s. In this section we consider the WMFUNI's operation at 40 Gb/s. Figure 4-33 shows the experimental setup for tests at 40 Gb/s. As before, a mode-locked fiber laser provides a 10-GHz pulse train with a carrier wavelength of 1547.5 nm. The power in this 10-GHz train is separated into three paths. The middle path enters a transmitter (Tx) where a $2^{31} - 1$ PRBS is modulated onto the 10-GHz pulse train. These data pulses enter a 10 Gb/s to 40 Gb/s multiplexer, which has multibit delays to decorrelate neighboring bits in the 40 Gb/s output. The 40 Gb/s data then enters the control port of the WMFUNI. The top path also enters the multiplexer, producing a 40 Gb/s clock train that enters the signal port of the WMFUNI. The bottom path enters the control port of the UNI, which serves here as a 40 Gb/s to 10 Gb/s demultiplexer. The 40-Gb/s WMFUNI output enters the UNI's signal port input. The UNI passes every fourth of these signal pulses into a pre-amplified optical receiver where a BER measurement is made. By adjusting the delay between signal and control in the UNI, we can choose which of the four 10-Gb/s channels enters the optical receiver.

Figure 4-33 shows the BER curves of all four 10-Gb/s channels of the WMFUNI. The back-to-back measurement is the same for all four plots. It is taken by first using the UNI to demultiplex the 40-Gb/s data output of the multiplexer down to 10 Gb/s. The BER of the UNI's output is then measured by the pre-amplified optical receiver. All four channels were measured down to an error rate of $\sim 10^{-9}$. Channel 1 has a 3.4-dB power penalty when compared to the back-to-back at an error rate of 10^{-9}.

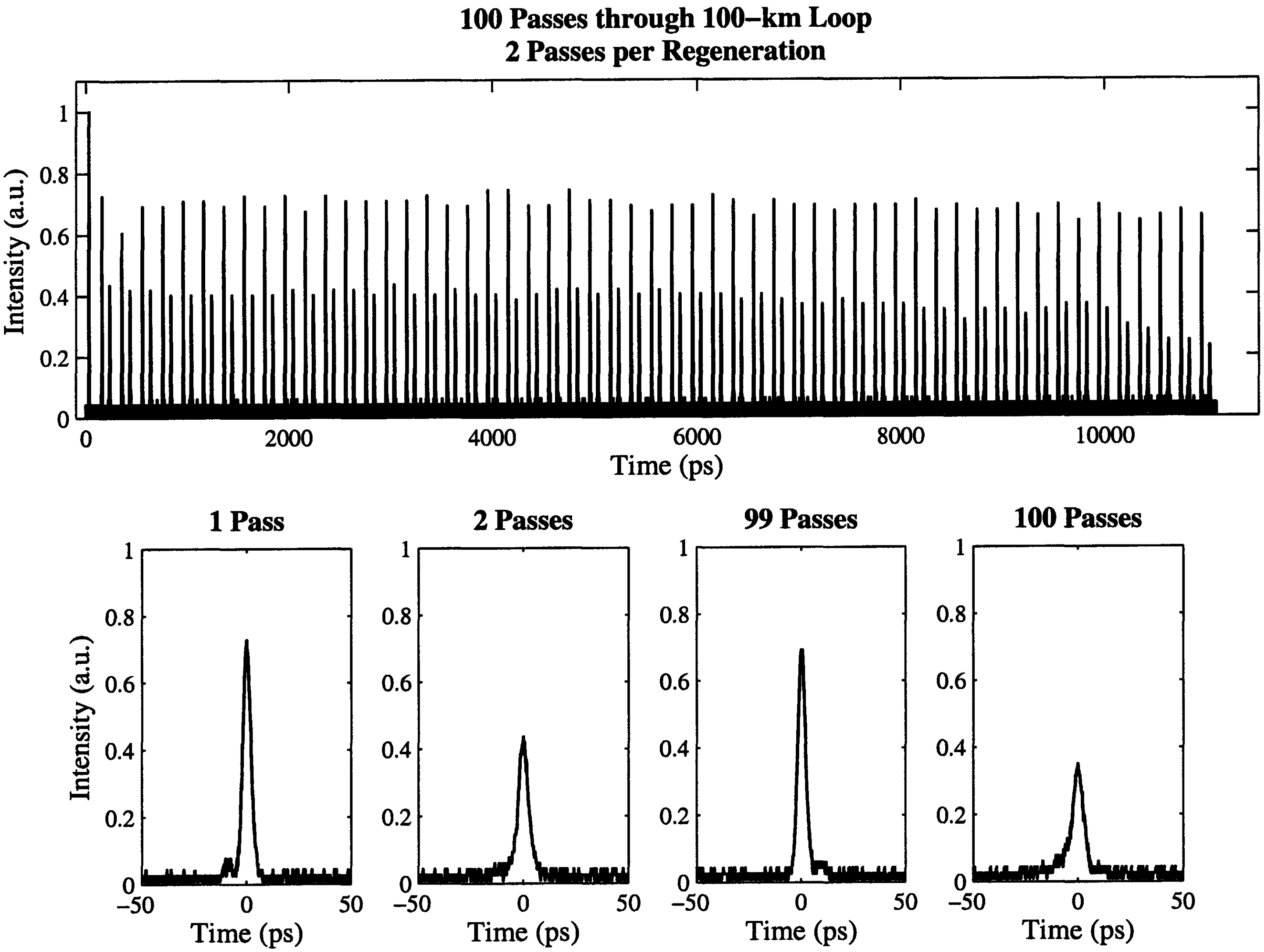

Figure 4-32: Cross-correlations of pulses through 100-km reconfigurable recirculating loop after 0 through 100 successive passes.

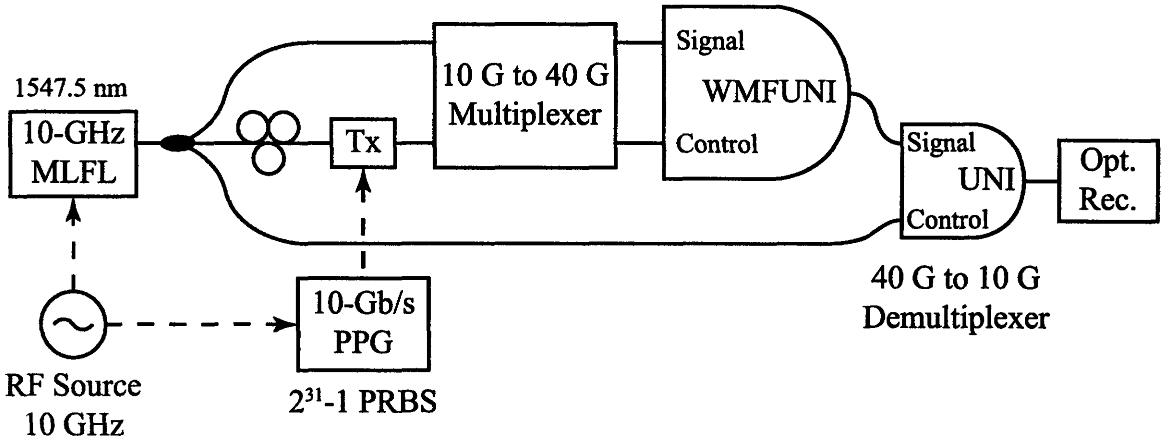

Figure 4-33: Experimental setup to test 40 Gb/s WMFUNI.

Channel 2 has a penalty of 3.6 dB, Channel 3 has a penalty of 6.0 dB, and Channel 4 has a penalty of 6.5 dB. The difference between the last two channels and the first two channels has several possible explanations. First, the multiplexer is a passive free-space device that, if not perfectly aligned, will produce a 40-Gb/s output whose four channels do not have equal optical powers. So, some of these unequal channels may not be operating at the peak of the WMFUNI's nonlinear response curve. The 1s of those channels will have a larger variance of energies, which causes the slope of BER curve at higher optical powers to become shallower. We see evidence of this shallowing in Channels 3 and 4 and, to some extent, Channel 2. Another possible explanation for the difference is reflections in the free-space multiplexer, which may affect some channels more than others.

4.6 Conclusions

The FUNI's single-arm geometry and nearly instantaneous nonlinear medium give it many useful properties. It is automatically biased, is stable to environmental changes like vibrations and temperature variations, and can operate on short optical pulses ($\sim$ 3 ps). Nonetheless, the FUNI is wavelength converting and sensitive to input polarization, both of which are usually undesirable in regeneration. It could be used as an all-optical switch or wavelength converter. The FUNI is, however, a fiber-based

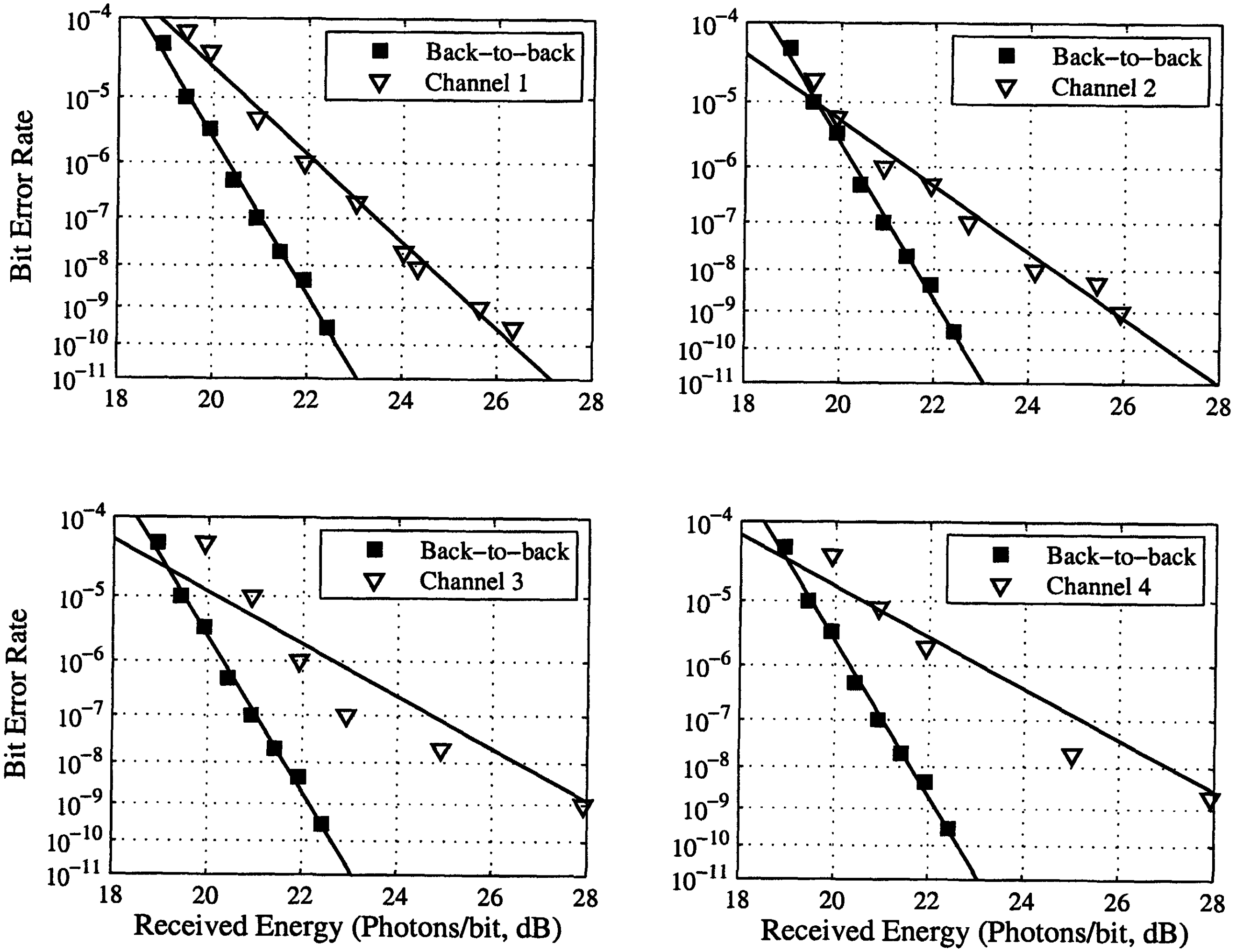

Figure 4-34: Bit-error rate tests for each of the four 10-Gb/s channels at the output of the WMFUNI.

switch, and its size limits it to applications that require little optical logic.

The WMFUNI, by adding an SOA wavelength converter to the control input, removes the sensitivity to input polarization while also making the switch wavelength maintaining. It also retains the FUNI's stability to environmental changes and its ability to operate on short pulses. These short pulses are useful for systems requiring ultrafast operation or highly sensitive operation when peak power must be high enough to rise above the noise.

Transmission experiments are the only sure test of a regenerator's performance. The WMFUNI successfully regenerated a 10-Gb/s data train in a 100-km recirculating loop. With $\sim$ 3-ps pulses, the WMFUNI should in principle operate in systems with data rates up to $\sim$ 100 Gb/s. We have seen that the WMFUNI operates at 40 Gb/s with additional penalty, but more experimentation is needed to see if it will still function as a regenerator at these rates.

So, the WMFUNI possesses many advantages over the FUNI. Still, the WMFUNI, like the FUNI, is too large for complicated logical operations, like header processing and label swapping [25, 26]. The most common all-optical switches for such applications are SOA-based interferometric switches, which is the subject of the next chapter.

Bibliography

[1] K. L. Hall and K. A. Rauschenbach, "100-Gbit/s bitwise logic," *Optics Letters*, vol. 23, pp. 1271–1273, Aug. 1998.

[2] Y. Ueno, S. Nakamura, and K. Tajima, "Penalty-free error-free all-optical data pulse regeneration at 84 Gbps with symmetric-Mach-Zehnder-type regenerator," in *Proc. of OFC 2001*, (Anaheim, CA), p. MG5, OSA, Mar. 2001.

[3] S. J. Savage, B. S. Robinson, S. A. Hamilton, and E. P. Ippen, "All-optical pulse regeneration in an ultrafast nonlinear interferometer with Faraday mirror polarization control," in *CLEO 2001 Technical Digest*, (Baltimore, MD), pp. 316–317, May 2001.

[4] S. Savage, B. Robinson, S. Hamilton, and E. Ippen, "All-optical pulse regeneration in an ultrafast nonlinear interferometer with Faraday mirror polarization stabilization," *Optics Letters*, vol. 28, no. 1, pp. 13–15, 2003.

[5] G. Agrawal and N. Olsson, "Self-phase modulation and spectral broadening of optical pulses in semiconductor laser amplifiers," *IEEE Journal of Quantum Electronics*, vol. 25, no. 11, pp. 2297–2306, 1989.

[6] G. Agrawal, *Nonlinear Fiber Optics.* San Diego, California: Academic Press, third ed., 2001.

[7] M. Jinno, "Effects of group velocity dispersion on self/cross phase modulation in a nonlinear Sagnac interferometer switch," *Journal of Lightwave Technology*, vol. 10, pp. 1167–1178, Aug. 1992.

[8] M. Jinno and M. Abe, "All-optical regenerator based on nonlinear fibre Sagnac interferometer," *Electronics Letters*, vol. 28, pp. 1300–1301, July 1992.

[9] I. Shake, H. Takara, K. Uchiyama, S. Kawanishi, and Y. Yamabayashi, "Vibration-insensitive nonlinear optical loop mirror utilizing reflective scheme," *IEEE Photonics Technology Letters*, vol. 12, pp. 555–557, May 2000.

[10] C. Vinegoni, M. Wegmuller, B. Huttner, and N. Gisin, "All optical switching in a highly birefringent and a standard telecom fiber using a Faraday mirror stabilization scheme," *Optics Commuications*, vol. 182, pp. 335–341, Aug. 2000.

[11] S. J. Savage, "All-optical pulse regeneration in a Faraday stabilized ultrafast nonlinear interferometer," Master's thesis, Massachusetts Institute of Technology, 2001.

[12] B. Robinson, S. Hamilton, S. Savage, and E. Ippen, "40 Gbit/s all-optical XOR using a fiber-based folded ultrafast nonlinear interferometer," *Optical Fiber Communication Conference*, pp. 561–563, 2002.

[13] J. Gordon and H. Haus, "Random walk of coherently amplified solitons in optical fiber transmission," *Optics Letters*, vol. 11, no. 10, pp. 665–667, 1986.

[14] D. Blumenthal, B. Olsson, G. Rossi, T. Dimmick, L. Rau, M. Masanovic, O. Lavrova, R. Doshi, O. Jerphagnon, J. Bowers, *et al.*, "All-optical label swapping networks and technologies," *Journal of Lightwave Technology*, vol. 18, no. 12, pp. 2058–2075, 2000.

[15] S. J. Savage, B. S. Robinson, S. A. Hamilton, and E. P. Ippen, "A wavelength-maintaining polarization-insensitive all-optical 3R regenerator," in *OFC 2006 Technical Digest*, (Anaheim, CA), 2006.

[16] S. Savage, B. Robinson, S. Hamilton, and E. Ippen, "Wavelength-maintaining polarization-insensitive all-optical 3R regenerator," *Optics Express*, vol. 14, no. 5, pp. 1748–1754, 2006.

[17] J. Leuthold, D. Marom, S. Cabot, J. Jaques, R. Ryf, and C. Giles, "All-optical wavelength conversion using a pulse reformatting optical filter," *Journal of Lightwave Technology*, vol. 22, no. 1, pp. 186–192, 2004.

[18] M. Nielsen, B. Lavigne, and B. Dagens, "Polarity-preserving SOA-based wavelength conversion at 40 Gbit/s using bandpass filtering," *Electronics Letters*, vol. 39, no. 18, pp. 1334–1335, 2003.

[19] Y. Liu, E. Tangdiongga, Z. Li, S. Zhang, H. deWaardt, G. Khoe, and H. Dorren, "Error-Free All-Optical Wavelength Conversion at 160 Gb/s Using a Semiconductor Optical Amplifier and an Optical Bandpass Filter," *Journal of Lightwave Technology*, vol. 24, no. 1, pp. 230–236, 2006.

[20] Y. Liu, E. Tangdiongga, Z. Li, H. de Waardt, A. Koonen, G. Khoe, H. Dorren, X. Shu, and I. Bennion, "Error-free 320 Gb/s SOA-based Wavelength Conversion using Optical Filtering," *Conference on Optical Fiber Communications (OFC)*, 2006.

[21] Y. Yamada, K. Sasayama, and K. Habara, "Demonstration of 30 circulations in a transparent optical-loop buffer for 2-channel FDM packets at a data rate of 2.5 Gb/s," *Optical Fiber Communication Conference*, vol. 2, pp. 107–108, 1996.

[22] K. Hall and K. Rauschenbach, "All-optical buffering of 40-Gb/s data packets," *IEEE Photonics Technology Letters*, vol. 10, no. 3, pp. 442–444, 1998.

[23] S. J. Savage, B. S. Robinson, S. A. Hamilton, and E. P. Ippen, "200-pass picosecond-pulse transmission through a regenerative recirculating fiber loop," in *CLEO 2006 Technical Digest*, (Long Beach, CA), May 2006.

[24] S. Chernikov, E. Dianov, D. Richardson, and D. Payne, "Soliton pulse compression in dispersion-decreasing fiber," *Optics Letters*, vol. 18, no. 7, pp. 476–478, 1993.

[25] J. Wang, B. Robinson, S. Hamilton, and E. Ippen, "40-Gbit/s all-optical header processing for packet routing," *Optical Fiber Communication Conference, 2006*, p. 3, 2006.

[26] D. Apostolopoulos, D. Petrantonakis, O. Zouraraki, E. Kehayas, N. Pleros, and H. Avramopoulos, "All-Optical Label/Payload Separation at 40 Gb/s," *IEEE Photonics Technology Letters*, vol. 18, no. 19, p. 2023, 2006.

Chapter 5

SOA Mach-Zehnder Interferometer

Before the development of the Erbium-doped fiber amplifier (EDFA) [1, 2], the semiconductor optical amplifier (SOA) was a leading candidate for optical signal amplification. In addition to a wide bandwidth of up to ~ 100 nm, it can achieve 30 dB of small signal gain [3]. Nonetheless, the SOA has several drawbacks as an amplifier. 1) The gains and output power are lower than those of the EDFA. 2) SOAs require high-quality anti-reflective coatings to prevent lasing in the device. 3) Crosstalk between wavelength channels in WDM systems is often large. 4) The SOA can create variations in the pulses' output amplitudes. 5) SOAs are not fiber-based amplifiers like EDFAs, so coupling losses are larger in SOAs, leading to higher noise figures. 6) Gain fluctuations in an SOA will cause nonlinear phase shifts in the signal propagating through the SOA.

This last problem becomes an advantage in certain applications. In fact, since the introduction of the EDFA, the SOA has found many new uses based on its nonlinear properties, including its ability to induce phase shifts [4]. We discussed some of these in Section 3.3. In this chapter we look at the SOA Mach-Zehnder interferometer (SOA-MZI) switch, an MZI switch in which the SOA serves as the nonlinear medium. Researchers have tested the SOA-MZI in many applications including wavelength conversion [5], label swapping [6, 7], an all-optical flip-flop [8], AND switching [9, 10], XOR switching [11], and data regeneration [12, 13].

In this chapter, we will examine a simple model for an SOA-MZI at several data rates. This will give us intuition for the behavior of single SOA-MZI switches. In regeneration, however, we are not just interested in the performance of a single SOA-MZI, but rather in cascades of SOA-MZI switches in which the output of one switch becomes the input for the next switch. Data patterning on the input to the switch causes amplitude variations on the output pulses. These amplitude variations cause problems when cascading the switches together, and we will investigate circumstances where such cascading will work.

One key advantage of SOA-based optical switches is their integrability onto solid-state chips. Through a collaboration with Alphion, we tested an integrated SOA-MZI at 10 Gb/s. These experiments suggested the possibility of the use of the SOA-MZI in optical data regeneration, which we confirmed in regeneration experiments in the 100-km transmission loop described in Chapter 4 [?].

5.1 SOA-MZI Model for Simulations

SOAs are a common tool in optics, and so it would be useful to predict how they behave in Mach-Zehnder interferometers. We can characterize an SOA by a few parameters. First, there is the carrier recovery time, τ_c. When an optical pulse propagates through the SOA, the SOA provides gain by stimulated emission of light, causing excited electrons to drop to lower energy states. τ_c is a measure of the time it takes for current injected into the SOA to re-excite the electrons. Second, there is the unsaturated gain, h_0, which is the gain given to a very weak pulse propagating through the SOA. Third, there is the saturation energy, E_{sat}, which is a measure of the amount of optical energy required for a short pulse to saturate the SOA, driving the gain down to near unity. Fourth, there is the linewidth enhancement factor, α, which we will use to calculate the phase shift that an SOA induces on optical pulses

Simulations help determine how changes in these four parameters affect performance, which can be used in the design of integrated switches. The MZI geometry is simple enough that an SOA-MZI model is straightforward to simulate in principle, although run times may still be long. In order to assess the SOA-MZI's performance, the simulations will also need a model for the optical pre-amplified receiver, which will measure the bit-error rate performance of the switch's output. The receiver has an EDFA pre-amplifier, so the receiver model must include noise added by the amplifier. Finally, the SOAs themselves add noise to the signal pulses. We will consider each of these issues in the following sections.

5.1.1 SOA Model

Section 3.3 described in detail the mathematical model used in this thesis to simulate SOA behavior [14]. We provide only a summary of those results for this chapter. Let the total integrated gain factor of the SOA be called $h(\tau)$, where τ is time. Let a pulse at the input of the SOA have an electric field of $A_{in}(\tau)\cos(\omega_c\tau + \phi_{in}(\tau))$, where $A_{in}(\tau)$ is the slowly varying envelope. A_{in} is a real function normalized so that $|A_{in}(\tau)|^2$ equals the optical power, $P_{in}(\tau)$. ω_c is the carrier frequency, and $\phi_{in}(\tau)$ is the optical phase. The optical field at the output of the SOA is given by [14]

$$P_{out}(\tau) = P_{in}(\tau)e^{h(\tau)} \tag{5.1}$$

$$\phi_{out}(\tau) = \phi_{in}(\tau) - \frac{1}{2}\alpha h(\tau) \tag{5.2}$$

where α is a constant usually between 3 and 8 and is often referred to as the linewidth enhancement factor. The integrated gain, $h(\tau)$, can be calculated from

$$\frac{dh(\tau)}{d\tau} = \frac{h_0 - h(\tau)}{\tau_c} - \frac{P_{in}(\tau)}{E_{sat}}\left[e^{h(\tau)} - 1\right]. \tag{5.3}$$

τ_c is the carrier recovery time, h_0 is the unsaturated gain, and E_{sat} is the saturation energy. As we can see from the second term on the right hand side, any input power, P_{in}, reduces the gain of the SOA. The first term shows, however, that the SOA gain recovers up to its unsaturated level of h_0 at a rate inversely proportional to τ_c.

We can solve Equation 5.3 by a standard fourth-order Runge-Kutta finite differencing solution. Figure 5-1 shows the Runge-Kutta solution to one such problem. The top plot shows the optical power of the pulse envelopes at the input of an SOA

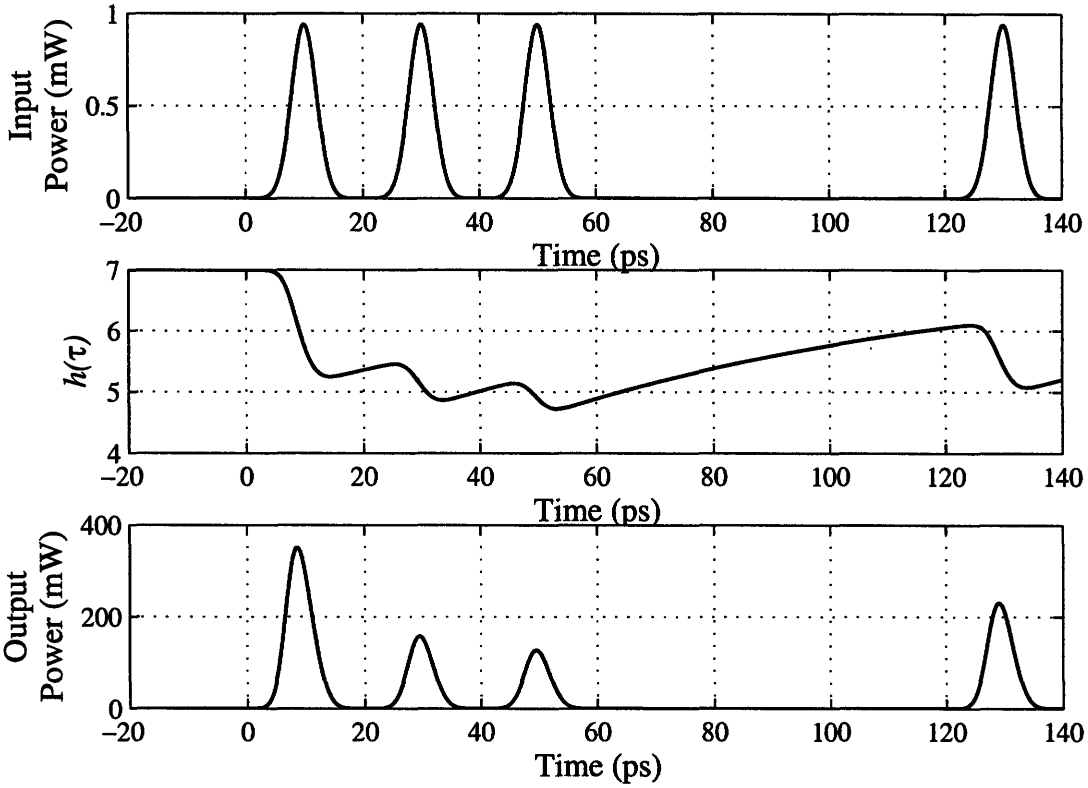

Figure 5-1: The top plot shows the optical pulse power at the input of the SOA. The middle plot shows the resulting value of $h(\tau)$. The bottom plot shows the output power of the SOA. In this SOA, $h_0 = 7$, $\tau_c = 75$ ps, and $E_{sat} = 1$ pJ.

in which $h_0 = 7$, $\tau_c = 75$ ps, and $E_{sat} = 1$ pJ. The pulses have an IFWHM of 5 ps and a pulse energy of 5 fJ. The middle plot shows how $h(\tau)$ changes in response to the input pulses. The bottom plot shows the optical power at the output of the SOA. The first three pulses quickly saturate the SOA until the gain recovery between pulses balances the gain depleted by the optical power of the pulse. Then the gain recovers in the gap without pulses so that the final pulse receives more gain. The resulting variation in output pulse energy is the main problem in the performance of SOA based optical switches.

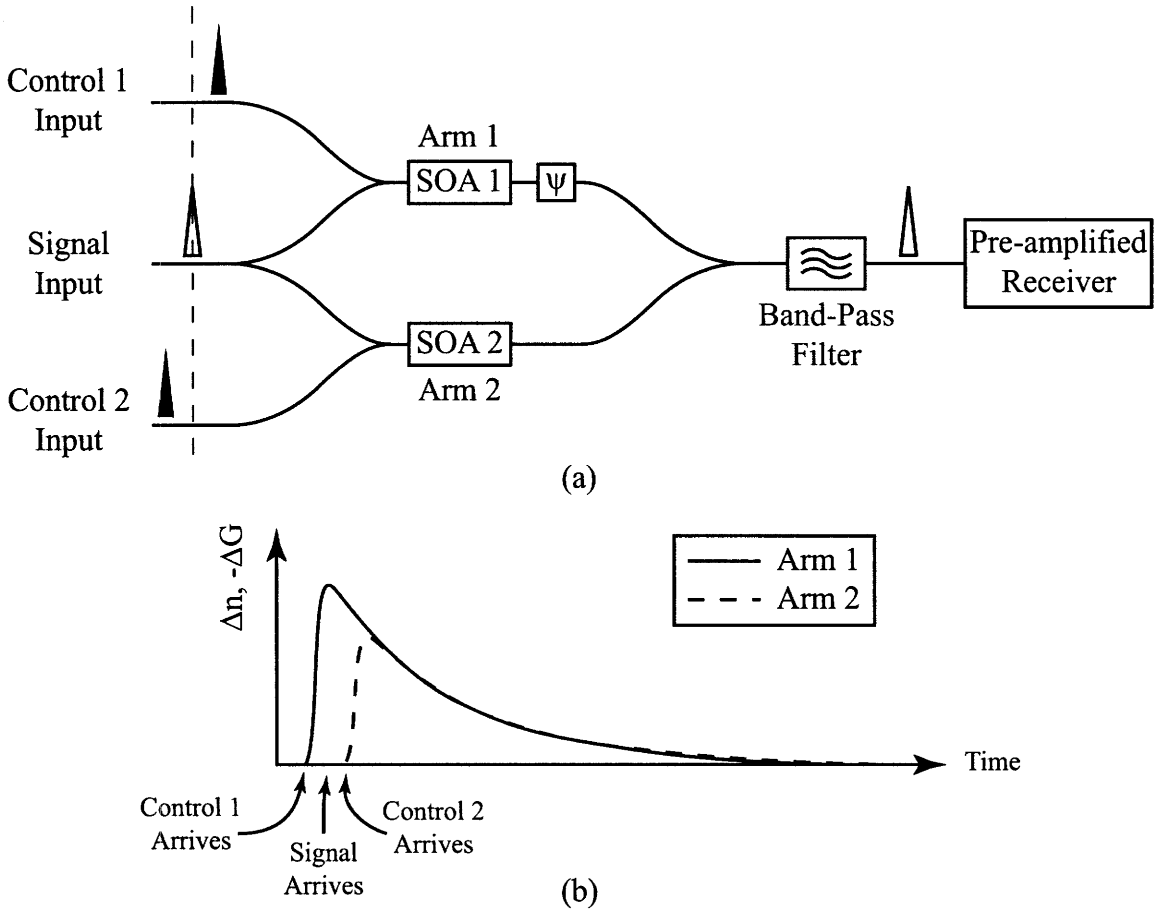

Figure 5-2: Model used for simulations of the SOA-MZI. The switch is a Mach-Zehnder interferometer, like that described in Section 2.2.1. One SOA in each arm serves as the nonlinear medium. The control pulse in Arm 1 enters the SOA-MZI first, turning the switch on. The signal pulse then enters both arms through a power splitter. Finally, the control pulse in Arm 2 enters the switch, turning it off.

5.1.2 SOA-MZI Model

Figure 5-2 shows the SOA-MZI model used in the simulations presented in this chapter. The signal pulses are split in a 50/50 coupler into both arms. A phase bias, ψ, in Arm 1 adjusts the interferometer so that the signal pulses destructively interfere at the output, blocking the signal pulse.

When a control pulse is present, its power is split. Some of its optical power enters the Control 1 Input and enters SOA1 before the signal pulse, changing the index of refraction of SOA1. This index change persists for a length of time on the order of τ_c and causes the SOA-MZI to switch to constructive interference so that the

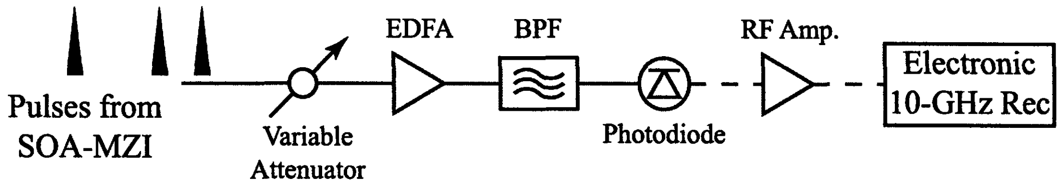

Figure 5-3: Schematic of the receiver used in Figure 5-2.

signal pulse in passed by the SOA-MZI. The rest of the control pulse power enters the Control 2 Input and enters SOA2 after the signal pulse, changing the index of refraction of SOA2 so that the SOA-MZI switches back to destructive interference. Control 2 exists only to re-balance the MZI so that the interferometer is rebalanced before the next set of pulses arrives. Finally, the band-pass filter blocks the control pulse and passes the signal pulse. The SOA-MZI's output then enters an optically pre-amplified receiver, the modeling of which is the subject of the next section.

5.1.3 Model of Pre-Amplified Receiver

A full characterization of the SOA-MZI's performance in simulation requires a model of the pre-amplified receiver used to measure the bit-error rate performance. The model given here is drawn from [15]. Figure 5-3 shows a schematic of the pre-amplified receiver used in Figure 5-1. An attenuator adjusts the power to the level we wish to test. An EDFA amplifies the signal, which then passes through a matched filter (BPF) before being converted to an RF signal and amplified again. This signal is then detected by an RF receiver. The receiver noise includes shot noise, thermal noise, and spontaneous emission noise added by the pre-amplifier. We assume that the spontaneous emission noise dominates the noise in the receiver.

The data are on-off keyed, so we start by assuming that the signal to be detected exists entirely in the time period $0 \leq t \leq T$, where T is the bit period. If the EDFA in the receiver were noiseless, we could represent its output signal with a basis set of real orthonormal functions, $\{\phi_k(t)\}$[1]:

$$s(t) = \sum_{\{k\}} s_k \phi_k(t),$$

where $\{k\}$ is the set of positive integers and the s_k are real-valued coefficients. If we include spontaneous emission noise in this signal, then $s(t)$ becomes a stochastic process. It would be convenient if we could simply add an independent noise term for each $\phi_k(t)$ mode above so that we obtain

$$s(t) = \sum_{\{k\}} (s_k + n_k) \phi_k(t), \tag{5.4}$$

where the n_k are independent random variables, but it is not obvious that we can do this.

So, first we must justify Equation 5.4. At this point, it is useful to introduce the auto-covariance function, $K_x(t, u)$, of any stochastic process $x(t)$:

$$K_x(t,u) \triangleq E\left\{[x(t) - \mu_x(t)]\,[x(u) - \mu_x(u)]\right\},$$

where $E\{r(t_0)\}$ denotes the expectation value of any stochastic process $r(t)$ at time $t = t_0$, and $\mu_r(t_0)$ denotes the mean value of $r(t)$ at time $t = t_0$. Now if $K_x(t, u)$ is positive definite, as it will be in the cases of interest to us, then we can obtain a complete orthonormal basis set using $K_x(t, u)$. We start with the integral equation

$$\lambda_k \phi_k(t) = \int_0^T K_x(t,u)\phi_k(u)\,du \qquad 0 \le t \le T, \tag{5.5}$$

where any $\phi_k(t)$ satisfying this equation is called an eigenfunction, and λ_k is its associated eigenvalue. An important result from the theory of integral equations states that if $K_x(t, u)$ is positive definite, then the $\phi_k(t)$ form a complete orthonormal set of basis functions on the interval $0 \le t \le T$ [16].

---

[1] The set $\{\phi_k(t)\}$ could, for example, be sines and cosines in a Fourier series, although we will see that a more convenient basis set exists.

This particular basis set is very useful when combined with the fact that the preamplifier's noise can be approximated as an additive white Gaussian process [17]. The Gaussian nature of the noise has an important consequence: as shown in [18], we can in fact use Equation 5.4, where the n_k are statistically independent Gaussian random variables[2]. Each n_k has zero mean and a variance of $N_0/2$ where $N_0 = N_{sp}h\nu(G-1)$ [17]. N_{sp} accounts for imperfections in the amplifier and is ideally 1, h is Planck's constant, ν is the frequency of the light, and G is the gain of the amplifier. Now, we would like to determine what form the $\{\phi_k(t)\}$ basis from Equation 5.5 takes. The noise is white, so $K_x(t,u) \propto \delta(t-u)$. Therefore, any function $\phi_k(t)$ satisfies Equation 5.5, so we can, in fact, choose any set of orthonormal basis functions we want. We will see the usefulness of this fact below.

Our model of the EDFA pre-amplifier is now complete. The EDFA's output is converted to an RF signal, which is then amplified. We assume that the photodiode and RF amplifier of Figure 5-3 have unity gain and are noiseless. This assumption is valid when the EDFA gain is large. The electronic receiver then integrates the signal energy over the bit period, the value of which we denote by the random variable x. As discussed more precisely in [19], a signal with bandwidth B and time spread T can be represented accurately by $2M = 2BT$ terms of Equation 5.4. So, the value of x measured by the receiver is

$$x = \int_0^T \left(\sum_{k=1}^{2M} (s_k + n_k)\phi_k(t) \right)^2 dt = \sum_{k=1}^{2M} (s_k + n_k)^2 \tag{5.6}$$

where we have used the orthonormality of the $\phi_k(t)$ to evaluate the integral. Using Laplace transform methods, we can derive the probability density function of x [15]:

$$f_E(x) = \frac{1}{N_0} \left(\frac{x}{E} \right)^{M-1/2} \exp\left(-\frac{x+E}{N_0} \right) I_{M-1}\left(2\frac{\sqrt{xE}}{N_0} \right)$$

where I_n is the nth modified Bessel function of the first kind, and $E = \sum_{k=1}^{2M} s_k^2$ is

---

[2] This result is a consequence of the Karhunen-Loève expansion applied to Gaussian stochastic processes.

the energy of the bit in the noiseless case.

We are now ready to calculate the bit-error rates. The receiver simply determines the value of a bit by thresholding x from Equation 5.6, deciding 1 if x is above the threshold γ and 0 otherwise. The probability that a 1-bit is incorrectly decided to be a 0-bit equals

$$P_1 = \int_0^{\gamma} f_E(x)\,dx = 1 - Q_M\left(\sqrt{2E/N_0}, \sqrt{2\gamma/N_0}\right) \tag{5.7}$$

where Q_M is the Marcum Q function of order M [20], $E = \sum_{k=1}^{2M} s_k^2$ is the optical energy contained in the bit from the noiseless case, and γ is the receiver's threshold. Similarly, the probability that a 0-bit is decided to be a 1-bit equals

$$P_0 = \int_{\gamma}^{\infty} f_E(x)\,dx = Q_M\left(\sqrt{2E/N_0}, \sqrt{2\gamma/N_0}\right). \tag{5.8}$$

Now we can exploit the freedom we have in choosing our basis set. We choose a basis so that $\phi_1(t)$ and $\phi_2(t)$ are sufficient to represent undistorted data pulses (i.e., $M = 1$; we need two basis functions so that we can represent both the in-phase and quadrature components of the pulse). The noise still exists in all modes, but the signal only exists in two modes. Moreover, if we assume that the band-pass filter in Figure 5-3 is perfectly matched to the input signal, then we can neglect n_k for $k > 2$.

5.1.4 Estimation of BER Performance of the SOA-MZI

The models presented above are sufficient to estimate the BER performance of an SOA-MZI at its optimum operating point. Unfortunately, even if we know the SOA parameters (h_0, τ_c, E_{sat}, and α), we still need to determine the two control pulse powers and the phase bias ψ that produce the optimum BER. This problem is computationally intensive. First, we choose a data pattern to test on the switch. Then, we choose values for the energies of the two control pulse trains and for the phase bias. We calculate the SOA outputs using the fourth-order Runge-Kutta method. The SOA outputs are rejoined at a coupler, so we add their outputs together, ignor-

Table 5.1: Parameters used for SOA-MZI simulations in Section 5.1.4.

Description	Symbol	Value	Units
Unsaturated Gain	h_0	7	–
Carrier Recovery Time	τ_c	100	ps
Saturation Energy	E_{sat}	1	pJ
Linewidth Enhancement Factor	α	5	–
Data Rate	R	40	Gb/s
Pulse Widths	T_{IFWHM}	8.33	ps
Delay Between Control Pulses 1 and 2	T_d	25	ps
Control Pulse Energy 1	E_1	36.3	aJ
Control Pulse Energy 2	E_2	26.8	aJ
Signal Pulse Energy	E_{sig}	–	aJ
Phase Bias	ψ	$\pi - 0.0076$	rads
Amplifier Efficiency Factor	N_0	1	–
Carrier Wavelength	λ_c	1550	nm

ing the control pulses at this point because they are filtered out. The resulting signal enters the receiver. To minimize the BER, we next find the value of γ that minimizes the error rate as calculated by Equations 5.7 and 5.8. The value of γ depends on the received power for which the BER is being calculated. Then, we repeat this calculation on a new set of values for the control pulse powers and phase bias.

Much of the simulation is written as MatLab scripts, although the most-used sections of code, which execute the Runge-Kutta and Marcum Q function calculations, are written in C. The Marcum Q function in particular requires a fast algorithm. I used those given by Shnidman in [21, 22][3]. I ran the simulations on a 32-processor grid of AMD64s and assumed that the signal power was too small to affect the gain dynamics in the SOAs. This assumption reduces the number of parameters to search through.

Table 5.1 shows the SOA and pulse parameters used in the simulations shown in this section. The simulation scanned over many possible values of control pulse energies and phase bias. The values shown in Table 5.1 are the ones that produced the lowest error rate at a received power of 18 dBphotons/bit. The control pulse

---

[3] In [22] Shnidman makes several corrections to his original paper and introduces a new error in the process. His formula for A has an easily corrected mistake.

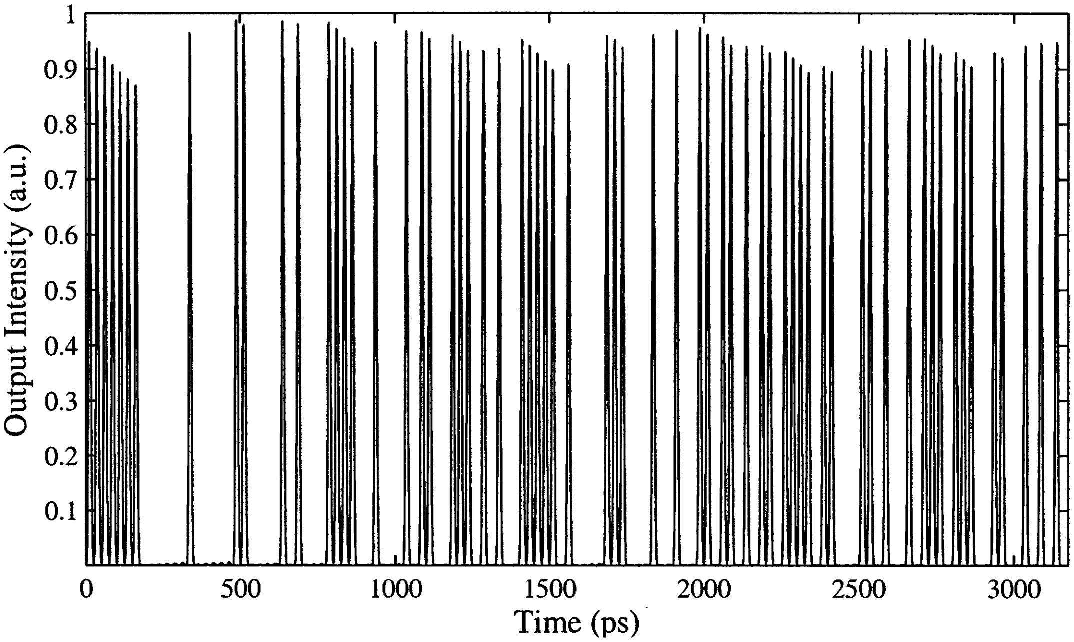

Figure 5-4: Intensity of the output of the SOA-MZI, showing the $2^7 - 1$ PRBS as well as some patterning on the 1s and 0s.

energies in both arms are extremely small. As we shall see, the switch still produces a good output, but the small control pulse energies makes the assumption of small signal pulse energy less likely. We will see in Section 5.1.5 how to test this assumption more precisely and we will see in Section 5.2 that simulating a chain of SOA-MZIs predicts higher control pulse power. In this section, however, we will assume that the signal pulse energy is less than a tenth of the control pulse energies so that the signal pulses will not significantly affect the SOA-MZI.

There is still one more parameter to consider. The Runge-Kutta calculation requires an initial condition for the integrated gain. We could let the initial integrated gain equal h_0, however it is more realistic to have the SOAs in some steady state at the beginning of the simulation. So, we simply input the optical data pattern into the control ports twice, but we only test the error rate on the second pattern. The data pattern used is the standard $2^7 - 1$ PRBS.

Figure 5-4 shows the intensity of the output of the SOA-MZI. There is amplitude patterning on the 1s and, to a lesser extent, the 0s. This patterning occurs because

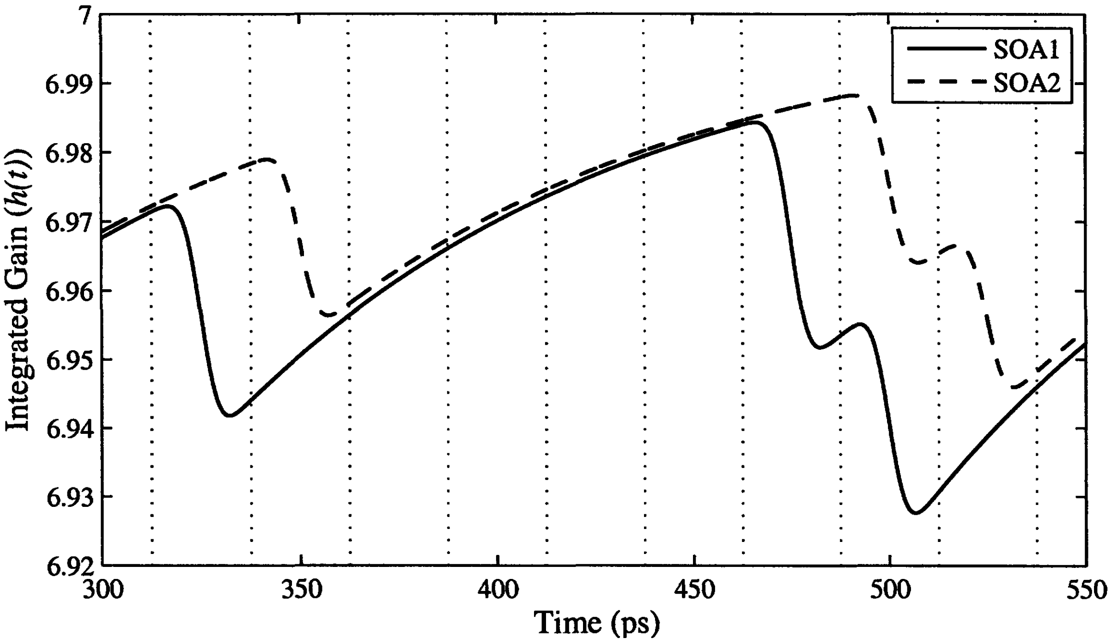

Figure 5-5: Integrated gains in both SOAs. The relative phase shift induced equals the difference in the two gains times $\alpha = 5$. This section of the gains corresponds with 10 bits of the pattern (0100000110). The vertical grid lines mark the center of the signal pulses.

the integrated gain in each SOA, and therefore the output of each SOA, depends on the pattern of pulses that have passed through them. We can see better how this patterning occurs in Figure 5-5, which shows the integrated gain, $h(t)$, in both SOAs over a 10 bit-period. The relative phase shift between the arms equals $\alpha\Delta h/2$ where Δh is the difference in $h(t)$ between the two arms. In the figure, the vertical grid lines mark the center of the signal pulses. The SOA-MZI is biased so that a zero relative-phase shift results in destructive interference of the signal pulse. Two effects switch the SOA-MZI to the on state. First, when a control pulse arrives, it first changes the gain in SOA1 while the gain in SOA2 continues to recover, leading to a relative phase shift that drives the SOA-MZI away from destructive interference. Then the control pulse arrives in SOA2, eliminating the relative phase shift and returning the SOA-MZI to destructive interference.

The second effect that switches SOA-MZI to the on state is the gain imbalance between the two arms. This gain imbalance implies there cannot be perfect interference, even if the two arms are out of phase. In fact, Figure 5-5 shows that Δh is ~ 0.04 for 1-bits, so the relative phase between the two arms is only ~ 0.1 rads. This phase shift corresponds with only a 1% transmissivity through the SOA-MZI. On the other hand, the gain difference in the two arms causes the ratio of the signal pulse power to go from 1:1 to 1.04:1. So, in this case gain effects are the dominant switching mechanism.

Figure 5-5 reveals other important behavior of the SOA-MZI that leads to patterning in the output amplitude. Consider the first 1-bit, which occurs at time 337.5 ps. The control pulse in SOA 1 arrives at time 325 ps and the control pulse in SOA 2 arrives at time 350 ps. The change in integrated gain in SOA 2 at time 350 ps is smaller than the change in integrated gain in SOA 1 at 325 ps, implying that the control pulse in Arm 2 is less than that of Arm 1. Simulations confirm that this is indeed true. To obtain a high extinction ratio, control pulse 2 should change the h in SOA 2 so that it equals the h in SOA 1. In this way, the two arms are perfectly matched and the zeros (e.g., at times 362.5 ps and 387.5 ps) will completely destructively interfere. We have to fix the ratio of the energies of control pulse 1 and control pulse 2, and it would be convenient to be able to choose a ratio that would always completely extinguish the 0-bits. Unfortunately, as can be seen from simulations and analysis of Equation 5.3, this cannot be done. The desired ideal ratio cannot be fixed, but rather it depends on the initial values of h in each SOA before each 1-bit. For example, in Figure 5-5, the gains in the SOAs before the 1-bit at time 337.5 ps is $\sim$6.97. The gains of the SOAs before the 1-bit at time 487.5 ps is $\sim$6.98. This difference is only slight in this case, but in Section 5.1.5 we will see that control pulse energies will have to be higher than they are in this case, and the value of h will vary over a much wider range than that shown in Figure 5-5.

With the data in Figure 5-4, we can determine the distribution of energies in 0-bits and 1-bits, shown in Figure 5-6. In this figure, the possible bit-energies have been divided into 1000 bins ranging from 0 up to the energy of the most energetic 1-bit. Using these data and Equations 5.7 and 5.8, we can determine the bit-error rate as a function of received power. Figure 5-7 shows the bit-error rate curve of the SOA-MZI

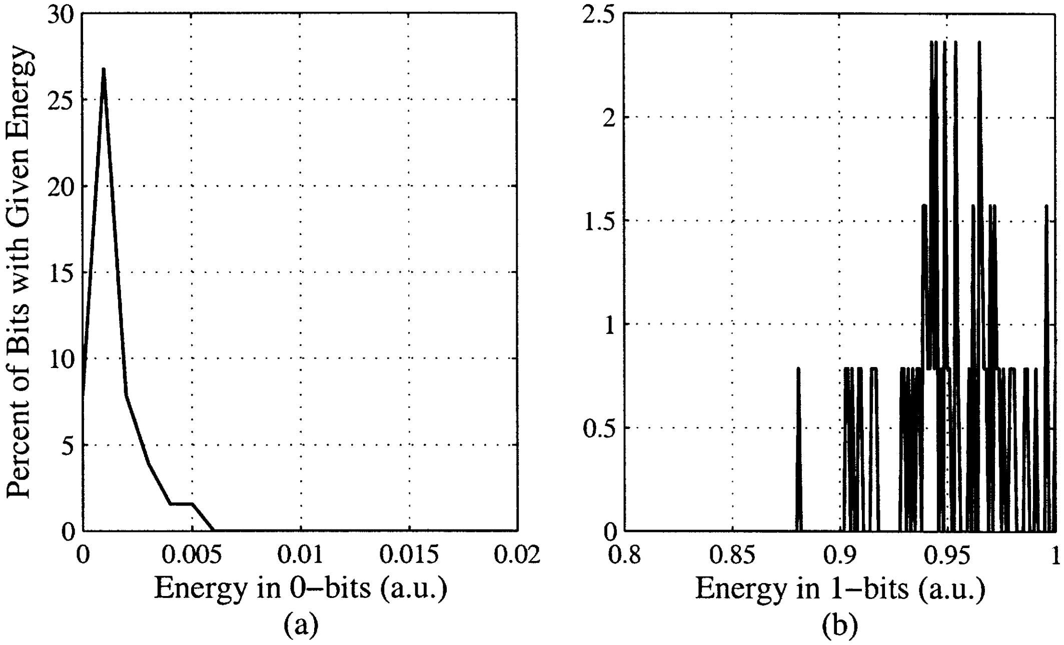

Figure 5-6: Distribution of energies in (a) 0-bits and (b) 1-bits, all normalized to the power in the bit with the most energy.

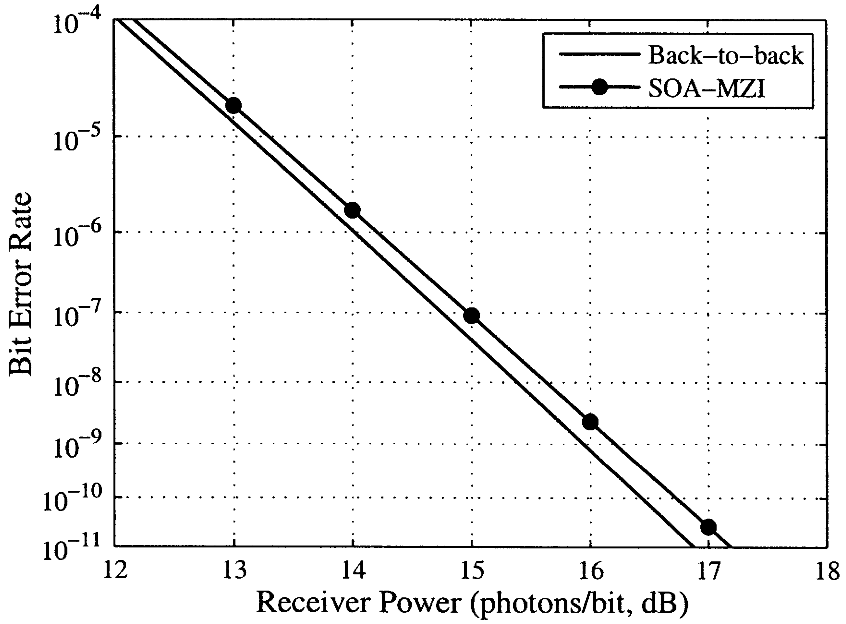

Figure 5-7: Simulated bit-error rate curve of the output of the SOA-MZI compared to the transmitter back-to-back.

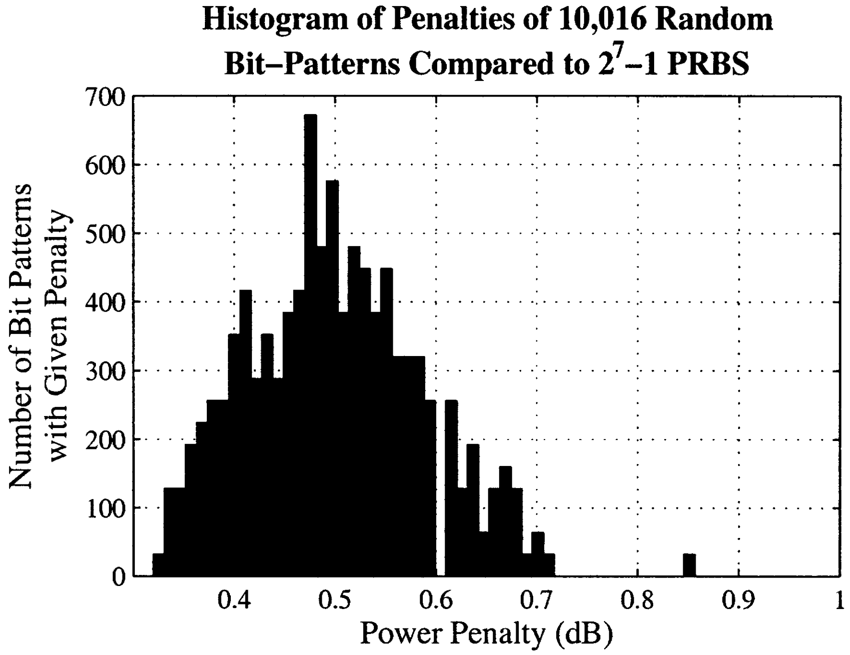

Figure 5-8: Histogram of power penalties of 10,016 random bit-patterns compared to the $2^7 - 1$ pattern at an error rate of 10^{-9}.

compared to that of a simulated transmitter back-to-back.

The simulations optimize the SOA-MZI for performance on a $2^7 - 1$ PRBS, just as most laboratory experiments test optical equipment of one of several pseudo-random bit streams. Figure 5-8 compares the SOA-MZI's performance on 10,016 random patterns of 127 bits with its performance on the $2^7 - 1$ PRBS. In the BER calculations for each of these data patterns, the simulation used the same value for the threshold, γ, that was calculated for the PRBS (in reality, there is a different value of γ for each received power). The figure shows a histogram of power penalties calculated for the random bit patterns, showing that all patterns tested perform within 1 dB of the PRBS.

5.1.5 Adding Noise to the SOA Models

We have so far neglected the noise added by the SOAs, considering only the noise added by the pre-amplifier in the optical receiver. In Section 5.1.4 we assumed that the effects of the signal pulses on the SOAs were small compared to those of the control pulses. This assumption implies that the signal pulses have to be very weak, so that noise becomes a large fraction of the optical energy output by the SOAs. In this section, we add noise to the SOAs in the SOA-MZI model.

In Section 5.1.3 we modeled noise added by the optical pre-amplifier in the receiver. We can adapt this model to the SOA-MZI model discussed in Section 5.1.2. Once again, we expand one signal pulse coming out of Arm 1 in the real-valued $\{\phi_k\}$ basis:

$$s_1(t) = \sum_{\{k\}} (s_{1,k} + n_{1,k})\phi_k(t). \tag{5.9}$$

Again, the sum is over the positive integers, $s_{1,k}$ is a real number, and $n_{1,k}$ is a Gaussian distributed random variable with zero mean and a variance of $N_0/2$. Similarly, we can expand the signal pulse exiting Arm 2 as

$$s_2(t) = \sum_{\{k\}} (s_{2,k} + n_{2,k})\phi_k(t). \tag{5.10}$$

As before, we assume the filter in Figure 5-2 is perfectly matched to $\phi_1(t)$ and $\phi_2(t)$, so that we can neglect all other terms.

At the output of the SOA-MZI, $s_1(t)$ and $s_2(t)$ sum together:

$$s(t) = \sum_{k=1}^{2} (s_{1,k} + s_{2,k} + n_{1,k} + n_{2,k})\phi_k(t). \tag{5.11}$$

To calculate BERs, we need the SOA-MZI's output intensity integrated over the full bit period, so

$$\begin{aligned} \xi &= \int_0^T \left(\sum_{k=1}^{2} (s_{1,k} + s_{2,k} + n_{1,k} + n_{2,k})\phi_k(t) \right)^2 dt \\ &= \sum_{k=1}^{2} (s_{1,k} + s_{2,k} + n_{1,k} + n_{2,k})^2, \end{aligned} \tag{5.12}$$

where we have used the orthonormality of the $\phi_k(t)$ to evaluate the integral. T is the bit period and ξ is the random variable of the SOA-MZI's output energy. If $n_{1,k} = 0$ and $n_{2,k} = 0$, then Equation 5.12, when applied to each bit at the SOA-MZI's output, simply reproduces a n energy distribution density figure like Figure 5-6. Adding noise into the SOAs, however, broadens the distribution of energies in both the 0s and the 1s.

Using standard properties of random variables, we know that if $n_{1,k}$ and $n_{2,k}$ are Gaussian variables with zero mean and a variance of $N_0/2$, then $s_{1,k}+s_{2,k}+n_{1,k}+n_{2,k}$ is also a Gaussian variable with a mean of $s_{1,k}+s_{2,k}$ and a variance of N_0 [23]. From Equation 5.12, we see that we want the sum of the squares of two Gaussian random variables, for which we will need the noncentral χ^2 distribution [24].

Let X_k be N independent Gaussian random variables with means μ_k and variances σ_k^2. Then the random variable

$$Z = \sum_{k=1}^{N} \left(\frac{X_k}{\sigma_k} \right)^2 \tag{5.13}$$

has a noncentral χ^2 distribution. Notice that this distribution does not describe the behavior of an arbitrary linear combination of squared Gaussian random variables. Instead the random variables must be weighted by $1/\sigma_k^2$. In our case, $X_k = s_{1,k} + s_{2,k} + n_{1,k} + n_{2,k}$ and, from Equation 5.12, we need the distribution for

$$\xi = \sum_{k=1}^{2} (X_k)^2 .$$

Fortunately, X_1 and X_2 both have the same variances, so

$$\xi = \sigma^2 Z$$

where $\sigma = \sigma_1 = \sigma_2$, allowing us to use the noncentral χ^2 distribution.

There is one more important simplification. It seems from Equation 5.12 that we need to know what fraction of the pulse amplitude is in the in-phase mode ($s_{1,1}$ and $s_{2,1}$) and what fraction is in the quadrature mode ($s_{1,2}$ and $s_{2,2}$). It turns out,

Table 5.2: Parameters used for SOA-MZI simulations in Section 5.1.5.

Description	**Symbol**	**Value**	**Units**
Unsaturated Gain	h_0	8	–
Carrier Recovery Time	τ_c	75	ps
Saturation Energy	E_{sat}	1	pJ
Linewidth Enhancement Factor	α	5	–
Data Rate	R	10	Gb/s
Pulse Widths	T_{IFWHM}	2	ps
Delay Between Control Pulses 1 and 2	T_d	10	ps
Signal Pulse Energy	E_{sig}	100	aJ
Amplifier Efficiency Factor	N_0	1	–
Carrier Wavelength	λ_c	1550	nm

however, that the noncentral χ^2 distribution has only two degrees of freedom, even though it can be the sum of many squared Gaussian random variables. The first degree of freedom is N in Equation 5.13, which equals 2 in our matched filter case. The second degree of freedom is

$$\delta = \sum_{k=1}^{N} \left(\frac{\mu_k}{\sigma_k} \right)^2 \tag{5.14}$$

where, in our case, $\mu_k = s_{1,k} + s_{2,k}$ and $\sigma_k = N_0$. Therefore, by Equation 5.12, we see that δ is simply the total output energy of the SOA-MZI in the noiseless case divided by σ^2, regardless of how the field is divided among the in-phase and quadrature modes.

With this model, we can test the effects of noise and signal pulse energy on the SOA-MZI. Table 5.2 shows the parameter set for two simulations of the SOA-MZI, one with noise in the SOAs and one without. Figure 5-9 shows the results of these simulations by plotting the optimal bit-error rate of the SOA-MZI at a range of control pulse energies in Arm 1. The solid plot shows the simulation without any SOA noise. For each control pulse energy in Arm 1, the simulation finds the phase bias and Arm 2 pulse energy that produces the lowest bit-error rate at a received power of 18 dBphotons/bit. The solid plot shows unrealistic behavior: extremely

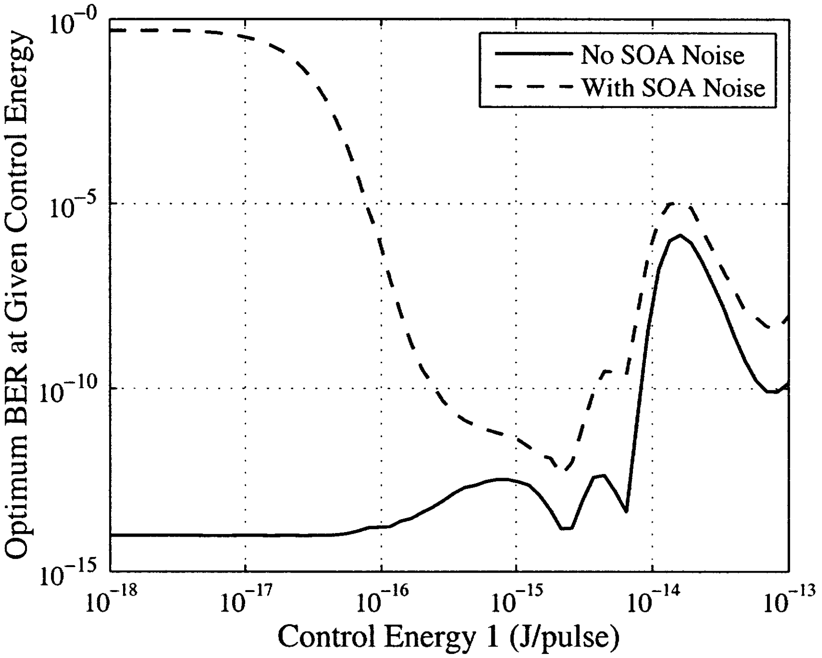

Figure 5-9: Optimal bit-error rates of the SOA-MZI over a range of control pulse energies in Arm 1. The bit error rates are taken at a received optical power of 18 dBphotons/bit.

small control pulse energies seem to produce excellent error rates. These very weak control pulses cause h to vary only slightly from h_0. As we saw in the discussion of Figure 5-5, this implies that we will be able to choose control energies in Arm 1 and Arm 2 that will extinguish 0-bits almost perfectly, leading to low bit-error rates.

The dashed plot of Figure 5-9 shows the same simulation using the same values for the control pulse energies and phase bias, but with noise added to the SOAs in the MZI. When the control pulse energies are very weak, very little of the signal power is output from the MZI. The noise, however, still has the same amount of energy because it depends on the gain, G, rather than on the signal or control energies. Therefore, the noise will dominate the SOA-MZI's output when the control pulses are weak. This fact is seen in the high bit-error rate that exists in the dashed plot for low control pulse energies.

Figure 5-9 suggests that adding noise to the SOAs does not affect bit-error rate performance too much for many control pulse energies. The dashed plot shows that the best performance is at a control pulse energy of E_1 = 2.15 fJ. In this case E_2 =

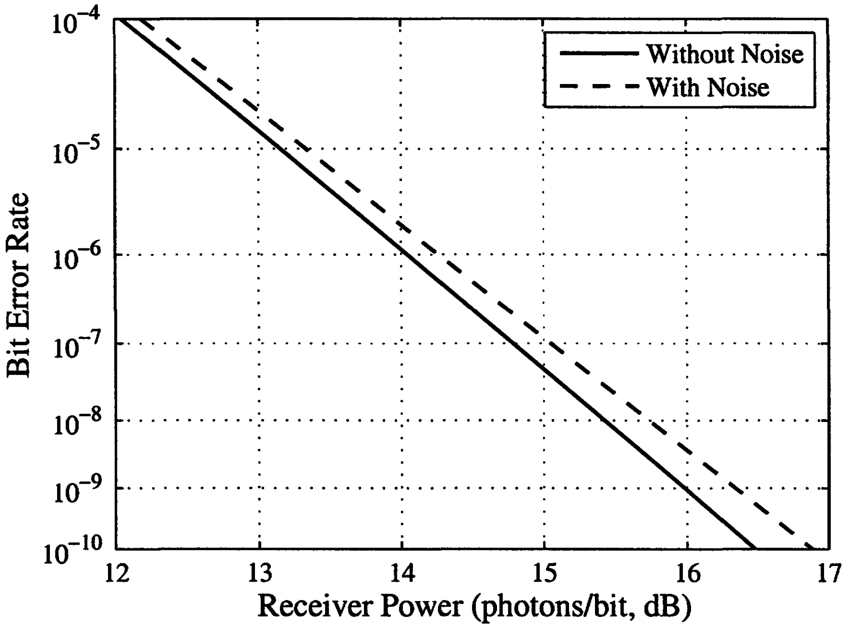

Figure 5-10: BER plots of SOA-MZI's output cases with and without noise in the SOAs.

1.52 pJ and $\psi = \pi - 0.02$ rads. Figure 5-10 shows bit-error rate plots of this operating point in the noiseless and noisy cases. The penalty at a BER of 10^{-9} is < 0.5 dB and there is only a slight slope change. So, with $E_{sig} = 0.1$ fJ, the noise doesn't dominate the SOA-MZI performance. For most simulations in the following sections, we will continue to use $E_{sig} = 0.1$ fJ because it is intense enough to avoid SOA noise problems and weak enough to avoid heavily saturating the SOAs. When the SOAs are saturated, our model becomes less accurate [25].

5.2 Simulation of a Cascade of SOA-MZIs

Optical switches used in regeneration must be cascadable. That is, we must be able to use the output of one optical switch as the control input of the next one in a chain of such switches. Figure 5-11 shows SOA-MZI switches used as regenerators in an optical link. The output of the first SOA-MZI propagates through the fiber link to an EDFA. The EDFA amplifies the data pulses to the proper energy so that they can serve as control pulses in the next SOA-MZI.

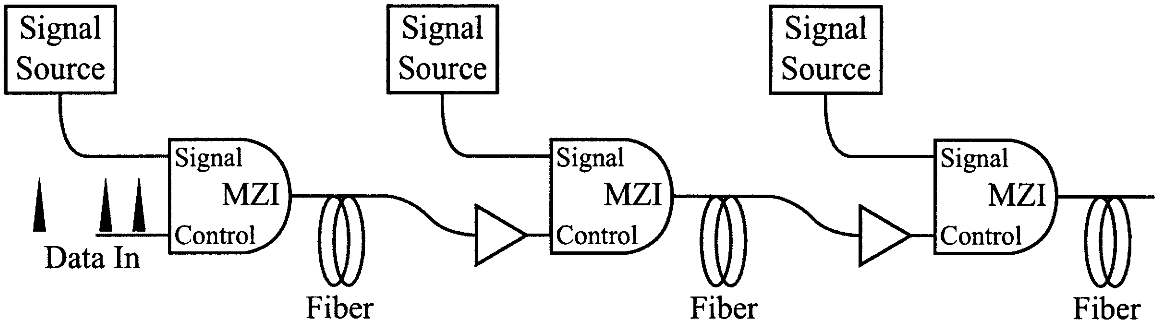

Figure 5-11: Cascade of SOA-MZI's in regeneration.

As we saw in Figure 5-4, the output bits of the SOA-MZI have amplitude variations. For example, assume a sequence of 1-bits follows a long sequences of 0-bits at the MZI input. The first 1-bit passes through unsaturated SOAs and so receives high gain, producing an intense output pulse. The final 1-bit in the sequence will receive the least gain, producing a weaker output pulse. So, when these output bits are used as the control inputs for the next switch, the earlier 1-bits will be more intense than later ones. This may lead to even earlier saturation of the SOAs and, therefore, even more severe amplitude patterning.

It is not clear that we can find an operating point of the SOA-MZIs to prevent this runaway increase in amplitude patterning. In this section, we'll examine the circumstances that will produce a successful cascade of SOA-MZIs. We can expect more success at 10 Gb/s, because the SOA recovery time of $\tau_c = 75$ ps is shorter than the 100-ps bit period. Therefore, the SOAs have time to recover nearly to their unsaturated state before every bit. At 40 Gb/s cascading becomes more difficult, but we will see operating points where it may succeed.

5.2.1 SOA-MZI Cascade at 10 Gb/s

Figure 5-11 shows the model for this section's simulation of an SOA-MZI cascade, although the simulations neglect the effects of the optical fiber. The SOA and optical pulse parameters are the same as those given in Table 5.2. The simulations treat the EDFAs as ideal amplifiers that add no noise to the optical pulses. They also neglect the effects of noise in the SOA. This approximation is necessary to keep the

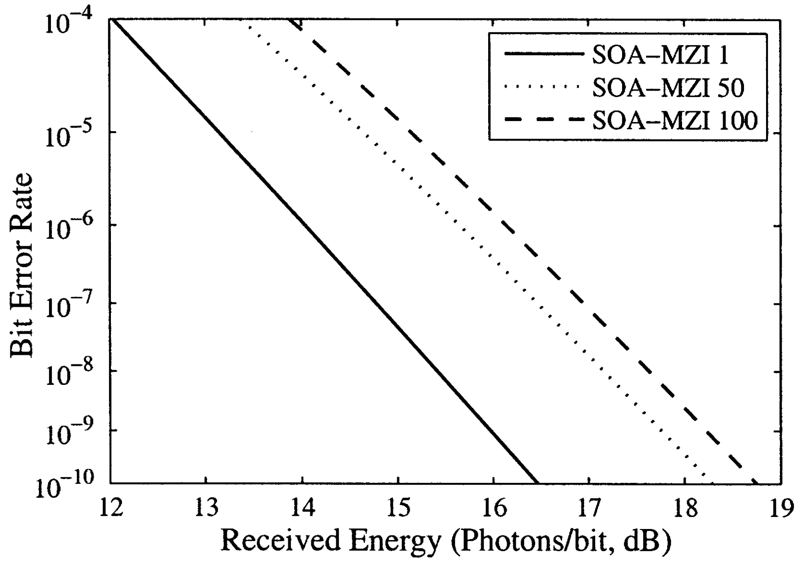

Figure 5-12: Simulated BER curves for an optical data stream in a cascade of SOA-MZIs taken after 1, 50, and 100 switches.

simulation runtimes reasonable. Otherwise we would need to run many instances of the simulation in a Monte Carlo simulation. As we will see, though, the pulse energies are high enough that we may safely neglect SOA noise in many cases. The simulation sets the amplifier gain before each SOA-MZI so that the average control pulse energy is the same for every SOA-MZI. Of course, each SOA-MZI adds amplitude patterning on the pulses, so that many pulses will vary around that average. As in the simulations of Section 5.1, we use the standard $2^7 - 1$ pseudorandom bit stream. Also, as before, the simulations send this PRBS pulse stream twice into the SOA-MZIs to simulate the effects of steady-state operation.

It is in fact possible to operate a cascade of SOA-MZI switches at 10 Gb/s. Section 5.3.2 presents experimental data for a cascade of 100 SOA-MZIs. The simulations also show that a cascade of switches at 10 Gb/s will operate out to 100 switches. Figure 5-12 shows simulated bit-error rate curves for the optical data stream in a cascade of SOA-MZIs after the 1st, 50th, and 100th switches. The optimal operating point was found by searching a space of values for E_1, E_2, and ψ. The best performance occurred at $E_1 = 2.23$ fJ, $E_2 = 1.48$ fJ, and $\psi = \pi + 0.025$ rads. By the 50th switch, most of the power penalty in the BER curves has already accumulated so that the

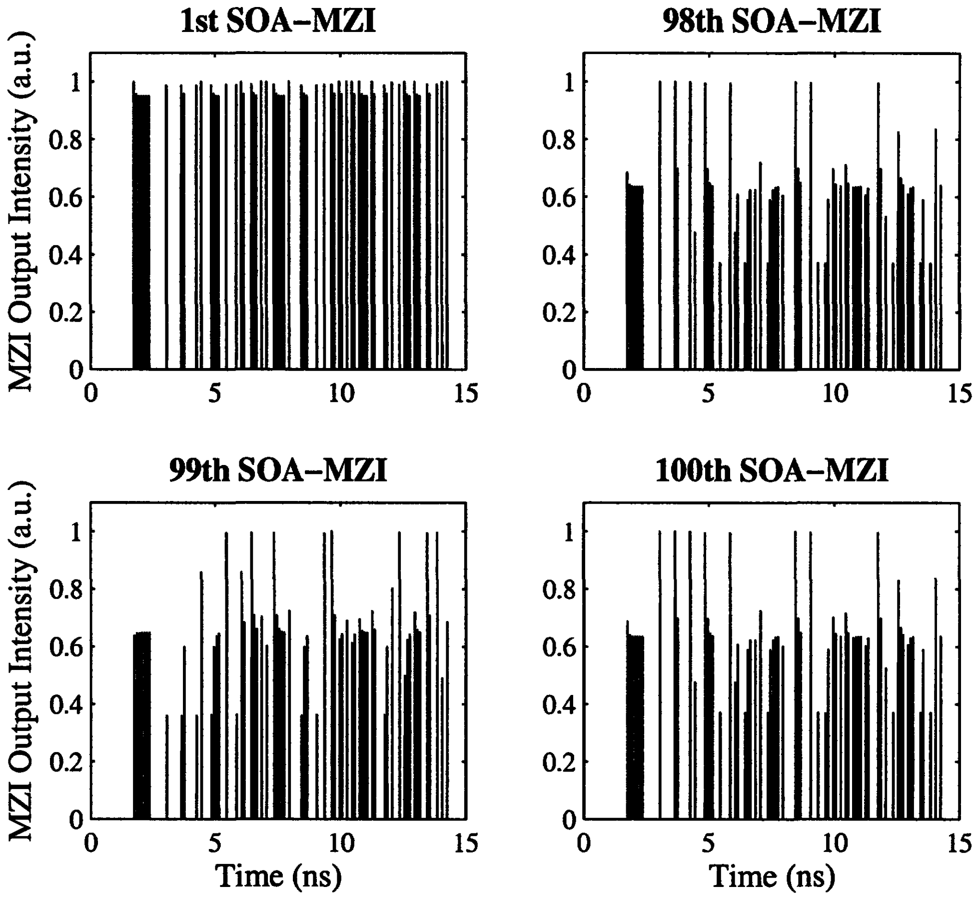

Figure 5-13: Output pulse intensity of 4 of the switches in the SOA-MZI cascade.

100th switch's performance is only slightly worse.

Figure 5-13 shows the output pulses of the 1st, 98th, 99th, and 100th SOA-MZI. The 98th and 100th are nearly identical because the cascade has reached an oscillating steady state. So the BER performance will not continue to worsen. This oscillating behavior likely occurs because the more intense control pulses actually produce a phase shift $> \pi$ so that the corresponding output signal pulse is weaker. Moreover, the most intense control pulses reduce the gain in the SOAs so that corresponding output signal pulses are weaker. Conversely, the weakest control pulses reduce the gain less, so the corresponding output signal pulses are more intense.

5.2.2 SOA-MZI Cascade at 40 Gb/s

At 40 Gb/s the bit period is only 25 ps, several times less than the recovery time $\tau_c = 75$ ps. So, now patterning effects are much more severe, and it becomes less certain that the SOA-MZIs can be cascaded as far as we saw in the previous section. In fact, when we apply the simulations of the previous section to a 40 Gb/s data stream, the bit-error rate performance becomes intolerable after only a few switches. Fortunately, we can relax a couple of constraints placed on the SOA-MZIs to obtain better performance.

The simulations in the previous section placed two implicit constraints on the cascades: 1) the SOA-MZIs do not invert the data pattern, and 2) the optical pulses in the SOA-MZIs are weak enough not to fully saturate the SOAs. With these two constraints on operation, the SOA-MZI cascade will not function at 40 Gb/s. Nonetheless, we will see that when we relax the first constraint, allowing the SOA-MZIs to invert the data pattern, the SOA-MZIs will be cascadable. Moreover, when we relax the second constraint, it may be possible that increasing the signal pulse energy will also make the the SOA-MZI cascadable. Signal pulse energies near E_{sat} will drive the SOAs close to saturation. Then weaker control pulses create the perturbations in the SOA gain that produce switching. So, most of the energy is in the signal pulses, which are present in every bit period. Thus the data patterning on the control pulses create less amplitude patterning on the output. The simulations do show that high signal pulse powers can improve performance of the cascade, although not out to 100 switches. Unfortunately, the model we have been using becomes less accurate as the SOAs become more saturated, so the conclusions we draw in such cases must be provisional. As we saw in Section 3.3, the gain is assumed to be proportional to the carrier-population inversion, which limits the range of accuracy to small changes in the carrier density.

Figure 5-14 shows the output pulses of 4 of the switches in a cascade of SOA-MZIs operating at 40 Gb/s. At the 5th SOA-MZI, there is already significant patterning in the optical pulses. By the 10th SOA-MZI, the original data pattern is no longer

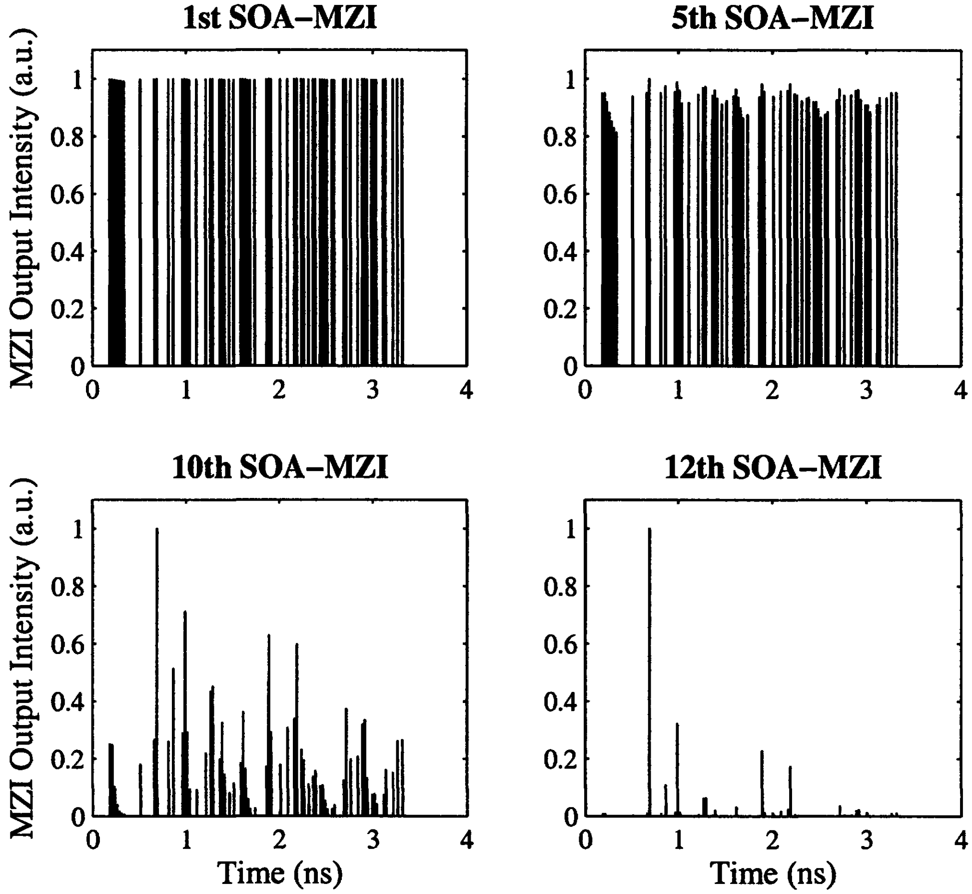

Figure 5-14: Output pulse intensity of 4 of the switches in the SOA-MZI cascade at 40 Gb/s.

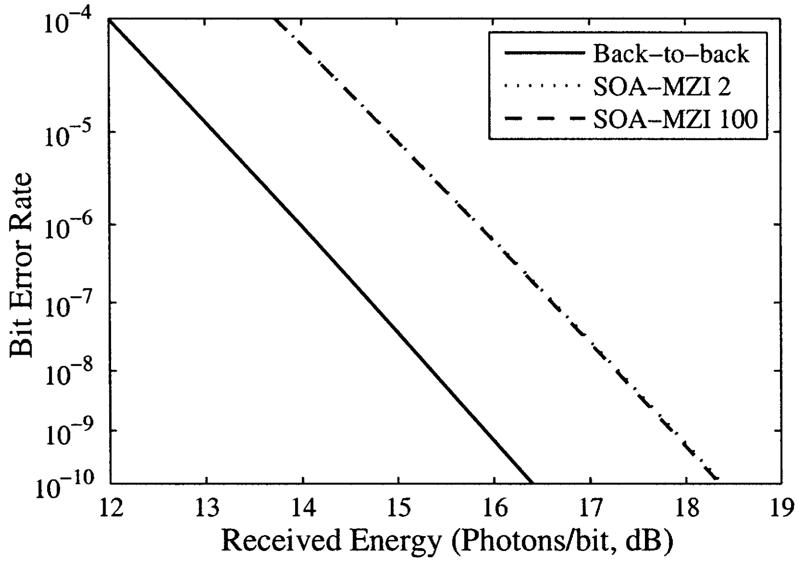

Figure 5-15: Simulated BER curves for an optical data stream in a cascade of inverting SOA-MZIs taken after 2 and 100 switches at 40 Gb/s compared with the BER curve of the transmitter back-to-back.

recognizable. By the 12th SOA-MZI, all the optical power has been concentrated in a few pulses. These pulses are the 1-bits that follow the long sequences of bits that are dominated by 0-bits. The most likely explanation is simply that the gain recovers during these sequences, concentrating more and more power in the 1-bits that follow them. As before, the SOA and optical pulse parameters are given in Table 5.2. This time, the optimum operating point was found by simulating the bit-error rate of a cascade of only 5 SOA-MZIs because longer cascades do not produce reasonable error rates. After searching over a space of possible values for E_1, E_2, and ψ, the simulation found the optimum BER performance at $E_1 = 13.4$ aJ, $E_2 = 10.5$ aJ, and $\psi = \pi$ rads.

If we allow the SOA-MZI to invert the bits in the data pattern, then the cascade does operate out to 100 switches. Now, of course, the data pattern is the correct one only after every other switch. Figure 5-15 shows the simulated bit-error rate curves of the optical data stream after the 2nd and 100th switches in the cascade. The BER curves of both these switches are nearly identical. A transmitter back-to-back BER curve is shown in the figure as well, and both switches show a 2 dB power penalty.

In inverting operation, the amplitude patterning introduced in the even numbered switches of the cascade compensate the amplitude patterning introduced by the odd

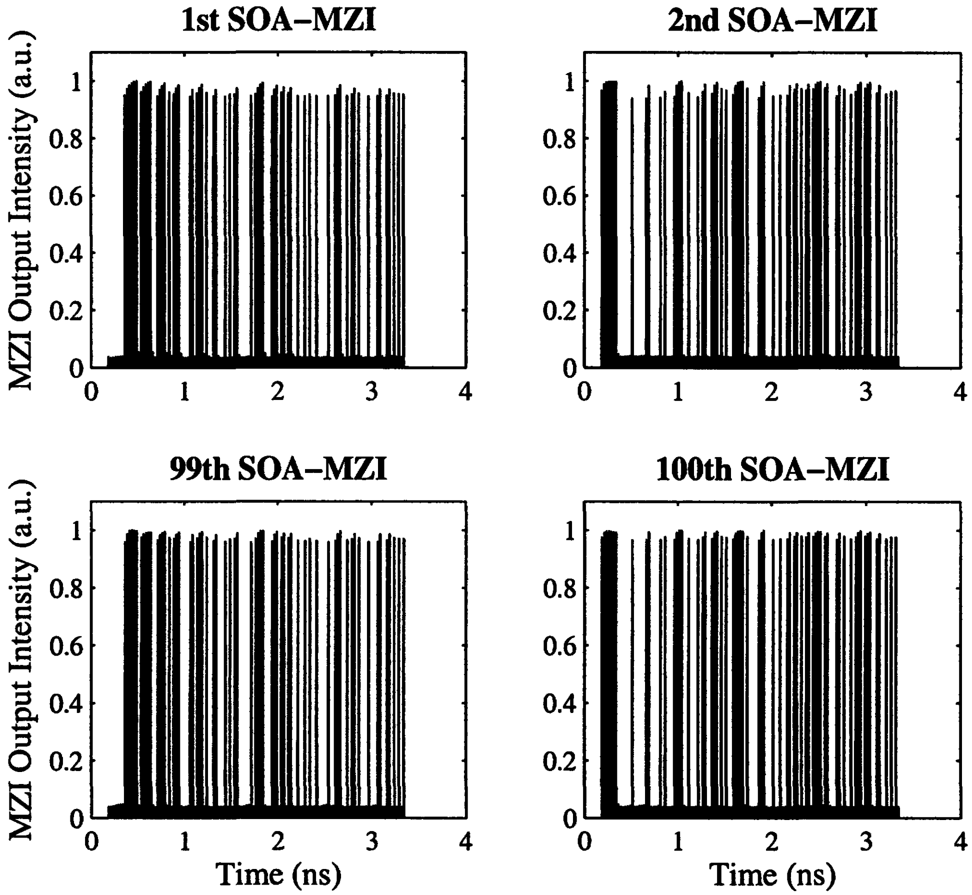

Figure 5-16: Output intensity of switches 1, 2, 99, and 100 in the inverting SOA-MZI cascade at 40 Gb/s.

numbered switches. We can see this compensation in Figure 5-16, which plots the output intensity of 4 of the switches in the inverting SOA-MZI cascade. In the plot of the 1st MZI's output, the first cluster of 1-bits has a rising amplitude, in contrast to the noninverting case in which pulses in groups of 1-bits have a falling amplitude (e.g., as in the upper-left plot of Figure 5-13). In the noninverting case the amplitudes of clusters of 1-bits at the output falls because the corresponding control pulses are also 1-bits. These 1-bits reduce the gain of the SOAs. In the inverting case, clusters of 1-bits at the output correspond to control pulses that are 0-bits with little energy. So the gain recovers during these gaps, and this gain recovery is reflected in a amplitude recovery in the output.

When we chain two inverting SOA-MZIs together, the output of the first one has clusters of 1-bits with rising amplitudes. These pulses become the control pulses in the second SOA-MZI. So, in clusters of control pulses that are 1-bits, the later control pulses are stronger, so the imbalance the MZI more than earlier control pulses. This switches out more of the signal pulse power. On the other hand, the gain by this time is depleted, compensating the increased switching. You can see this clearly in Figure 5-16 where amplitude patterning in the 1-bits in the outputs of the 1st and 99th SOA-MZIs is reduced in the 2nd and 100th SOA-MZIs.

As mentioned before, there are two mechanisms for switching in the SOA-MZI: the phase difference caused by the difference between h in the two arms, and the gain imbalance caused by changes in h with time. In the noninverting SOA-MZI, these two mechanisms work together, but in the inverting SOA-MZI they work against each other. In an inverting SOA-MZI, the control pulses produce the phase shift to cause destructive interference, but the gain imbalance generated makes that interference incomplete. This fact explains the poor extinction of 0-bits in Figure 5-16.

It also suggests that α, the constant of proportionality between shift in h and the shift in phase, should play a more significant role in inverting SOA-MZIs than in noninverting SOA-MZIs. Figure 5-17 shows the optimal BER as a function of control pulse energy, E_1 for a cascade of 11 SOA-MZIs. The solid curve shows the simulation for $\alpha = 5$ and the dashed curve for $\alpha = 0$. There is a difference in performance.

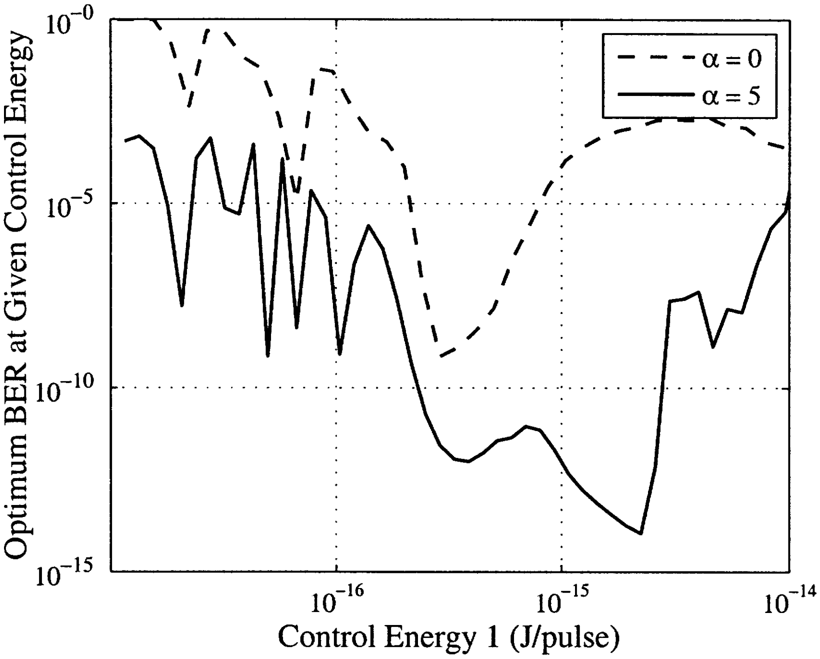

Figure 5-17: Optimal BER as a function of E_1 at two different values of α for the 10-Gb/s cascade.

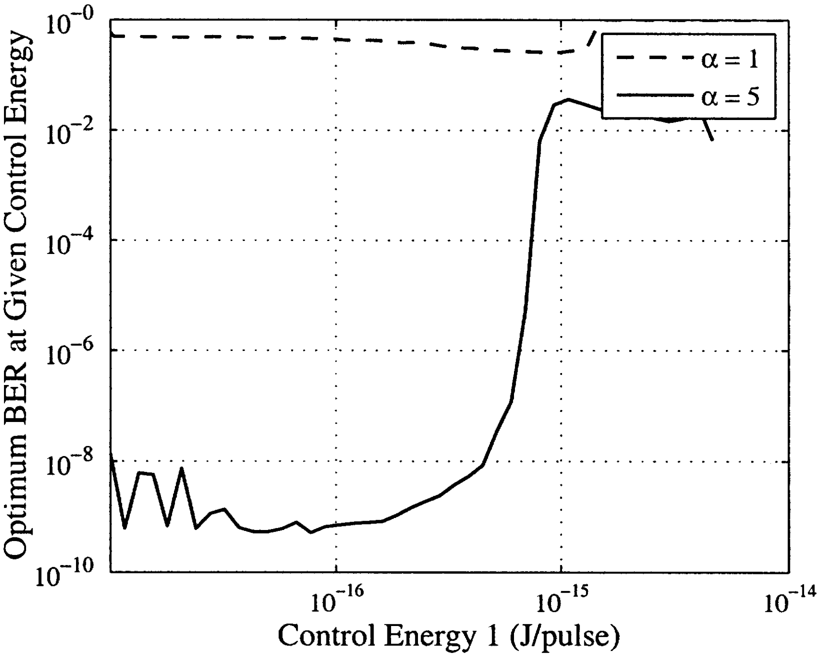

Figure 5-18: Optimal BER as a function of E_1 at two different values of α for the 40-Gb/s cascade.

Nonetheless noninverting switching does not require a phase shift. Figure 5-18 shows the same plot for a cascade of 7 SOA-MZIs at 40 Gb/s. The difference between $\alpha = 1$ and $\alpha = 5$ is very large, reflecting the complete reliance of the inverting SOA-MZI in a differential phase shift.

5.3 Integrated SOA-MZI

The simulations of Section 5.1 suggest that SOA-MZI switches can be chained together without producing a runaway increase in the BER's power penalty. This fact in turn means that the SOA-MZI is a candidate for all-optical data regeneration. This section presents results of performance tests on an integrated SOA-MZI all-optical switch provided by Alphion. Jade Wang has demonstrated wavelength converting operation with the Alphion switch at 10 Gb/s [26].

This section contains these results as well as results of tests of the SOA-MZI as a regenerator in the 100-km loop described in Section 4.4. SOA-MZI's have been tested in regenerative recirculating loops before, usually when operated in a data inverting mode. Here I describe a noninverting wavelength maintaining SOA-MZI which uses the SOA wavelength converter of Section 4.3.1 at the control input of the SOA-MZI [27]. The wavelength maintaining SOA-MZI, like the WMFUNI, can function as a regenerator in a 100-km recirculating fiber loop.

5.3.1 SOA Mach-Zehnder Interferometer

Figure 5-19 shows the schematic diagram of the Alphion SOA-MZI switch we tested in all-optical regeneration. SOA 4 and SOA 5 serve as the nonlinear media for switching, like the 2 SOAs in Figure 5-2. The extra SOAs in the figure (1, 2, 3, and 6) are necessary to compensate coupling losses between the fiber connectors and the chip as well as loss in the integrated waveguides. Finding the correct bias currents to drive the SOAs on the chip is a difficult task. Jade Wang developed a solution, which she used to find the optimal bias currents [26].

As with the WMFUNI, we used the SOA wavelength converter of Section 4.3.1 so

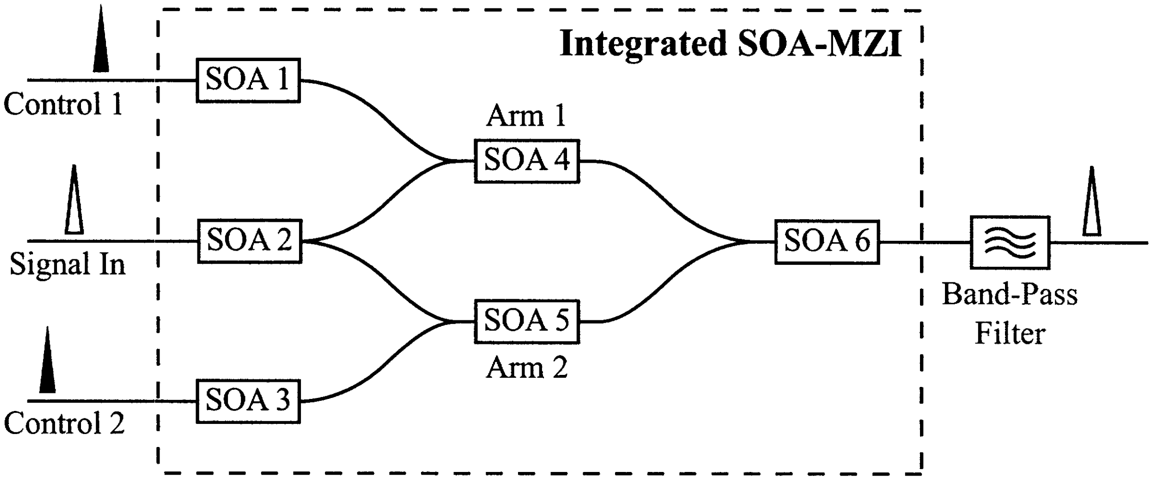

Figure 5-19: Schematic of the Alphion integrated SOA-MZI optical switch.

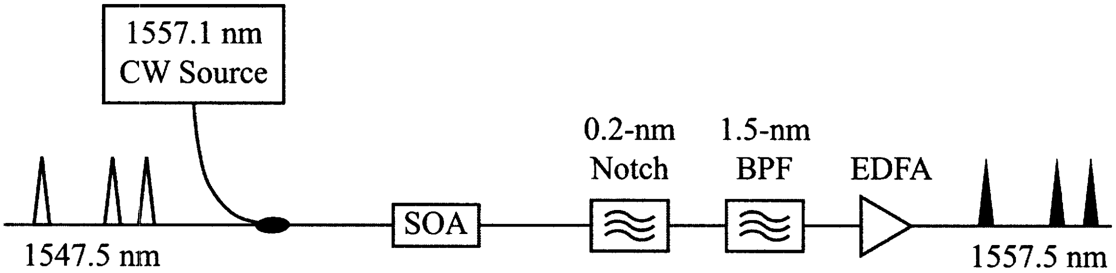

Figure 5-20: Schematic of the SOA wavelength converter presented in Section 4.3.1.

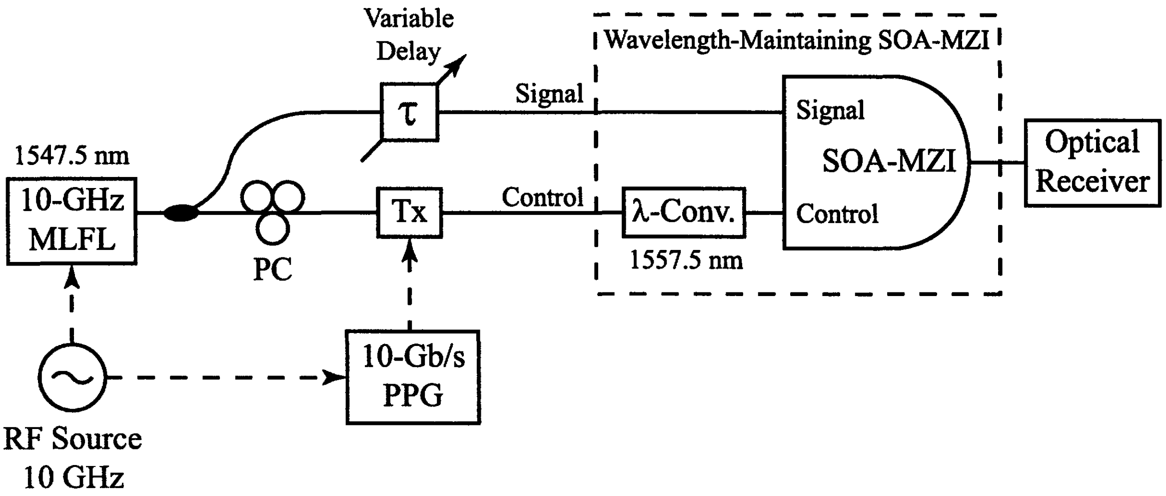

Figure 5-21: Schematic of the wavelength-maintaining SOA-MZI setup for a BER measurement.

that the incoming signal and control pulses would have the same carrier wavelength. Figure 5-20 shows the basic schematic of the wavelength converter. Figure 5-21 shows the wavelength-maintaining SOA-MZI setup for a bit-error rate test. A single 10-GHz mode-locked fiber laser provides pulses with a carrier wavelength of 1547.5 nm for both the the signal and control input ports. A transmitter, Tx, driven by a pulse pattern generator, modulates a $2^{31} - 1$ PRBS onto the control pulse train. The wavelength converter shifts the carrier wavelength of the control pulses to 1557.5 nm. These wavelength-converted pulses enter the SOA-MZI and their power is divided into the two arms of the MZI. The pulses entering Arm 2 are delayed by $\sim$ 15 ps with respect to those entering Arm 1. An optically pre-amplified receiver measures the BER of the SOA-MZI's output. Figure 5-22 shows the logical performance of the wavelength-maintaining SOA-MZI. The SOA-MZI shows a 1.2-dB penalty compared to the back-to-back measurement at an error rate of 10^{-9}.

As discussed in Section 4.2.3, a regenerator must be able to tolerate random variations in the timing of the control pulses. To measure this tolerance, we use the switching window, the measurement of which was described in Section 4-16. The width of the switching window approximately equals the amount of timing variation in the control pulses that the SOA-MZI can tolerate. Figure 5-23 shows the switching window of the wavelength-maintaining SOA-MZI. Its IFWHM is 15 ps.

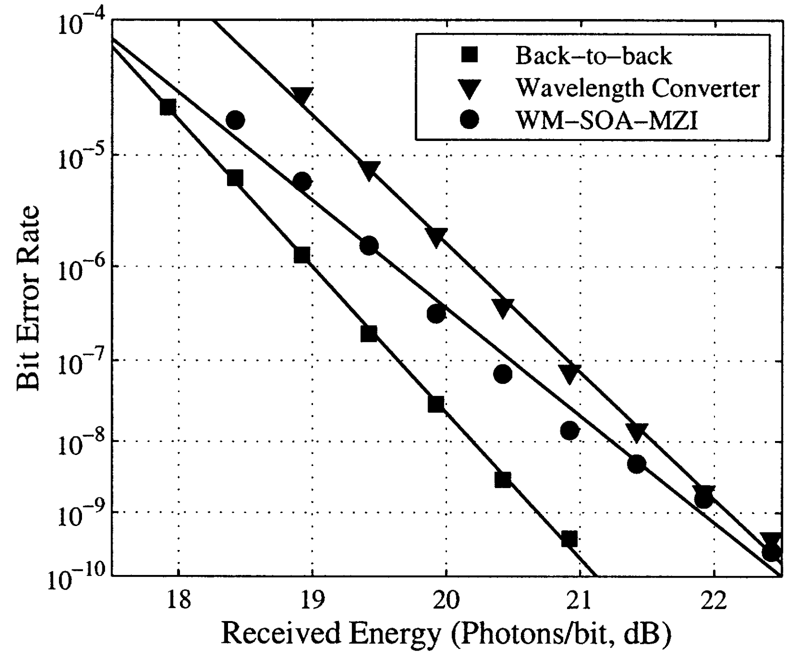

Figure 5-22: BER curves of the SOA wavelength converter and the wavelength-maintaining SOA-MZI, compared to a transmitter back-to-back.

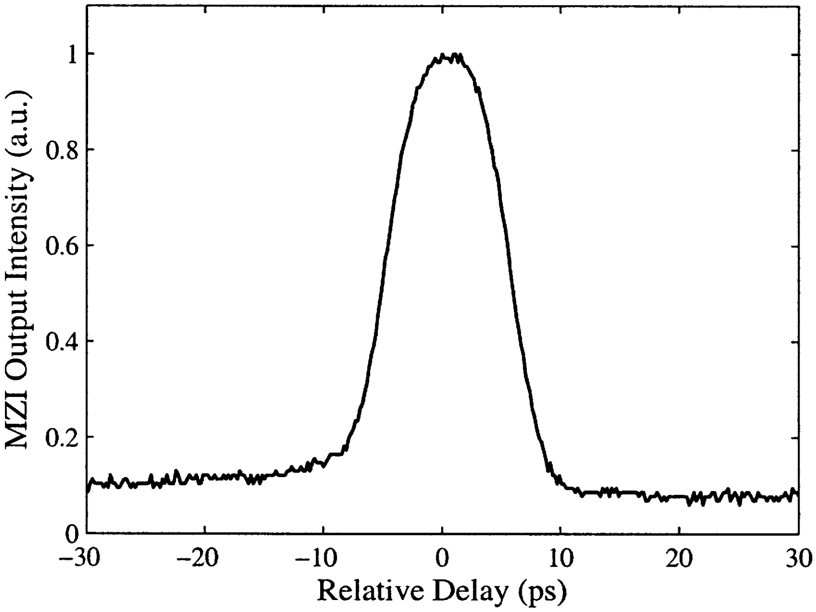

Figure 5-23: Switching window of the SOA-MZI. This plot shows the average output power of the SOA-MZI as a function of relative delay between the signal and control pulses.

5.3.2 The Wavelength-Maintaining SOA-MZI All-Optical Regenerator

Figure 5-24 shows the 100-km recirculating loop used to test the SOA-MZI's regenerative performance [?]. As above the optical pulse train is generated by a 10-GHz mode-locked fiber laser that is then modulated in the transmitter (Tx) with a $2^{31}-1$ PRBS. The loop itself contains two 50-km sections of large effective area fiber (LEAF) along with 3.2 km of dispersion compensation fiber (DCF). The DCF has a highly positive second order dispersion to compensate the negative second order dispersion that exists in the LEAF. Two EDFAs compensate loss in the loop, a single-polarization fiber isolator (SPFI) maintains a constant polarization, two variable attenuators control power in the loop, and a loop acousto-optic (A/O) modulator blocks pulses in the loop when necessary. There is also a variable delay to keep the loop length an integer number of bit periods long so that the control and signal pulses temporally overlap in the wavelength-maintaining SOA-MZI for all loop passes.

At the beginning of the loop experiment the load A/O modulator is closed, allowing data pulses to enter the loop. At the same time, the loop A/O modulator is open, discarding any pulses that are already in the loop. Once the loop is loaded with data, the loop A/O modulator closes, and the load A/O modulator opens. The data then recirculate through the loop 100 times, or ~10,000 km. As we saw in Figure 4-28, without regeneration, the cross-correlation of the pulses in the loop show fast deterioration of the pulses on successive passes. As before the cross-correlation is given by

$$C(\tau) = \int_{-\infty}^{+\infty} I(t) I_s(t-\tau)\, dt,$$

where $I(t)$ is the intensity envelope of the pulse being measured and $I_s(t)$ is the intensity envelope of the sample pulse.

Figure 5-25 the cross-correlation of the data pulses after passing 1 through 114 times through the loop with the wavelength-maintaining SOA-MZI regenerator placed in the recirculating loop. The data are taken by tapping off the loop data pulses right after the SOA-MZI. The cross-correlation of the 0-pass pulses have an IFWHM 5 ps.

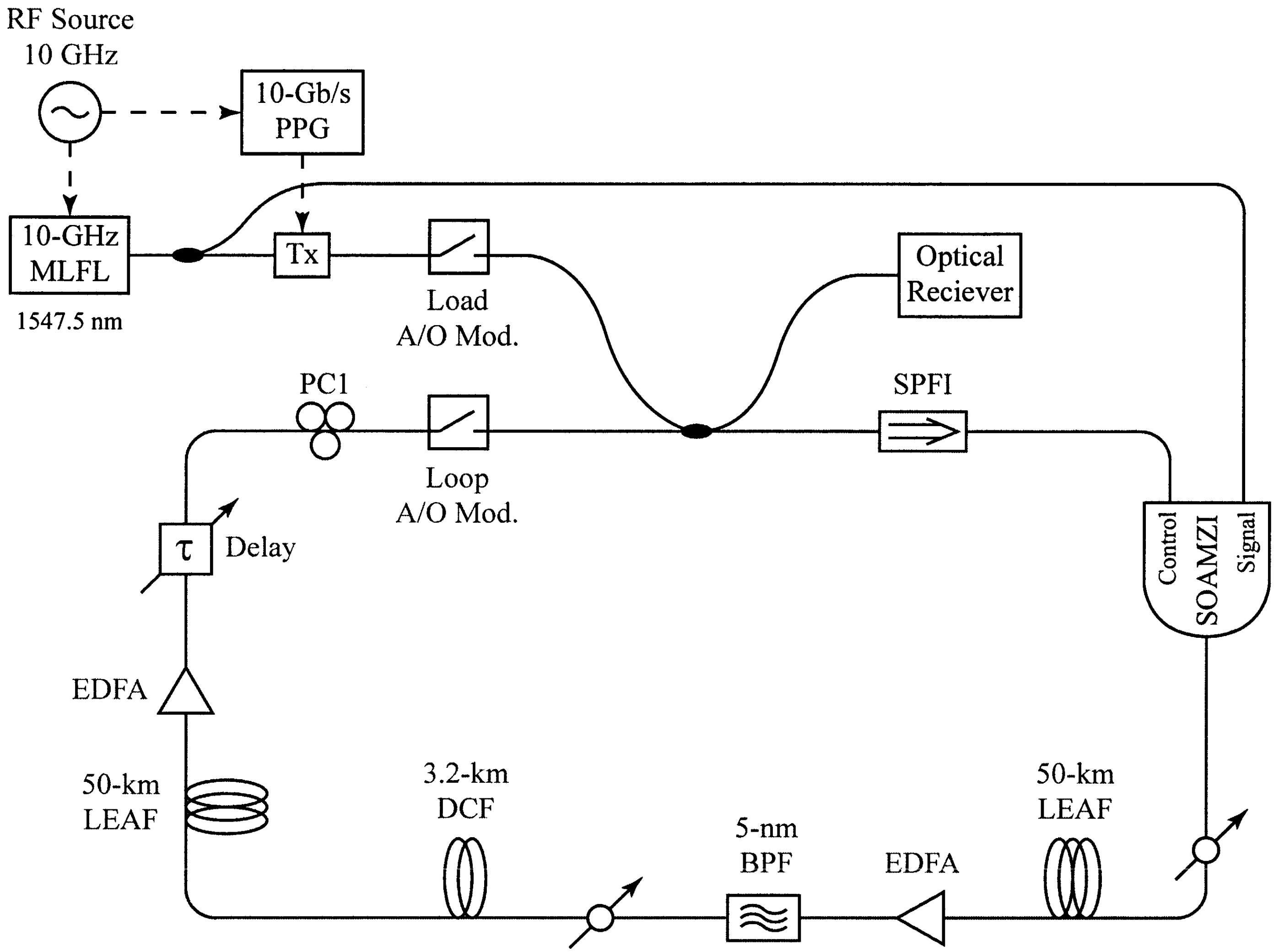

Figure 5-24: Schematic of the 100-km recirculating loop using the wavelength-maintaining SOA-MZI as a regenerator.

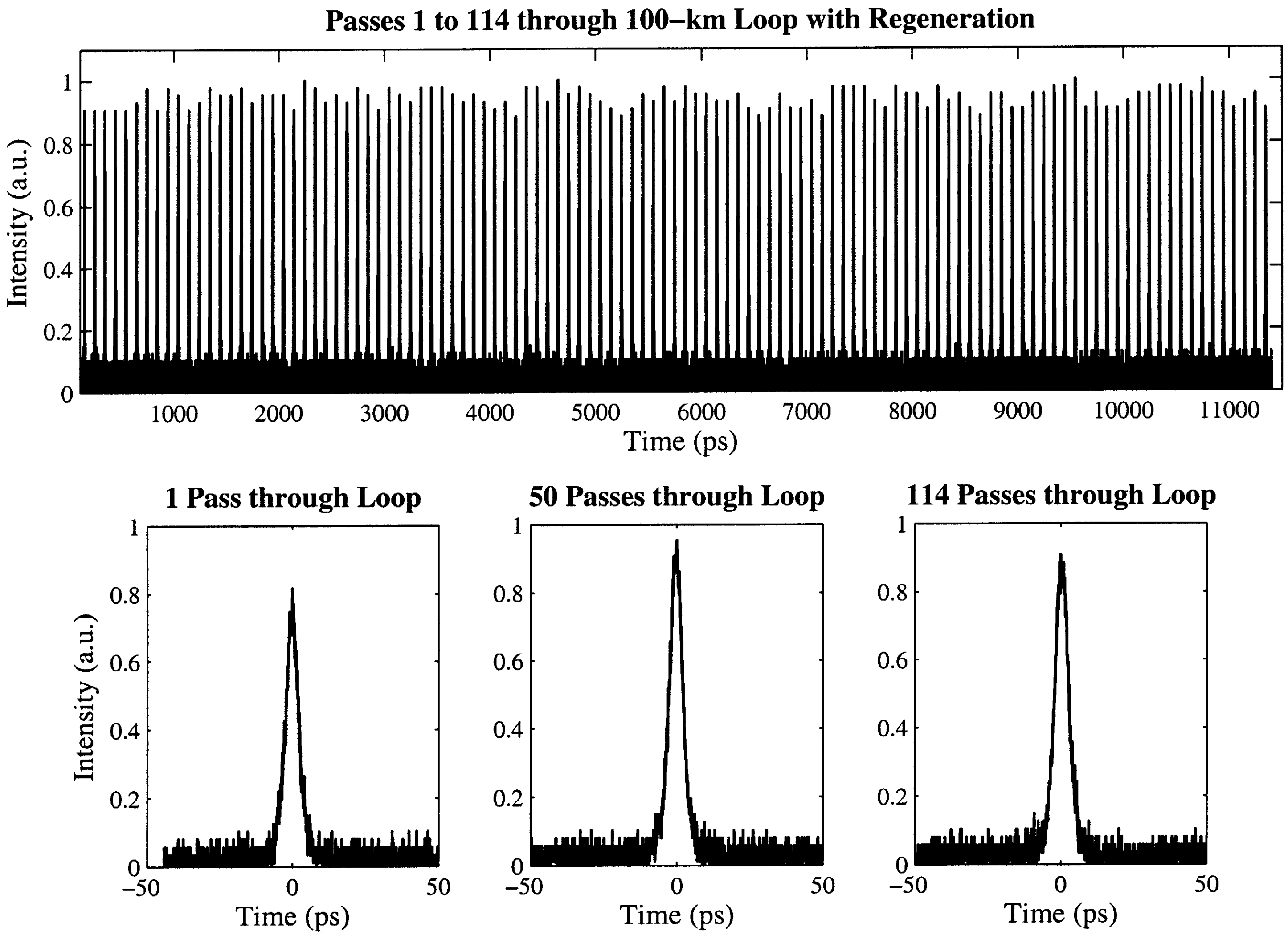

Figure 5-25: Cross-correlations of pulses through 100-km regenerative recirculating loop after 1 through 114 successive passes. The three smaller plots zoom in on the pulses after 1, 50, and 114 passes.

After 50 and 114 passes through the regenerator, the cross-correlation of the data pulses still have IFWHMs of 5 ps.

Figure 4-30 shows BER plots of the data pulses in the loop after 10 and 100 passes. The data are taken by tapping off the data pulses in the loop right after the WMFUNI. These data then enter a pre-amplified optical receiver, which is controlled by a gate signal from the same pulse generator that drives the two acousto-optic modulators. This gate signal ensures that the optical receiver only measures the bit-error rate during the 10th pass or the 100th pass. In these data, the wavelength-maintaining SOA-MZI has a 1.1-dB power penalty penalty compared to the transmitter back-to-back at an error rate of 10^{-9}. After 10 passes through the loop, the loop data have a power penalty of 1.3 dB. After 100 passes, the loop data have a power penalty of 1.6 dB compared to the back-to-back with no visible error floor.

5.4 Conclusions

Previous experimental work on SOA-MZIs have shown full switching operation at up to 80 Gb/s [9] and demultiplexing operation from 160 Gb/s to 4×40 Gb/s [28]. Moreover, SOA-MZIs have been used in regenerative loop experiments at up to 40 Gb/s [12]. In this experiment, the 40 Gb/s optical data stream is loaded onto a 300-km loop. The data propagates through the loop 100 times, and is regenerated each time. The regenerator itself is actually of cascade of two optical switches: a data inverting SOA switch using cross-gain modulation and a data inverting SOA-MZI switch. Simulations of the SOA-MZI all-optical switch, presented in Section 5.2, suggest that such an experiment at 40 Gb/s might be difficult at best. The simulations do suggest, however, that an SOA-MZI regenerator may function well if the SOA-MZI inverts the data, just as in [12].

This chapter, however, presented tests of an SOA-MZI optical switch that does not invert the data. This SOA-MZI switch can be adapted to all-optical regeneration, as shown in Figure 5-11. We used transmission experiments to test the SOA-MZI regenerator's performance. The wavelength-maintaining SOA-MZI successfully

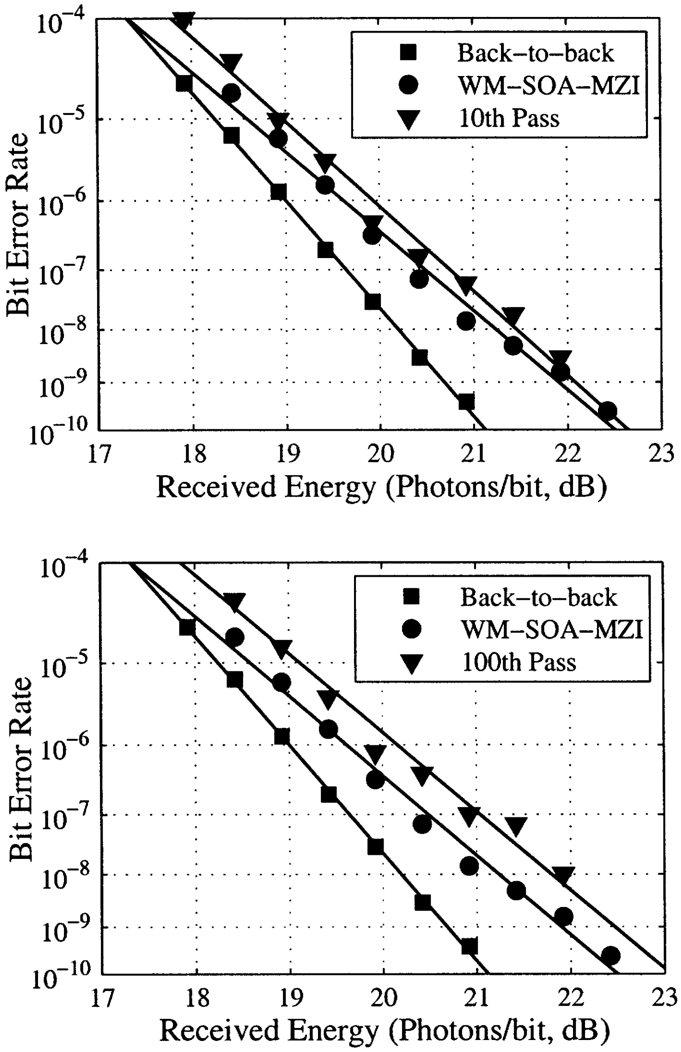

Figure 5-26: Bit error rates of the loop data after 10 passes (top) and 100 passes (bottom) through the regenerator. Both are compared to BER curves of the transmitter back-to-back and of the data after 1 pass through the regenerator.

regenerated a 10-Gb/s data train in a 100-km recirculating loop, shown in Figure 5-24. With $\sim$ 3-ps pulses, the wavelength-maintaining SOA-MZI should in principle operate in systems with data rates up to $\sim$ 100 Gb/s. The simulations suggest that a single SOA-MZI can operate at such high rates. As mentioned above, operation of a cascade of SOA-MZI switches, as in Figure 5-11, is more difficult. Further work is required to determine if the SOA-MZI of Figure 5-19 will operate as a regenerator at $>$ 40 Gb/s.

Bibliography

[1] R. Mears, L. Reekie, I. Jauncey, and D. Payne, "Low-noise Erbium-doped fibre amplifier operating at 1.54 μm," *Electronics Letters*, vol. 23, p. 1026, 1987.

[2] E. Desurvire, J. Simpson, and P. Becker, "High-gain Erbium-doped traveling-wave fiber amplifier," *Optics Letters*, vol. 12, no. 11, pp. 888–890, 1987.

[3] R. Ramaswami and K. Sivarajan, *Optical networks*. San Francisco, California: Morgan Kaufmann Publishers, second ed., 2002.

[4] K. L. Hall, G. Lenz, A. M. Darwish, and E. P. Ippen, "Subpicosecond gain and index nonlinearities in InGaAsP diode lasers," *Optics Communications*, vol. 111, pp. 589–612, Oct. 1994.

[5] S. Nakamura, Y. Ueno, and K. Tajima, "168-Gb/s all-optical wavelength conversion with asymmetric-Mach-Zehnder-type switch," *IEEE Photonics Technology Letters*, vol. 13, no. 10, pp. 1091–1093, 2001.

[6] D. Blumenthal, B. Olsson, G. Rossi, T. Dimmick, L. Rau, M. Masanovic, O. Lavrova, R. Doshi, O. Jerphagnon, J. Bowers, *et al.*, "All-optical label swapping networks and technologies," *Journal of Lightwave Technology*, vol. 18, no. 12, pp. 2058–2075, 2000.

[7] D. Apostolopoulos, D. Petrantonakis, O. Zouraraki, E. Kehayas, N. Pleros, and H. Avramopoulos, "All-Optical Label/Payload Separation at 40 Gb/s," *IEEE Photonics Technology Letters*, vol. 18, no. 19, p. 2023, 2006.

[8] R. Clavero, F. Ramos, J. Martinez, and J. Marti, "All-Optical Flip-Flop Based on a Single SOA-MZI," *IEEE Photonics Technology Letters*, vol. 17, no. 4, pp. 843–845, 2005.

[9] H. Dong, H. Sun, Q. Wang, N. Dutta, and J. Jaques, "All-optical logic and operation at 80 Gb/s using semiconductor optical amplifier based in the Mach-Zehnder interferometer," *Microwave and Optical Technology Letters*, vol. 48, pp. 1672–1675, 2006.

[10] K. L. Hall and K. A. Rauschenbach, "100-Gbit/s bitwise logic," *Optics Letters*, vol. 23, pp. 1271–1273, Aug. 1998.

[11] H. Chen, G. Zhu, Q. Wang, J. Jaques, J. Leuthold, A. Piccirilli, and N. Dutta, "All-optical logic XOR using differential scheme and Mach-Zehnder interferometer," *Electronics Letters*, vol. 38, no. 21, pp. 1271–1273, 2002.

[12] B. Lavigne, E. Balmefrezol, P. Brindel, B. Dagens, R. Brenot, L. Pierre, J.-L. Moncelet, D. de la Grandiere, J.-C. Remy, J.-C. Bouley, B. Thedrez, and O. Leclerc, "Low input power all-optical 3R regenerator based on SOA devices for 42.66 Gbit/s ULH WDM RZ transmissions with 23 dB span loss and all-EDFA amplification," *Optical Fiber Communications Conference*, 2003.

[13] Z. Zhu, M. Funabashi, Z. Pan, L. Paraschis, and S. Yoo, "10 000-Hop Cascaded In-Line All-Optical 3R Regeneration to Achieve 1 250 000-km 10-Gb/s Transmission," *IEEE Photonics Technology Letters*, vol. 18, no. 5, pp. 718–720, 2006.

[14] G. Agrawal and N. Olsson, "Self-phase modulation and spectral broadening of optical pulses in semiconductor laser amplifiers," *IEEE Journal of Quantum Electronics*, vol. 25, no. 11, pp. 2297–2306, 1989.

[15] P. Humblet and M. Azizoglu, "On the bit error rate of lightwave systems with optical amplifiers," *Journal of Lightwave Technology*, vol. 9, no. 11, pp. 1576–1582, 1991.

[16] F. Tricomi, *Integral Equations.* New York: Dover Publications, 1985.

[17] A. Yariv, *Optical electronics.* New York: Holt, Rinehart and Winston, third ed., 1985.

[18] H. Van Trees, "Detection, Estimation, and Modulation Theory Part I," 1968.

[19] H. Landau and H. Pollak, "Prolate spheroidal wave functions, Fourier analysis and uncertainty-III: The dimension of the space of essentially time-and band-limited signals," *Bell System Technology Journal*, vol. 41, no. 4, pp. 1295–1336, 1962.

[20] J. Proakis, *Digital communications.* New York: McGraw-Hill New York, 1995.

[21] D. Shnidman, "The calculation of the probability of detection and the generalized Marcum Q-function," *IEEE Transactions on Information Theory*, vol. 35, no. 2, pp. 389–400, 1989.

[22] D. Shnidman, "Note on the calculation of the probability of detection and the generalized Marcum Q-function," *IEEE Transactions on Information Theory*, vol. 37, no. 4, 1991.

[23] A. Papoulis, *Probability, Random Variables, and Stochastic Processes.* New York: McGraw-Hill, 1991.

[24] N. Johnson, S. Kotz, and N. Balakrishnan, *Continuous Univariate Distributions.* New York: John Wiley, 1995.

[25] J. Leuthold, M. Mayer, J. Eckner, G. Guekos, H. Melchior, and C. Zellweger, "Material gain of bulk 1.55 m InGaAsP/InP semiconductor optical amplifiers approximated by a polynomial model," *J. Appl. Phys*, vol. 87, no. 1, pp. 618–620, 2000.

[26] J. P. Wang, B. S. Robinson, S. A. Hamilton, E. P. Ippen, R. Mu, H. Wang, L. Spiekman, and B. B. Stefanov, "A performance optimization method for SOA-MZI devices," in *OFC 2007 Technical Digest*, (Anaheim, CA), 2007.

[27] M. Nielsen, B. Lavigne, and B. Dagens, "Polarity-preserving SOA-based wavelength conversion at 40 Gbit/s using bandpass filtering," *Electronics Letters*, vol. 39, no. 18, pp. 1334–1335, 2003.

[28] M. Heid, S. Jansen, S. Spalter, E. Meissner, W. Vogt, and H. Melchior, "160-Gbit/s demultiplexing to base rates of 10 and 40 Gbit/s with a monolithically integrated SOA-Mach-Zehnder interferometer," *European Conference on Optical Communication*, vol. 3, 2002.

Chapter 6

Future of All-Optical Data Regeneration

As discussed in Chapter 1, all-optical switching is not ready to compete with electronics in complicated logic and may remain so [1]. All-optical switches, however, may become useful in optical data regeneration [2], and there is evidence that all-optical regenerators have a performance advantage over electronic regenerators [3]. We saw two all-optical regenerators evaluated in this thesis, the WMFUNI and the SOA-MZI, both of which are based on interferometer switches. They both successfully regenerated a 10-Gb/s data pattern in transmission experiments over distances greater than 10,000 km. Simulations and experimental work suggest that extension of these results to 40 Gbit/s is possible.

With these results in hand, we now consider what the future course of regeneration in optical communications may be. There are many different designs for 3R and 4R all-optical regenerators, but most of them rely on one of only two different nonlinear media: semiconductor optical amplifiers (SOAs) and optical fiber. Each of these media have their advantages, which we will consider in this section. It is possible, of course, that the ultimate solution will be entirely different. For example an exotic nonlinear medium or new ultrafast electronics. It is even possible that regenerators will be dispensed with entirely, in favor of transmission links and modulation formats that do not require regeneration at all. We will briefly consider each of these questions in this Chapter.

6.1 Choice of Nonlinear Medium

Optical fiber and SOAs have important differences that guide the design of all-optical switches and regenerators. For example, fiber has such a weak nonlinearity that interferometric switches based on fiber require kilometer-long sections of it. Most interferometers are two-path interferometers, like the Mach-Zehnder, and such interferometers are difficult to stabilize when they are many meters long, to say nothing of thousands of meters. This fact is why the design of the WMFUNI of Chapter 4 is based on a single-arm interferometer in which the two pulses are separated in time in a single arm rather than being separated into separate arms. Unfortunately, this means that the pulses in the WMFUNI must be half as long as they otherwise would be in order to prevent the interference of neighboring bits. Thus, the WMFUNI forces the network to be less bandwidth efficient.

We could instead try to find a medium that is much more nonlinear than optical fiber, allowing us to use a very small two-arm Mach-Zehnder interferometer design. In Chapter 5 we saw such a design. The SOA-MZI switch we tested was integrated on a chip only ~1 cm long. Temperature controllers on the chip kept the Mach-Zehnder interferometer at the appropriate bias point. SOA-based regenerators also have a power advantage because of the high optical powers that fiber-based regenerators use to overcome fiber's weak nonlinearity. I estimate that the optical amplifiers used in the WMFUNI consume on the order of ~20 Watts of electrical power. The amplifiers in the SOA-MZI consume on the order of ~2 Watts of electrical power.

Nonetheless, fiber-based switches and regenerators do have one obvious advantage over SOA-based designs: as discussed in Chapter 4 optical fiber is a nearly instantaneous nonlinear medium. SOAs, on the other hand, have recovery times that can last several bits. This fact implies that the behavior of SOA-based switches will depend on not just the current bit being processed, but previous ones as well. In Chapter 5 we saw that the SOA-MZI's output pulses had variations in amplitude that depended on the data pattern. We also saw how this patterning can become worse in a cascade of switches, where the output of one switch becomes the input of the next, as in regeneration. These patterning effects can become more severe at higher data rates, as the simulations at 10 Gb/s and 40 Gb/s in Chapter 5 imply. Indeed the fastest regeneration result to date is of a fiber-based regenerator at 160 Gb/s over 186 km and three regeneration stages [4, 5]. An SOA-based regenerator has been tested at 160 Gb/s, but without a transmission test its performance is difficult to assess [6].

So, optical fiber's nonlinearity is too weak, and the SOA's nonlinearity is not instantaneous. A more far-off solution is the development of a medium with both a strong and instantaneous nonlinearity. Highly nonlinear fiber (HNLF) has been studied many years, although until recently HNLFs have had large chromatic dispersion at 1550 nm [7]. Experimental work on HNLFs includes 2R all-optical regeneration [8]. HNLFs cannot be integrated onto chips, so photonic crystals have been studied as an integrable nonlinear medium. Such devices can in theory produce very strong nonlinearities for switches [9], but experimental demonstrations have produced less than optimal nonlinearities with high insertion losses [10, 11].

6.2 Possibility of an Opto-Electronic Solution

All-optical regenerators are not yet the obvious solution. One advantage to all-optical signal regeneration, perhaps the primary commercial advantage, is the removal of costly optical to electrical to optical (OEO) transceivers, as we saw in Figure 1-4. All-optical solutions, however, are not the only possibility for next-generation networks. For example, Infinera has worked to reduce the cost of OEO transceivers through monolithic integration of optical and electronic devices onto indium-phosphide [12].

Even with significant cost reductions in opto-electronic designs, all-optical regeneration still has a speed advantage. SOA-based regenerators operate at data rates up to 40 Gb/s [13], and fiber-based regenerators operate at rates up to 160 Gb/s [4], where both results are for a single wavelength-channel. But all-optical regenerators are not ready for commercialization, so we should compare all-optical regenerator speeds not with opto-electronic speeds today, but rather with speeds 5 or 10 years from now. Already, we can see in the literature a number of electronic and opto-electronic tools operating at speeds approaching those of all-optical tools.

One such tool is the modulated optical transmitter, which provides the transceiver's electrical to optical conversion. Directly modulated laser sources, in which a laser diode is made to pulse by a direct modulation of the current drive, have been demonstrated up to 30 GHz [14]. Laser diodes can also be externally modulated by an electro-optic intensity modulator. Lithium niobate intensity modulators have been demonstrated at rates approaching 100 GHz [15, 16]. Unfortunately, lithium niobate modulators typically require swings in the drive voltage up to $\sim$5 Volts. InP-based devices, among others, can operate with lower drive voltages down to less than 2 Volts and with bandwidths up to 40 GHz [17, 18]. On the other side of the OEO conversion are the photodetectors that execute the optical to electrical conversion. Commercial InGaAs photodetectors already achieve 40-GHz bandwidths. Research work has extended bandwidths to 100 GHz in InP structures [19]. Other research has focused on increasing the photocurrent produced by photodetectors with, for example, avalanche photodiodes, although gain-bandwidth products still only reach 200 GHz [20].

Electronic processing has also advanced to high rates. A common measure of the upper limit of electronic processing speeds is data multiplexing, in which to lower rate data streams are combined into a single high rate data stream. Recently, a 2:1 electronic multiplexer was demonstrated at 60 Gb/s [21], and a 4:1 electronic multiplexer was demonstrated at 100 Gb/s [22]. More complicated circuitry is also possible, including a pseudo-random bit-stream generator that operates at 100 Gb/s [23]. Electronic processing at 100s of Gb/s involves many difficulties, but it is a well-established industry that cannot be ignored.

6.3 Transmission without Regeneration

Another avenue of research is unregenerated transmission. Instead of periodically regenerating the data signal, one can try to engineer the signal so that it will propagate through the fiber with less distortion. There are several ways to achieve unregenerated transmission, including pre-distorting the pulses to compensate distortions in the fiber and the use of exotic data modulation formats. Optical fiber propagation affects different modulation formats in different ways. For example, in links with uncompensated polarization-mode dispersion, return-to-zero ON/OFF keyed formats perform better than nonreturn-to-zero ON/OFF keyed formats, and differential phase-shift keyed formats perform even better [24]. Phase-shift modulation formats also often perform better in links with nonlinear effects because their intensity envelopes need not vary in time. So, changes in modulation formats could expand the available channel capacity and propagation distances in existing networks without the need for regeneration. Some recent results include 1.7-Tb/s transmission over 5,200 km [25], 6.4-Tb/s transmission over 2,100 km [26], and 25.6-Tb/s transmission over 240 km [27].

The advantage of unregenerated transmission is that it pushes the hardware to the ends of the optical fiber rather than placing regenerators along the entire link. So, hardware and performance upgrades can be achieved by making changes at the transeivers where we have the easiest access. Unfortunately, in a network, different data packets will take different optical paths through the network. So each packet may have to be modulated or pre-distorted for its particular path, which may make management of network resources a very difficult problem.

As we have seen, there are many ways to compensate and correct distortions caused by propagation through networks. This thesis has focused on all-optical interferometric regenerators, but there are other possible solutions. We have seen many of them in this chapter, and none of them today is the clear answer. It is certain, however, that research into data regeneration will continue to be an area of intense research. One such area of research is the simultaneous regeneration of many data channels, each modulated onto a different wavelength of light. When erbium-doped fiber amplifiers, which could amplify many wavelength channels simultaneously, became available, network capacity burst forward. A similar burst could follow the design of a successful multi-wavelength regenerator. This thesis has presented several promising ideas for all-optical regenerators, and with further development they could see application in low-power, ultrafast, multi-wavelength regeneration. They only require the arrival of a new nonlinear material or new device to make them ready for commercial application.

Bibliography

[1] H. Caulfield, C. Vikram, and A. Zavalin, "Optical logic redux," *Optik*, vol. 117, no. 5, pp. 199–209, 2006.

[2] O. Leclerc, B. Lavigne, E. Balmefrezol, P. Brindel, L. Pierre, D. Rouvillain, and F. Seguineau, "Optical regeneration at 40 Gb/s and beyond," *Journal of Lightwave Technology*, vol. 21, no. 11, pp. 2779–2790, 2003.

[3] B. Mikkelsen, G. Raybon, T. N. Nielsen, U. Koren, B. I. Miller, and K. Dreyer, "Opto-electronic and all-optical wavelength translators and their cascadability," *Optical Fiber Communication Conference*, vol. 4, 1999.

[4] S. Watanabe, F. Futami, R. Okabe, Y. Takita, S. Ferber, R. Ludwig, C. Schubert, C. Schmidt, and H. Weber, "160 Gbit/s optical 3R-regenerator in a fiber transmission experiment," *Optical Fiber Communications Conference*, 2003.

[5] C. Schubert, R. Ludwig, S. Watanabe, E. Futami, C. Schmidt, J. Berger, C. Boerner, S. Ferber, and H. Weber, "160 Gbit/s wavelength converter with 3R-regenerating capability," *Electronics Letters*, vol. 38, no. 16, pp. 903–904, 2002.

[6] J. Leuthold, L. Moller, J. Jaques, S. Cabot, L. Zhang, P. Bernasconi, M. Cappuzzo, L. Gomez, E. Laskowski, E. Chen, A. Wong-Foy, and A. Griffin, "160 Gbit/s SOA all-optical wavelength converter and assessment of its regenerative properties," *Electronics Letters*, vol. 40, no. 9, pp. 554–555, 2004.

[7] K. Hansen, J. Jensen, C. Jacobsen, H. Simonsen, J. Broeng, P. Skovgaard, A. Petersson, and A. Bjarklev, "Highly Nonlinear Photonic Crystal Fiber with Zero-Dispersion at 1.55 μm," *Optical Fiber Communication Conference (Optical Society, of America, Washington, DC, 2002) PDFA9.*

[8] P. Petropoulos, T. Monro, W. Belardi, K. Furusawa, J. Lee, and D. Richardson, "2R-regenerative all-optical switch based on a highly nonlinear holey fiber," *Optics Letters*, vol. 26, no. 16, pp. 1233–1235, 2001.

[9] M. Yanik, S. Fan, M. Soljacic, and J. Joannopoulos, "All-optical transistor action with bistable switching in a photonic crystal cross-waveguide geometry," *Optics Letters*, vol. 28, no. 24, pp. 2506–2508, 2003.

[10] M. Soljacic and J. Joannopoulos, "Enhancement of nonlinear effects using photonic crystals," *Nature Materials*, vol. 3, no. 4, pp. 211–219, 2004.

[11] J. Joannopoulos, P. Villeneuve, and S. Fan, "Photonic crystals: putting a new twist on light," *Nature*, vol. 386, no. 6621, pp. 143–149, 1997.

[12] L. Geppert, "A quantum leap for photonics," *IEEE Spectrum*, vol. 41, no. 7, pp. 16–17, 2004.

[13] G. Raybon, Y. Su, J. Leuthold, R. Essiambre, T. Her, C. Joergensen, P. Steinvurzel, and K. Feder, "40 Gbit/s pseudo-linear transmission over one million kilometers," *Optical Fiber Communication Conference*, 2002.

[14] K. Sato, "Semiconductor light sources for 40-Gb/s transmission systems," *Journal of Lightwave Technology*, vol. 20, no. 12, pp. 2035–2043, 2002.

[15] K. Noguchi, H. Miyazawa, and O. Mitomi, "75 GHz broadband Ti: LiNbO 3 optical modulator with ridge structure," *Electronics Letters*, vol. 30, no. 12, pp. 949–951, 1994.

[16] B. Thomsen, D. Reid, R. Watts, L. Barry, and J. Harvey, "Characterization of 40-Gbit/s pulses generated using a Lithium Niobate modulator at 1550 nm using frequency resolved optical gating," *IEEE Transactions on Instrumentation and Measurement*, vol. 53, no. 1, pp. 186–191, 2004.

[17] L. Zhang, J. Sinsky, D. Van Thourhout, N. Sauer, L. Stulz, A. Adamiecki, and S. Chandrasekhar, "Low-voltage high-speed travelling wave InGaAsP-InP phase modulator," *IEEE Photonics Technology Letters*, vol. 16, no. 8, pp. 1831–1833, 2004.

[18] K. Tsuzuki, T. Ishibashi, T. Ito, S. Oku, Y. Shibata, R. Iga, Y. Kondo, and Y. Tohmori, "A 40-gb/s InGaAlAs-InAlAs MQW n-i-n Mach-Zehnder Modulator with a drive Voltage of 2.3 V," *IEEE Photonics Technology Letters*, vol. 17, no. 1, pp. 46–48, 2005.

[19] H. Bach, A. Beling, G. Mekonnen, R. Kunkel, D. Schmidt, W. Ebert, A. Seeger, M. Stollberg, and W. Schlaak, "InP-based waveguide-integrated photodetector with 100-GHz bandwidth," *IEEE Journal of Selected Topics in Quantum Electronics*, vol. 10, no. 4, pp. 668–672, 2004.

[20] S. Demiguel, X. Zheng, N. Li, X. Li, J. Campbell, J. Decobert, N. Tscherptner, and A. Anselm, "High-responsivity and high-speed evanescently-coupled," *Electronics Letters*, vol. 39, no. 25, pp. 1848–1849, 2003.

[21] D. Kehrer, H. Wohlmuth, I. AG, and G. Munich, "A 60-Gb/s 0.7-V 10-mW monolithic transformer-coupled 2:1 multiplexer in 90 nm CMOS," *IEEE Compound Semiconductor Integrated Circuit Symposium*, pp. 105–108, 2004.

[22] T. Suzuki, Y. Nakasha, T. Takahashi, K. Makiyama, T. Hirose, and M. Takikawa, "144-Gbit/s selector and 100-Gbit/s 4:1 multiplexer using InP HEMTs," *IEEE MTT-S International Microwave Symposium Digest*, vol. 1, 2004.

[23] H. Knapp, M. Wurzer, W. Perndl, K. Aufinger, J. Bock, T. Meister, C. Res, I. Technol, and G. Munich, "100-Gb/s 2/sup 7/-1 and 54-Gb/s 2/sup 11/-1 PRBS generators in SiGe bipolar technology," *IEEE Journal of Solid-State Circuits*, vol. 40, no. 10, pp. 2118–2125, 2005.

[24] C. Xie, "Comparison of PMD sensitivity for different modulation formats," *2003 Digest of the LEOS Summer Topical Meetings*, 2003.

[25] C. Rasmussen, S. Dey, F. Liu, J. Bennike, B. Mikkelsen, P. Mamyshev, M. Kimmitt, K. Springer, D. Gapontsev, and V. Ivshin, "Transmission of 40× 42.7 Gbit/s over 5200 km UltraWave® fiber with terrestrial 100 km spans using turn-key ETDM transmitter and receiver," *28th European Conference on Optical Communication*, vol. 5, 2002.

[26] G. Charlet, J. Antona, S. Lanne, P. Tran, W. Idler, M. Gorlier, S. Borne, A. Klekamp, C. Simonneau, L. Pierre, Y. Frignac, M. Molina, F. Beaumont, J.-P. Hamaide, and S. Bigo, "6.4 Tb/s (159× 42.7 Gb/s) Capacity Over 21× 100 km Using Bandwidth-Limited Phase-Shaped Binary Transmission," *28th European Conference on Optical Communication*, vol. 5, 2002.

[27] A. Gnauck, G. Charlet, P. Tran, P. Winzer, C. Doerr, J. Centanni, E. Burrows, T. Kawanishi, T. Sakamoto, and K. Higuma, "25.6-Tb/s C+L-Band Transmission of Polarization-Multiplexed RZ-DQPSK Signals," *Optical Fiber Communication Conference, Postdeadline Session*, 2007.